IDENTIFICATION AND EVOLUTION OF TECTONIC FAULTS IN THE GREATER FAIRBANKS AREA, ALASKA

By

Rachel A. Frohman

RECOMMENDED:

Dr. Catherine Hanks

Dr. Richard Koehler

Dr. Wesley Wallace
Advisory Committee Chair

Dr. Paul McCarthy, Chair
Department of Geosciences

APPROVED:

Dr. Paul Layer
Dean, College of Natural Science and Mathematics

Dr. John Eichelberger
Dean of the Graduate School

12/8/14
Date

IDENTIFICATION AND EVOLUTION OF TECTONIC FAULTS IN THE GREATER FAIRBANKS AREA, ALASKA

A

THESIS

Presented to the Faculty

of the University of Alaska Fairbanks

in Partial Fulfillment of the Requirements

for the Degree of

MASTER OF SCIENCE

By

Rachel A. Frohman, B.S.

Fairbanks, Alaska

December 2014

Abstract

I have identified evidence for potentially active northeast-striking faults in the greater Fairbanks area and have developed a model for their evolution that defines the character of faults and timing of structural events. Seismicity, topographic data, and geological and geophysical maps show that potentially active faults correspond with previously mapped bedrock faults, topographic lows, and magnetic anomalies. Seismicity indicates that faults in Interior Alaska have low to moderate tectonic activity; geomorphic and structural analyses of mapped faults indicate they are dominantly left-lateral strike-slip, but have smaller normal or reverse components. The normal component of slip increases to the west toward the Nenana basin based on tilted fault block geometries observed in seismicity. Deformed Pliocene to Quaternary strata, placer deposits presumably related to tectonic-induced stream capture events, and geomorphic anomalies such as valley and basin asymmetry, barbed drainages, and changes in river morphology all suggest Pliocene-Quaternary tectonic activity along northeast-striking left-lateral faults.

Northeast-striking faults have been at least episodically active since the late Cretaceous. Northeast-striking fault-hosted gold deposits related to ~90 Ma intrusions suggest that fault parallel extension fractures or tension veins formed at ~90 Ma during a period of northwest-southeast extension. Thermochronological data are consistent with exhumation at ~56-42 Ma, possibly resulting from dextral shearing between the Denali and Tintina faults. Northeast-striking faults were reactivated as normal faults along pre-existing extensional trends. Thermochronological data suggest that strike-slip displacement on the Tintina fault significantly decreased at ~42 Ma. However, dip-slip motion continued along northeast-striking faults after

42 Ma as a result of contraction related to northward plate convergence. Drainage restorations, high-levels of background seismicity, and focal mechanisms support the hypothesis that at ~6 Ma, significant left-lateral motion occurred along northeast-striking faults and has continued to the present.

Table of Contents

Page

List of Figures

Page

List of Tables

Page

List of Appendices

Page

Acknowledgements

I would first like to recognize and thank my advisor, Dr. Wesley Wallace, for his care, encouragement, and constructive advice throughout the duration of my research. Also, I would like to thank my other committee members, Dr. Catherine Hanks and Dr. Richard Koehler, for their support and guidance and for the funding opportunities they have provided. I would like to thank the Department of Geosciences for the teaching assistantships and resources which have allowed me to successfully complete my research and also the Alaska Division of Geological and Geophysical Surveys, especially Dr. Richard Koehler, for providing the opportunity of an internship which included insightful field experiences, funding, and plentiful resources for completing my research. I would like to express my appreciation to the other funding agencies that financially supported my thesis work, which include the American Association of Petroleum Geologists Grants-In-Aid Program, the Geological Society of America Graduate Student Research Grant Program, BP Alaska, and the Geophysical Society of Alaska. I would like to thank Jeff Benowitz and Paul O'Sullivan for their valuable insights on apatite thermochronology. Finally, I would like to express my appreciation for the support of my family, friends, and colleagues at the University of Alaska Fairbanks and the Alaska Division of Geological and Geophysical Surveys.

Chapter 1: Introduction

1.1 Overview

The structural setting of southern Alaska is characterized by many strike-slip and contractional structures that accommodate northwest directed plate convergence. Strike-slip deformation extends into interior Alaska, which results in a significant seismic hazard for the greater Fairbanks area.

The neotectonic framework of Interior Alaska is defined by a series of linear, northeast-trending seismic zones including the Rampart, Minto Flats, Fairbanks, and Salcha seismic zones (Figures 1.1 and 1.2). These zones are characterized by diffuse seismicity; multiple moderate to large magnitude earthquakes, including twelve magnitude 6.0-7.3 earthquakes in the last 100 years; and focal mechanisms that indicate dominantly left-lateral strike-slip motion (Page et al., 1991; Ratchkovski and Hansen, 2002; Ruppert et al., 2008; Figure 1.1). In the 1930s and 1960s, magnitude 7.3 and 6.5 earthquakes occurred in the Salcha and Rampart seismic zones, respectively (Figure 1.1) and caused extensive ground failures, fissures, and landslides (Bramhall, 1938; Ruppert et al., 2008). Despite the occurrence of moderate to large magnitude earthquakes within the greater Fairbanks area, no surface ruptures have been documented and few studies have specifically focused on searching for surface evidence of young deformation.

The poor understanding of seismogenic structures contributes to large uncertainties in seismic hazard assessments, which ultimately affects multi-million dollar infrastructure and public safety in urban areas in and around Fairbanks. Identifying and characterizing seismogenic structures in Interior Alaska will help to develop a consistent tectonic model and will help

contribute to the understanding of strike-slip deformation inboard of subduction zones around the world.

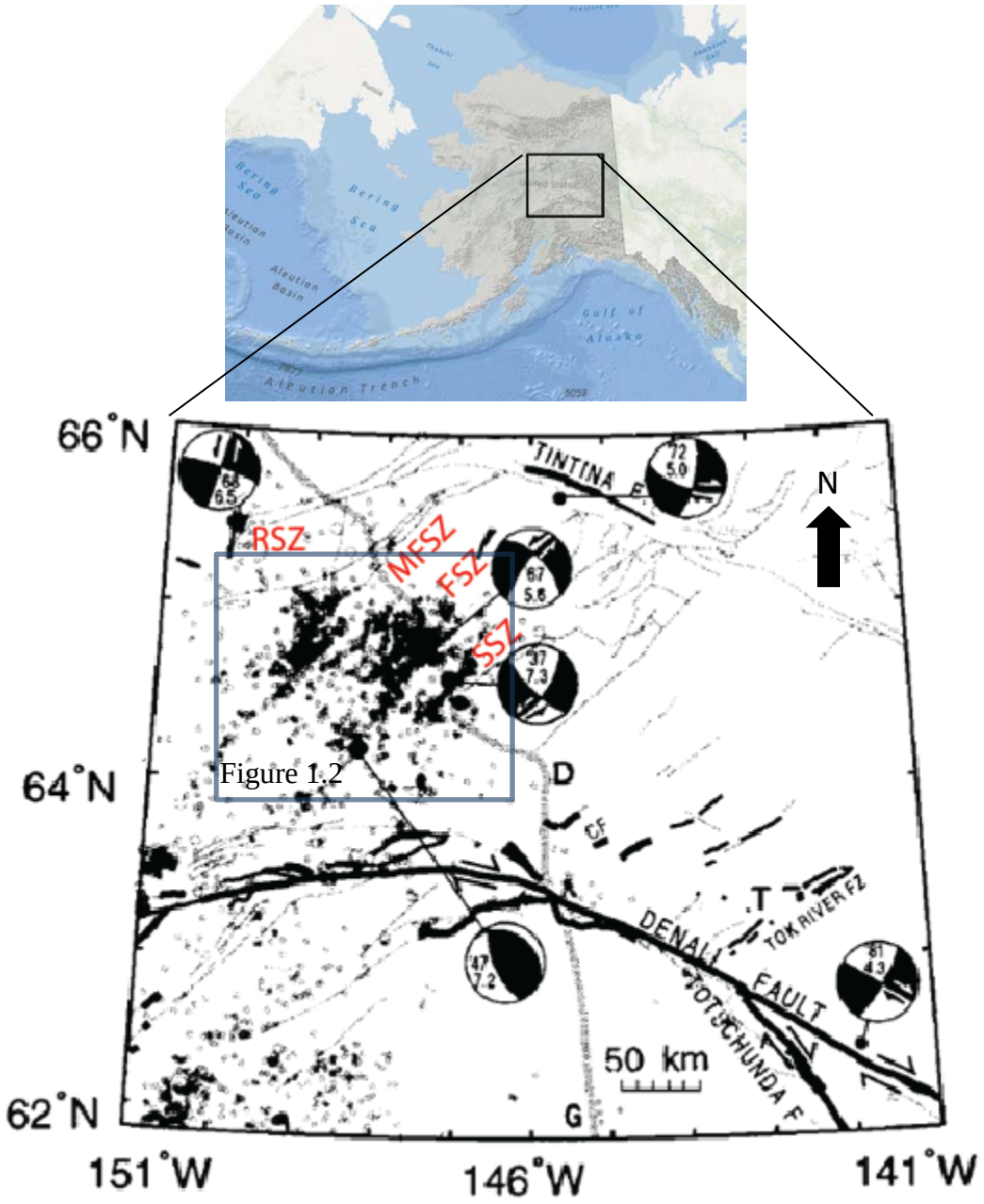

Figure 1.1: Map of Alaska and seismicity map (modified from Page et al., 1995) showing historical earthquakes of central Alaska: MFSZ, Minto Flats seismic zone; FSZ, Fairbanks seismic zone; SSZ, Salcha seismic zone; and RSZ, Rampart seismic zone.

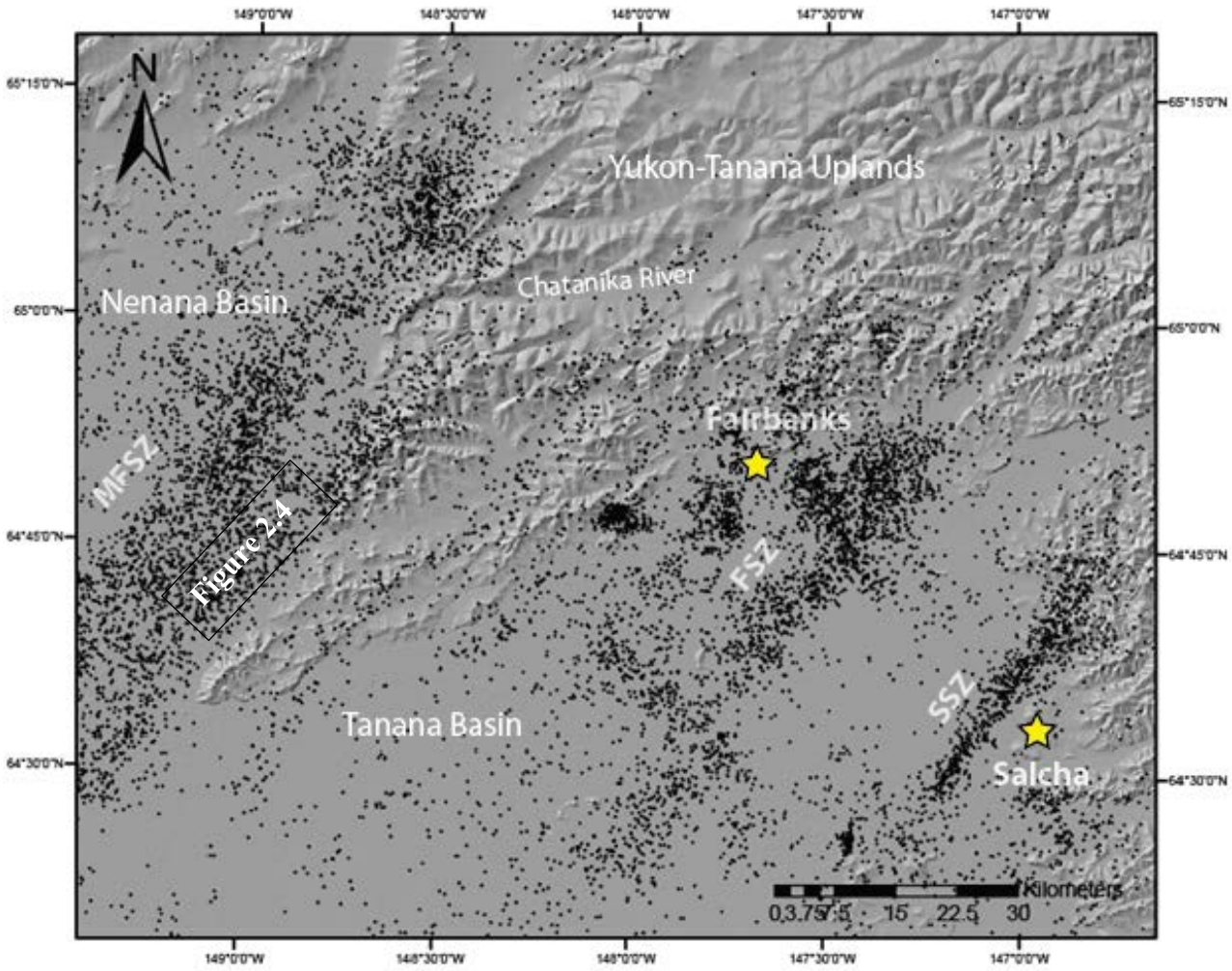

Figure 1.2: Study area location and seismicity map including major physiographic features. Hypocenters (black dots) from the Alaska Earthquake Information Center (AEIC, 2011) include events up to 30 km in depth. Location of map is shown in Figure 1.1.

Previous researchers have speculated that abandoned drainages, underfit streams, and abrupt changes in river morphology may indicate active tectonism in Interior Alaska (e.g., Lesh and Ridgway, 2007). Others have noted stream capture, bedrock highs in valley bottoms, major local differences in elevation of gold-bearing gravels, and anomalously deep accumulations of gold-bearing gravels as possible indicators of active tectonism in the Fairbanks area (e.g., Metz, 1991). However, these speculations have lacked sufficient structural or surficial geologic data to

make reliable interpretations. Thus, the main goal of this thesis is to provide critical information needed for understanding the character of seismogenic faults and their history, in part so that tectonic models of Interior Alaska may be refined.

1.2 Study Area Location

The study area is located around Fairbanks in central Alaska and includes the western Yukon-Tanana uplands, the northern margin of the Tanana basin, and the eastern margin of the Nenana basin (Figure 1.2). The study area also encompasses Salcha and extends north to the Chatanika River drainage. It includes structures within the Minto Flats, Fairbanks, and Salcha seismic zones, although field studies were primarily focused on structures within the Fairbanks seismic zone.

1.3 Hypotheses and Objectives

The main hypotheses investigated in this thesis are that some of the northeast-striking potentially active faults around the greater Fairbanks area formed in Late Cretaceous time, have been at least periodically active since Late Tertiary time, and have influenced the geology, landscape, and drainage patterns since at least Neogene time. These hypotheses are supported by a multitude of geochronologic, geologic, geomorphic, and structural geologic data from this study and previous studies that better defines the Cenozoic tectonic regime.

The overall objectives of this research are to: 1) determine how faults in the greater Fairbanks area evolved over time by: analyzing and synthesizing geological, geophysical and topographic data; conducting outcrop analysis of fault exposures; and interpreting apatite fission-track data; 2) identifying surface geologic evidence for neotectonic deformation by conducting

quantitative geomorphological analyses of the landscape and drainages; and 3) integrating these detailed observations with regional observations into a consistent tectonic model for Interior Alaska.

1.4 Importance of Research

This research will contribute to our understanding of the regional and local tectonic evolution of Interior Alaska. It will also contribute to better assessments of seismic hazards in the Fairbanks area, the evolution of petroleum systems in the Nenana basin, and the formation of placer gold deposits in the Fairbanks Mining District.

Accurate seismic hazard assessment is essential for the infrastructure of the Trans-Alaska pipeline system (TAPS), a multi-billion dollar project that transports oil from the North Slope to Valdez (White, 2012). It is also important for the construction of future gas pipelines and the safety of urban areas, especially the densely populated greater Fairbanks area, which spans the Fairbanks seismic zone.

Tectonics controls many geologic factors of a petroleum system, such as sediment flux and basin position, geometry, and subsidence. The Nenana basin is currently being explored for oil and gas. The basin is most prospective near the north end, which is on the western border of the Yukon-Tanana uplands and receives deposits from the Yukon-Tanana uplands and the Fairbanks area (Van Kooten et al., 2012). A better understanding of the thermal and structural history of the Nenana basin is important for evaluating source rock potential and hydrocarbon maturation. Understanding the unroofing history of the Yukon-Tanana uplands could provide

valuable insight on the depositional history of reservoir rocks within the northern part of the basin.

Finally, several examples of stream capture inferred to be the result of active tectonics in the Fairbanks area resulted in sediment reworking and flow reversals that contributed to the tilt, offset, or formation of placer deposits (Metz, 1991). Understanding these captured drainage patterns and how they were influenced by structures in the past could potentially help define zones of active deformation, re-evaluate current prospects, and identify new prospects in the Fairbanks area. Vertical displacement on young structures also could have resulted in previously unrecognized changes in thickness of or depth to placer deposits.

Chapter 2: Regional Setting

The study area is bounded by two regional-scale right-lateral strike-slip faults: the Denali fault to the south and the Tintina fault to the north (Figures 1.1 and 1.2). The timing of motion and displacement along both the Denali and Tintina faults is important for understanding tectonic models of Interior Alaska that will be explained in the following sections.

2.1 Regional Structures

2.1.1 The Denali Fault

The Denali fault is an active, right-lateral strike-slip fault that extends for more than 2000 km from southeastern Alaska to the Bering Sea (Haeussler, 2008; Figure 2.1). It is one of several regional physiographic and structural features in southern and south-central Alaska that display northward convex curvature (e.g., the Tintina fault and the southern Alaska margin; Figure 2.1). The axis of these curved regional physiographic and structural features is referred to as the oroclinal hinge (Haeussler, 2008). This oroclinal hinge spans a distance of ~100 km. The Denali fault was the source of the 2002 M7.9 Denali fault earthquake which ruptured along the central and eastern Denali fault and parts of the Totschunda and Susitna Glacier faults (Eberhart-Phillips et al., 2003; Haeussler et al., 2004).

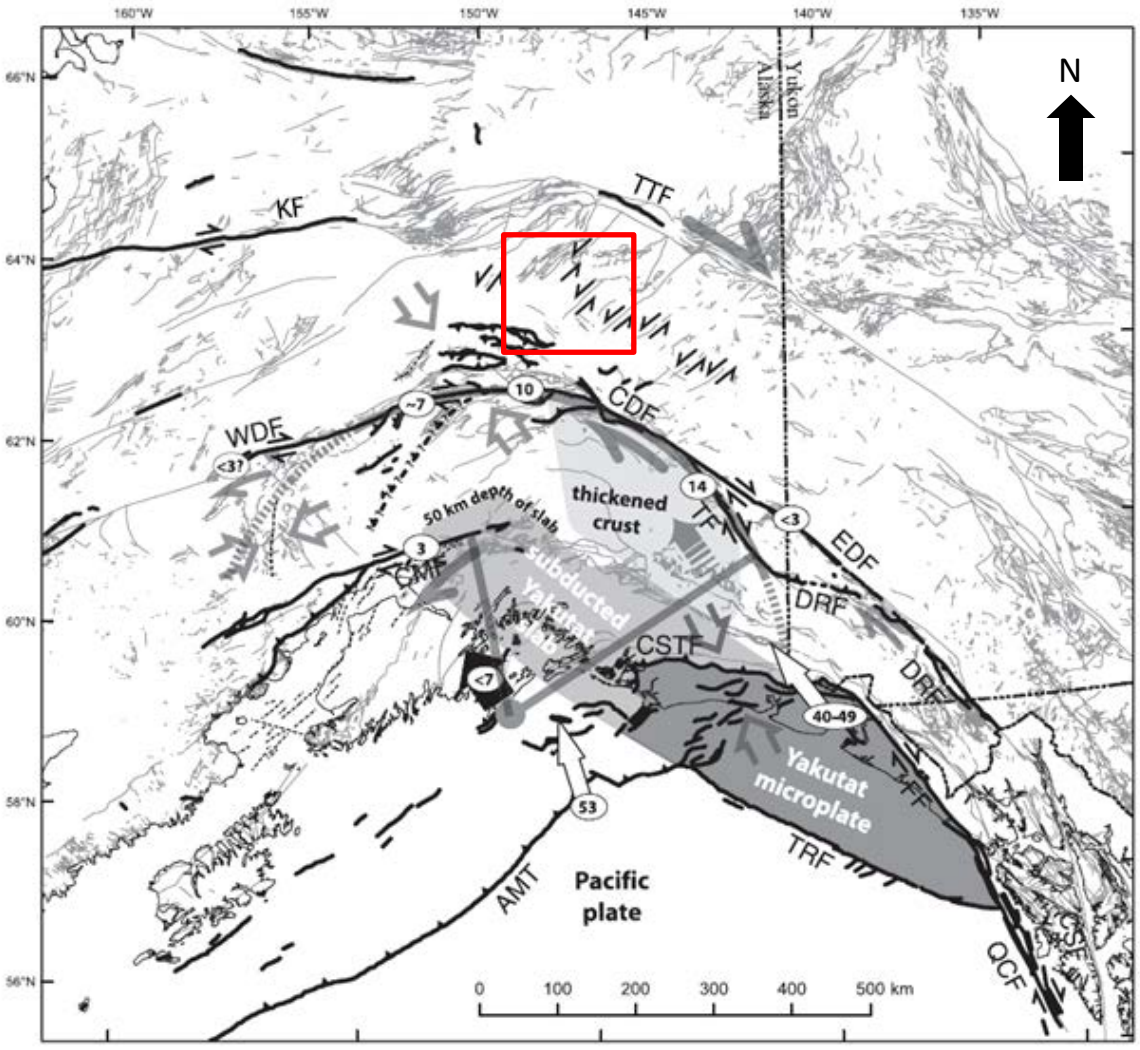

Figure 2.1: Neotectonic model from Haeussler (2008) of southern Alaska. Study area is outlined in red. Thick arrows pointed toward each other represent areas of shortening. Fault or block slip rates in white ovals are mm/yr. Black arrow represents northwestward migration of the Southern Alaska Block (SOAK). Fault names: KF, Kaltag fault; TTF, Tintina fault; WDF, western Denali fault; CDF, central Denali fault; EDF, eastern Denali fault; DRF, Duke River fault; LCF, Lake Clark fault; CSTF, Chugach-St. Elias thrust fault; AMT, Aleutian megathrust; QCF, Queen Charlotte fault; TRF, Transition fault; CSF, Chatham Strait fault; FF Fairweather fault.

The pre-Tertiary history of the Denali fault is very unclear. Nokleberg and others (1985, 1994) estimated ~400 km of right-lateral displacement since the early Tertiary on the eastern part of the Denali fault based on K-Ar hornblende and biotite isotopic ages (~56 Ma) of a deformed and metamorphosed quartz diorite batholith and the metasedimentary rocks it intruded. These rocks are part of an assemblage of metamorphic and igneous rocks termed the Maclaren terrane that can be correlated with the Kluane Schist and the Ruby Range batholith in the southern Yukon Territory. Benowitz and others (2012) used a range of dating methods including U-Pb, $^{40}Ar/^{39}Ar$, and apatite fission-track analysis, as well as petrological analyses, to constrain syn-tectonic magmatic, metamorphic, and rapid exhumation events in the Cottonwood terrane in the eastern Alaska Range. They concluded that at least 100 km of right-lateral displacement occurred from ~51 Ma to ~25 Ma and 300 km of right-lateral displacement occurred since ~25 Ma along the eastern Denali fault.

Much evidence exists for Quaternary offset along the Denali fault, including shutter ridges, scarps, vegetation lineations, and offset drainages (Haeussler et al., 2004; Koehler et al., 2011; Schwartz et al., 2012; Koehler, 2013). Cosmogenic dating of offset moraines and other glacial features along the central Denali fault suggests slip rates of about 10 mm/yr (Matmon et al., 2006; Haeussler, 2008; Mariaux, 2009). However, slip is not homogeneous along the length of the fault. Higher slip rates (14 mm/yr) were determined on the eastern Denali fault and lower slip rates (9 mm/yr) were determined on the central Denali fault, implying that slip rates decrease toward the west along the fault (Fletcher, 2002; Matmon et al., 2006; Haeussler, 2008; Mariaux et al., 2009).

2.1.2 The Tintina Fault

The Tintina fault system is a major right-lateral strike-slip fault and extends for more than 1000 km from central Alaska through the Yukon Territory (Figure 2.1). It lies parallel to the Denali fault and about 250 km to the north.

Only a few studies characterize the timing of displacement along the Tintina fault. Earlier studies interpreted approximately 450 km of right-lateral displacement between middle Cretaceous and Late Eocene or Oligocene time (Gabrielse, 1985). Gabrielse and others (2006) suggested that 400 to 430 km of right-lateral displacement occurred during Middle to Late Eocene time (~48-41 Ma) on the Tintina and Northern Rocky Mountain Trench faults and splays, based on restorations across the Tintina fault of northwest-vergent thrust faults in central and western Yukon Territory and Eocene alkalic igneous rocks. Saltus (2010) suggested about 490 km of apparent right-lateral displacement during the Eocene based on matching magnetic anomalies across the fault. He concluded that ~60 km of offset was accommodated by extension between late-Early Cretaceous and latest Cretaceous, presumably related to extensive Late Cretaceous magmatism. Gabrielse and others (2006) reported Paleocene to Eocene deformed bimodal volcanic and plutonic rocks in local, minor, fault-bounded basins along the Kechika, Spinel, and Northern Rocky Mountain Trench faults. The basins locally contain Eocene dikes that appear compatible with dextral shear on bounding faults. Gabrielse and others (2006) also reported offset of Eocene structural culminations and related erosional surfaces of Paleocene to Eocene conglomerates along the Spinel fault, which could suggest younger Late Eocene or Oligocene movement.

In Interior Alaska, Till and others (2007) reported 60 Ma (Ar/Ar) emplacement and transtensional deformation of plutons and metamorphic rocks along the Victoria Creek fault, a splay of the Tintina fault that may connect westward with the Kaltag fault. Apatite fission-track ages from south of the Victoria Creek fault recorded a cooling event at 45 Ma, and periods of local exhumation as young as 18 Ma between the Victoria Creek fault and the Tozitna fault, a splay of the Tintina fault that is just north of the Victoria Creek fault (Till et al., 2004).

Significant right-lateral displacement on the Tintina fault decreased in Canada by ~42 Ma, based on a granitic body (K/Ar age of 41.6 ± 2.2 Ma) that flanks the Northern Rocky Mountain Trench and is only slightly deformed (Evenchick, 1988; Gabrielse et al., 2006).

Evidence for Quaternary movement along the Tintina fault is limited to shallow scattered seismicity (up to M5) and a Holocene scarp along the Medicine Lake lineament (Foster et al., 1983; Plafker et al., 1994; Figure 2.1). Additionally, Weber and Foster (1982) inferred Tertiary and possible Quaternary movement along the Preacher Creek lineament based on a 6 m high scarp and stream bank exposures of the fault that show Tertiary conglomerates in fault contact with older slate, quartzite, and greenstone. Quaternary movement is located directly to the northeast of the Minto Flats, Fairbanks, and Salcha seismic zones, and east of the oroclinal hinge. The Kaltag fault is considered by some authors (e.g., Patton and Hoare, 1968; Till et al., 2003) to be the western extension of the Tintina fault, however, the connection between the two faults is poorly understood (Page et al., 1995).

2.2 Clockwise Block Rotation in Interior Alaska

Previous research indicates that a number of the active structures in Interior Alaska are the products of right-lateral shear and contraction driven by subduction of the Pacific plate and the buoyant Yakutat microplate in southern Alaska (e.g., Page et al., 1995; Ratchkovski and Hansen, 2002; Bemis and Wallace, 2007; Lesh and Ridgway, 2007; Haeussler, 2008). Current neotectonic models suggest that collision and subduction of the buoyant Yakutat plate in southern Alaska drives counterclockwise motion of the crust south of the Denali fault (Southern Alaska Block) about a pole located south of Prince William Sound (Haeussler, 2008; Figure 2.1). The collision also drives contractional deformation north of the Alaska margin accommodated by the Alaska Range Northern Foothills Fold and Thrust Belt (Bemis et al., 2012). Page and others (1995) proposed a block rotation model in which the Minto Flats, Fairbanks, and Salcha seismic zones define northeast-striking, left-lateral faults (Figure 2.2). They interpreted these seismic zones as boundaries of a series of crustal blocks that rotate clockwise within a dextral simple-shear zone bounded by two primary, right-lateral east-west striking fault systems: the Denali fault system to the south and the Tintina fault system to the north (Figure 2.2).

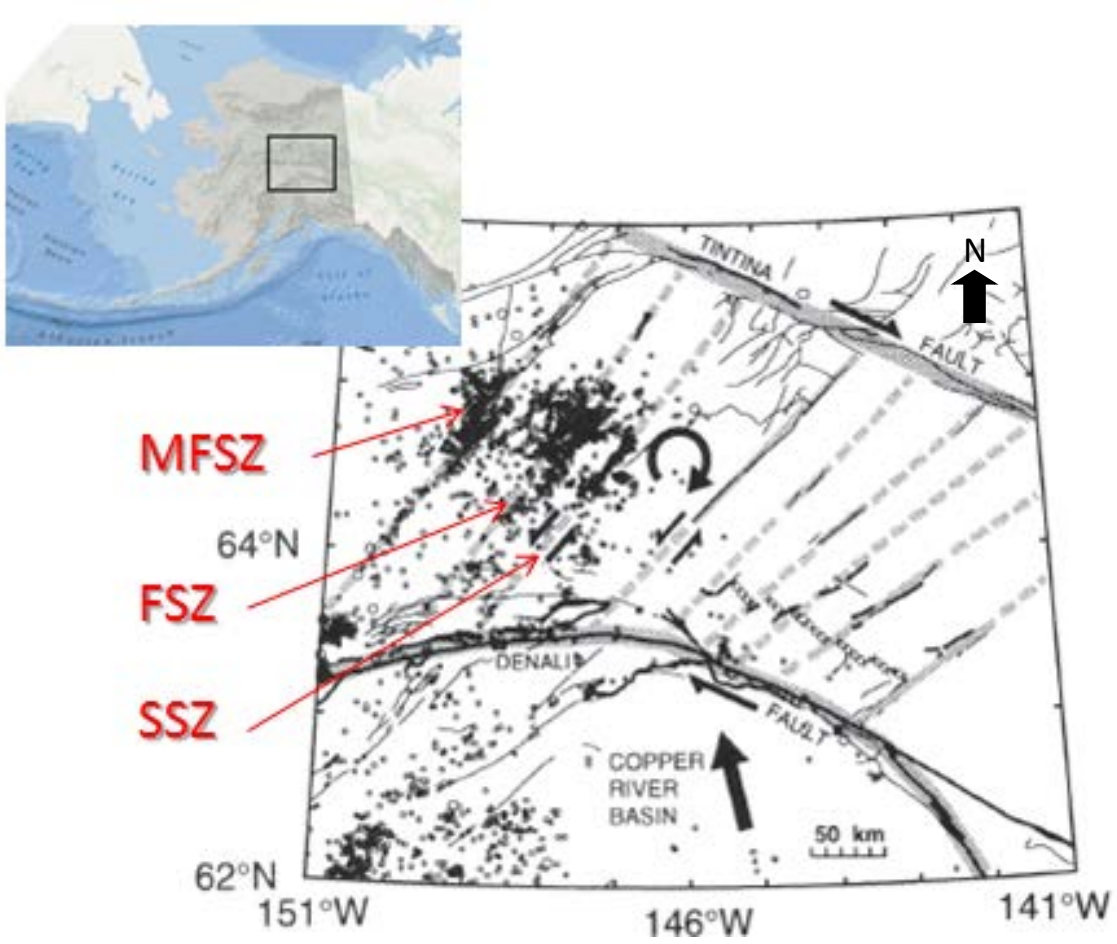

Figure 2.2: Clockwise block rotation model after Page and others (1995). MFSZ, Minto Flats seismic zone; FSZ, Fairbanks seismic zone; SSZ, Salcha seismic zone.

The evidence presented in the previous sections suggests that significant right-lateral motion along the Tintina and Denali faults began at ~60 and ~56 Ma, respectively, and that the majority of right-lateral displacement along the Tintina fault ceased by ~42 Ma. However, significant right-lateral displacement continued along the Denali fault and may even have increased substantially since ~25 Ma (Benowitz et al., 2012). This implies that significant horizontal shear between the Denali and Tintina faults occurred between ~56 and 42 Ma, but that displacement on the Tintina fault was limited after that.

2.3 Geology of the Fairbanks Area

2.3.1 Bedrock Geology

The bedrock geology of the greater Fairbanks area is dominated by metamorphic assemblages of the Yukon-Tanana terrane, which extends for over 2000 km from southeastern Alaska and western Canada to the western-most Yukon-Tanana uplands in east-central Alaska (Newberry et al., 1996; Wilson et al., 1998). The Yukon-Tanana terrane includes metasedimentary, metavolcanic, and metaplutonic rocks of Late Precambrian to early Mesozoic protolith age interpreted to have been metamorphosed during collision of a magmatic arc terrane with North America in Early Mesozoic time (Newberry et al., 1996; Hansen and Dusel-Bacon, 1998).

The most detailed (1:63,360 scale) geologic mapping in the region was done by Newberry and others (1996) in the Fairbanks Mining District. This map was built upon earlier mapping efforts compiled and published by Robinson and others (1990). It covers the western portion of the Yukon-Tanana terrane and includes the northeast part of the Fairbanks quadrangle, the southeast part of the Livengood quadrangle, and the southwest part of the Circle quadrangle. Newberry and others (1996) described the rocks within the Fairbanks Mining District as consisting of four structurally juxtaposed metamorphic sequences. They described these sequences as "…1) amphibolite facies metasedimentary and metavolcanic rocks of the Proterozoic [protolith age] Fairbanks Schist; 2) Ordovician to Upper Devonian [protolith age] low grade metamorphic phyllites of the Birch Hill Sequence; 3) the amphibolite facies metavolcanic and metasedimentary rocks of the Muskox Sequence, which contains Upper Devonian U-Pb zircon ages; and 4) the eclogite facies Chatanika Terrane, which contains

protoliths of Devonian-Mississippian age." The Fairbanks Schist is the dominant bedrock unit of the Fairbanks Mining District (Newberry et al., 1996).

Newberry and others (1996) mapped many continuous and closely spaced northeast-striking, high-angle faults that dip steeply to either the northwest or the southeast. Many of these northeast-striking faults exhibit apparent left-lateral offset ranging from a few meters to several kilometers and vertical offsets of up to one kilometer. Also, northeast-striking faults are commonly interconnected by west-northwest-striking faults that are interpreted as thrust faults. Newberry and others (1996) also noted northwest-verging isoclinal folds cut by later northeast-verging isoclinal to open folds. These fold episodes are inferred to correlate with several episodes of regional metamorphism.

2.3.2 Development of a Northeast-Striking Structural Grain

In the Fairbanks Mining District and throughout the Yukon-Tanana uplands, mid- to Late Cretaceous time was characterized by pulses of widespread granitic intrusions at ~110 Ma and 94-87 Ma (Newberry et al., 1996; Dusel-Bacon and Murphy, 2001). Trace and major element compositions indicate a within-plate signature (Newberry et al., 1996; Wilson et al., 1998; Dusel-Bacon and Murphy, 2001). Many ~90 Ma granitic intrusions were associated with gold-mineralization along regional northeast to northwest-striking faults and shear veins in the Fairbanks Mining District such as the Ryan Lode, Fort Knox, and Dolphin deposits (Bakke, 1995; McCoy et al., 1997; Bakke et al., 2000; McCoy, 2000; Thompson and Newberry, 2000; Rhys et al., 2003).

The Ryan Lode gold deposit is located west of Fairbanks in Ester, Alaska, and west of the Fairbanks seismic zone. McCoy and others (1997) dated hydrothermal and intrusion-related minerals along the Ryan Lode fault (N22°E; Avalon, 2014) and Curlew intrusive using the $^{40}Ar/^{39}Ar$ dating method. Hydrothermal white mica along the Ryan Lode fault yielded an age of 89.1 ± 0.3 Ma and hydrothermally altered schist yielded an age of 87.6 ± 0.3 Ma. In the Curlew intrusive, hornblende and biotite from quartz diorite yielded ages of 90.2 ± 0.3 Ma and 90.2 ± 0.3 Ma, respectively. The intrusion is cut by the Curlew shear zone (N15°W), which implies that the shear zone is younger than gold mineralization (Avalon, 2014), but the age of the hydrothermal white mica along the Ryan Lode fault suggests that faulting occurred just a few million years after the intrusion.

The Pogo gold deposit, located roughly 80 km southeast of Fairbanks, is cut by southeast-dipping normal faults and east- to northeast-striking, steeply dipping left-lateral faults. Both sets of faults appear to have exploited and overprinted earlier syn- to post-mineralization 92.7 ± 0.3 Ma mafic dikes (Rhys et al., 2003; Figure 2.3).

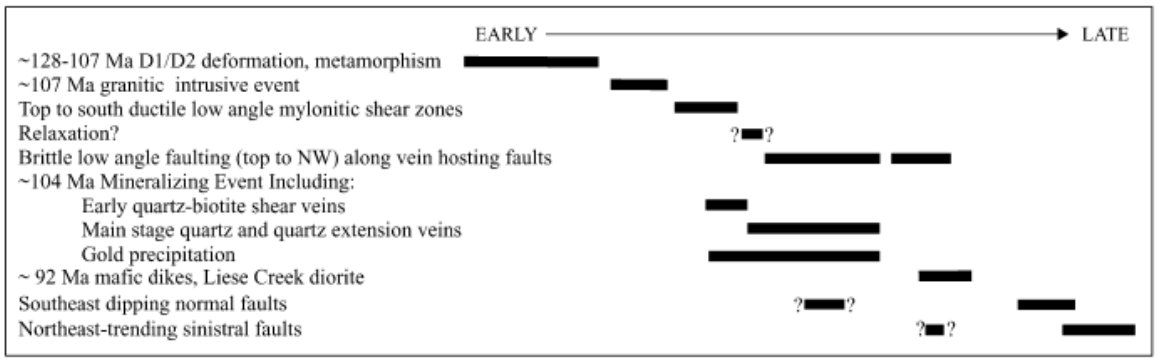

Figure 2.3: Relative timing of geologic events at the Pogo gold deposit (Rhys et al., 2003)

Rhys and others (2003) suggested that these auriferous structures formed during a protracted phase of low-magnitude northwest-southeast to north-south extension that occurred prior to Early Tertiary dextral shear. They based this conclusion on the comparable geometry of extension veins and shear veins of the Pogo deposit to that of auriferous faults and shear veins with steeply dipping extension veins in many of the gold-hosting deposits in the Fairbanks Mining District.

Available evidence from the Ryan Lode and the Pogo gold deposit suggests that a northeast-striking structural grain developed in the Fairbanks area at ~93-90 Ma was inherited by later structures.

2.3.3 Basaltic Volcanism

Roe and Stone (1993) and Newberry and others (1996) noted that 55-50 Ma ($^{40}Ar/^{39}Ar$) tholeiitic and alkalic olivine basalts are scattered throughout the Fairbanks Mining District, mostly within the Fairbanks seismic zone. These include basalt deposits of Lakloey Hill, Brown's Hill, and Birch Hill. Others are preserved at Fourth of July Hill and in Fairbanks Creek. These basalts were interpreted to have erupted in sub-aerial and sub-aqueous environments (Newberry et al., 1996). The basalts were linked to mafic and felsic bimodal volcanism that produced co-magmatic mafic dikes, shallow felsic plutons, and mafic and felsic volcanic rocks of Early Tertiary (60-50 Ma) age throughout the Yukon-Tanana uplands locally for hundreds of kilometers (Bacon et al., 1990; Foster et al., 1994; Moll-Stalcup et al., 1994; Newberry et al., 1996; Dusel-Bacon and Murphy, 2001). Trace element characteristics suggest a within-plate geochemical signature for these bimodal volcanic rocks (Bacon et al., 1990; Newberry et al., 1996; Dusel-Bacon and Murphy, 2001). The distribution of the bimodal rocks and the within-

plate signature have been interpreted to represent a regional-scale extensional event at ~60-50 Ma (Dusel-Bacon and Murphy, 2001). The age range (~56-50 Ma) of the basalts suggests that basaltic volcanism was relatively short-lived, but this age range is based on dating of only a few deposits in the Fairbanks area.

2.3.4 Surficial Geology

The Fairbanks area was not glaciated during the last glacial period in the Pleistocene; most sediments were deposited in a periglacial environment, and are largely perennially frozen today (Péwé, 1975). The hills in the Fairbanks Mining District are blanketed by Quaternary eolian loess derived from glaciated parts of central Alaska. These loess deposits commonly include ash interbeds (Péwé, 1975; Newberry et al., 1996). Drainage valleys contain re-transported loess and solifluction deposits interbedded with or underlain by auriferous and non-auriferous gravel deposits (Péwé, 1975). Many peat deposits also exist within the lower elevation areas (Newberry et al., 1996).

Péwé and others (1966) mapped a northeast-striking fault in Quaternary deposits on the eastern margin of the Nenana basin that extends for 20 km and has a southeast-side-up component (Péwé et al., 1966; Brogan et al., 1975). This fault was later named the "Minto fault" by Gedney and others (1972). It is expressed as scarps up to 4 meters high (Figure 2.4) and can be correlated with the Minto Flats seismic zone (Brogan et al., 1975; MFSZ, Figure 1.2). These escarpments are linear and correspond closely with the break in slope along the western Yukon-Tanana uplands. However, Page and others (1995) suggested that the scarp is not fault-related, but instead is a terrace of the Nenana River.

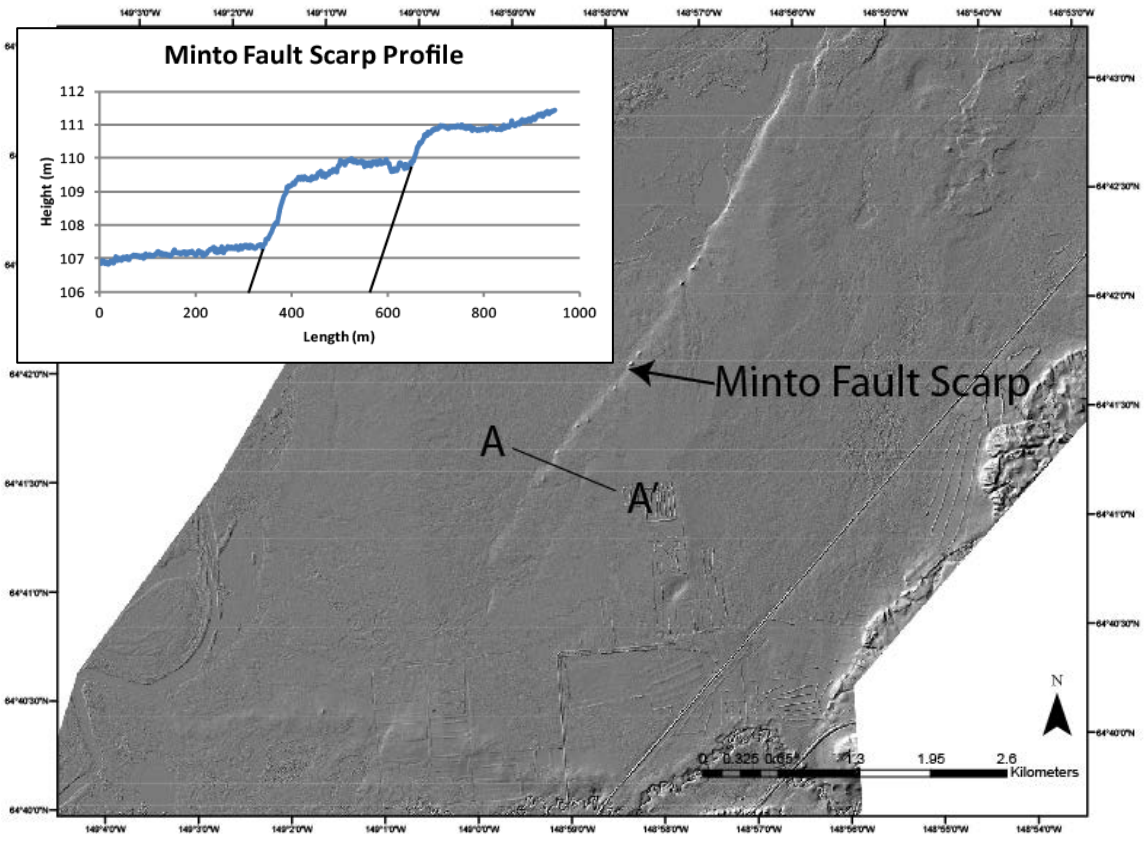

Figure 2.4: LiDAR hillshade of the Minto fault scarp. Location of figure is shown in Figure 1.1b.

2.4 Previous Work: Neotectonics of Interior Alaska

2.4.1 Seismic and Geodetic Studies

Numerous studies have attempted to qualitatively characterize deformation patterns associated with active northeast-striking seismic zones in Interior Alaska. Ratchkovski and Hansen (2002) calculated moment tensor solutions for relocated earthquakes and constructed a map of maximum and minimum horizontal stress axes of central Alaska (Figures 2.5 and 2.6). The focal mechanisms indicate dominantly left-lateral strike-slip motion within the Minto Flats,

Fairbanks, and Salcha seismic zones (Figure 2.5). The stress map indicates that the maximum horizontal compressive stress axis rotates clockwise from SE-NW to SSW-NNE from west to east across the Interior (Figure 2.6). The authors argued that this pattern is consistent with a stress regime expected if the North American plate were deforming plastically due to rigid intrusion of the Pacific plate in southern Alaska.

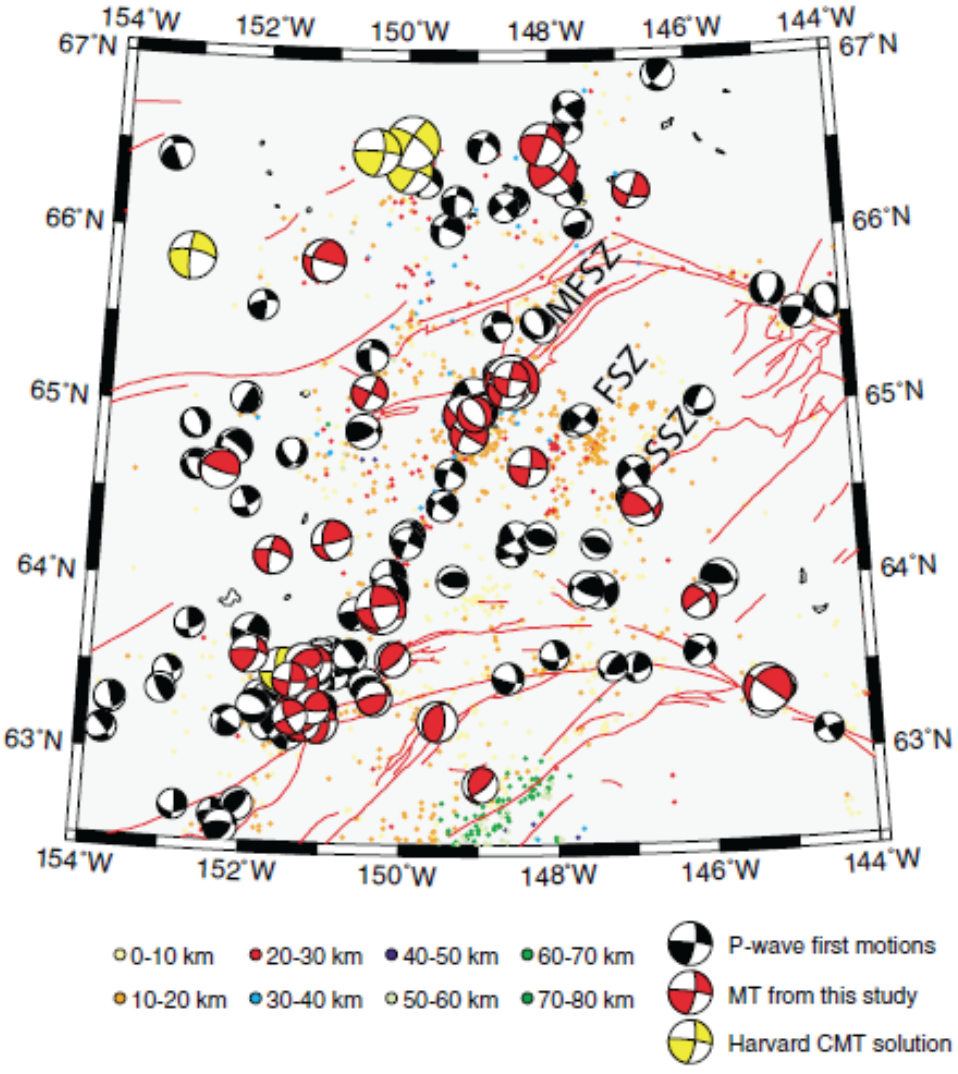

Figure 2.5: Focal mechanism map of Interior Alaska (from Ratchkovski and Hansen, 2002). MFSZ, Minto Flats seismic zone; FSZ, Fairbanks seismic zone; SSZ, Salcha seismic zone.

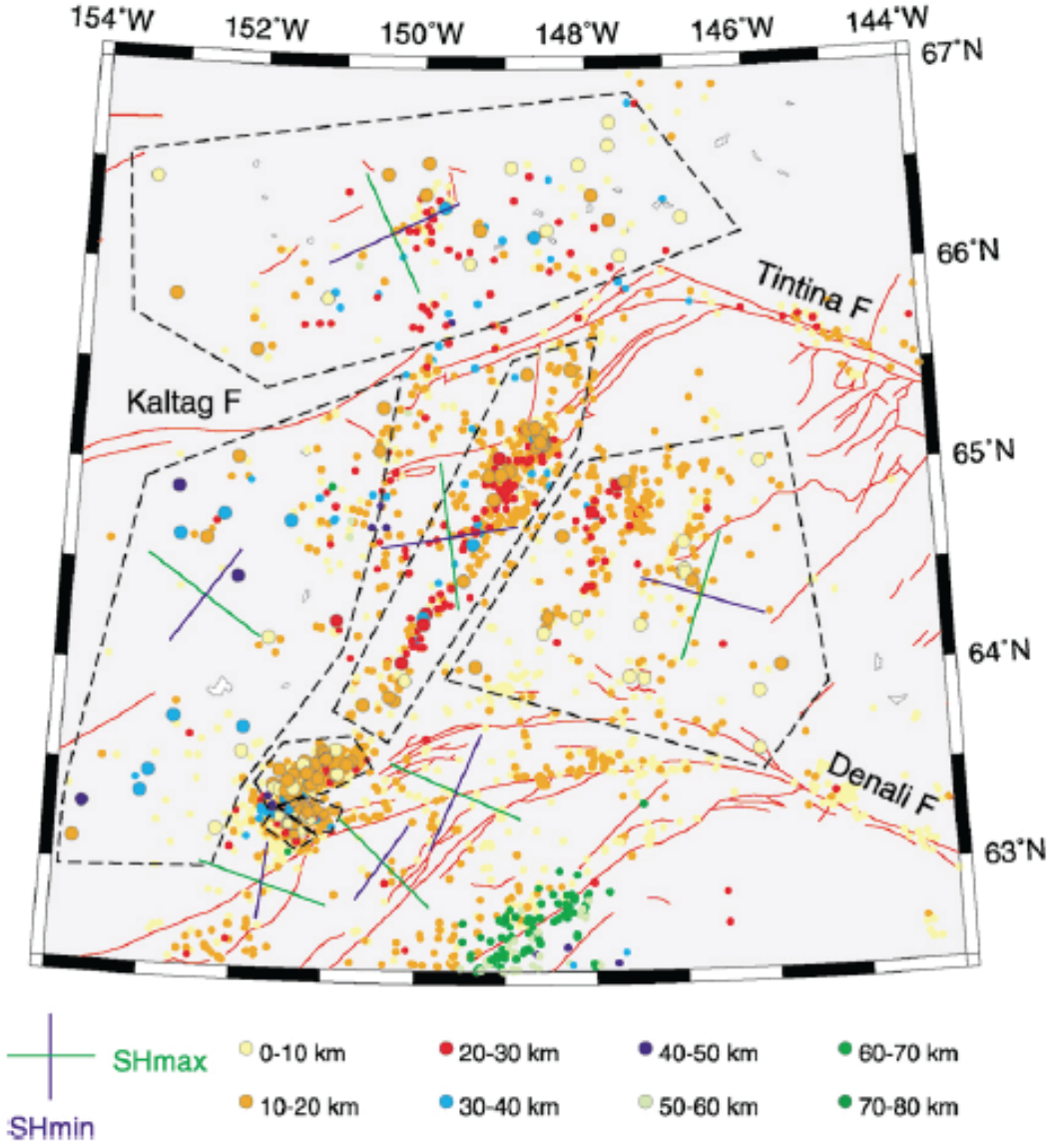

Figure 2.6: Map of maximum and minimum horizontal stress axes of Interior Alaska. Polygons represent populations of earthquakes used to calculate the stress axes (from Ratchkovski and Hansen, 2002).

Ruppert and others (2008) constructed a seismicity map of Interior Alaska that included relocated earthquakes. This map shows a more refined representation of the Fairbanks seismic zone that actually includes four seismic lineations that become more diffuse farther east (Figure

2.7). The Minto Flats seismic zone is more continuous and coherent than other northeast-trending seismic zones. However, the Minto Flats seismic zone becomes complicated toward its northern end, where it appears to separate into two discrete zones, and toward its southern end, where it intersects with the Denali fault and forms a cluster of earthquakes known as the Kantishna Cluster (Figure 2.7; Ratchkovski and Hansen 2002; Ruppert et al., 2008).

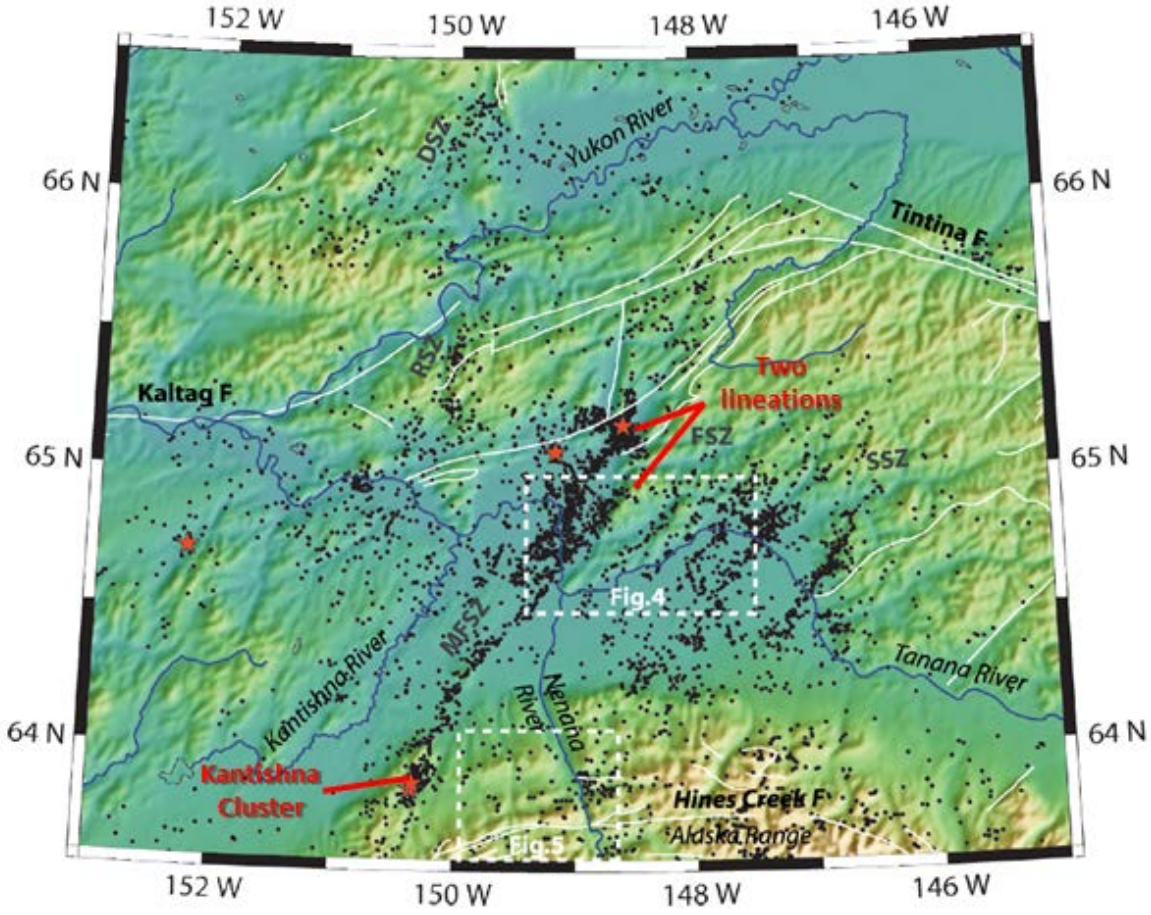

Figure 2.7: Seismicity map of double-difference relocated earthquakes (from Ruppert et al., 2008). White dashed boxes and red stars can be disregarded.

Fletcher (2002) estimated the strain rate across these northeast-striking seismic zones using 55 GPS sites over a span of four years prior to the 2002 Denali fault earthquake. She

concluded that the strain rate across the Minto Flats, Fairbanks, and Salcha seismic zones was small--a total of 2 mm/year with an uncertainty of 1-2 mm/year. The earthquakes in the Kantishna cluster have focal mechanisms that display varying strike-slip, thrust, and normal components.

2.4.2 Geomorphological Studies

Lesh and Ridgway (2007) argued that the geomorphology of major rivers in the Tanana foreland basin and the northern foothills of the Alaska Range reflects active deformation. Particularly, they noted that at the western edge of the Yukon Tanana uplands, in the northern Tanana basin, and the Fairbanks area, the Tanana River has responded to active uplift along a northeast-trending structure they referred to as the "Nenana Structure" (Figure 2.8). Lesh and Ridgway (2007) did not specify the structural character of the Nenana structure, but may have been referring to a continuation of the Minto fault, or a fault or fold related to the Minto Flats seismic zone. Lesh and Ridgway (2007) used three lines of evidence to support active uplift along this structure. The first indicator is that the Tanana River is dominantly characterized as a braided system but becomes channelized as it crosses the southern nose of the structure, then becomes braided again downstream once it crosses the structure. Second, they noted convexity in the longitudinal profile of the Tanana River as it crosses the structure. Lastly, they noted that the Tanana River has been deflected southwestward around the higher topography near the town of Nenana. They hypothesized that the Tanana River originally flowed farther north and as the structure propagated southward, the Tanana River was forced to abandon its channel and establish a new channel south of the higher topography of the western Yukon-Tanana uplands (Figure 2.8). They inferred that the migration of the river left a series of wind gaps and

interpreted the Goldstream and Little Goldstream Creeks to be previous positions of the Tanana River based on observations of underfit streams, low gradients, and similar pebble and cobble detritus to that found along the modern bed of the Tanana River.

The conclusions of Lesh and Ridgway (2007) were largely based on interpretation of stream profiles and DEMs and their proposed "Nenana Structure" was not directly observed in the field. They acknowledged that changes in the fluvial geomorphology and longitudinal profiles could be influenced by large volumes of coarse bedload delivered to the Tanana River by the Nenana River during the latest Wisconsin deglaciation. However, this possibility was not critically evaluated.

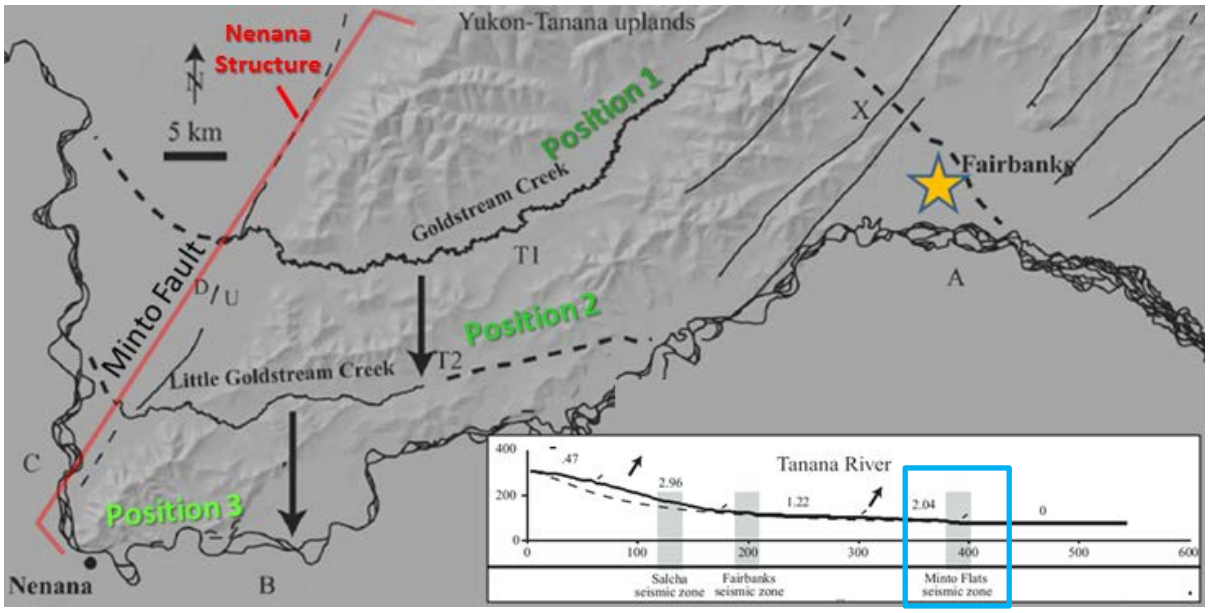

Figure 2.8: Geomorphic interpretation of the western Yukon-Tanana uplands by Lesh and Ridgway (2007). Bold dashed lines represent wind gaps, lines represent mapped faults, arrows represent inferred direction of river migration. Tanana River stream profile shows convexity as it crosses the Minto Fault or the "Nenana Structure" (blue box).

Metz (1991) inferred local tectonism in the Yukon-Tanana uplands based on geomorphological features in the Fairbanks Mining District. A few of these features include: 1) large and local differences in elevation of stream divides and major gold placer deposits; 2) stream valley asymmetry; 3) pronounced linearity of stream drainages; and 4) opposite direction of stream flow in adjacent valleys.

Metz (1991) noted several cases of presumed stream capture that have resulted in barbed drainages in which major gold placer deposits have been documented. He hypothesized that stream capture events have reversed the flow of several drainages. These flow reversals reworked stream gravels and contributed to the deposition of gold placer deposits. These drainage reversals may be reflected by the location of placer deposits along Goldstream, Cripple,

and Ester Creeks. Metz (1991) noted that placers, which typically accumulate in the lower reaches of streams, were deposited as a result of drainage reversals and subsequent reworking of gravels along the upper reaches of streams. He speculated that movement along young faults contributed to these drainage reversals. However, capture events may have been caused by climate change in the Pleistocene and/or Pliocene, when placers were deposited as a result of stream rejuvenation, but this possibility has not been verified.

Metz (1991) was the first to note valley asymmetry in the Fairbanks area and acknowledged that it could be related to differential slope transport in permafrost areas. North-facing slopes are commonly steeper because they have less exposure to solar radiation, thus they are less susceptible to thawing and erosion by solifluction, and south-facing slopes should have increased freeze-thawing and erosion by solifluction, leading to lower slope angles. However, he also noted that in many drainages in the Fairbanks area, south-facing slopes are actually steeper and others show no difference in slope angle on either side, and thus a dependent relationship between slope orientation and slope angle was not defined.

Newberry (2010) noted an example of possible tectonic-induced stream capture in Livengood along Livengood Creek, where a drainage reversal was interpreted in a 10 Ma gold placer bench deposit (Figure 2.9). Core compositions of placer gold revealed silver-leached rims. These tend to develop when an aerated stream exposes the gold grain to oxygen and causes the silver that is dissolved in the gold to oxidize and diffuse out of the gold (Newberry, 2010). Consequently, as the grains are carried downstream, this causes gold fineness to increase downstream from the source. However, placer gold fineness from this bench deposit increases systematically upstream from the source; microprobe analysis revealed that all gold

compositions are from the same source (Figure 2.9). This atypical increase in placer gold fineness upstream indicated a drainage reversal within the last 10 Ma (Newberry, 2010). This interpretation is supported by chromite concentrations that increase upstream from all of the chromite sources in the area. Athey and Craw (2004) attributed this drainage reversal to tilting and vertical offset along the Minto fault, which is located at the western-most end of the Livengood Bench. They also noted that the Livengood Bench must be raised 260 m to restore it to its past paleo-surface. If the interpretation of Athey and Craw (2004) is correct, then a subsidence rate of 0.026 mm/yr for the past 10 million years along the Minto fault can be inferred.

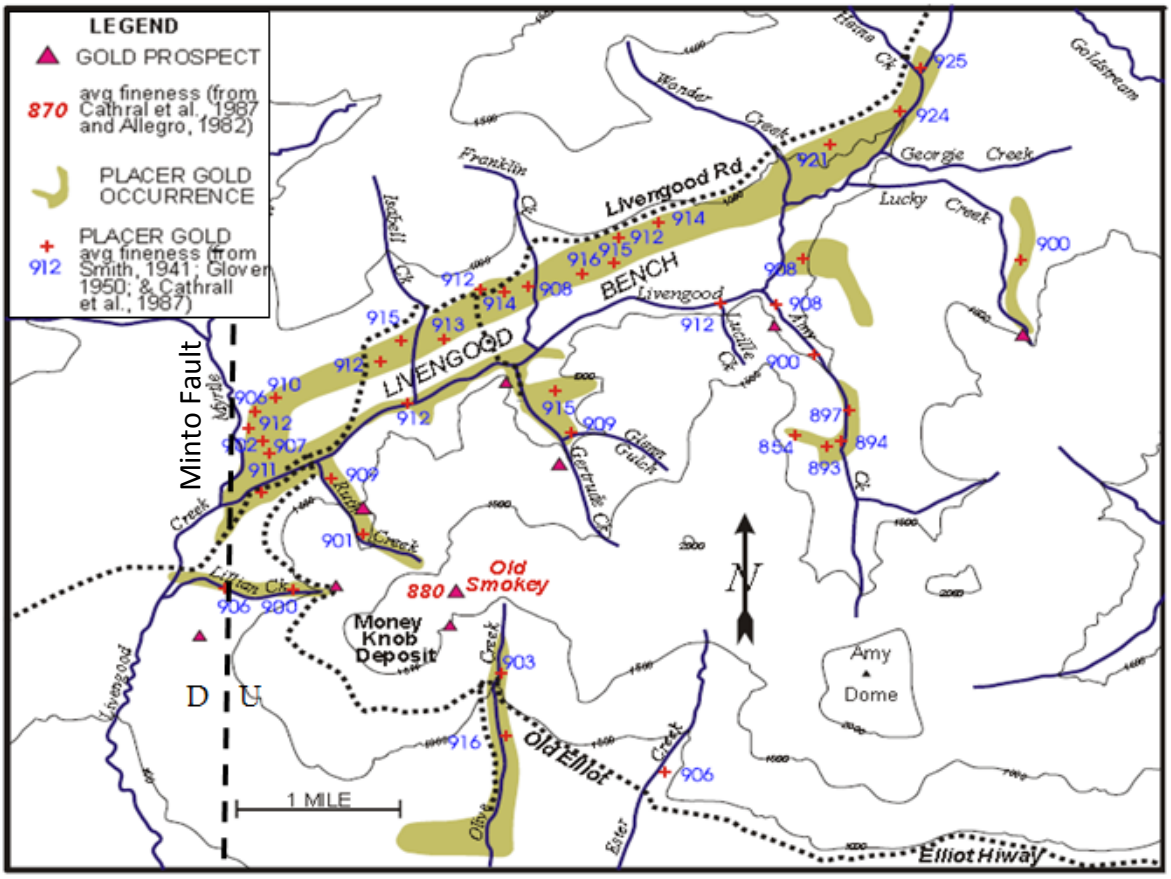

Figure 2.9: Map showing the location of the Livengood Bench with respect to the Minto fault (modified from Newberry, 2010). Placer gold fineness in the Livengood Bench increases upstream along present day Livengood Creek.

Previous attempts to assess regional deformation patterns in Interior Alaska, particularly in the greater Fairbanks area, have been qualitative and the association with active uplift has been speculative. For this project, I conducted more quantitative analyses to assess regional deformation patterns by employing a combination of geomorphic, structural, and relative and absolute dating techniques.

Chapter 3: Data and Methodology

Poor or limited outcrop exposures warranted a combination of remote-sensing and field-based approaches to address the main hypotheses. The systematic phases of my analyses were to: 1) synthesize geological, geophysical, and topographic data and map potentially active northeast-striking faults; 2) conduct geomorphic reconnaissance and morphometric analyses using digital elevation models (DEMs) in order to evaluate potential tectonic activity and assist in interpreting the structural character of potentially active faults; 3) conduct structural analyses of fault exposures in order to define shear-sense of slip, magnitude of offset, and relative timing of faulting; and 4) conduct apatite fission-track analyses in order to place faults in tectonic context with respect to major events and assess fault evolution over time.

3.1 Data

3.1.1 Geological and Geophysical Maps

Geological maps (e.g. Newberry et al., 1996; Wilson et al., 1998) and regional gravity and magnetic maps (e.g., Meyer et al., 1996; Burns et al., 2004) were mainly used for integrative analysis with digital elevation models (DEMs) and earthquake hypocenters to map potentially active faults. However, geological maps were also utilized for several other components of this thesis which include: 1) comparison of drainage patterns and topographic anomalies to structural trends; 2) identification of possible fault exposures for field data collection; 3) evaluation and interpretation of structural data; and 4) interpretation of apatite fission-track data.

3.1.2 Digital Elevation Models

I constructed a mosaic of two different bare earth DEMs with different resolutions: 1/3 arc second (or ~10 meters resolution) and 2 arc seconds (or ~60 meters resolution) (Gesch et al., 2002). These were projected in ArcMap using the North American Datum 1983 UTM Zone 6 projected coordinate system. Unfortunately, a single high-resolution DEM did not cover the northern part of the study area. To cover this area, I constructed a mosaic of the ~10 m and ~60 m DEMs. I mosaicked the two DEM raster datasets in ArcMap using the "Mosaic" tool, which allows two or more raster datasets to be combined into a single seamless raster dataset. Where data cells overlapped, I set the tool to keep only the first raster dataset's data, which was the USGS ~10 m DEM.

I used LiDAR bare earth DEMs of ~1 m accuracy to conduct geomorphic analyses (Hubbard et al., 2011). The Alaska Division of Geological and Geophysical Surveys acquired this survey along a one-mile swath along the proposed Alaska Stand Alone Pipeline (ASAP) corridor. Part of this survey included lower Goldstream Creek, the eastern margin of the Nenana basin, and part of the city of Fairbanks.

3.1.3 Earthquake Hypocenters

I obtained earthquake hypocenter data from Natasha Ruppert (personal communication, 2011), a seismologist for the Alaska Earthquake Information Center. Natasha compiled a list of earthquake hypocenters within my study area boundaries and filtered them to include only hypocenters $\leq$ 30 km in depth. The margin of error associated with the locations is highly variable and could be anywhere from <1 km to 20-30 km in areas with lower quality

instrumentation. The source of error depended on station distribution and number of wave arrival picks that could be analyzed and used for locating.

3.2 Fault Mapping

Poor exposure made it difficult to do field-based mapping. Consequently, I mapped seismic lineaments using a combination of data sets. I primarily used earthquake hypocenters to accurately locate the surface traces and dips of potentially active faults. However, I also juxtaposed earthquake hypocenters with faults from geologic maps (Newberry et al., 1996; Wilson et al., 1998), gravity and magnetic maps (Meyer et al., 1996; Burns et al., 2004), and topography from DEMs (Gesch et al., 2002; Hubbard et al., 2011) to better constrain the interpreted traces of potentially active faults.

3.2.1 Mapping Technique

I projected earthquake hypocenters in ArcMap according to depth and overlaid them on georeferenced geologic and geophysical maps (e.g., Newberry et al., 1996; Wilson et al., 1998; Meyer et al., 1996; Burns et al., 2004) using the North American Datum (1983) UTM Zone 6 projected coordinate system. In order to better constrain the location of fault traces where faults are not mapped, I overlaid earthquake hypocenters with depths of <5 km on a mosaicked DEM to compare them to topographic lows or linear drainage valleys. Then, in order to better define fault dip directions and dip angles, I selected earthquake hypocenters along a northwest-striking transect across the Minto Flats, Fairbanks, and Salcha seismic zones and plotted them according to depth. The transect spanned 126 km x 17 km in order to capture a sufficient number of earthquakes that could be projected with sufficient accuracy to adequately assess fault dip.

3.3 Geomorphic Reconnaissance and Morphometry

Landscape evolution is governed by both large scale geological and surficial processes (e.g. climate change, tectonism, or volcanism), and local-scale processes (e.g. vegetation distribution, weathering, or artificial infrastructure). Because of this wide variety of land-shaping mechanisms, it is difficult to pinpoint a single process that may have influenced landscape evolution over a long period of time. However, by knowing how a particular set of processes may affect the landscape or drainage shape, certain mechanisms may be ruled out.

Morphometry, a sub-discipline of geomorphology, is defined as the quantitative measurement of landscape shape (Keller and Pinter, 2002). Landforms can be quantified based on size, elevation, and slope. Geomorphic indices are tools of morphometry. They are useful for analyzing landscape to assess the mechanisms controlling landscape evolution, for example, climate change or tectonic activity. By understanding the close relationship between active tectonism and topography and by employing morphometric analyses, structural features may be identified and interpreted.

It must be noted that geomorphic indices do not directly determine the role of tectonic activity. However, landscape evolution may be quantified by combining multiple geomorphic indices along with an assessment of regional geology and climate. Using this data, the consequences of active tectonism can be inferred, and the character of potentially active structures can be interpreted.

3.3.1 Geomorphic Reconnaissance

Rivers and streams are sensitive to small disturbances because of the many processes (e.g., sediment load, flow velocity, slope, etc.) that need to be in balance (Keller and Pinter, 2002). Thus, a simple drainage map may be used to rapidly identify areas where there may be a possible disruption in a river or stream system.

In order to identify areas that exhibit a possible tectonic disturbance, I conducted a reconnaissance investigation of drainage characteristics. The reconnaissance investigation involved analyzing DEMs and drainage maps to identify peculiar drainage patterns that mimic structural trends, abrupt changes in river morphology, and asymmetrical, incised, and underfit streams. All of these anomalies have been noted in the Fairbanks area by previous authors (e.g., Metz, 1991; Lesh and Ridgway, 2007) and were used as indicators for identifying potentially active structures.

I identified prominent linear and barbed drainage patterns in a drainage map of the Fairbanks area. Since water tends to exploit planes of weakness, strongly linear drainages can indicate the presence of a fault that may be controlling the flow pattern. Likewise, drainages that exhibit 90°+ downstream turns into adjacent valleys can indirectly reveal local uplift and/or the presence of a fault via the process of stream capture. For instance, if base level drops due to uplift along a fault, headward migration of a stream can occur and the stream may intercept the headwaters of the weaker stream, consequently reversing its flow direction.

I examined river morphologies, particularly along Little Goldstream Creek, Goldstream Creek, and Chatanika River, as potential indicators of tectonic activity. Areas with higher

gradients tend to produce more sinuous rivers and areas with lower gradients tend to produce straighter rivers. Thus, structures that may impede a given drainage and cause slope variability may cause changes in drainage behavior and morphology. As mentioned previously, Lesh and Ridgway (2007) identified changes in river morphology of the Tanana River from braided to channelized and used them as an indicator of crossing the inferred "Nenana Structure."

Additionally, I investigated DEMs for asymmetrical, incised, and underfit streams. Asymmetrical stream valleys commonly indicate the presence of ground tilt, since water will tend to follow gravitational forces in a given direction. For instance, if a drainage cross-cuts a fault block that is tilting to the south, the drainage will preferentially migrate to the south and commonly leave behind a set of asymmetrical terraces that are wider and better developed on the north side of the valley. However, the causal mechanism for valley asymmetry must be taken into careful consideration, especially in a sub-arctic environment such as Fairbanks where differential permafrost weathering and solifluction slope modification are important processes.

Incised valleys may indirectly indicate the presence of tectonic uplift. For example, as bedrock uplifts along a fault, base level will drop relative to the uplifted side and a given stream will begin to carve into its valley floor in order to achieve equilibrium at the new base level. Like valley asymmetry, stream incision is not a direct indicator of active faulting, since other processes such as sea level drop or local changes in base level may produce the same effect.

Another indirect indicator of active tectonics is underfit streams. Underfit streams can indicate that the proto-drainage that occupied a given valley was once larger than it is at present. Underfit streams can imply a possible stream capture event in which the water from a given drainage was diverted to a larger, more aggressive drainage. As mentioned above, stream

capture may be linked to tectonic activity. The mechanism that created a given underfit stream must be carefully considered with respect to factors such as recent changes in climate. For instance, the Fairbanks area was considered a periglacial environment in the Pleistocene, when rigorous cycles of freezing and permafrost weathering ensued (Péwé, 1975). At this time, the climate could have produced larger rivers and streams that are expressed today as underfit streams.

After I completed the reconnaissance investigation, I focused the morphometric analyses on drainages and topographic features in the areas with the highest density of geomorphic anomalies. I used the following geomorphic indices to identify and quantitatively analyze areas of potential tectonic activity and interpret the character of tectonic structures: basin asymmetry factor, transverse topographic symmetry factor, stream-length gradient index, mountain front sinuosity, and valley floor width-to-height ratio.

3.3.2 Drainage Basin Asymmetry Factor

The drainage basin asymmetry factor (AF) provides a quantitative measurement of the symmetry of a drainage basin. Typically, a tectonically undisturbed drainage basin in stable conditions will develop a symmetrical drainage network, whereas a drainage basin situated on an active fault block may reflect migration of the drainage network toward the direction of tectonic tilt, resulting in asymmetry. This index is most credible under the assumption that each drainage basin is underlain by the same rock type and that regional dip or localized climate has a negligible effect on the drainage flow direction (Keller and Pinter, 2002).

The basin asymmetry factor is defined as $AF = 100(A_r/A_t)$, where AF is the basin asymmetry factor, A_r is the area of the basin to the right (facing downstream), and A_t is the total area of the drainage basin (Keller and Pinter, 2002; Figure 3.1). A stable drainage network yields AF values of about 50 and values significantly greater or lesser may suggest tilt. Values greater than 50 indicate tilt to the left and values less than 50 indicate tilt to the right (Cox, 1994; Burbank and Anderson, 2001; Keller and Pinter, 2002).

I calculated the basin asymmetry factor using the measure tool in ArcMap. I drew a polygon to encompass the area of the drainage basin of interest, using fifth level hydrologic unit watershed boundaries from the National Watershed Boundary Dataset as a guide. I calculated AF along the Little Goldstream, Goldstream, and lower Chatanika drainage basins because they are close and perpendicular to the Minto Flats seismic zone, where Lesh and Ridgway (2007) suggested possible southward tilt along the "Nenana Structure."

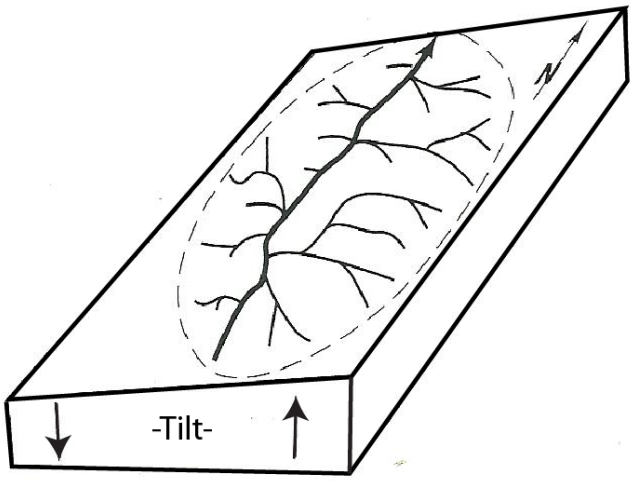

Figure 3.1: Block diagram illustrating drainage basin asymmetry (Keller and Pinter, 2002). A hypothetical AF value for this block diagram would be ~70.

3.3.3 Transverse Topographic Symmetry Factor

The transverse topographic symmetry factor (T) is another index utilized to assess drainage basin asymmetry that can complement the AF index. This index is defined as $T = D_a/D_d$, where T is the topographic symmetry factor, D_a is the distance from the midline of the drainage to the midline of the active meander belt, and D_d is the distance from the midline of the drainage basin to the basin divide (Keller and Pinter, 2002; Figure 3.2). A perfectly symmetric drainage basin yields a value of 0 and as asymmetry increases, T approaches a value of 1. This index can be used to identify the direction of drainage migration, which may correlate to the direction of regional ground tilt. This index, like AF, is based on the assumption that the dip of the bedrock has a negligible effect on the direction of stream migration. Therefore, T reflects a vector with a bearing and a magnitude from 0 to 1. T is typically calculated at different segments of the stream valley and the values are averaged to identify anomalous zones of asymmetry. Like the AF, T may not be used to provide direct evidence of ground tilt from active tectonic structures, but it is used to rapidly identify possible tilt and may be combined with other geomorphic indices to identify the character of an active structure (Keller and Pinter, 2002).

I calculated T along the lower Goldstream Creek and Chatanika River drainage basins and approximated the theoretical midline of each drainage basin. I drew the segment lines along lower Goldstream and Chatanika river valleys at a spacing of five kilometers.

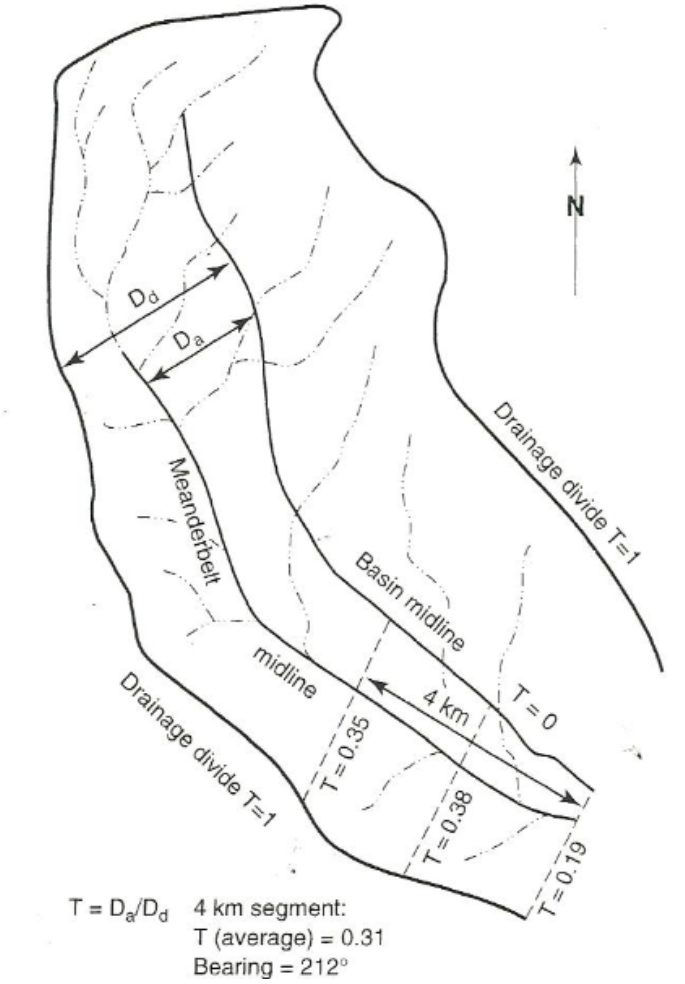

Figure 3.2: Diagram from Cox (1994) showing how T is calculated (Keller and Pinter, 2002).

3.3.4 Stream-Length Gradient Index

Graded rivers typically develop a smooth, concave upward longitudinal profile that reflects the balance between gradient and discharge (Burbank and Anderson, 2001). Variations in the graded river profile may be observed as knickpoints.

Knickpoints can be caused by: 1) streams crossing a more resistant rock type; 2) climate-induced stream rejuvenation; and 3) local obstructions or sea level drop. Knickpoints can develop in a stream profile where rock resistance changes. For instance, a longitudinal profile

along the Potomac River demonstrates that significant changes in SL values occur over changing lithology types such as shale, siltstone, sandstone, and carbonate (Keller and Pinter, 2002). However, in the Fairbanks area, drainages are incising through soft colluvial deposits, mostly loess. In some cases, drainages reach the underlying bedrock, which is mostly quartzose and pelitic schist that erodes relatively easily (Wilson et al., 1998). In the timescale of landscape evolution, stream profiles adjust to differing rock types relatively quickly, which makes the stream-length gradient index a suitable tool for measuring recent tectonic activity (Keller and Pinter, 2002).

Climate-induced stream rejuvenation can also produce knickpoints in a stream profile as well as stream capture. A period of climate change may increase flow velocities and headward erosion, resulting in renewed down-cutting that may disrupt the profile and create a new knickpoint. Also, increased headward erosion can result in the interception of the headwaters of another drainage.

I generated longitudinal stream profiles along drainages that crossed nearly perpendicular to the Fairbanks and Salcha seismic zones. However, I focused morphometric calculations on the area at the margin of the Nenana basin where the break in slope displays a strong correlation to the Minto fault (Figure 2.8). Based on previous studies of an active range-bounding fault and lack of infrastructure, this area in particular showed greater potential for geomorphic anomalies associated with active faulting.

The stream-length gradient index is defined as $SL = (\Delta H/\Delta L)L$, where SL is the stream-length gradient index, ΔH is the change in elevation of the reach (i.e., the section of interest along the channel), ΔL is the length of the reach, and L is the total channel length from the

midpoint of the reach to the highest point of the channel (Hack, 1973; Keller and Pinter, 2002; Figure 3.3). SL provides a means of quantifying variations in the gradient of the river profile. Since rivers are sensitive to changes in slope, this index can be used to identify irregular values that may indicate departure from an equilibrium stream profile due to an active tectonic structure.

I generated longitudinal profiles of several streams around the Fairbanks area, however, only a select few were chosen to calculate SL. SL was determined for Goldstream Creek, Little Goldstream Creek, and the Chatanika River. I carefully chose these drainages based on their east-west trends, which are nearly perpendicular to the Minto Flats and Fairbanks seismic zones and thus more likely to show variations in gradient from potentially active faults. I produced longitudinal profiles from the 10-meter and 60-meter resolution DEMs (Gesch et al., 2002) using the interpolate line tool in the 3d Analyst extension for ArcMap.

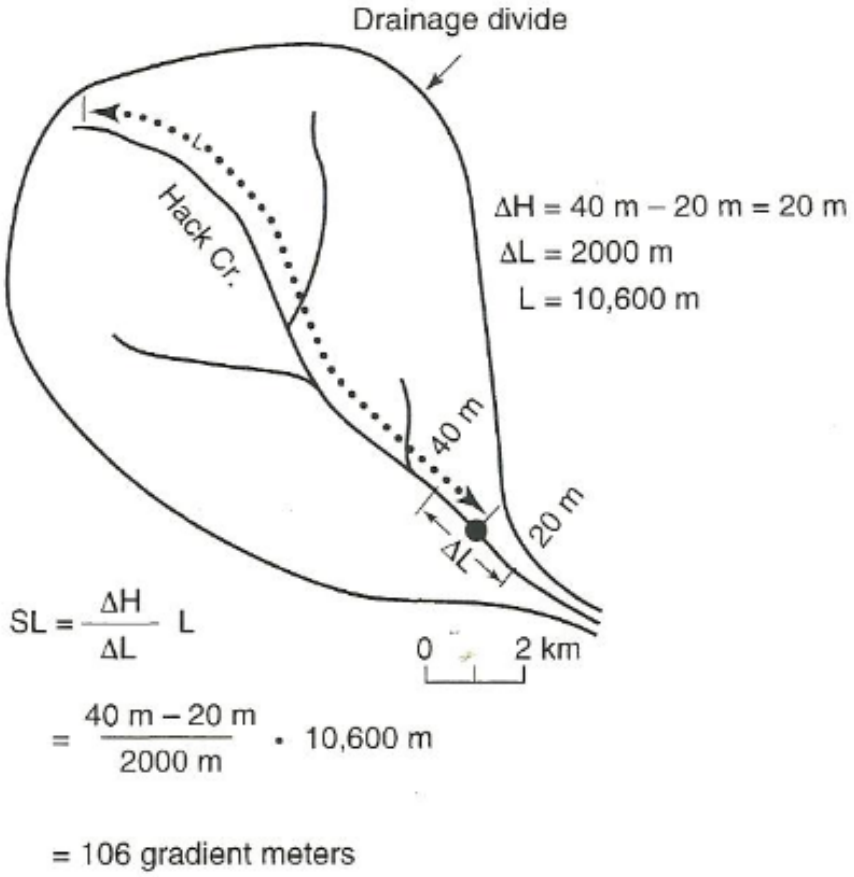

Figure 3.3: Diagram showing how SL is calculated using the hypothetical Hack Cr. (Keller and Pinter, 2002).

3.3.5 Mountain Front Sinuosity

The mountain front sinuosity index is defined as $S_{mf} = L_{mf}/L_s$, where S_{mf} is the mountain front sinuosity index, L_{mf} is the length of the mountain front along the break in slope at the foot of the mountain front, and L_s is the straight-line length of the mountain front (Keller and Pinter, 2002; Figure 3.4). This index is a valuable reconnaissance tool that reflects the balance between erosional forces of streams that tend to produce an irregular mountain front and planar steep active faults that produce a straight mountain front (National Research Council, 1986). A study

by Bull and Mcfadden (1977) on the Garlock fault concluded that active range-bounding fronts generally had an S_{mf} between 1 and 1.6, moderately active fronts had a Smf between 1.4 and 3, and inactive mountain fronts had an S_{mf} of greater than 5 (Keller and Pinter, 2002). Since interpretation of mountain front sinuosity can be complicated by lithologies, stream size, and climate, this index is more useful in conjunction with valley floor width-to-height ratio and should be used more as a qualitative guide for classifying the level of tectonic activity at the mountain front (Burbank and Anderson, 2001).

Using the measure tool in ArcMap, I calculated S_{mf} along the margin of the Nenana basin where the break in slope displays a strong correlation with the Minto fault.

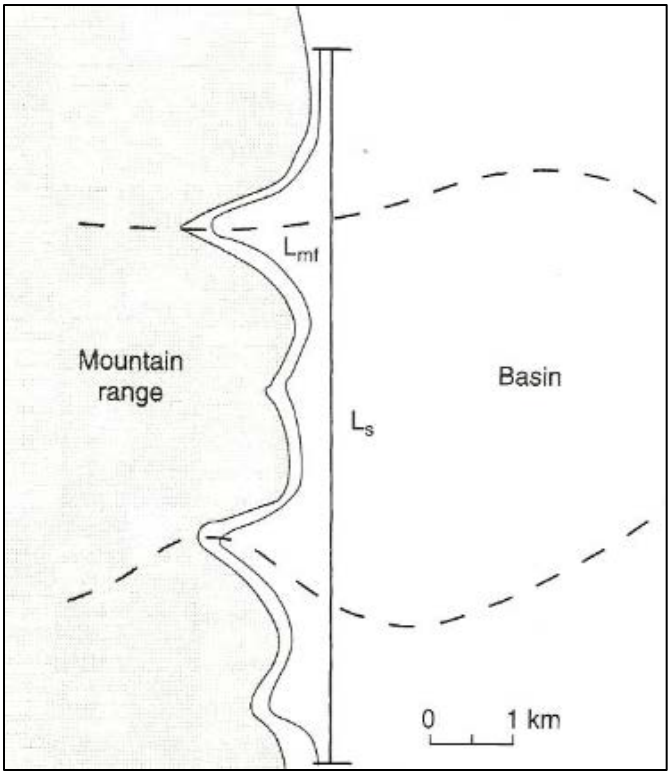

Figure 3.4: Diagram illustrating S_{mf} (Keller and Pinter, 2002).

3.3.6 Valley Floor Width-To-Height Ratio

The valley floor width-to-height ratio is defined as $V_f = 2V_{fw} /[E_{ld} -E_{sc}) + (E_{rd}-E_{sc})]$, where V_f is the valley floor width-to-height ratio, V_{fw} is the width of the valley floor, E_{ld} is the elevation of the left (facing downstream) drainage divide, E_{rd} is the elevation of the right drainage divide, and E_{sc} is the elevation of the valley floor (Keller and Pinter, 2002; Figure 3.5). Bull and McFadden (1977) tested the V_f index for mountain fronts at the Garlock fault and found that the index varied from 0.05 to 47. The low values corresponded to the most tectonically active areas. Generally, values of less than 1 correspond to deeply incised V-shaped valleys, which are associated with high uplift rates; values greater than 1 typically correspond to U-shaped valleys, which tend to be associated with low uplift rates or glaciation (Keller and Pinter, 2002).

I calculated V_f along Little Goldstream, Goldstream, and Chatanika valleys approximately 1.5 km east of the pronounced break in slope. I traced the profiles as perpendicular to the valley as possible. The profiles were constructed using the ArcMap interpolate line tool on the 10-meter resolution USGS DEM.

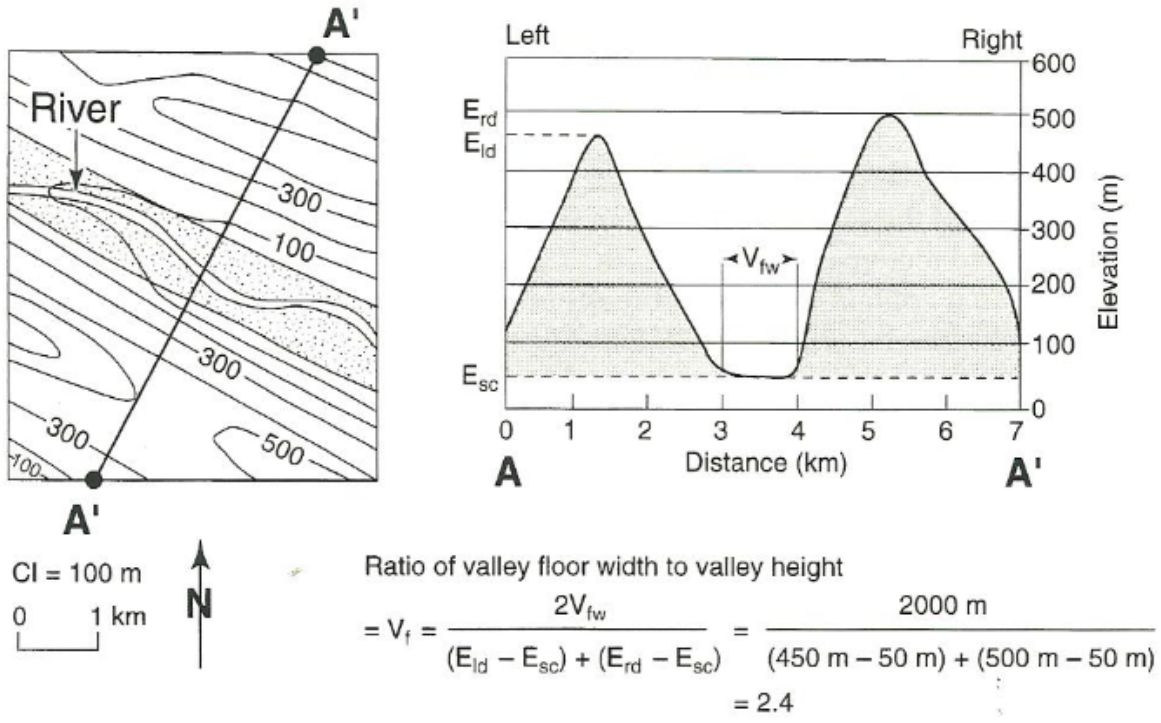

Figure 3.5: Idealized diagram of how V_f is calculated (Keller and Pinter, 2002).

3.4 Structural Analyses

In order to gain a better understanding of the tectonic framework of the Fairbanks area, the structural character of faults must be defined. I collected structural and stratigraphic data at quarries and roadcuts mostly within the Fairbanks Mining District, where Newberry and others (1996) have mapped the geology in detail. I documented attitude and shear-sense of slip as well as surficial stratigraphic deposits from fault exposures that displayed possible tectonic deformation. I determined the relative ages of stratigraphic layers by comparing them to surficial deposits from the Fairbanks area that were characterized in detail by Péwé (1975).

3.4.1: Data Collection

I used geologic maps (e.g., Newberry et al., 1996 and Wilson et al., 1998) in conjunction with satellite imagery and seismicity to seek out faults exposed in bedrock. Northeast-striking faults were targeted because of their close correlation with the trends of seismicity. In the Fairbanks Mining District, gold or basalt deposits are commonly near or associated with northeast-striking, high-angle faults, thus the main targets for data acquisition were abandoned or active gold mines and basalt quarries because they were the most likely sites to have exposed fault surfaces. I collected structural data from fault exposures at road cuts along the Parks highway from as far west as Nenana to as far east as Salcha, and along Chena Hot Springs road.

At most field sites, data collection consisted of taking attitude measurements of fault surfaces with a Brunton compass and identifying, measuring, and interpreting kinematic indicators. Kinematic indicators were critical for interpreting the shear-sense and direction of slip on a given fault plane since, at many exposures, faults typically cut schist or basalt that contained no stratigraphic markers. Therefore, more information was necessary in order to determine the sense of slip. Such criteria included slickensides, subsidiary fractures, slickenfibers, drag folds, and synthetic or antithetic Riedel shears. Many fault exposures had one or more of these features. I collected kinematic data on every fault surface possible at each field site; however, some sites did not have any measurable kinematic indicators.

Data collection also involved characterizing the lithologies of surficial deposits at fault exposure sites and documenting any deformation observed in them. This was necessary to determine if there was recent tectonic, anthropogenic, or climate-induced deformation. If there

was sufficient evidence to suggest tectonic deformation in the sediments, relative age was inferred based on the known or relative ages of the deformed strata.

3.4.2: Analytical Technique

I imported structural data for each field site into StereoStat V1.6.1 structural analysis software, which was used to plot fault attitudes and fault plane lineations in equal area, lower hemisphere projections. I created stereoplots of poles to fault planes and fault lineations, which show the direction of motion and shear sense, of the hanging wall, where known, for each field site.

3.5: Apatite Fission-Track Thermochronology

Apatite fission-track thermochronology is a useful measuring tool for understanding low temperature thermal history in the upper crust. It can be used to assess a variety of geological problems including landscape evolution, timing and rates of faulting, and climatic changes (Donelick et al., 2005). Since fission tracks in apatite are sensitive to thermal resetting above ~120° C, they can be used to document the latest stages of cooling. This is particularly useful for understanding an active tectonic region. For the purposes of this study, apatite fission-track thermochronology was used to constrain the timing, rates, and regional patterns of cooling that occurred throughout the western Yukon-Tanana uplands.

The spontaneous fission of ^{238}U results in two separate fragment nuclei that repel each other. The kinetic energy produced by this process leaves a single, measureable damage trail within the crystal lattice of an apatite grain (Naeser, 1976; Donelick et al., 2005). The damage trail repairs itself through the process of annealing, which is defined as partial to complete

erasure of tracks (Naeser, 1976). The Partial Annealing Zone (PAZ) is the temperature window of ~60 to ~120° C (Green et al., 1986; Laslett et al., 1987). As annealing progresses within the PAZ to higher temperatures (~110-120° C), the average length of an etchable fission track becomes progressively shorter until it is completely erased (Naeser, 1976). At lower temperatures within and below the PAZ (< 60° C), fission tracks are retained (Ketcham et al., 1999). The cooling age is a function of the track density or number of tracks per unit area and the apatite crystal's ^{238}U concentration (Naeser, 1976).

3.5.1 Apatite Fission-Track Sampling Strategy

Sample selection was governed by the availability of bedrock exposure, rock type, and location relative to mapped faults and seismic lineations. The ideal collection strategy was to sample perpendicular to mapped faults and seismic lineations and on either side of a fault trace, preferably at specific distance intervals. However, since bedrock exposures were limited to road cuts and quarries along highways, I collected samples along lines oblique to mapped faults and seismic lineations rather than perpendicular, and samples were not collected at specific distance intervals from a fault trace. Samples were collected at road cuts and quarries along the Parks Highway from Nenana to Salcha and from west to east along Chena Hot Springs Road. I collected all of the samples except for sample 1338-17, which was collected by my colleague Alec Rizzo.

Bedrock exposures along the transect consist primarily of quartzite and schist of the Fairbanks Schist Unit (Newberry et al., 1996), although quartzite was mainly targeted at each sample location due to its larger grain size and relatively greater tendency to contain apatite. A previous apatite fission track study conducted in Interior Alaska by Dusel-Bacon and Murphy

(2001) noted that schists and phyllites in particular were challenging lithologies from which to obtain reliable apatite fission-track data due to the low uranium content of their apatites. They explained that this may be due to the presence of titanite, zoesite, or both, in which uranium is preferentially partitioned, resulting in apatites with low uranium concentrations. These low-uranium apatites typically yield few fission tracks and poor counting statistics. This same challenge to obtaining reliable data is reflected in the apatite fission-track results from this study.

Wesley Wallace and I selected 15 metamorphic rock samples from the Yukon-Tanana upland transect for analysis. Details for each sample are shown in the results chapter. Samples that appeared more quartz-rich in hand sample were given higher priority over samples that appeared more micaceous. Also, since apatites are common detrital constituents of medium- to coarse-grained clastic sedimentary rocks, samples that were coarser-grained were given higher priority.

My colleague, Nilesh Dixit, collected two additional samples from well cuttings from the Nunivak #1 well in the southern Nenana basin. Sample 1338-18 consisted of sands collected from the early to middle Miocene Sanctuary, Suntrana, and Lignite Creek formations of the Usibelli Group (Wahrhaftig et al., 1969) over a depth interval of 1830 ft (5560-7390'). Sample 1338-19 consisted of sands collected from Paleocene formations over a depth interval of 2010 ft (9010-11,020'). Samples were sent to Apatite to Zircon, Inc. in Viola, Idaho, where the apatites were separated and analyzed.

3.5.2 Sample Preparation

Samples were prepared by Apatite to Zircon, Inc. (AtoZinc). Preparation techniques are described in detail by Donelick and others (2005). AtoZinc determined uranium concentrations in apatites by using laser ablation combined with inductively coupled plasma-mass spectrometry (LA-ICP-MS) of $^{238}U/^{43}Ca$ ratios with a primary and secondary standard zeta age calibration. This technique used spot laser analyses. They reported pooled ages ± 1σ with asymmetrical errors for a population of apatite grains

Track length measurements and counts were made by AtoZinc analyst Paul O'Sullivan using a Zeiss Axioplan microscope at 2000x dry magnification using unpolarized, transmitted light with or without reflected light.

3.5.3: HeFty Modeling

HeFty modeling was performed by Paul O'Sullivan from A to Z, Inc. A HeFty inverse model is based on the construction of a forward model that predicts how a fission-track thermochronometric system might have evolved based on temperature-dependent annealing behaviors and parent-daughter decay relationships, and assuming particular starting conditions and a time-temperature history. The inverse model employs a statistical and algorithmic approach to predict the time-temperature history by constraining the present-day and assumed starting conditions of the sample (Ketcham, 2005).

Each model must have two time-temperature window constraints to determine fitting path solutions. Paul O' Sullivan used a default temperature of 5° C for the present surface temperature since it represents the average surface temperature for Interior Alaska. He added additional

constraint boxes based on the combination of pooled ages, stratigraphic ages (for samples 1338-18 and 1338-19), mean track lengths, and maintaining consistency throughout the samples. Models for samples 1338-18 and 1338-19 included additional stratigraphic age and temperature constraints, as these were sedimentary samples from the Nunivak #1 well.

Paul O'Sullivan generated all model paths using a Monte Carlo scheme and displayed the results with a best fit model, weighted mean path, and path envelopes depicting confidence ranges of the minimum and maximum potential time-temperature paths. He generated up to three adequately fitting models that represent the data for each sample.

3.5.4: Analysis of Apatite Fission-Track Data

I used the HeFty inverse modeling results to determine cooling rates through the PAZ and to analyze overall cooling patterns with respect to northeast-striking faults. Drastic differences in cooling rates across a small distance can be used comparatively to identify the presence of a fault. In theory, cooling rates can then be used to approximate exhumation rates along upthrown fault blocks. I approximated cooling rates from each sample's time-temperature curve by taking the slope of the weighted mean path of all fitted histories through a well-constrained closure temperature window of 60-120° C (Gleadow et al., 1986). I used model 1 of each sample to calculate the cooling rates because each model 1 consistently assumed a starting surface temperature of 0°C for metamorphic rocks and contained the highest goodness-of-fit values. Based on the pooled ages of the samples, an assumed starting temperature of 0°C was appropriate.

Cooling rates may be derived using either the weighted mean path or the best-fit model. The weighted mean path is the product of the Monte Carlo simulation, which evaluates up to tens of thousands of independent time-temperature paths and arrives at the weighted average fitting path. The best-fit path uses an algorithm that optimizes previously tried paths to arrive at a best goodness-of-fit statistical value and it usually works best with fewer degrees of freedom (Ketcham, 2005). I used the weighted mean path to determine cooling rates because it can be used to admit higher uncertainty given the large degrees of freedom in the data.

After I determined cooling rates, I overlaid pooled ages on geologic maps (e.g., Newberry et al., 1996 and Wilson et al., 1998), seismic lineations, and DEMs in ArcMap to analyze relationships between pooled ages, faults, and topography. I constructed pooled age versus distance plots and pooled age versus cooling rate plots to further analyze cooling trends with distance from the Minto fault. These plots helped determine faulting patterns over time.

In theory, the sense of vertical offset may be determined by comparing pooled ages across mapped faults. For example, if samples yield a significantly higher pooled age on the east side of a fault than the west side, this could imply that the eastern fault block was exhumed earlier and the west side of the fault stayed in the partial annealing zone for some time after faulting. In some cases, this may not reflect most recent movement, because apatites can record the last significant exhumation event, which may be the result of a different sense of movement than the most recent movement if that movement has small vertical offset.

Chapter 4: Results

4.1: Fault Mapping

In contrast to the three major seismic zones (Minto Flats, Fairbanks, and Salcha) generally identified in the literature (Plafker et al., 1994; Page et al., 1995; Ratchkovski and Hansen, 2002; Koehler et al., 2012), seismicity actually indicates that the Fairbanks and Minto Flats seismic zones can be sub-divided into multiple linear, northeast-trending seismic zones (Ruppert et al., 2008; Figures 2.7 and 4.1). Seismicity in the Minto Flats seismic zone and closest to the western edge of the Fairbanks seismic zone is the most diffuse, which suggests many splays and cross faults (Figure 4.1; Page et al., 1995). However, it is worth noting that some of the shallower seismicity could be related to mining activity, especially closer to the eastern margin of the Fairbanks seismic zone where there are active basalt quarries.

I mostly mapped regional scale, northeast-striking faults because the scarcity of earthquake hypocenters results in low data resolution that does not allow more detailed mapping of cross faults. The structural components of the map include multiple northeast-striking faults and one northwest-striking fault. I assigned names to faults that were not previously recognized and they are annotated in Figures 4.2 and 4.3. Figure 4.3 overlays the seismically defined fault traces with previously mapped faults (Newberry et al., 1996; Wilson et al., 1998).

It is important to emphasize that the red faults shown in Figs. 4.2 and 4.3 are interpreted potentially active faults based primarily on the distribution of seismicity. Their traces have been refined slightly to correspond with topographic lineations, mapped bedrock faults, and offsets and/or lineations in geophysical data. None of the interpreted faults has demonstrable Pliocene

or younger surface rupture except for a small segment of the Chena Ridge fault where it crosses Cripple Creek. Actual surface traces may be different from what is shown on the map.

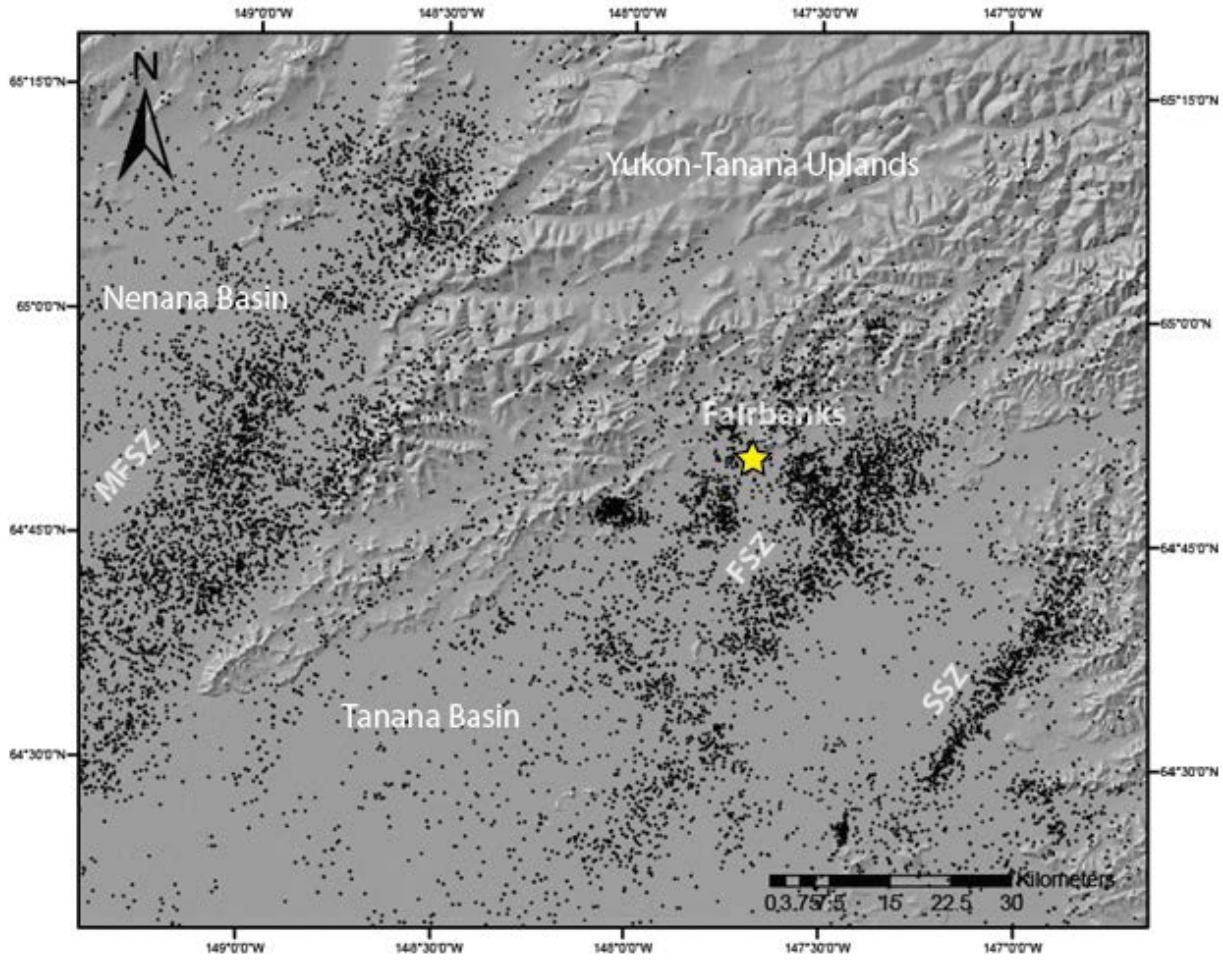

Figure 4.1: Map of seismicity (AEIC, 2011) in the Fairbanks area. MFSZ, Minto Flats seismic zone; FSZ, Fairbanks seismic zone; and SSZ, Salcha seismic zone.

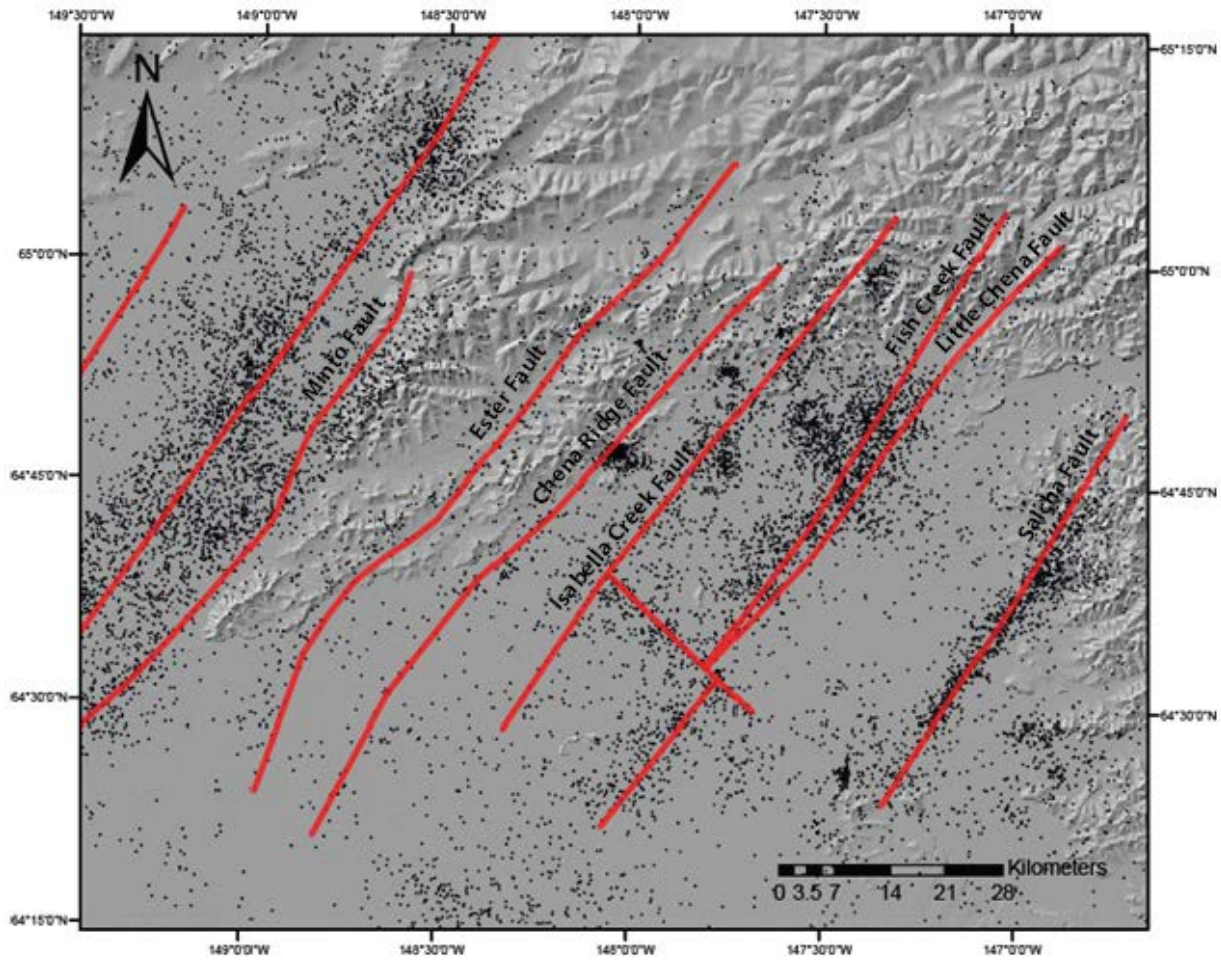

Figure 4.2: Map of seismicity overlain by faults interpreted from a best fit to seismicity (red). Faults are informally named.

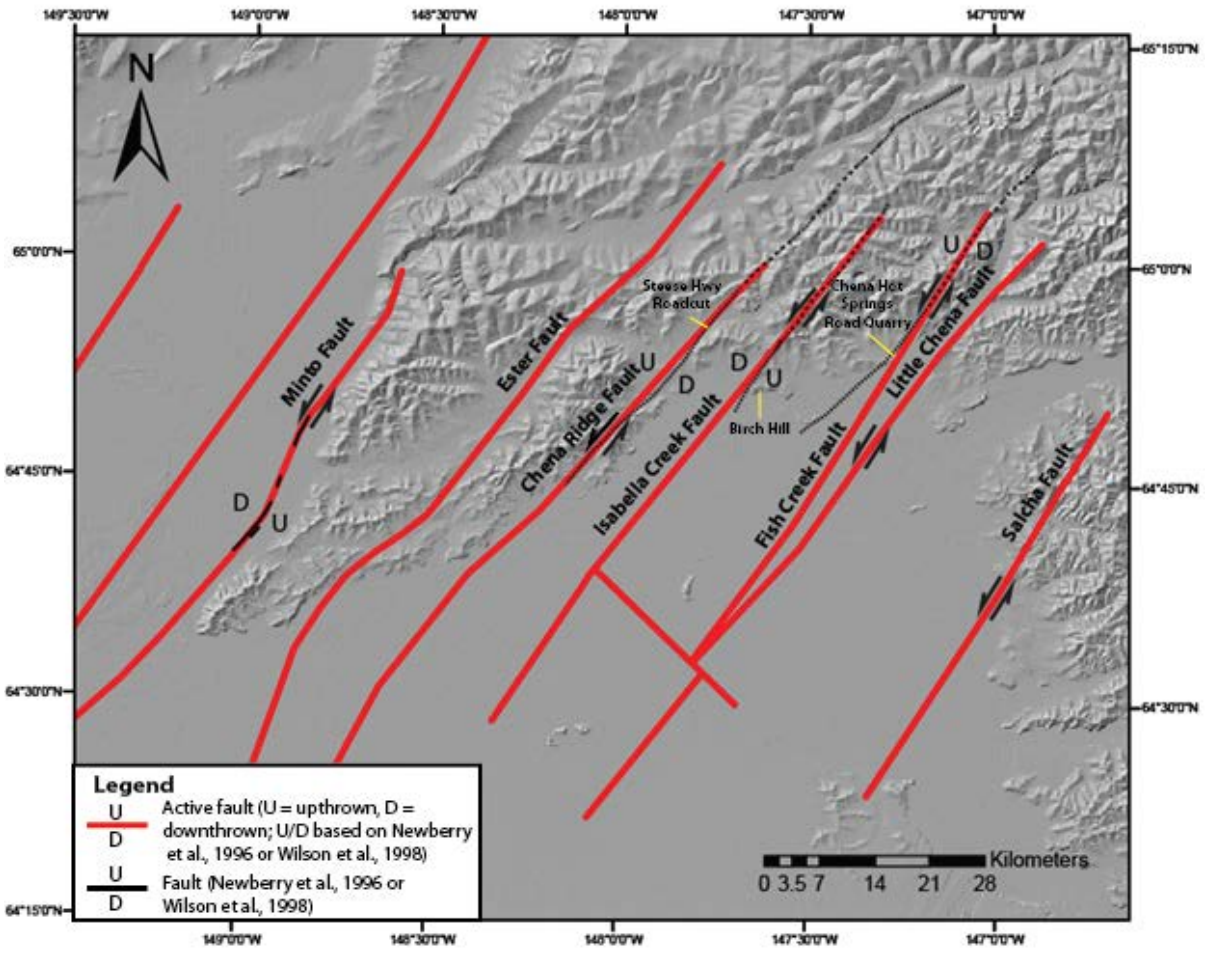

Figure 4.3: Map of potentially active faults in the Fairbanks area. Interpreted faults (red) are overlain by previously mapped faults from Newberry et al. (1996) and Wilson et al. (1998).

The majority of seismically-defined faults that I have interpreted tend to correlate closely with topographic lows and/or drainage valleys. The Ester and Chena Ridge faults apparently bend toward the west near the Tanana River (Figure 4.2). A topographic low follows these faults, showing the same bending pattern. A northwest-striking fault appears to intersect with, and offset, the Fish Creek and Little Chena faults in an apparent left-lateral strike-slip sense.

Several interpreted faults, including the Minto, Chena Ridge, Isabella Creek, and Fish Creek faults, correlate with previously mapped faults (Newberry et al., 1996; Wilson et al., 1998; Figure 4.3). The previously mapped Minto fault (Wilson et al., 1998; Figure 4.3) correlates with a continuous seismic lineation in the eastern part of the Minto flats seismic zone and with the topographic break in slope at the front of the Yukon-Tanana uplands (Figures 4.1 and 4.2). A regional Bouguer gravity map (Meyer et al., 1996) shows a sharp contrast from ~0 to -50 mgal at the east margin of the Nenana basin, where the Minto fault is mapped (Figure 4.4). This suggests significant vertical displacement along the Minto fault.

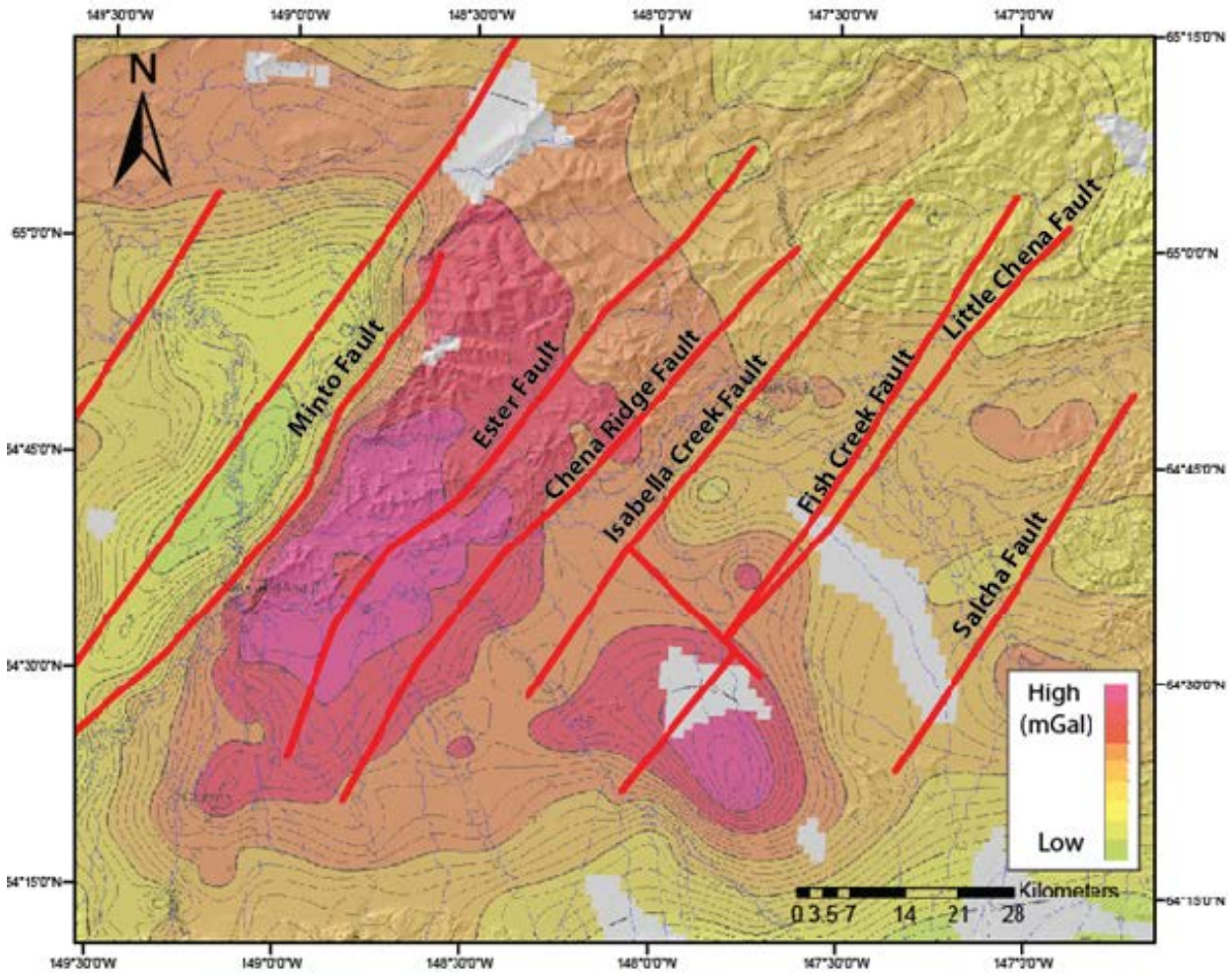

Figure 4.4: Potentially active faults overlain on a regional Bouguer gravity map of Interior Alaska (Meyer et al., 1996).

The Chena Ridge fault produced a M3.8 earthquake swarm in May of 2009 (AEIC, 2011). The earthquake swarm was concentrated in one area located on the west side of Chena Ridge near the head of Cripple Creek. The rupture length was approximately 3 km and focal mechanisms indicated left-lateral-normal motion for this earthquake swarm (AEIC, 2011; Figure 4.5). The Chena Ridge fault is on trend with a mapped fault to the northeast that displays ~1 km of apparent left-lateral offset (Newberry et al. 1996). The mapped fault has variable dip-slip

offset along its length. In the southwest, it juxtaposes Precambrian protolith-age schist to the east against Devonian protolith-age eclogite to the west and is interpreted as being down to the west. To the northeast the fault is inferred as down to the east based on down-dropped Tertiary basalt. The opposite sense of displacement along strike indicates long term lateral displacement.

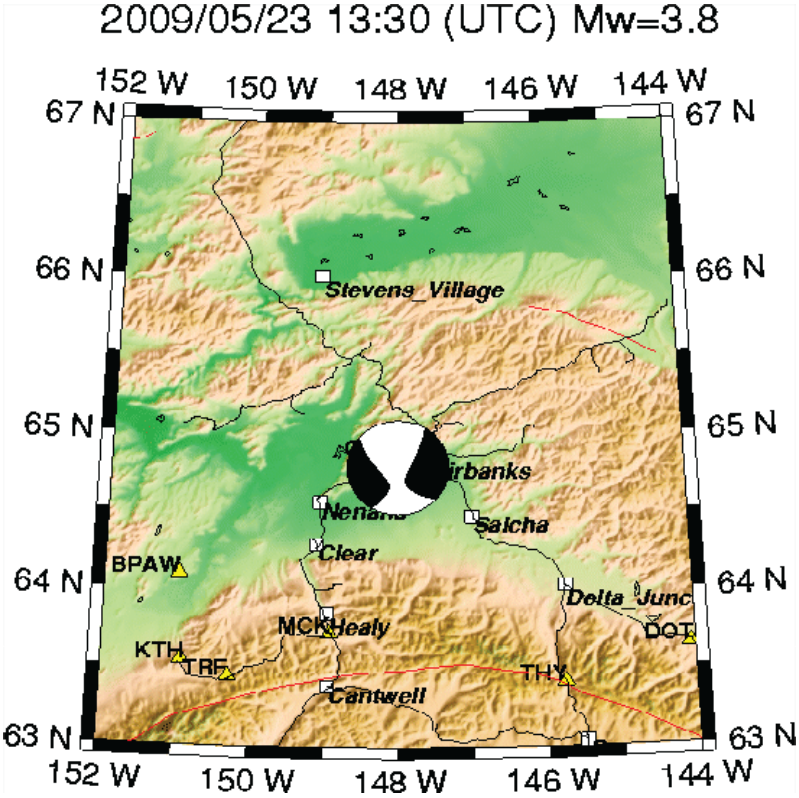

Figure 4.5: Left-lateral-normal focal mechanism of the May 2009 earthquake swarm along the Chena Ridge fault (AIEC, 2011).

The seismicity that defines the Isabella Creek fault is fairly diffuse. The Isabella Creek fault is on trend with a mapped fault that displays 0.5 to 2 km of apparent left-lateral offset of Precambrian protolith-age amphibolite, schist, and marble (Newberry et al., 1996). These rocks also correlate with discontinuous magnetic anomalies that can be restored with approximately 0.5-2 km of apparent left-lateral offset (Burns et al., 2004; Figure 4.6). Near Birch Hill (Figure

4.3), Newberry and others (1996) showed this fault as exposed and down to the west, where Devonian protolith-age slate, phyllite tuff, and quartzite to the east are juxtaposed against Precambrian protolith-age schist to the west. I visited this area and this fault was not exposed. To the northeast, Newberry and others (1996) indicated that this fault is exposed along the Steese Highway. I attempted to visit this exposure but the roadcut where it was mapped was overgrown with vegetation (Figure 4.3). Northeast of the Steese Highway roadcut (Figure 4.3), Newberry and others (1996) inferred that the fault cuts Late Cretacous ($^{40}Ar/^{39}Ar$) Granite and is down to the west.

The seismicity that defines the Fish Creek fault is diffuse and forms the eastern margin of the Fairbanks seismic zone. The Fish Creek fault is on trend with a mapped fault that displays up to 3 km of apparent left-lateral offset of Precambrian protolith-age amphibolite, schist, and marble (Newberry et al., 1996). These rocks correlate with discontinuous magnetic anomalies that can be restored with approximately 3 km of apparent left-lateral offset (Burns et al., 2004; Figure 4.6). This fault is also on trend with a quarry along Chena Hot Springs road that exposes multiple shear zones (4.3). Northeast of the quarry, Newberry and others (1996) inferred the fault to be down to the east. To the east of Birch Hill, Newberry and others (1996) interpreted the fault to cut through Tertiary basalt in Brown's Hill quarry, where multiple northeast-striking faults are well exposed. I mapped this fault differently than Newberry and others (1996) because the seismic zone that defines the fault does not appear to be on trend with Brown's Hill Quarry, but instead is southeast of Brown's Hill Quarry.

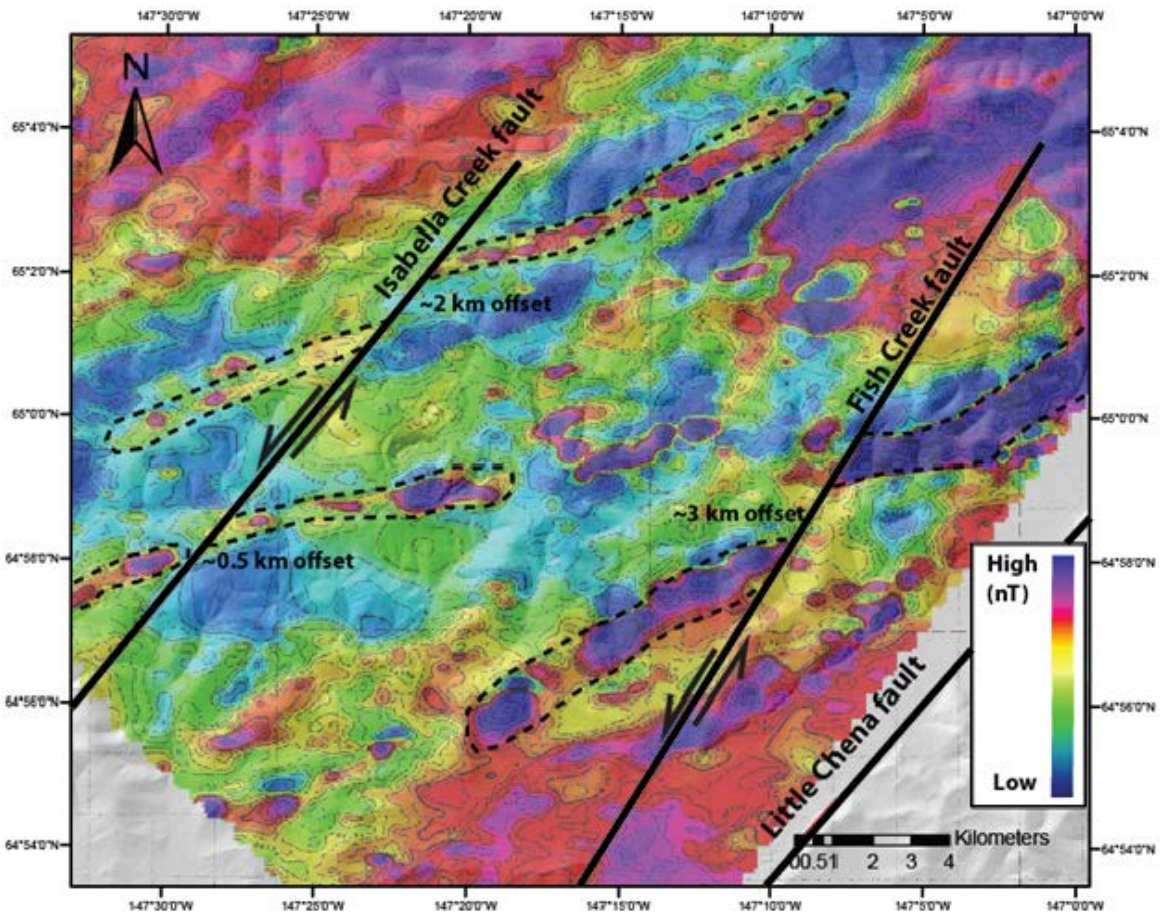

Figure 4.6: Faults overlain on a total magnetic anomaly map of the Fairbanks Mining District (modified from Burns et al., 2004). Dashed lines represent magnetic anomalies that represent amphibolite, schist, and marble rock units from Newberry and others (1996).

After plotting the inferred surface traces, I constructed a perpendicular transect of earthquake hypocenters normal to fault strike to assess dip directions and dip angles (Figures 4.7 and 4.8). Due to diffuse seismicity and analytical uncertainty in locations (1-30 km), cross-sectional fault dips are uncertain. However, careful examination of the deeper hypocenters reveals several stair-step-like offsets in the base of seismicity that may correspond with faults (Figure 4.8b). Interpreted faults dip either to the southeast or northwest and dips range from approximately 50° to 88° (Figure 4.8b). Focal mechanisms from the 1967 M5.6 and 1937 M7.3

in the Fairbanks and Salcha seismic zones (Figure 1.1) correspond with the dip directions that I have interpreted for faults 6, 7, and 8 (Fish Creek, Little Chena, and Salcha faults), respectively. It appears that hypocenter depth increases slightly to the west and the densest clusters of seismicity are at depths between 10 and 20 km. Also, in the eastern half of the cross section, faults appear to be steeper, whereas in the western half of the cross section, faults appear less steep and show stair-step-like offsets in the east-dipping base of seismicity. These patterns are consistent with dominantly strike-slip faulting to the east and a greater component of normal faulting to the west, with shallower dips and tilted fault block geometries. If steps in the base of seismicity correspond to offset fault blocks, they indicate normal displacements of at least 2.5-6 km.

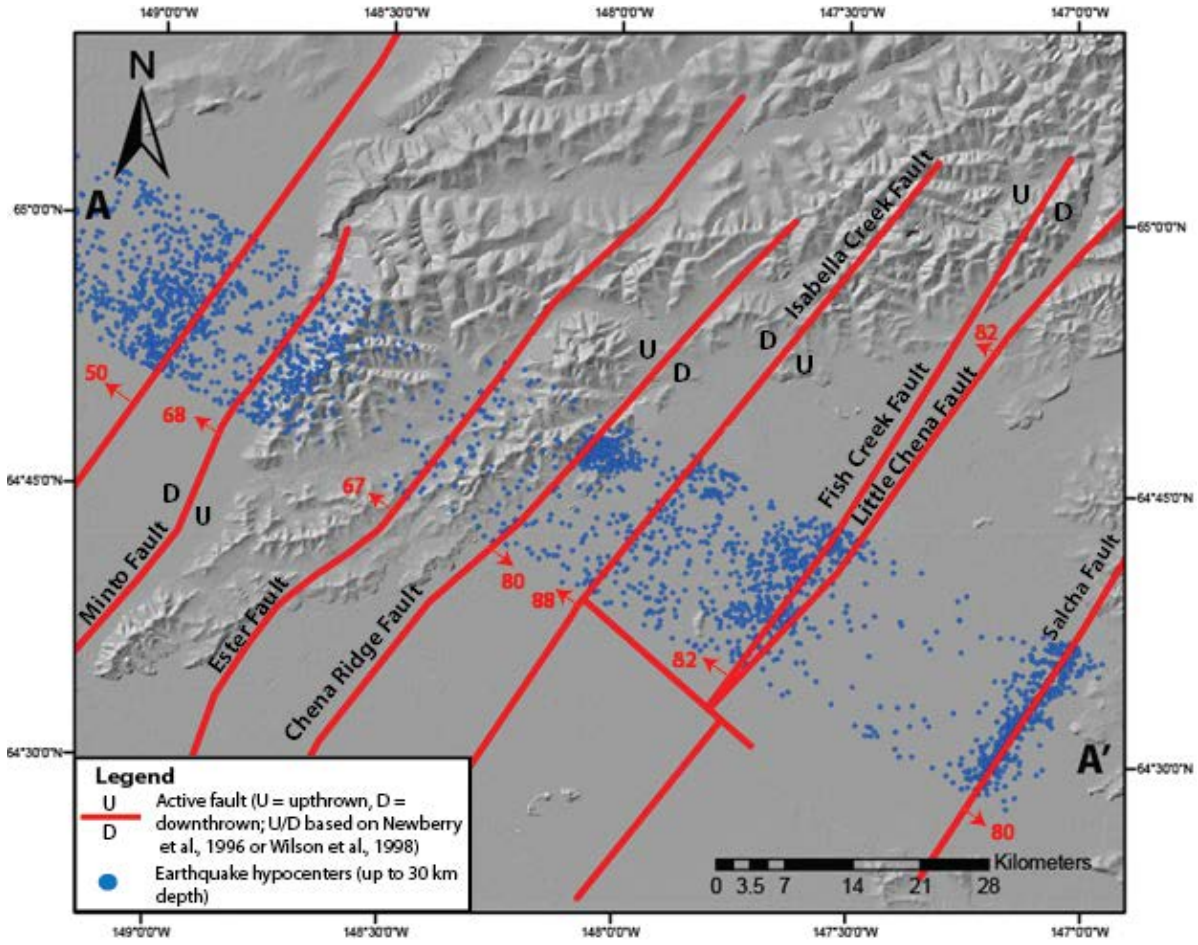

Figure 4.7: Plan view map of hypocenter swath projected into cross section with inferred fault dips labeled. A-A' cross section of seismicity is shown in Figure 4.8.

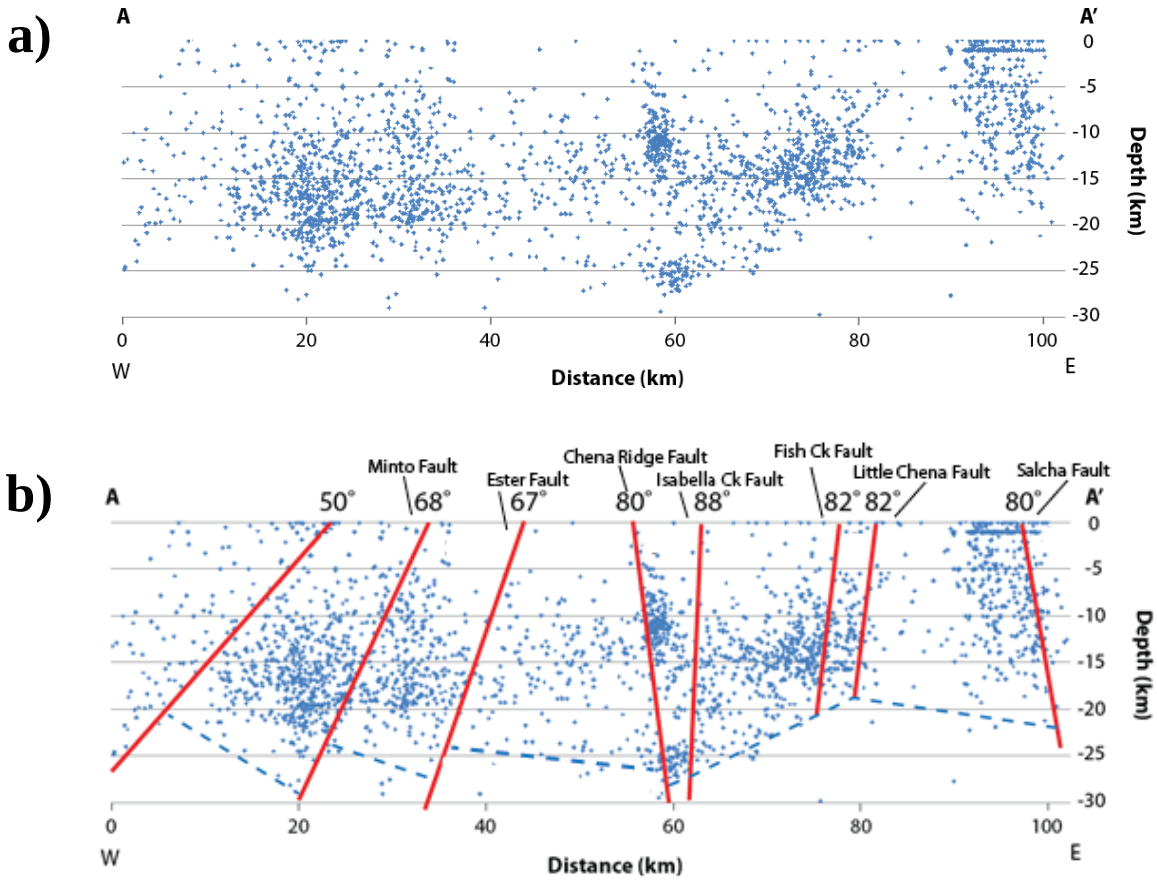

Figure 4.8: Cross section of hypocenter swath. a) Uninterpreted cross section, and b) interpreted cross section with fault dip angles. Numbered faults in 4.7 correspond with faults in 4.8b. Blue dashed lines correspond to the base of seismicity. Cross section scale is 1:1. Margin of error for hypocenter depth is highly variable and can be anywhere from 1-30 km.

No mapped faults correspond to the Ester fault, Little Chena fault, or Salcha fault, thus my interpretations are solely based on seismicity. The Ester fault can be defined by a narrow, linear zone of seismicity (Figure 4.2). The Ester fault dips 68° to the northwest and the offset in the base of seismicity suggests normal displacement of ~3 km (Figure 4.8b).

The Little Chena fault is much more difficult to define because it is associated with a diffuse zone of seismicity (Figure 4.1). It forms the eastern boundary of the Fairbanks seismic

zone and is in close proximity to the Fish Creek fault to the west (<5 km). It also follows the Little Chena River valley. I have interpreted the Little Chena fault to converge with the Fish Creek fault to the south. The Little Chena fault dips 82° to the northwest and seismicity does not appear to extend as deep (~20 km) as it does to the west for the Minto, Ester, Chena Ridge, and Isabella Creek faults (~30 km minimum depth; Figure 4.8b).

A 6.1M earthquake occurred in 1967 (Figure 1.1) just south of where the Fish Creek fault and Little Chena fault merge into one fault (Figure 4.2; Page et al., 1995). Seismicity in this zone is moderately diffuse. This was the first of a series of ≤6.1 quakes and aftershocks that occurred from 1967 to 1979. Some of these have been interpreted (Gedney et al., 1980) to represent a northwest-striking right-lateral cross fault. I have interpreted this seismic zone to represent a northwest-striking fault that offsets the Fish Creek/Little Chena merged fault in an apparent left-lateral strike-slip sense.

The Salcha seismic zone produced a 7.3M earthquake in 1937 (Figure 1.1; Page et al., 1995). The focal mechanisms for this earthquake suggest left-lateral strike-slip motion. The seismic zone that defines the Salcha fault is relatively short and narrow and contains a high density of earthquakes (Figure 4.1). The dip of the Salcha fault is difficult to define because earthquakes appear more diffuse in cross section view (Figure 4.8b). I have interpreted the fault to dip 80° to the southeast. Like the Little Chena and Fish Creek faults, seismicity does not extend as deep (~20 km) as it does to the west for the Minto, Ester, Chena Ridge, and Isabella Creek faults (~30 km minimum depth; Figure 4.8b).

4.2: Geomorphic Reconnaissance and Morphometry

A reconnaissance investigation of the drainage morphology and topography was the first phase of the geomorphic analysis. Patterns and anomalies that I could identify on drainage maps and DEMs could then be examined further with more quantitative morphometric tools to analyze landscape and drainage shape.

4.2.1 Geomorphic Reconnaissance

Analysis of the topography and drainage morphology revealed several noteworthy patterns and anomalies. These include barbed drainages, strongly linear drainages, asymmetrical valleys, incised valleys, underfit streams, and changes in river morphology. Some of these were first noted by Metz (1991).

Barbed drainages or drainages that turn 90° + downstream into an adjacent valley, commonly indicate a possible stream capture event. The most significant of the barbed drainages are shown in Figure 4.9 and lie over or directly adjacent to my interpreted potentially active fault traces. These include Bonanza Creek, Cripple Creek, Moose Creek, Happy Creek, Sheep Creek, Nugget Creek, and Fish Creek. Some of them make nearly 180° turns into adjacent stream valleys. Several of these drainages may have produced wind gaps (Figures 2.8 and 4.9) as a result of stream capture (Metz, 1991). In addition, the Tanana River, Little Goldstream Creek, and Goldstream Creek all turn 90°+ to the north at the margin of the Nenana basin (Lesh and Ridgway, 2007; Figures 2.8 and 4.9). Individual stream capture events will be further assessed in the discussion section (Chapter 5).

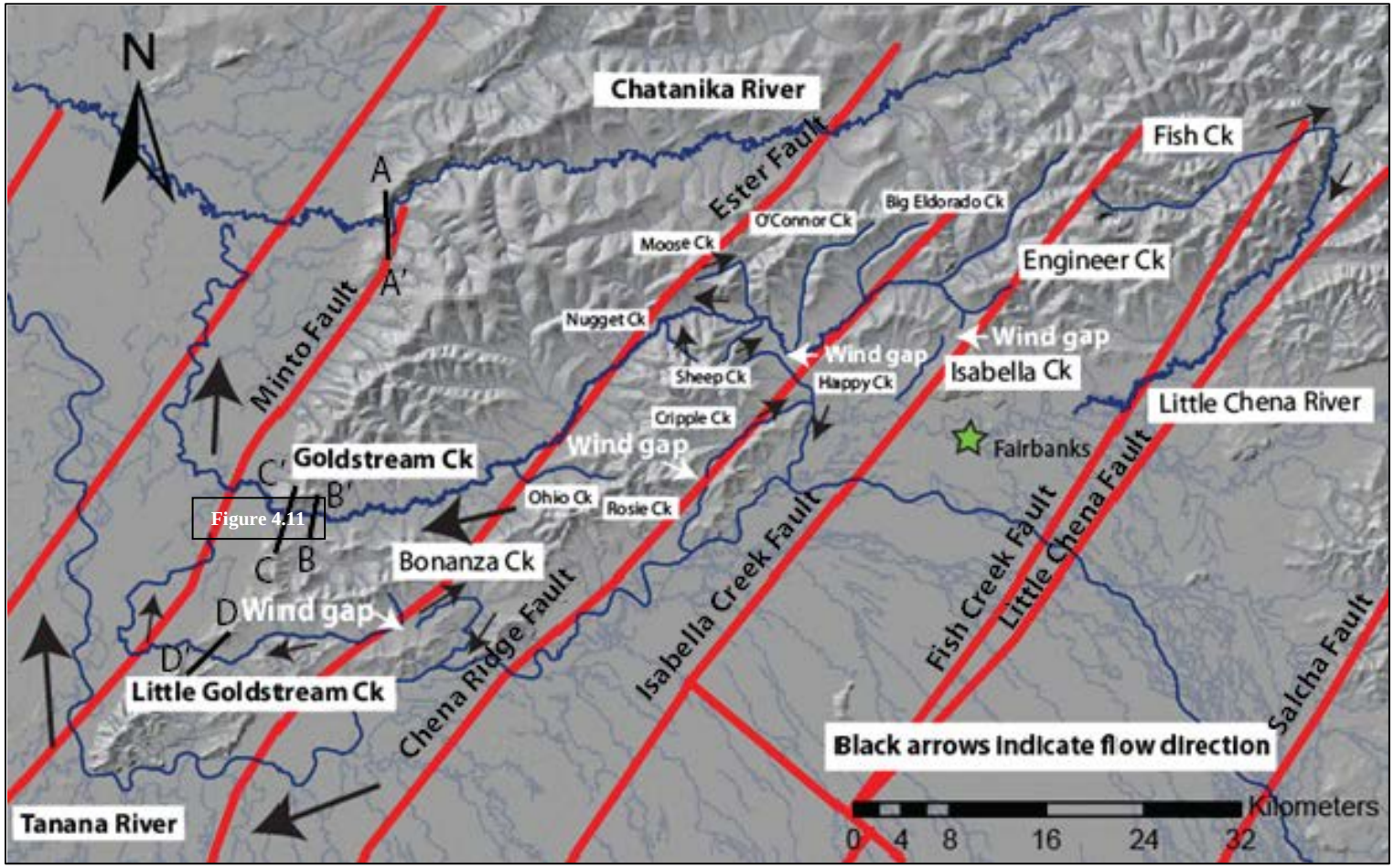

Figure 4.9: Drainage map of the Fairbanks area. Named drainages display features that suggest they may have been affected by active structures. Barbed drainages include Bonanza Creek, Cripple Creek, Moose Creek, Happy Creek, Sheep Creek, Nugget Creek, and Fish Creek. Black arrows indicate flow direction.

Pronounced linearity of drainages may indicate preferential flow along a fault, since water tends to erode more fractured rock and find the path of least resistance. Several drainages tend to follow the northeast-southwest structural fabric of the Fairbanks area, and some of them are situated in mapped fault valleys (Figure 4.9). These drainages include the upper reaches of Cripple Creek, Rosie Creek, Moose Creek, O'Connor Creek, Engineer Creek, Isabella Creek, and Big Eldorado Creek.

Valley asymmetry can be an indicator of ground tilting. Cross sections of DEMs along the lower Chatanika River reveal a steep and narrow north valley wall and a more broad and gentle south valley wall, which indicates asymmetry steeper toward the north (Figure 4.10).

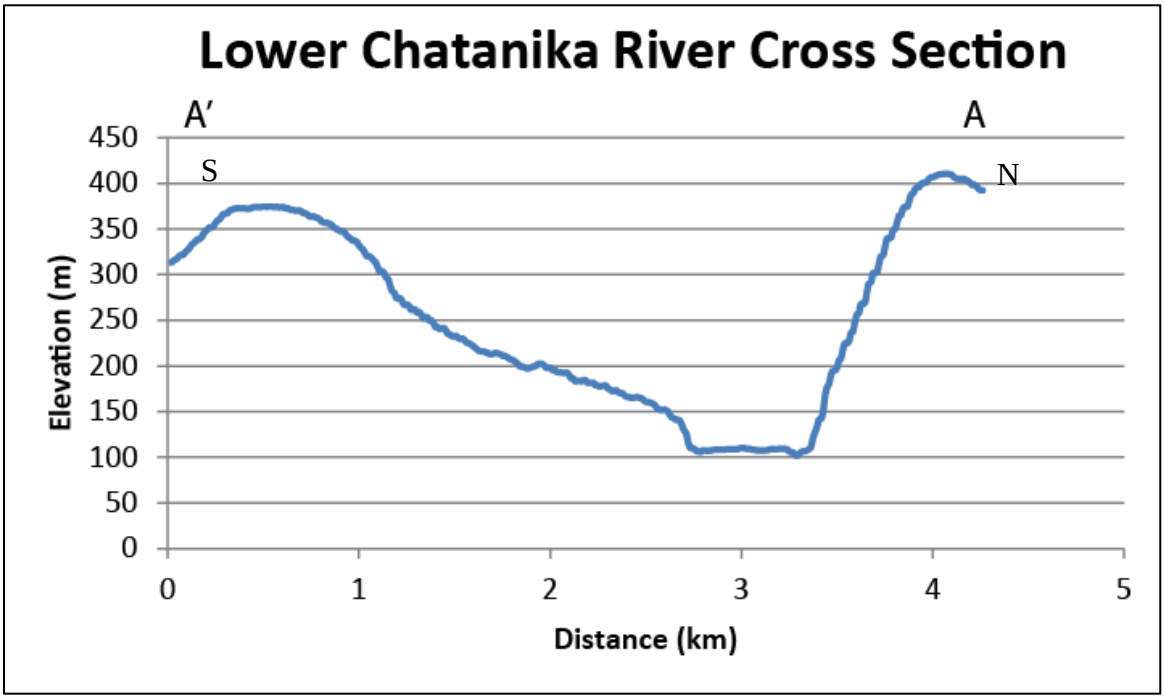

Figure 4.10: Cross section of lower Chatanika river valley showing asymmetry to the north. Location of cross section shown in Figure 4.9.

A LiDAR DEM of the lower Goldstream valley reveals asymmetrical development of terraces across the bottom of the valley (Figures 4.11 and 4.12a). I identified six terraces in a broad stair step configuration on the north side of the valley. These range from approximately 5 to 15 m in height, but the terraces on the south side of the valley cannot be correlated to terraces on the north side of the valley because they are too closely spaced and not well expressed. The asymmetrical development of terraces along the lower Goldstream valley may indicate asymmetry steeper to the south. Figure 4.12b shows a much longer cross section that spans the drainage divides north and south of lower Goldstream valley. The cross section reveals a steeper south valley wall and gentler north valley wall, which shows asymmetry steeper to the south.

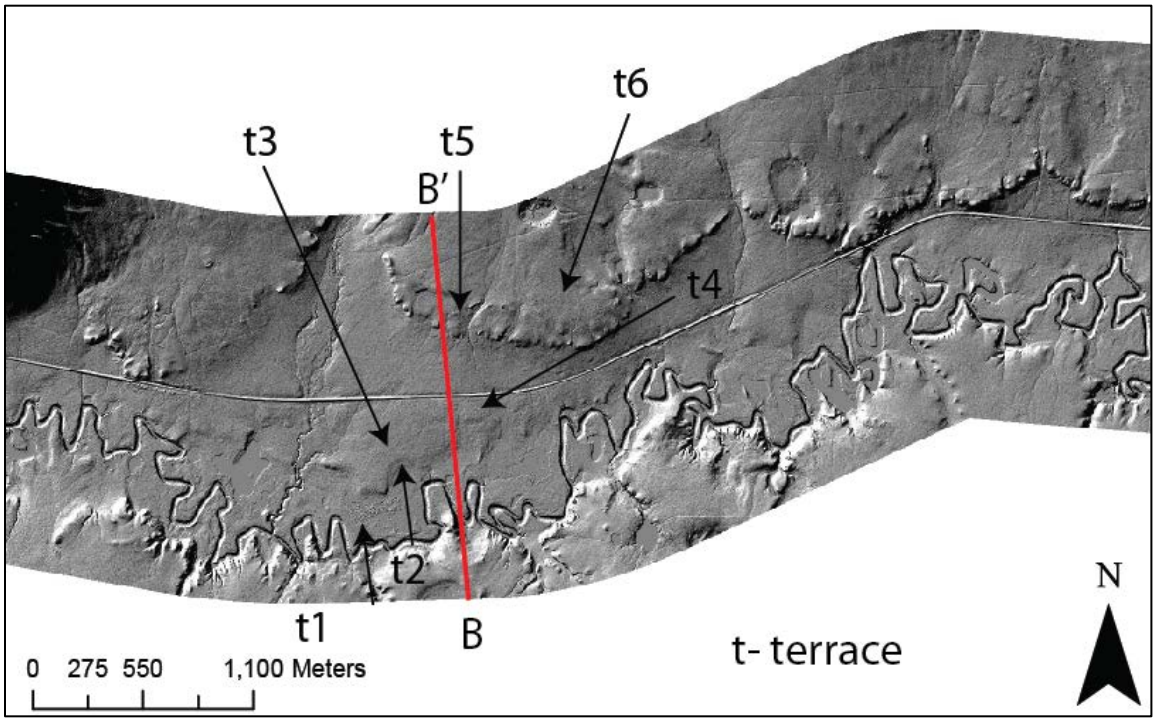

Figure 4.11: Map of lower Goldstream valley with cross section line shown in red. Location of LiDAR section shown in Figure 4.9.

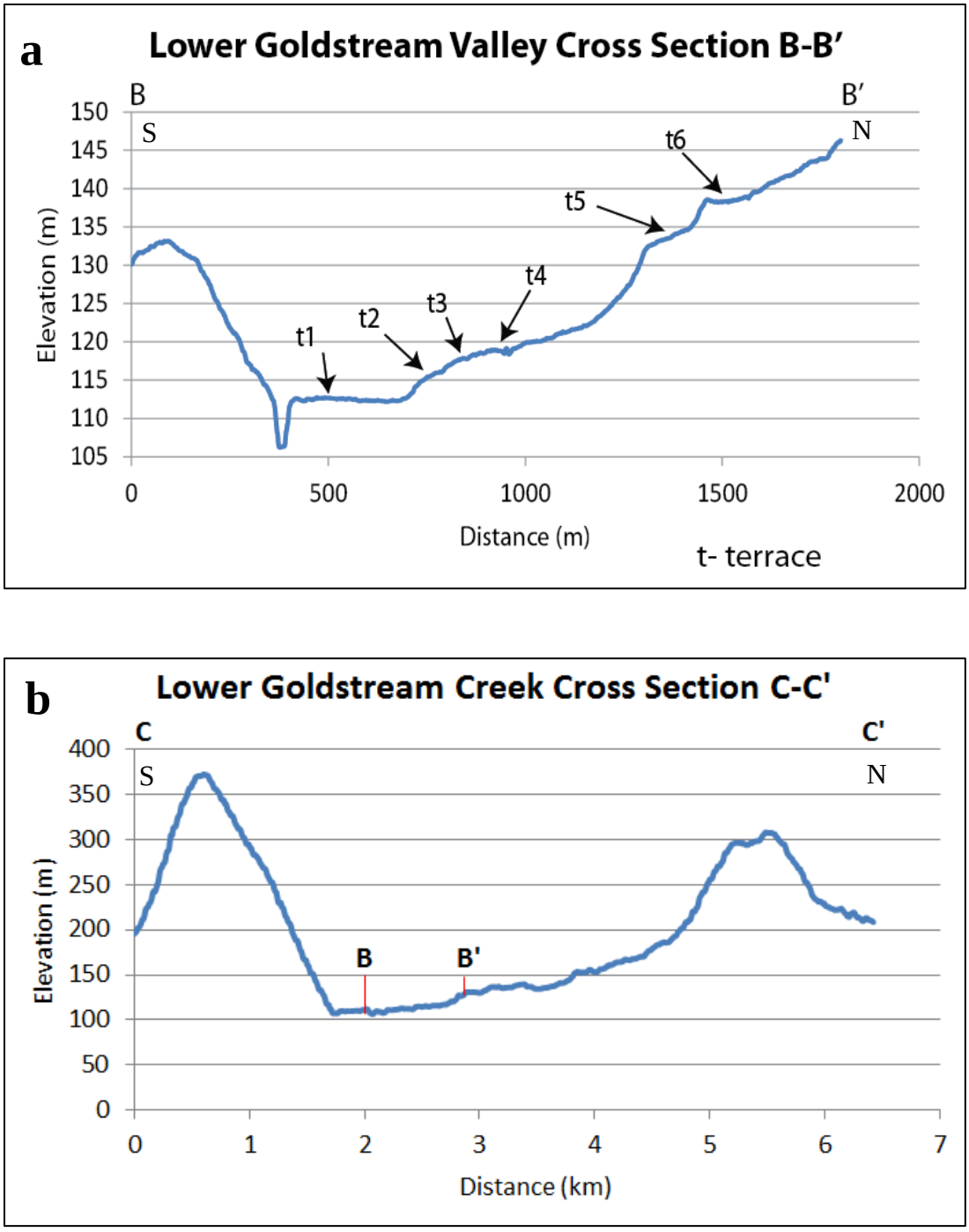

Figure 4.12: Lower Goldstream valley cross sections showing: a) asymmetrical development of terraces (t); and b) valley asymmetry and the location of B-B'. Location of cross sections shown in Figure 4.9.

The cross section for lower Little Goldstream Creek does not show any evidence of valley asymmetry (Figure 4.13).

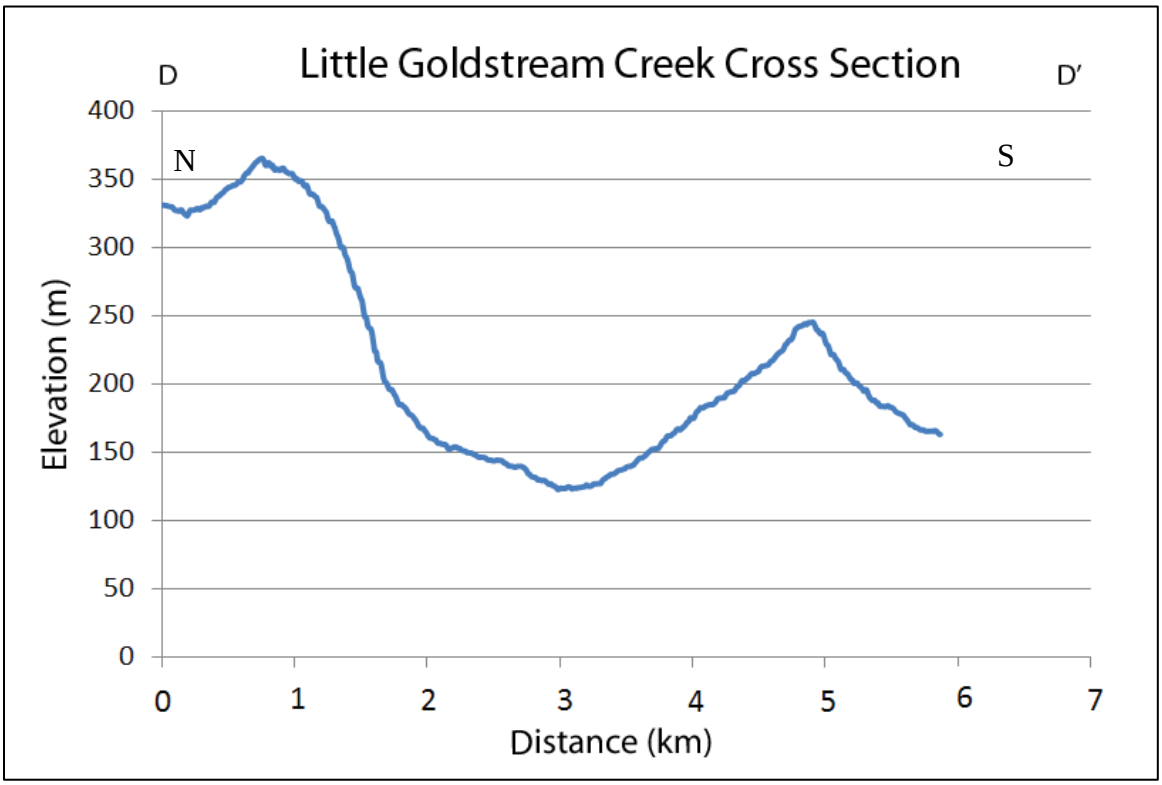

Figure 4.13: Little Goldstream Creek cross section showing symmetrical valley walls.

Stream incision is an indicator of changes in base level, which can possibly be linked to tectonic uplift. LiDAR DEMs of lower Goldstream Creek show a deep v-shaped channel where Goldstream Creek is actively incising (Figure 4.12a). Also, the Chatanika River has carved deeply into bedrock at the margin of the Nenana basin, creating a steep south-facing valley wall (Figure 4.10). In the same area, the river makes an abrupt turn to the west before exiting into the Nenana basin. At this point the river becomes less sinuous until it exits into the Nenana basin, where it changes to a sinuous pattern again.

4.2.2 Drainage Basin Asymmetry Factor

I chose to calculate the drainage basin asymmetry factor (AF) for Little Goldstream Creek, Goldstream Creek, and the Chatanika River because they reveal asymmetrical valleys, are associated with barbed drainages, and are perpendicular to the strike of interpreted faults. The AF values for Little Goldstream Creek, Goldstream Creek, and the Chatanika River basins are 54, 33, and 74, respectively (Table 4.1; Figure 4.14). An AF value of 50 implies that the drainage basin is symmetrical. The value for the Little Goldstream Creek drainage basin indicates that it is nearly symmetric; however, the AF values for Goldstream Creek and the Chatanika River imply slight tilts to the south and to the north, respectively.

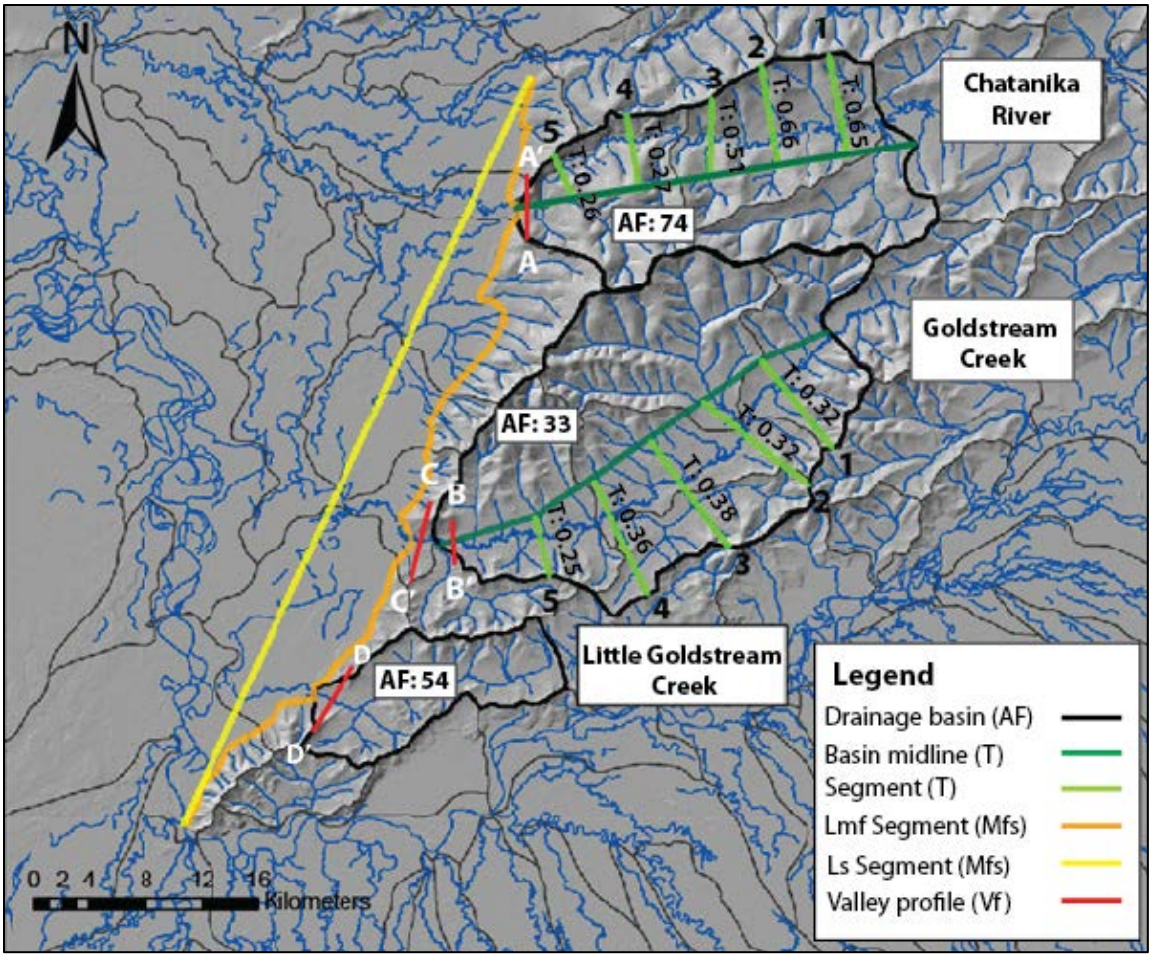

Figure 4.14: Geomorphic indices map including segments or polygons used for calculating the basin asymmetry factor (AF), transverse topographic symmetry factor (T), mountain front sinuosity index (M_{fs}), and the valley floor width-to-height ratio (V_f). Numbers along green lines correspond to T segments in table 4.2.

Table 4.1: Numerical results of morphometric calculations

	Basin Asymmetry Factor (AF)	Transverse Topographic Symmetry Factor (T)	Mountain Front Sinuosity (Smf)	Valley Floor Width to Height Ratio (Vf)
Little Goldstream Creek	54	--	1.1	2.8
Goldstream Creek	33	0.33	--	4.3
Chatanika River	74	0.47	--	2.1

4.2.3 Transverse Topographic Symmetry Factor

I calculated the transverse topographic symmetry factor (T) as a supplement to AF. I only calculated it on the Goldstream Creek and Chatanika River drainage basins because of the AF evidence for tilt in those two drainage basins (Figure 4.14). The average T values for Goldstream Creek and the Chatanika River are 0.33 and 0.47, respectively (Table 4.1). The values for each individual T segment are shown in Table 4.2. Since T is a vector, I calculated the bearings of the T segments and averaged them (Table 4.2).

T values along the Chatanika River include a wide range (0.26-0.66) and appear to increase upstream. This indicates that the Chatanika River valley is increasingly asymmetric farther upstream. The average value of 0.47 reflects moderate asymmetry along the Chatanika River drainage basin and suggests that a moderate amount of tilt may be causing preferred migration to the north-northwest at an average bearing of 350°. T values along Goldstream Creek are relatively consistent throughout the drainage basin and average 0.33, indicating low

asymmetry. Although T values are low, the data suggests a slight amount of tilt may be causing preferred migration to the southeast at an average bearing of 147°.

Table 4.2: Numerical results of individual T segments

	T Segment	Bearing
Goldstream Creek	1) 0.32	167°
	2) 0.32	156°
	3) 0.38	130°
	4) 0.36	144°
	5) 0.25	140°
	Average T: 0.33	**Average Bearing: 147°**
Chatanika River	1) 0.65	338°
	2) 0.66	352°
	3) 0.51	365°
	4) 0.27	349°
	5) 0.26	346°
	Average T: 0.47	**Average Bearing: 350°**

4.2.4 Stream-Length Gradient Index

I calculated the stream-length gradient index (SL) along Little Goldstream Creek, Goldstream Creek, and the Chatanika River (Figure 4.15). The resulting longitudinal stream profiles are shown in Figures 4.16, 4.17, and 4.18 with SL values. I constructed other stream profiles along drainages that appear distinctly linear, barbed, or within close proximity to a potentially active fault, or that were noted by Metz (1991) to indicate possible tectonic activity. These are shown in Appendix A.

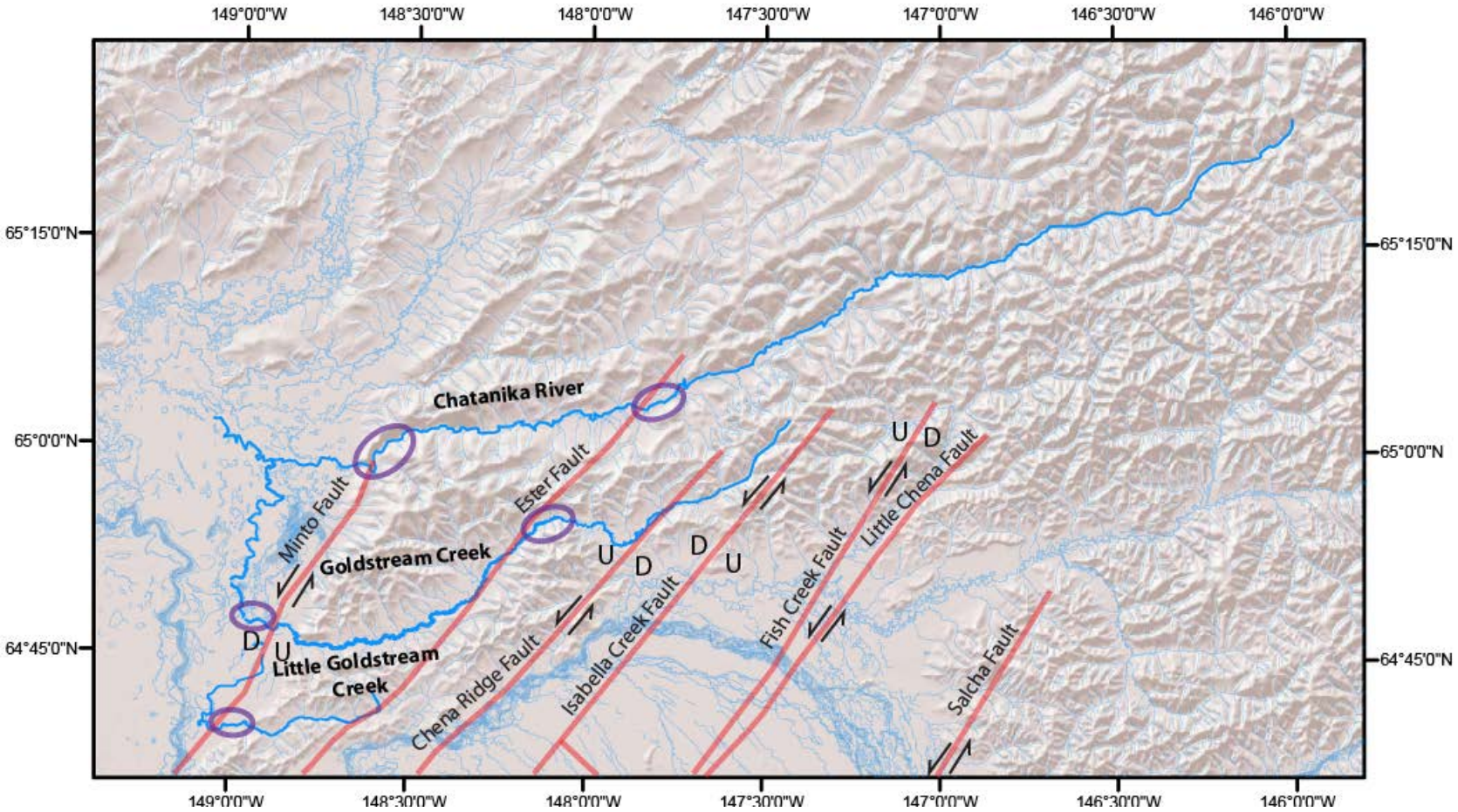

Figure 4.15: Drainage map showing knickpoints in purple ellipses and longitudinal profiles (bold blue lines) of Little Goldstream Creek, Goldstream Creek, and the Chatanika River. Longitudinal profiles are shown in Figures 4.16, 4.17, and 4.18.

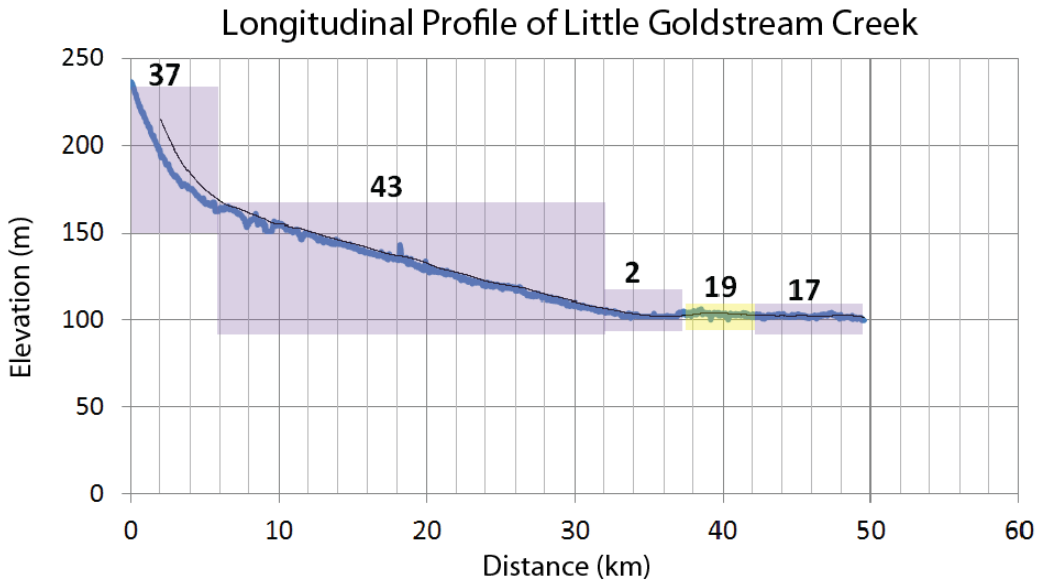

Figure 4.16: Longitudinal profile of Little Goldstream Creek. SL values are in bold type and knickpoints are highlighted in yellow. Purple boxes illustrate the segment of the stream that SL was calculated.

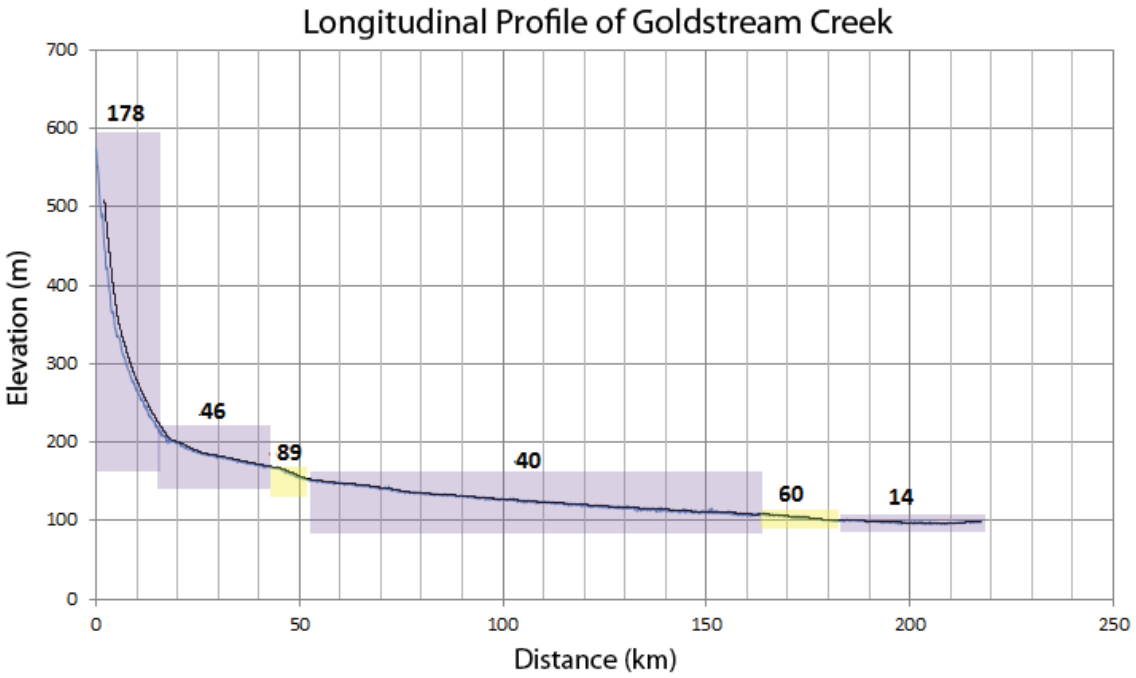

Figure 4.17: Longitudinal profile of Goldstream Creek. SL values are in bold type and knickpoints are highlighted in yellow. Purple boxes illustrate the segment of the stream that SL was calculated.

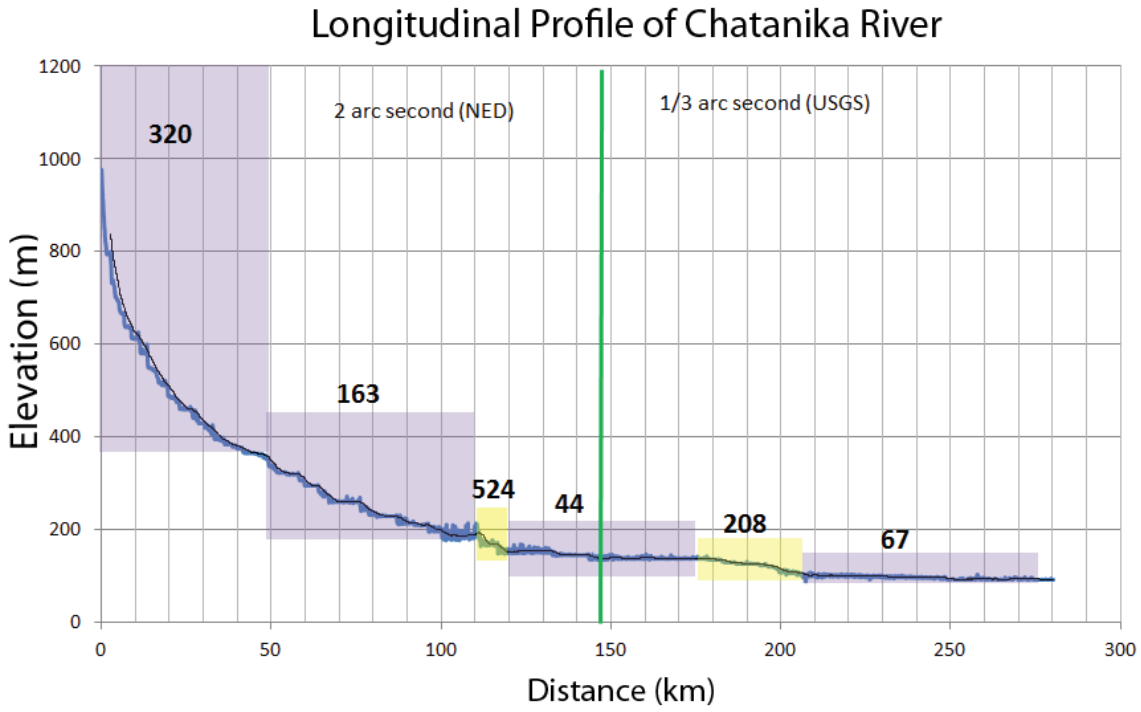

Figure 4.18: Longitudinal profile of Chatanika River. SL values are in bold type and knickpoints are highlighted in yellow. Purple boxes illustrate the segment of the stream that SL was calculated.

The stream length gradient index confirms a knickpoint in the lower reaches of Little Goldstream Creek at the pronounced break in slope as the stream exits into the Nenana basin (Figures 4.15 and 4.16). In this area, SL decreases from 43 to 2, then increases to 19. Little Goldstream Creek's profile also shows a steep gradient in the upper reaches for about 6 km, a linear constant gradient for about 36 km in the middle reaches, and an increase from 2 to 19 in the lower reaches. Near the lower reaches of the stream, an area where the elevation apparently increases over a distance of 2 km is likely related to a glitch in the DEM data. Little Goldstream Creek's profile does not show the typical concave, exponential curve of a graded profile but rather an atypical long, linear reach (Figure 4.19). The shape of the curve is more comparable to

the profile of an immature river that has not yet reached equilibrium, or where the balance between discharge and erosion is constant (Burbank and Anderson, 2001).

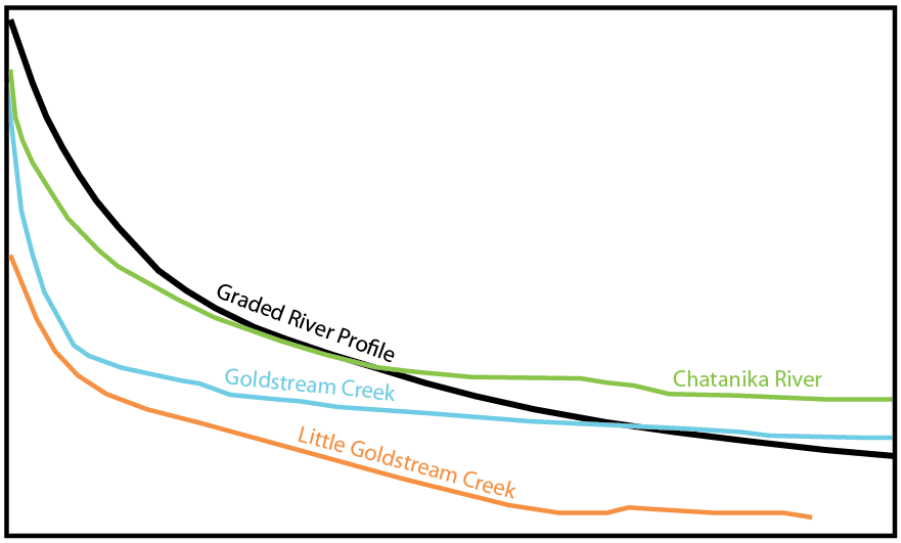

Figure 4.19: Superimposed longitudinal profiles of Little Goldstream and Goldstream Creeks and the Chatanika River, and a typical graded river profile (Burbank and Anderson, 2001).

Two knickpoints can be identified along Goldstream Creek's profile (Figure 4.17). The first knickpoint is located near the upper reaches, where the SL abruptly increases from 46 to 89 and then decreases again to 40. The second knickpoint is less noticeable, less steep on the downslope side, and is located near the lower reaches of the stream where the SL increases from 40 to 60 and then decreases to 14. The profile for Goldstream Creek shows a steep gradient in the upper reaches and a gentle gradient in the middle to lower reaches (Figure 4.19). This is comparable to a mature river profile that has remained in equilibrium for a long period of time (Burbank and Anderson, 2001).

One knickpoint can be observed in the lower reaches of the Chatanika River profile where SL abruptly increases from 44 to 208 (Figure 4.18). Since the DEM was of two different

resolutions (1/3 arc second and 2 arc seconds; Figure 4.18) along the river profile, it was difficult to identify knickpoints with certainty within the 2 arc second DEM boundaries because of its low resolution. However, near the middle reaches of the river, the profile shows an abrupt drop in elevation over a relatively short distance (10 km) along a low gradient part of the profile. Another knickpoint could be present in the middle reaches of the river where the SL abruptly increases from 163 to 524, and then decreases to 44. This location is also on trend with a mapped fault (Figure 4.15). Upstream from the knickpoint in the middle reaches, a step-like pattern of small elevation changes over a short distance suggests that these steps are more likely a product of noise in the DEM data. In contrast to Little Goldstream Creek's profile, Chatanika River's profile shows a concave curve typical of a graded river that has reached equilibrium (Burbank and Anderson, 2001; Figure 4.19).

4.2.5 Mountain Front Sinuosity

I calculated the mountain front sinuosity index (S_{mf}) along the pronounced break in slope at the eastern margin of the Nenana basin (Figure 4.14). The S_{mf} in this part of the mountain front has a value of 1.3 (Table 4.1). According to the classification of S_{mf} values determined by Bull and McFadden (1977), the S_{mf} value of 1.3 suggests a low sinuosity mountain front. Low sinuosity mountain fronts may indicate that the active tectonic forces that produce a straight mountain front outpace the erosive forces of drainages that carve through and create irregularities in a mountain front (Keller and Pinter, 2002).

4.2.6 Valley Floor Width-To-Height Ratio

Cross sections for Little Goldstream Creek, Goldstream Creek, and Chatanika River are shown in Figures 4.9, 4.10, 4.12, and 4.13. V_f values based on these cross sections are 2.8, 4.3, and 2.1, respectively (Table 4.1). According to the classification of V_f values determined by Bull and McFadden (1977), these values represent moderately U-shaped valleys and can be associated with low uplift rates (i.e. values >1).

4.3 Structural Analyses of Fault Exposures

Several quarries, mines, and exposures yielded significant structural and/or stratigraphic information: the Beacon Bald quarry, the Ryan Lode mine, Cripple Creek mine, and Brown's Hill quarry (Figure 4.20). All other faults exposed at quarries and roadcuts visited provided few data or lacked slip-sense indicators, primarily due to poor exposure. However, these latter exposures still yielded valuable structural information that is consistent with observations made at locations that provided more abundant and/or useful information.

The type of structural information acquired consisted of a combination of fault attitude, slip, and surficial stratigraphic data. Fault attitudes and slip data had the highest priority and are the main focus throughout this section. Surficial stratigraphic data were only recorded where available and needed.

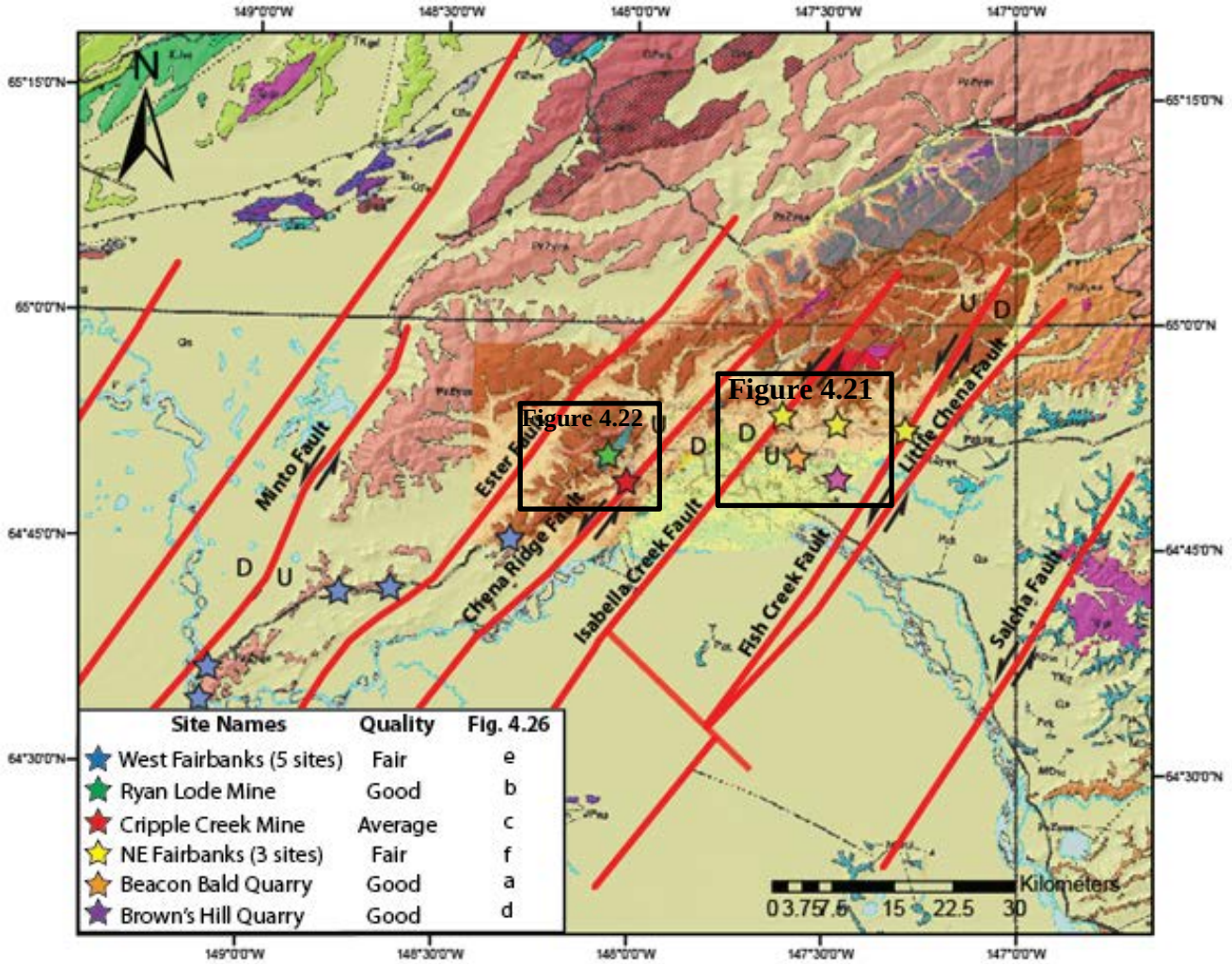

Figure 4.20: Map showing locations of all fault exposures visited in the study area; letters correspond to stereonets in Figure 4.26. Quality of fault exposures based on rating scale: poor, fair, average, good, and excellent.

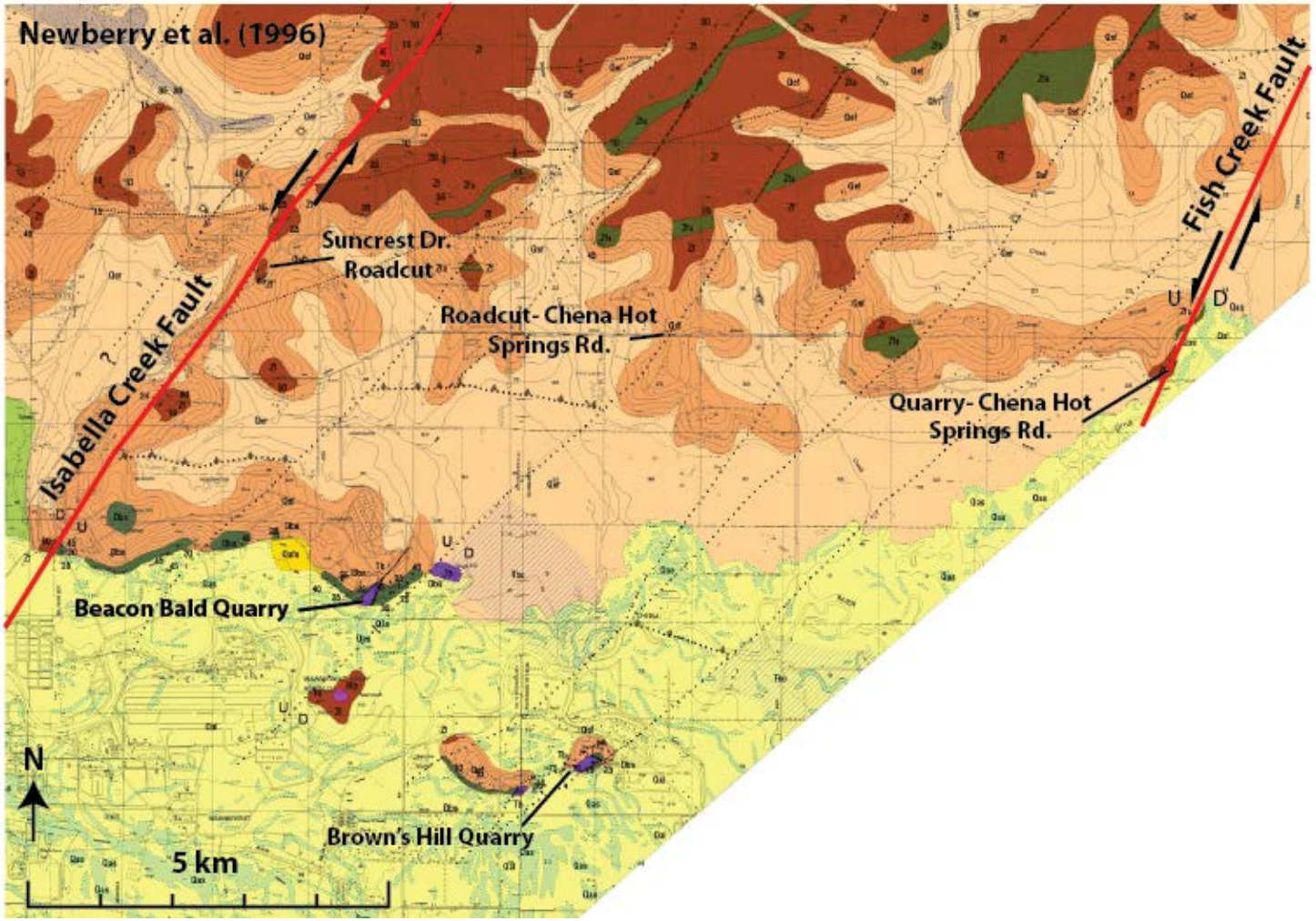

Figure 4.21: Map showing significant fault exposures northeast of Fairbanks (Newberry et al., 1996). Location of map is shown in Figure 4.20. Key to geologic units is shown in Figure 4.23.

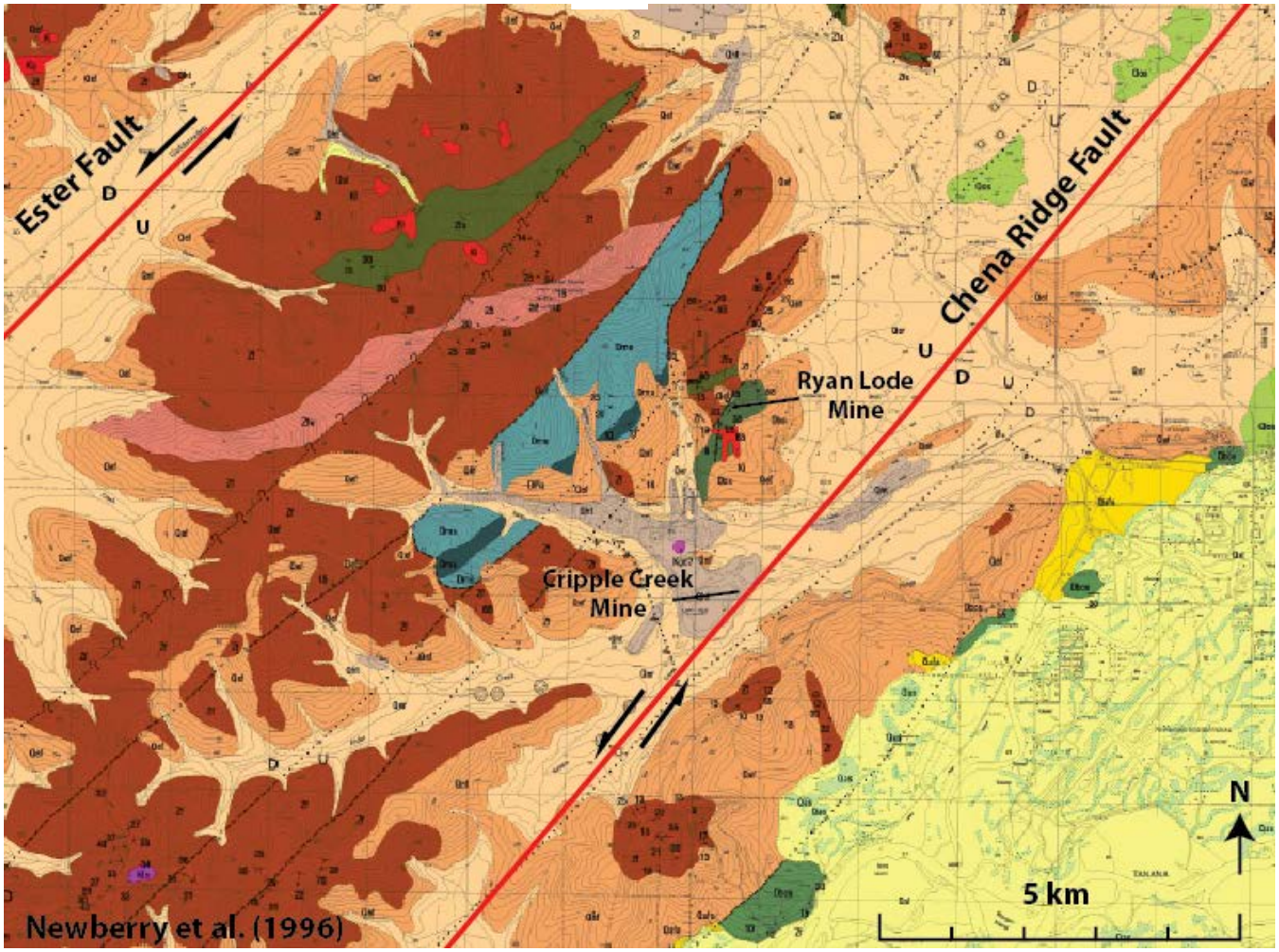

Figure 4.22: Map showing significant fault exposures west of Fairbanks (Newberry et al., 1996). Location of map is shown in Figure 4.20. Key to geologic units is shown in Figure 4.23.

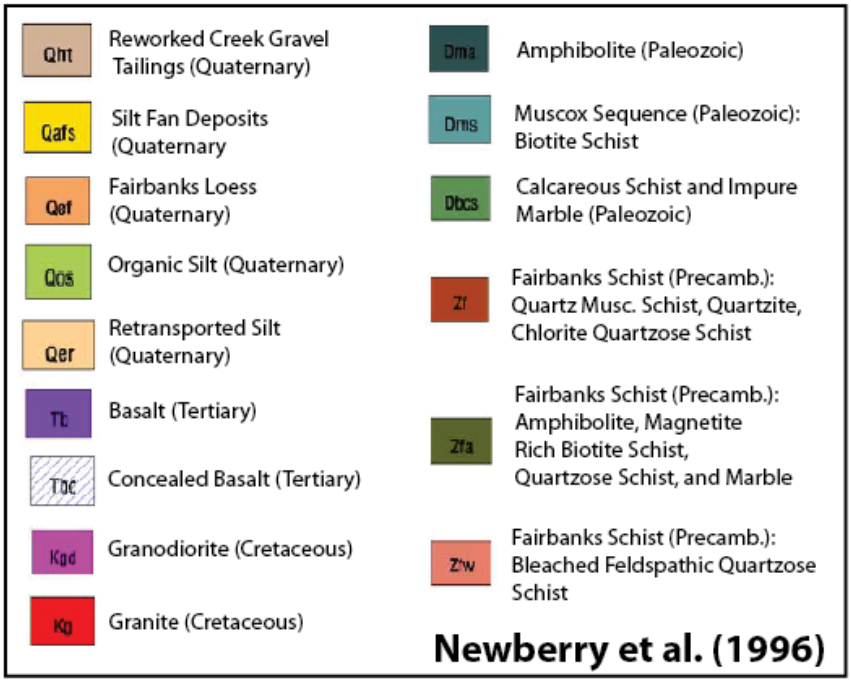

Figure 4.23: Key to geologic units from Figures 4.21 and 4.22 (Paleozoic and Precambrian rocks are protolith ages; Newberry et al., 1996).

4.3.1 Beacon Bald Quarry

The Birch Hill fault is located in the abandoned Beacon Bald basalt quarry inside the Fort Wainwright army post and east of the Isabella Creek fault (Figures 4.21 and 4.23). The quarry contains a roughly 50 meter high exposure of a northeast-striking fault within Eocene basalt (~55 Ma; Newberry et al., 1996). Another poorly exposed fault about 30 meters to the southeast juxtaposes basalt against quartzose phyllite of the Birch Hill Sequence (Newberry et al., 1996). The well-exposed, planar fault surface within the basalt on the northwest side of the quarry is nearly vertical, with dips between 80° and 90° from west-southwest to east-southeast. Toward the northwest corner of the quarry, a remnant of basalt breccia is preserved on the east face of the fault surface. Mounds of this basalt breccia are also exposed in the middle of the quarry. The

north and northeastern flanks of the quarry are overlain by unconsolidated eolian silt of Quaternary age (Fairbanks Loess; Newberry et al., 1996).

The fault surface on the northwest wall of the quarry reveals many slickenlines ranging from several centimeters to several meters long. There are two main types of slickenlines: longer slickenlines (>1 m) tend to be deeper, wider (+5 cm), bleached, and more continuous, while shorter slickenlines (<10 cm) are commonly shallower, thin, discontinuous, and polished. Slickenlines that plunge ~40° to 78° S tend to be the longer type and are commonly overprinted by slickenlines that plunge <40° S and are of the shorter type (Figure 4.24a and 4.25a). The fault face commonly contained unfilled extension fractures perpendicular to the plunge of the slickenlines. The fault face also exhibits common straight, discordant, cm-scale left-stepping surfaces on the main fault plane that are perpendicular to and overprinted by south-plunging slickenlines (Figure 4.24b). Based on these characteristics, I interpret these left-stepping surfaces to be antithetic Riedel shears that signify left-lateral motion. The fault contains another set of slightly crescent-shaped ridges that plunge to the north. They contain slickenlines on the gouged surfaces that plunge to the south and are perpendicular to the ridges (4.24c). I interpret these ridges to be synthetic Riedel shears that signify left-lateral and down-to-west motion. The host rock is very fine basaltic cataclastite, which suggests that these structures were superimposed on fault rocks that formed earlier.

The southeast flank of the quarry does not expose a bedrock fault surface like the northwest flank does, but remnants of fault gouge are exposed along the bottom of the quarry wall and floor. The surficial deposits above the bedrock on the southwest flank of the quarry consist of bluish-gray, friable, phyllitic fault gouge overlain by poorly consolidated reworked

loess and sub-angular to angular pebble to cobble-sized clasts of schist, quartz, and basalt. This grades into a top layer of poorly consolidated loess and peat. Closer examination of the loess deposits on the quarry wall revealed many linear, slickenline-like grooves with orientations similar to those of slickenlines found on the bedrock fault face on the opposite quarry wall (Figure 4.24d). Grooves plunge between 10° and 17° S and appear in the fault gouge on polished surfaces and reworked loess layers, but not in the overlying top loess layer. They also are present at least 5 cm into the outcrop underneath layers peeled from the face of the quarry wall. In addition, numerous fractures diverge southeastward at small angles (<10°) into the main wall (Figure 4.24d). The orientation of these fractures is consistent with left-lateral synthetic Riedel shears.

I could not determine if these grooves were related to the fault or if they were a product of cryoturbation, slope creep, or deformation by a bulldozer clearing the southeast wall of the quarry, which could give a similar appearance. However, if these structures are in fact fault-related slickenlines, they could indicate a left-lateral sense of movement sometime in the Quaternary period during the early stages of loess deposition.

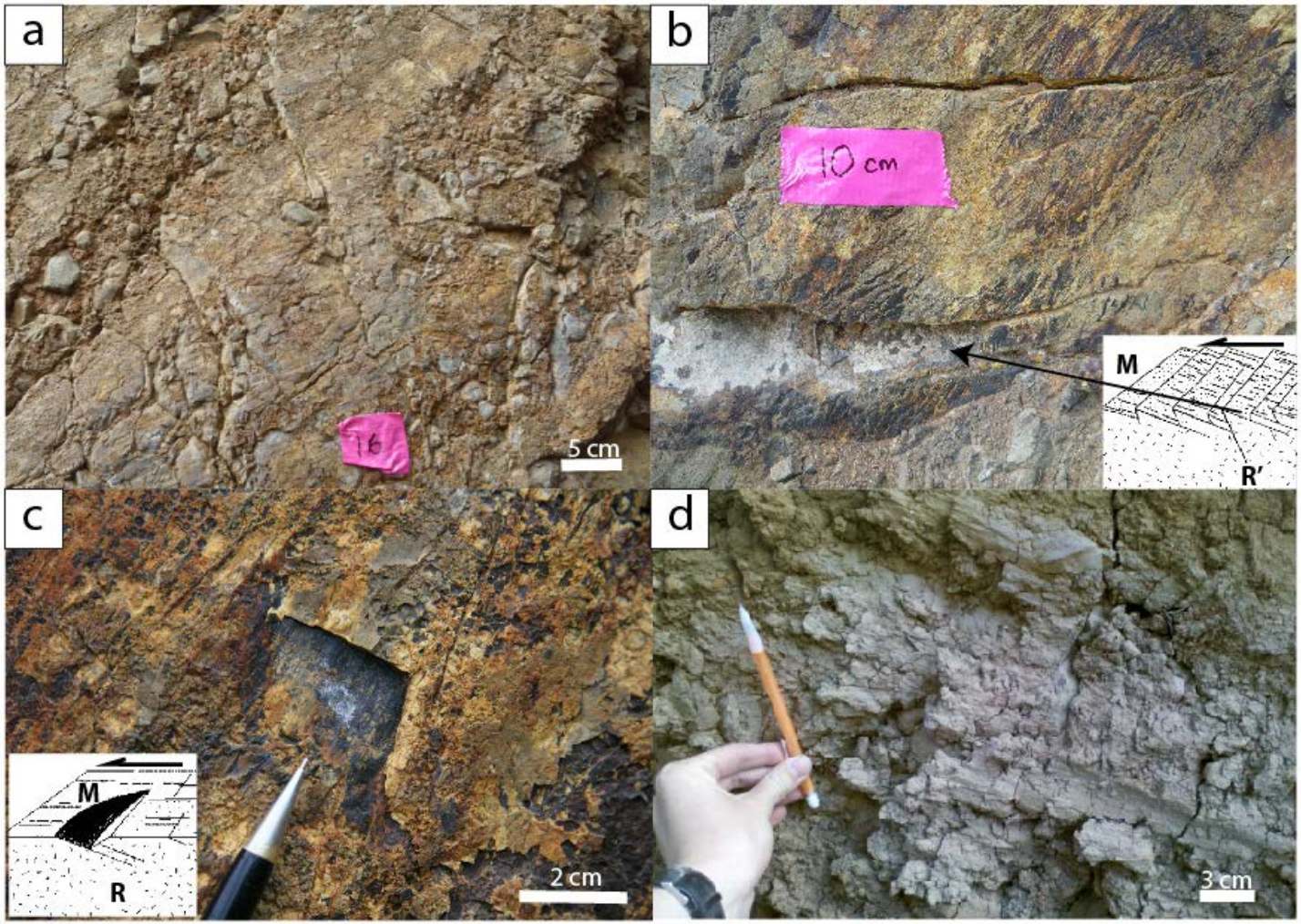

Figure 4.24: Photos showing structural features of the Birch Hill fault that include: a) slickenlines, b) antithetic Riedel shears, c) synthetic Riedel shears, and d) grooves in Quaternary loess. Diagrams on photos b and c are from Fossen (2010). M, master fault plane; R', antithetic Riedel shear; R, synthetic Riedel shear.

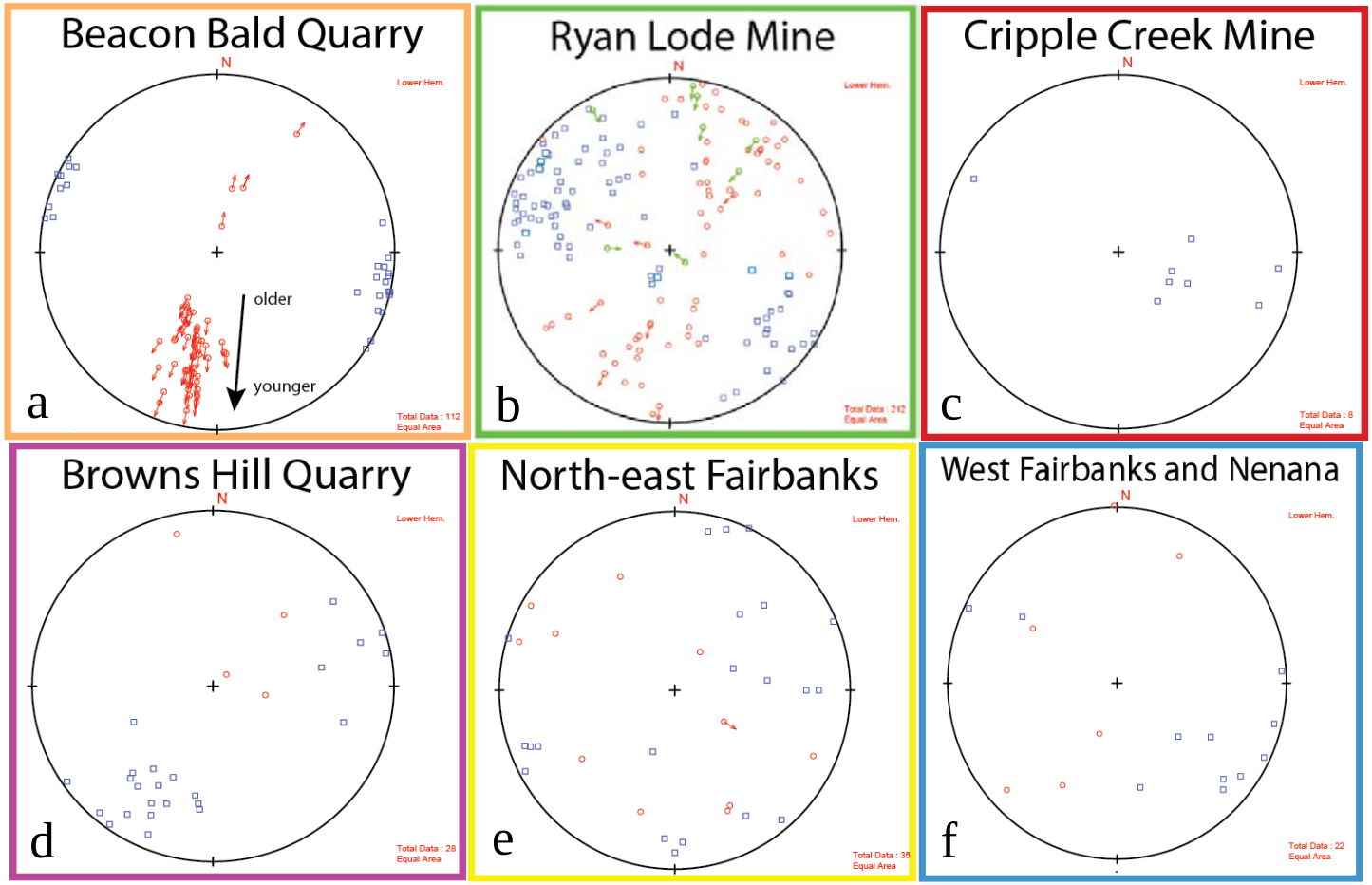

Figure 4.25: Stereoplots of fault data in the Fairbanks area. Faults are plotted as poles (blue squares) and lineations are plotted as red circles. Arrows indicate slip direction on the hanging wall where known. Red arrows indicate normal slip and green arrows indicate reverse slip. Fault data are plotted in lower hemisphere and equal area projection. Colored outlines correspond to colored stars in Figure 4.20.

At the northwest corner of the quarry a layer of surficial basalt breccia appears to have been deposited on an erosion surface above the basalt and does not show obvious vertical offset. Above the basalt breccia layer, conjugate fractures that dip steeply from northwest to southeast are concentrated in Quaternary loess (Newberry et al., 1996) and are localized above and parallel to the fault (Figure 4.26). The fractures show small vertical offset of ~1-2 cm, but there is no evidence of significant vertical offset. Given the fracture orientations and that they are localized above the fault, they may possibly be tectonic. Alternatively, they may be related to slope settlement, landsliding, or toppling of the quarry walls. The lack of significant vertical offset along the fractures suggests that there has been no significant vertical movement since the loess was deposited.

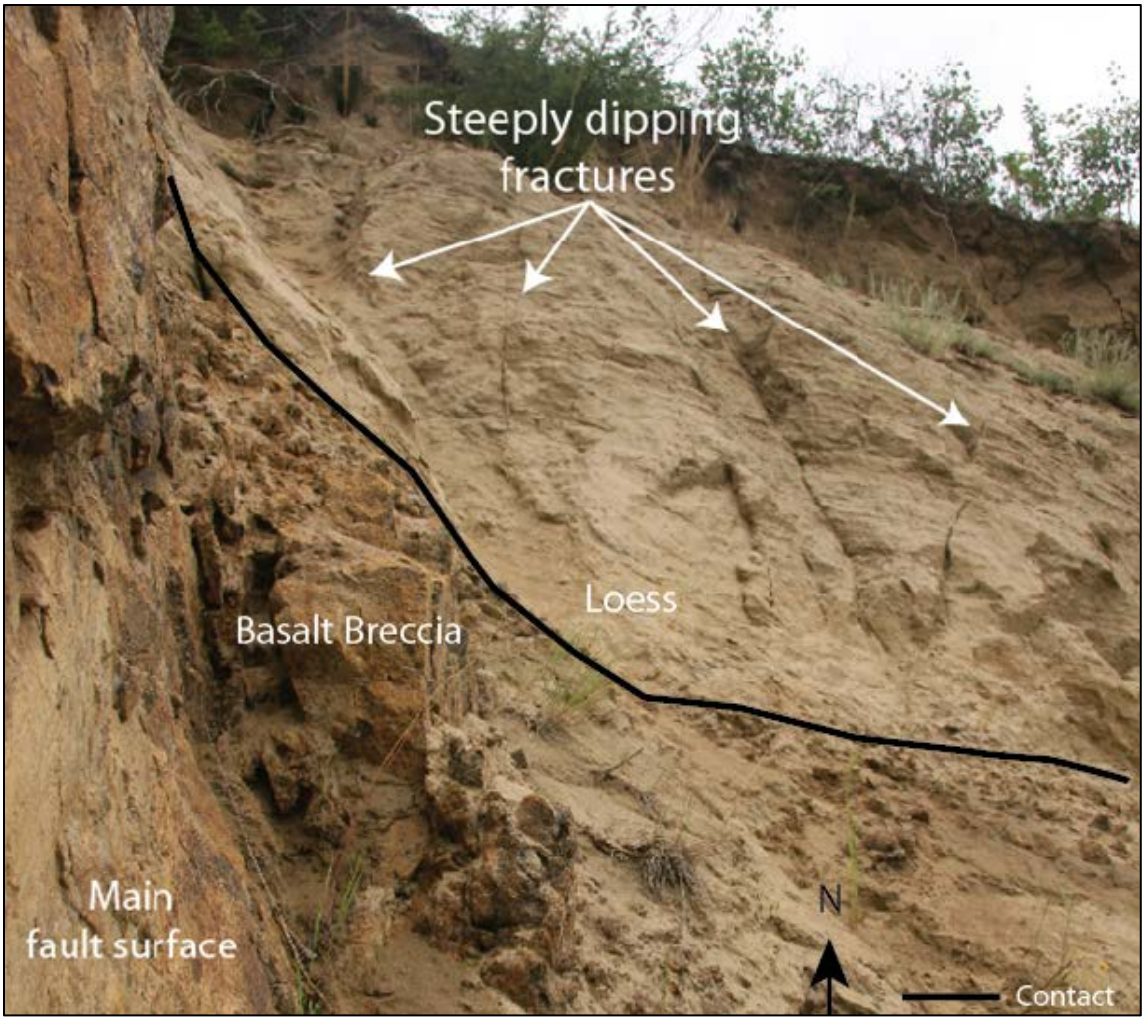

Figure 4.26: Photo showing steeply dipping fractures in loess above the fault face at the northeast side of the Beacon Bald quarry.

The combination of slickenline data, kinematic indicators, and geology indicate that this fault exhibits dominantly west side down left-lateral motion overprinted by dominantly left-lateral motion, and that larger movements were mostly west side down and smaller movements were mostly left-lateral (Figure 4.25a).

4.3.2 Ryan Lode Mine

The Ryan Lode Mine is an abandoned gold mine in Ester approximately 9 miles west of Fairbanks, located west of the Chena Ridge fault (Figure 4.22). The property has been mined on and off since 1911; production finally ceased in 2004. In total, 19,820 ounces of gold and 14,330 ounces of silver have been produced from two gold-hosting shear zones, the Ryan Lode fault and the Curlew fault (Avalon, 2014).

Both the north and south pits of the Ryan Lode expose highly fractured schist and quartzite of the Fairbanks Schist Unit (Newberry et al., 1996). Pits at the Ryan Lode mine expose a steeply-dipping northeast-striking shear zone that is over two km long, 300 m wide, and displays over one km of apparent left-lateral displacement (Avalon, 2014). The deeper and more extensive north pit exposes many small-scale shear zones and planar faults that are exposed along strike and, in the south pit, these structures are exposed down dip (Figure 4.27). The shear zones and faults are discontinuous and range in width and length from several centimeters to several meters. Many are closely associated with graphitic schist or graphitic fault gouge. Also, the vast majority of faults are mineralized with calcite, quartz, or both. The majority of faults and shear zones strike northeast and dip either to the southeast or northwest with dips mostly from 40° to 86° (Figure 4.25b). The south pit wall reveals several local negative flower structures (Figure 4.27).

Many of the faults and shear zones expose different kinematic indicators that I used to interpret the direction and sense of slip. These include slickenlines, slickenfibers, synthetic Riedel shears, and drag folds. Slickenlines, slickenfibers, and synthetic Riedel shears range from <1 cm to 5 cm in length and plunge anywhere from 4° to 88° to the north or south in no

particular relative order of timing. All slickenfibers consist of calcite. Several individual fault planes reveal slickenfibers that step and plunge in opposite directions and are commonly overprinted by slickenlines (Figure 4.28). Fault surfaces commonly contain slickenlines on sheets of calcite that were superimposed on other calcite sheets indicating several episodes of slip (Figure 4.28). The plunge directions of the slickenfibers and slickenlines indicate nearly pure normal, normal-left-lateral, and reverse-left-lateral slip. Northeast-trending drag folds are common in the schist along footwalls and hanging walls of faults and indicate normal and reverse motion (Figure 4.29).

I conducted a paleostress analysis for the Ryan Lode Fault zone using StereoStat. From the steroplots, I identified two sets of conjugate faults. Both sets are of roughly the same northeast-striking orientation, but are based on different shear-senses identified in the field. I averaged the orientations and the slip indicators to obtain an average great circle as well as an average lineation orientation and direction of each fault set. I imported the averaged fault orientation and slip data and conducted a principal component analysis in StereoStat. This method employs a statistical algorithm based on the orientation data and arrives at three eigenvectors that correspond to the three principal stress axes of the Andersonian Theory of Faulting (Anderson, 1951).

Based on the orientation of two sets of conjugate faults, the principal component analysis function of StereoStat generated two plots that show the principal stress axes, Sigma 1, 2, and 3. One set indicates normal motion (Figure 4.30a) and the other set indicates reverse motion (4.30b) based on the orientations of Sigma 1, 2, and 3. Both paleostress analyses indicate dip-slip motion at the time of origination based on the orientation of Sigma 2, but gentle plunges of the lineations

suggest strike-slip motion. Based on the orientation of the Sigma 1, 2, and 3 axes for both plots, the faults likely originated as normal faults. The reverse faults are unlikely to have originated as reverse faults because the angle that S3 bisects between them is too small (Figure 4.30b). These faults were likely reactivated as reverse faults when Sigma 1 and Sigma 3 traded places. Strike-slip motion likely occurred after fault origination.

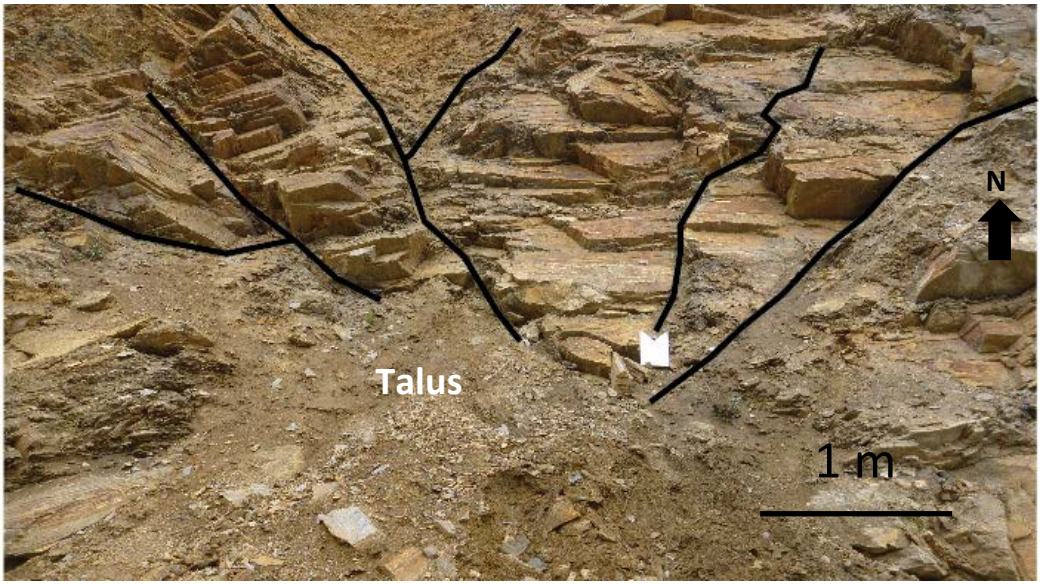

Figure 4.27: Negative flower structure exposed in the south pit of the Ryan Lode mine.

Figure 4.28: Slickenfibers and slickenlines that plunge in opposite directions on a southeast-dipping fault surface. Arrows represent direction of fault motion as indicated by slickenfibers.

Figure 4.29: Normal and reverse drag folds exposed in the south pit of the Ryan Lode mine.

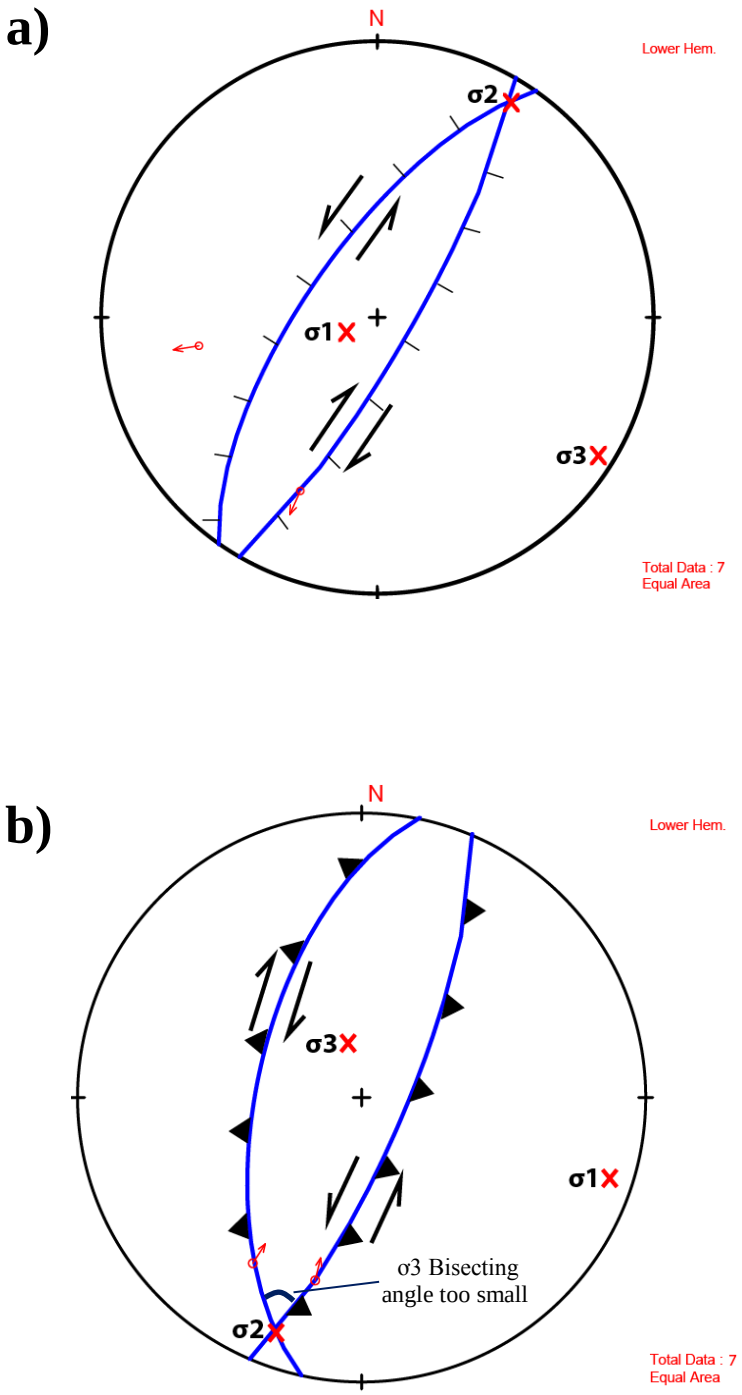

Figure 4.30: Paleostress analyses on two sets of conjugate faults from the Ryan Lode fault. a) showing normal motion, and b) showing reverse motion. Faults are plotted as blue great circles, lineations are plotted as red circles. Red arrows correspond to slip direction on the hanging wall. Red x's correspond to Sigma 1 (σ1), Sigma 2 (σ2), and Sigma 3 (σ3).

4.3.3 Cripple Creek Mine

Boswell (1979) described the auriferous gravel, termed the Cripple Gravel (Péwé 1975), at Cripple Creek as very deep (18-51 m) and overlain by hundreds of feet of barren gravel and reworked loess. The Cripple Creek pay channel was a paleo-channel of Ester Creek that diverged from the present Ester Creek opposite the mouth of Ready Bullion Creek (Figure 4.31, Péwé et al., 1989). Subsequent to gravel deposition, significant faulting and tilting ensued, resulting in a 5-8% grade on the surface of the gravel and bedrock (Boswell, 1979). The Cripple Gravel mostly consists of reworked solifluction debris, hence it might be representative of a periglacial climate at the end of the Pliocene and Early Pleistocene (Péwé, 1975).

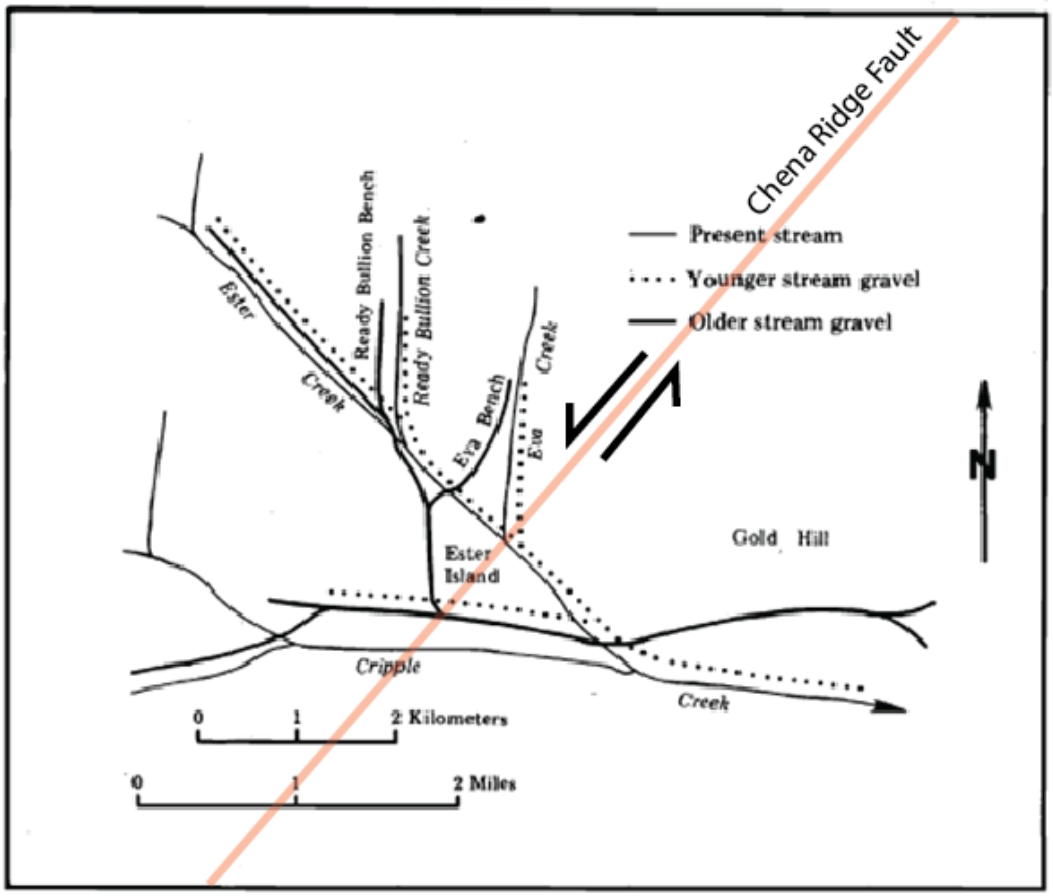

Figure 4.31: Map of Pliocene, Pleistocene, and present stream gravels near the confluence of Cripple and Ester Creeks (from Péwé et al., 1989). Map also shows approximate location of the Chena Ridge fault.

A mining pit located along Cripple Creek and along the Chena Ridge fault (Figure 4.22) temporarily (2012) revealed a 7 x 15 m north-facing, moderately exposed wall of graphitic schist bedrock overlain by fine to coarse, angular to sub-rounded, poorly sorted, unconsolidated, moderately-bedded auriferous gravel (4.32a). This exposure has since been destroyed by continued mining activity. Bedding in the gravel package appeared to be warped into a symmetrical anticline with close inter-limb angles that spanned ~12m across (4.32b). The gravel was in sharp contact with and overlain by an unconsolidated, homogenous, organic-rich package

of loess. A top layer of reworked gravel with loess interbeds and lenses lay unconformably on top of the loess but also in contact with the gravel where the gravel bed appeared thinned at the apex of the anticline.

The quarry wall exposed several planar and irregular faults. The strike of the faults was north-northeast with dips between 27° and 80° to the northwest or southeast (Figure 4.25c). The lower angle faults toward the west side of the pit (Faults 3 and 4; Figure 4.32b, e, and f) were associated with fault breccia of bleached and discolored clay gouge and brecciated material. Brecciated material consisted of chunks of schist, quartz, gravel, and loess (Figure 4.32f). The faults displayed different apparent relations to the gravel. The westernmost of the steeper planar faults (Fault 1; Figure 4.32b and d) juxtaposed graphitic schist against tan to bleached schist below the gravel layer, but appeared to terminate at the base of the gravel. Fault 2 was located towards the east flank of the pit wall and juxtaposed gravel against loess and penetrated about halfway into the loess bed (Figure 4.32b and c). Along the gravel-loess fault contact there was minor discoloration in the loess and small fractures appeared to radiate out into the loess. The depositional contact between the loess and the above reworked gravel and loess package on the hanging wall appeared slightly upwarped (Figure 4.32b). No lineations or kinematic indicators were present on either fault 1 or fault 2, but the loess and gravel packages served as stratigraphic markers to determine an apparent reverse sense of offset for fault 2 of approximately 2 m. Fault 1 terminated directly beneath the apex of the anticline, so it is likely that fault 1 is a reverse fault and mostly contributed to warping the gravel into an anticline.

Faults 3 and 4 were located on the western-most side of the pit. Fault 3 was irregular and appeared to parallel the basal gravel contact (Figure 4.32e). At the top-most tip of the fault, the

bedding appeared more vertical and chaotic, and fragments of schist were mixed with gravel. The appearance of the bedding suggests that the fault cut into the gravel, but there was no evidence that the fault continued into the overlying reworked gravel and loess package. It was difficult to determine the sense of offset of fault 3, but given the appearance of fault breccia on the hanging wall near the tip of the fault and gravel on the footwall, and that the gravel bed is warped into an anticline, the sense of offset is likely reverse. Stratigraphic markers indicated an approximate apparent displacement of 0.5 m.

Fault 4 appeared to cut fault breccia in a small area near the tip of fault 3 (Figure 4.32f). The nature of the fault was planar and there was discoloration along the fault plane. No stratigraphic markers or slip indicators were available to determine the sense of offset for this fault.

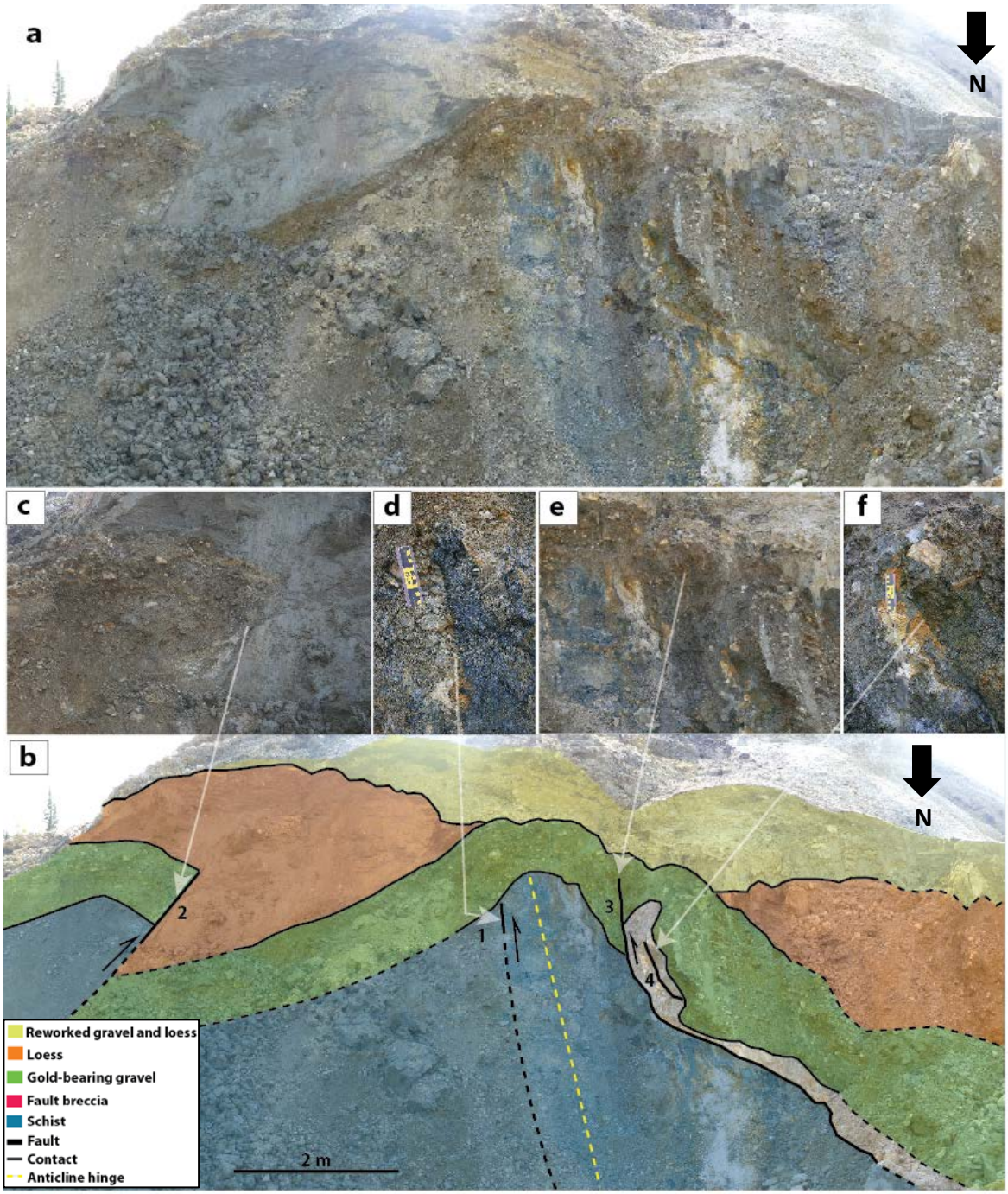

Figure 4.32: Structural interpretation of the Cripple Creek mine pit. a) uninterpreted pit exposure, b) structural interpretation of pit exposure, c) photo of fault 2, d) photo of fault 1, e) photo of fault 3, and f) photo of fault 4.

In the adjacent area to the west and on the other side of the pit wall, a northeast-striking slip surface (Fig 4.33a) was exposed that contained slumped material (Figure 4.33b). The slumped material consisted of light gray to bleached sand- to cobble-sized brecciated rock fragments, similar to the fault breccia found near the faults in the adjacent pit. The slip surface exposed two sets of lineations. The top-most set of lineations plunged ~90° and the underlying set of lineations plunged ~70° NE. It appeared that the slump may recently have moved down-dip under the influence of gravity along a pre-existing fault plane. The orientation of the slip surface closely matches the projected orientation of fault 3.

About 50 meters to the northeast another structure of similar character and dimensions was on trend with the anticline described above (Figure 4.33c). This structure appeared to be a symmetrical anticline with close interlimb angles that spanned ~10 m across. This anticline was aligned with the northeast projection of the anticline in the main pit and may be the same structure (Figure 4.32b). Unfortunately, the exposure could not be examined in detail due to flooding as a result of mining activity. Stratigraphic layers laterally equivalent to the folded layers were examined, but could not be correlated with the anticline exposed in the main pit. However, through careful examination of the photo, it appears that this structure consists of the same sedimentary layers as in the main pit, except that the gravel in this location is much more oxidized.

The structural and stratigraphic features observed in the pit support a tectonic origin. This includes the close association and proximity of an anticline that folds parallel-bedded gravel of uniform thickness with fault planes, brecciated material, and clay gouge. It is unlikely that climate-induced processes could account for structural features such as the anticline and closely

associated faults, including the northeast projection of the anticline on the other side of the flooded pit. However, it is likely that some features were caused by rigorous mining activity, such as the observed slump and related faults.

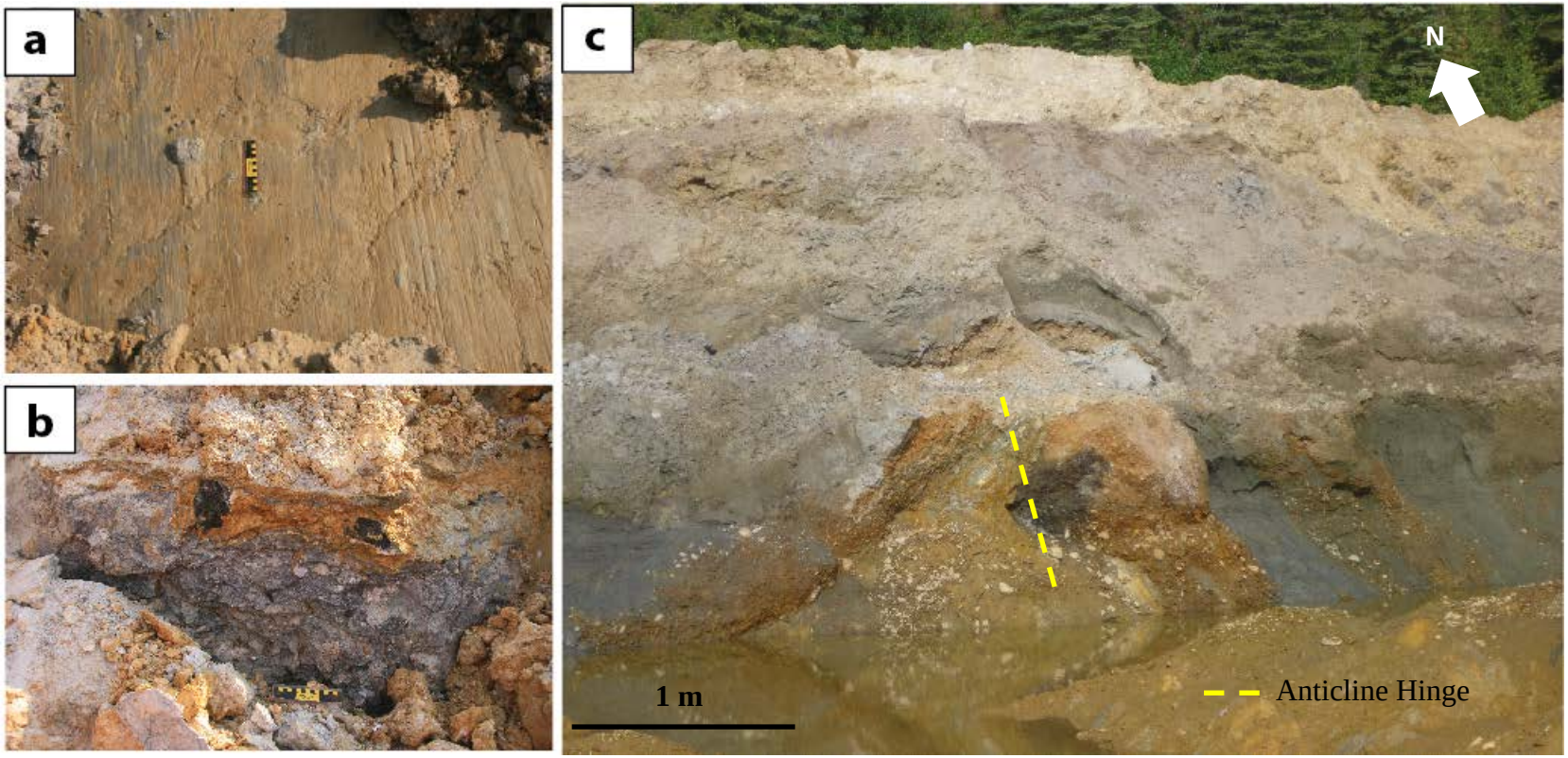

Figure 4.33: Structures in areas adjacent to the main pit at the Cripple Creek mine. a) Lineations along an exposed slump surface, b) brecciated material, c) anticline that may be a projection of the anticline in the main pit.

The appearance of the bedding and uniform thickness of the gravel package support that at least one or more events on fault 1 warped the gold-bearing gravel deposit into an anticline after deposition of the gravel, which would indicate faulting in the Pliocene. Fault 2 offset the gold-bearing gravel deposit and the basal part of the overlying loess package, but did not cut through the entire package. Although the loess has not been locally dated, regional loess studies around Fairbanks suggest that the age of the loess could be Illinoian (130-191ka) (Péwé, 1975) or significantly older, up to 3 Ma (Westgate et al., 1990; Péwé et al., 2009). Thus, the event or events on fault 2 occurred in the Pliocene and possibly later. Fault 3 cut at least into the basal part of the gravel package, which would indicate a maximum age of Pliocene. The unconformity at the base of the reworked gravel and loess package and the slight thinning of the gravel bed at the apex of the anticline suggest that a portion of the loess and gravel were eroded prior to the deposition of the reworked gravel and loess package. The cause of erosion is uncertain. One possible mechanism to explain the erosion is reactivation of faults that uplifted, folded, and led to erosion of the gravel and loess packages, perhaps during or after deposition of the loess. Alternatively, the erosion could be related to river floodplain processes or anthropogenic modification of the site.

The faults exposed at Cripple Creek mine are along the projection of the Chena Ridge fault (Figure 4.22). The faults in the pit strike north-northeast and the mapped fault strikes northeast. The slightly different orientations suggest that the faults in the pit could be interpreted as reverse splay faults from the master left-lateral Chena Ridge fault.

4.3.4 Brown's Hill Quarry

(I was unable to make personal observations at Brown's Hill quarry, so the following section is based on field notes and photos by Wesley Wallace.)

Brown's Hill quarry is an active basalt quarry located a few miles east of Fairbanks and west of the Fish Creek fault (Figure 4.23). The bottom of the pit in the quarry has a 250 meter long east-facing wall that exposes multiple planar faults within basalt and schist of the Birch Hill Sequence (Figures 4.34 and 4.35; Newberry et al., 1996). Faults strike west-northwest or east-southeast and dip moderately to steeply either to the north-northeast or south-southwest. Dips range between 50° and 90° (Figure 4.25d). Faults display rare slip indicators such as slickenlines, stepped slickenfibers, footwall drag folding, and offset lithologic markers; all indicate normal or normal-left-lateral motion. Observable normal displacement ranges from 1-10 meters.

At the southern end of the east-facing pit wall, a concentric antiform within schist is bounded to the north and south by normal faults to form a horst (Figure 4.34 and 4.36). At the crest of the anticline, basalt unconformably overlies schist; this unconformity appears to be folded (Figure 4.36). The schistosity on the upper part of the fold is at a low angle to the unconformity and the dip of the folded unconformity increases toward the northern fault. The concentric geometry of the fold, folding of and flexural slip within the schistosity, and folding of the unconformity support that folding occurred after basalt extrusion and possibly during faulting, rather than during metamorphism of the schist. Across the road to the southeast, the unconformity and top of the horst are higher, suggesting a slight tilt to the northwest.

The north end of the pit wall reveals another larger horst with a gently south-dipping unconformable contact between the schist and basalt, suggesting tilt to the south. The fault distribution and geometries can be interpreted as a south-tilted fault graben between two down-to-north normal faults with another significant down-to-south normal fault to the south of the tilted fault block (Figure 4.34). Normal faults with west-northwest strike are atypical of the Fairbanks area. Their orientation and tilted fault block geometries suggest that they could be in an extensional stepover between two larger northeast-striking left-lateral faults.

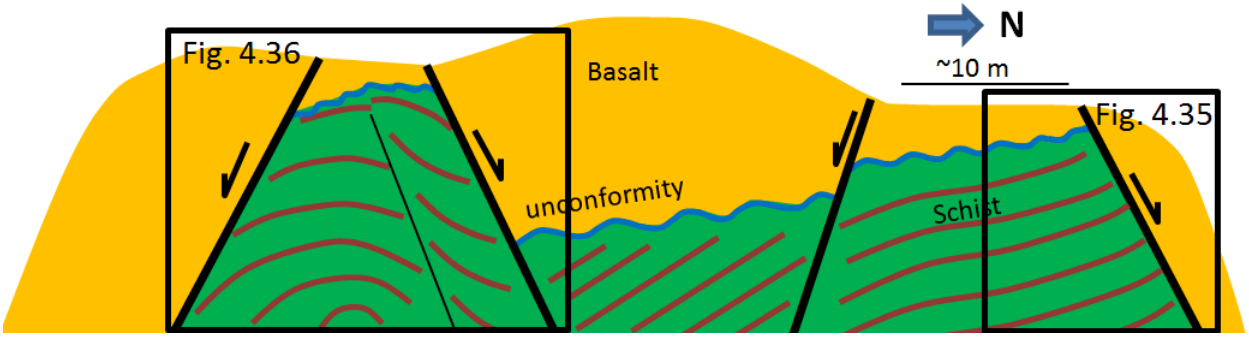

Figure 4.34: Conceptual map of the quarry wall showing structural features and rock units including schist (green with red lines to indicate foliation) and basalt (yellow).

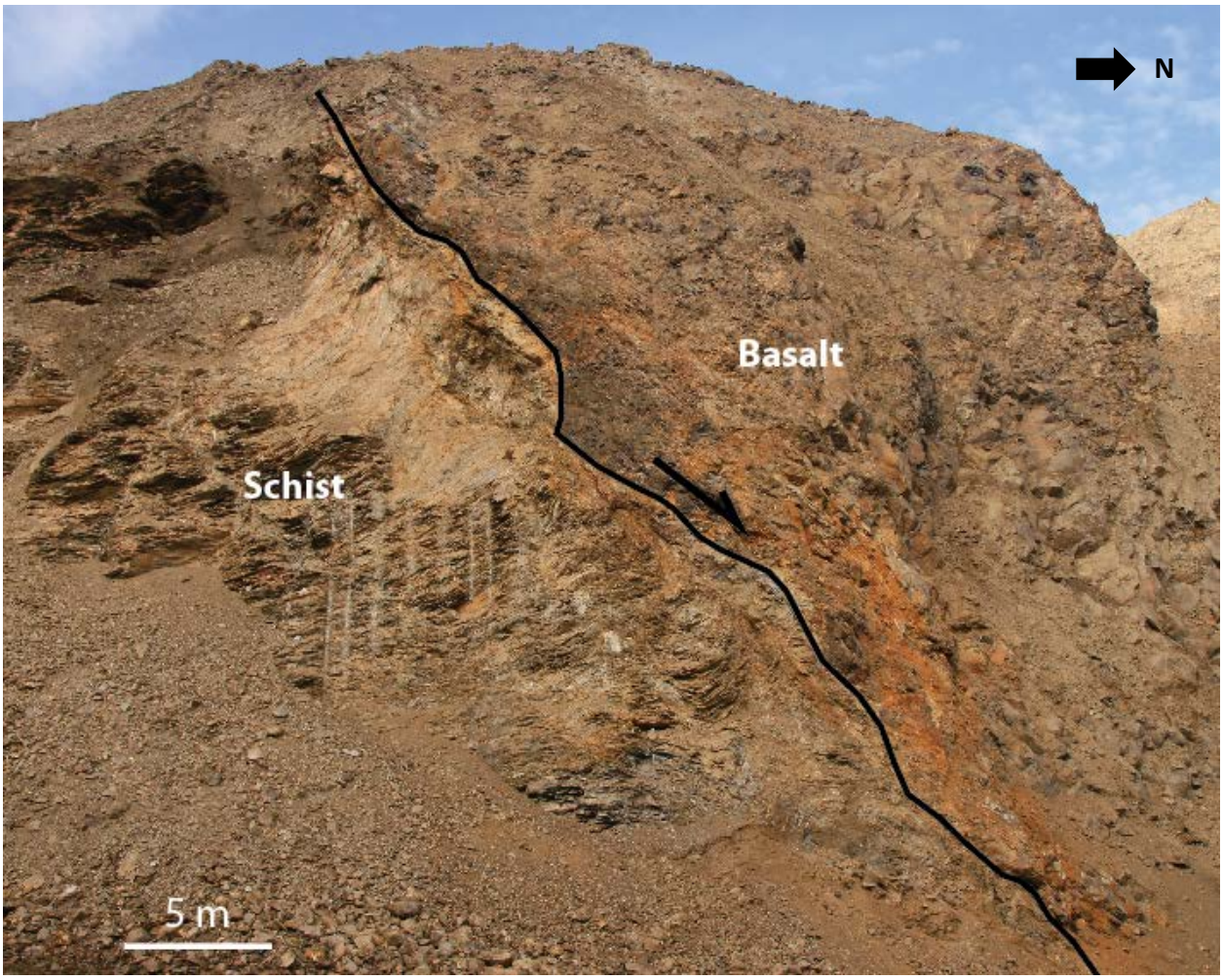

Figure 4.35: Photo showing a normal fault juxtaposing basalt against schist. Location of photo is shown in Figure 4.34.

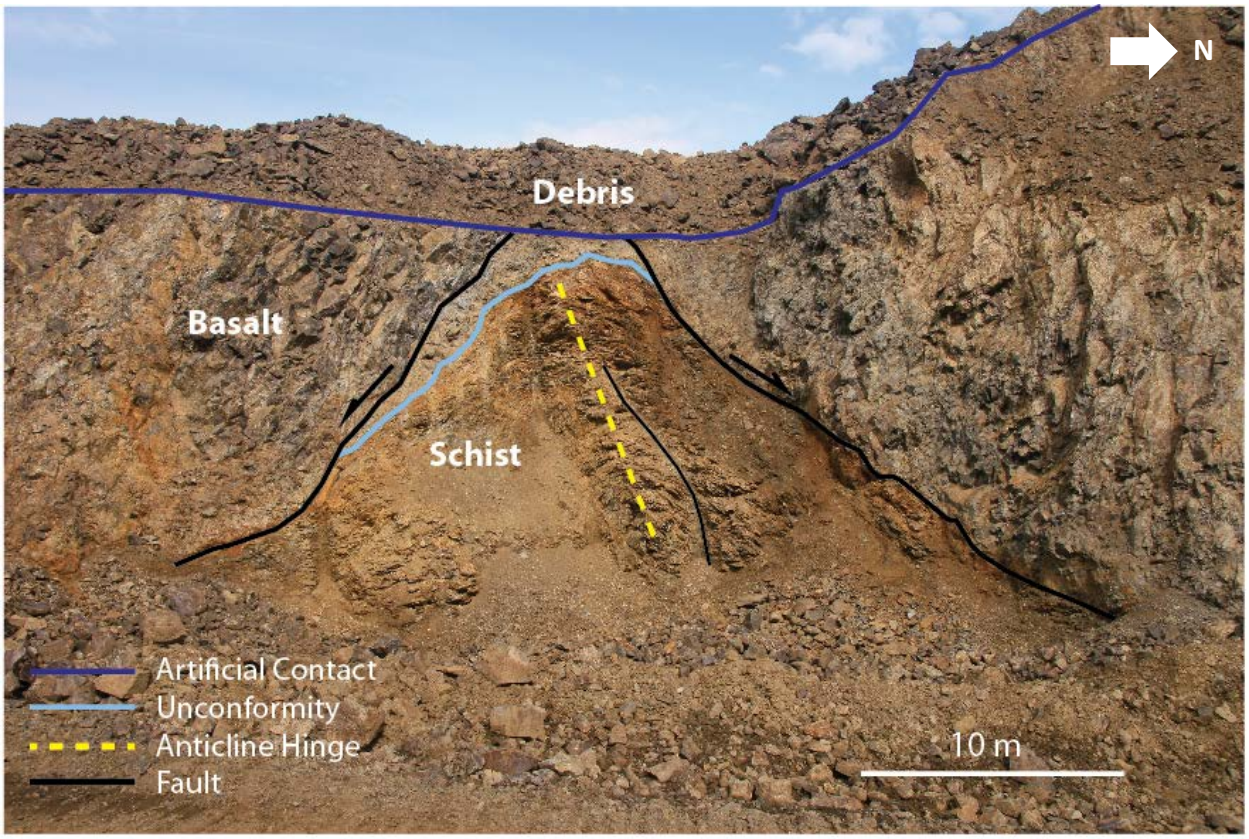

Figure 4.36: Photo showing an anticline within schist unconformably overlain by basalt. Location of photo is shown in Figure 4.34.

4.3.5 West Fairbanks and Nenana

Faults in west Fairbanks and the Nenana area are exposed along various roadcuts including the Nenana bridge area, and miles 321, 325, and 338 along the George Parks Highway (Figure 4.21). These exposures are located east of the Minto and Ester faults. Faults along roadcuts are typically poorly exposed and only a few data were acquired at each location. However, they were all of similar character, and thus all data were grouped together to represent faults of western Fairbanks and the Nenana area.

Faults are exposed in various forms of schist and quartzite of the Fairbanks Schist Unit (Newberry et al., 1996; Wilson et al., 1998). Faults dominantly strike southwest and northeast and dip steeply to the northwest and southeast. Dips range between 39° and 87° (Figure 4.25e). The majority of faults form shear zones that range in width from 20 cm to 3 m and are filled typically with calcite, quartz, or fault gouge. Fault gouge commonly consists of pulverized graphitic schist and clay.

Some fault surfaces display slickenlines but lack other slip indicators, thus, the sense of slip is inconclusive. However, slickenlines dominantly plunge south between 20° and 58° (Figure 4.25e). A steeply (87°) southeast-dipping fault near the Nenana bridge has both north- and south-plunging slickenlines, indicating an opposing sense of movement over time on the same fault plane.

An exposure at milepost 338 reveals a 50 meter wide zone of deformation with multiple shear zones and faults. Shear zones span up to 5 meters and commonly include graphitic schist and/or graphitic fault gouge. Faults and shear zones are highly weathered and poorly exposed, thus attitude and slip measurements were difficult to obtain. However, two fault planes were measured toward the west end of the roadcut; both strike southwest and dip northwest between 39° and 50°. The orientation of shear zones is similar to that of the measured faults: striking northeast or southwest and dipping steeply to the northwest or southeast (Figure 4.25e). The overall deformation zone appears to be on trend with a northeast-striking, down-to-east fault that cuts through Ester Dome (Newberry et al., 1996). No deformation was observed in the surficial deposits along any of these structures.

4.3.6 Northeast Fairbanks

Faults northeast of Fairbanks are exposed in various roadcuts just east of the Steese Highway and along Chena Hot Springs Road (Figure 4.22). These exposures are located between or along the Fish Creek and Isabella Creek faults.

A freshly excavated roadcut along Suncrest Drive north of Chena Hot Springs Road and east of the Steese Highway exposes a good example of one of these faults. This fault zone spans about 100 meters, is on strike with a mapped east-northeast-striking fault (Newberry et al., 1996), and is close to a junction between the east-northeast-striking fault and the Isabella Creek fault (Figure 4.22). The fault zone contains multiple small shear zones and faults within schist. Like many other fault exposures around Fairbanks, the shear zones commonly contain graphitic schist or fault gouge.

There are three dominant orientations of faults in northeast Fairbanks: 1) northeast to southwest; 2) north-northwest to south-southeast; and 3) west-northwest to east-southeast. All faults dip steeply, mostly between 70°-90° (Figure 4.25f) Many faults display shallow to steeply plunging slickenlines, indicating dip-slip and strike-slip components of motion, but lack other slip indicators. Possible slickenfibers on one east-southeast-striking fault indicate normal-left-lateral motion.

Above the schist bedrock are sedimentary layers of sand- to pebble-sized fragments of reworked schist overlain by a thick package of loess (Figure 4.37). The loess package contains a layer of tephra at the base, possibly the Ester Ash bed (Péwé, 1975). Reworked silt-pebble-sized fragments of tephra and loess overlay this fine tephra layer. Toward the central part of the

roadcut, well-defined and organized gravel with schist clasts and basal tephra beds are offset by a fault that displays approximately 20 cm of normal offset and appears to upwarp the reworked loess/tephra and loess layers (Figure 4.37). The underlying bedrock is covered with talus, thus it could not be determined if the fault extends into the bedrock.

A sharp and well-defined fault in consolidated sediments and upwarping of the overlying layers favor a tectonic origin for this fault. However, the surface above the fault is flat and does not show evidence of surface displacement. Frost wedging is common in central Alaska and can induce faulting. However, that mechanism would require frost wedging within bedrock in this case. If this fault is tectonic, the age of faulting is constrained to post-deposition of the Ester Ash bed. The age of the Ester Ash bed is inferred to be 130-191 ka (Péwé, 1975) or 0.81 +/- 0.07 Ma (Preece et al., 1999).

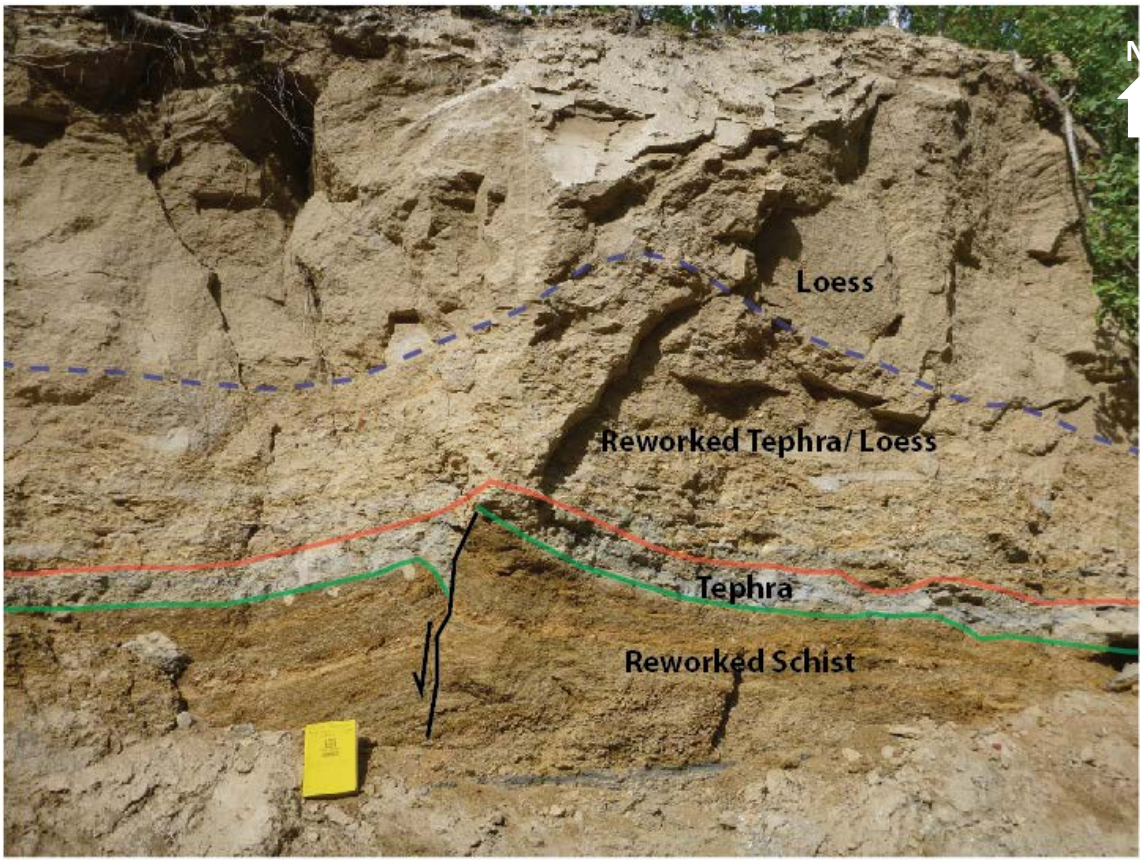

Figure 4.37: Normal fault cutting sediments at a roadcut along Suncrest Drive northeast of Fairbanks. Stratigraphic relationships suggest possible Pleistocene faulting based on offset of the Ester Ash bed (Péwé, 1975).

Structural data were also collected at exposures along Chena Hot Springs road between mileposts 5 and 11. Faults at this location strike northwest-southeast and dip either to the northeast or southwest. Some faults have slickenlines with plunges between 12° and 30° to the northwest or southeast, indicating dominantly strike-slip motion.

A quarry near mile 11 on Chena Hot Springs Road exposes a series of northwest-southeast-striking faults and shear zones in a wide and highly fractured zone of deformation (Figure 4.22). Due to relatively poor exposure, only some faults in this area were measured. This

fault zone appears to be on trend with the Fish Creek fault, which joins a mapped fault (Newberry et al., 1996; Wilson et al., 1998) to the north. The northwest-striking faults found in the quarry are likely conjugates to the Fish Creek fault.

4.4 Apatite Fission-Track Data

Tables 4.3 and 4.4 summarize details of the apatite fission-track samples collected during this study, including the sample number or name, A to Z sample number, generalized rock type, the geographic coordinates for each sample, and the elevation or depth at which each sample was collected. A summary of the apatite fission-track age and length data is given in Tables 4.5 and 4.6, and a corresponding map with sample locations and pooled ages is shown in Figure 4.38. Complete age and length data tables are provided in Appendices B1 and B2.

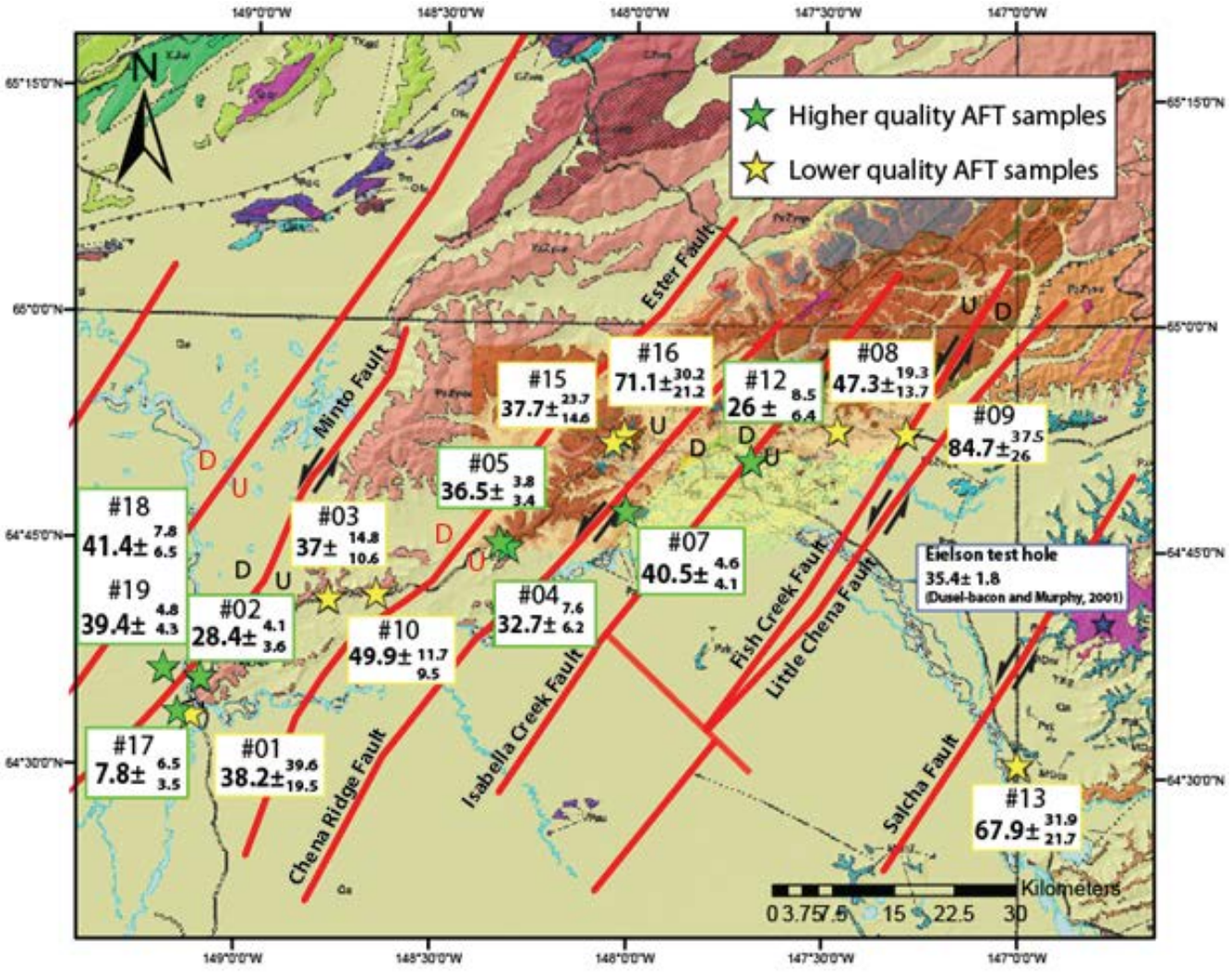

Figure 4.38: Apatite fission-track sample location map showing sample locations (stars) and pooled ages ± 1 sigma error.

Table 4.3: Sample details for metamorphic rocks collected from a transect across the western Yukon-Tanana uplands.

Well ID	Latitude	Longitude
Nunivak #1	64.57202	-149.215333

Sample Number	A2Z Sample Number	Lithology Type	Latitude	Longitude	Elevation (m)
FROH008.5	1338-01	Quartzite	64.56955	-149.103833	137
FROH009	1338-02	Quartzite	64.606233	-149.087883	177
FROH011	1338-03	Quartzite	64.696883	-148.7634	320
FROH012	1338-04	Schist	64.761	-148.307917	455
FROH013	1338-05	Quartzite	64.7652	-148.326433	395
FROH016	1338-06	Schist	64.787667	-147.976767	197
FROH017	1338-07	Quartzite	64.802783	-148.003467	345
FROH019	1338-08	Schist	64.892433	-147.450367	243
FROH020	1338-09	Quartzite	64.888117	-147.273983	177
FROH024	1338-10	Quartzite	64.705717	-148.64325	407
FROH031	1338-12	Quartzite	64.858533	-147.673917	146
FROH032	1338-13	Quartzite	64.524383	-146.987533	198
FROH035	1338-15	Schist	64.877433	-148.03675	659
FROH036	1338-16	Schist	64.885267	-148.012317	475
AR-001	1338-17	Schist	64.56949	-149.10292	130

Table 4.4: Sample details for sediments collected from the Nunivak #1 well in the southern Nenana basin.

Sample Batch	A2Z Sample Number	Depth (ft)	Sample Description	Formation Name	Formation Age	Present Temperature (°c)
1	1338-18	5560-5590	very fine sand	Lignite Creek Fm.	13.9	50.3
1	1338-18	5650-5680	very fine sand	Lignite Creek Fm.	13.9	51.0
1	1338-18	6550-6580	fine-med. sand	Suntrana Fm.	15.1	58.5
1	1338-18	6640-6670	fine-med. sand	Suntrana Fm.	15.1	59.3
1	1338-18	6730-6760	fine-med. sand	Suntrana Fm.	15.1	60.0
1	1338-18	6820-6850	fine sand	Suntrana Fm.	15.1	60.8
1	1338-18	7120-7150	very fine sand	Sanctuary Fm.	16.6	63.3
1	1338-18	7360-7390	very fine sand	Sanctuary Fm.	16.6	65.3
2	1338-19	9010-9040	very fine sand	Paleocene Fm.	57.8	79.0
2	1338-19	9130-9160	very fine sand	Paleocene Fm.	57.8	80.0
2	1338-19	9250-9280	very fine sand	Paleocene Fm.	57.8	81.0
2	1338-19	9310-9340	fine sand	Paleocene Fm.	57.8	81.5
2	1338-19	9520-9550	fine sand	Paleocene Fm.	60.6	83.3
2	1338-19	9850-9880	very fine sand	Paleocene Fm.	60.6	86.0
2	1338-19	9940-9970	very fine sand	Paleocene Fm.	60.6	86.8
2	1338-19	10030-10060	fine sand	Paleocene Fm.	60.6	87.5
2	1338-19	10090-10120	fine sand	Paleocene Fm.	60.6	88.0
2	1338-19	10180-10210	fine sand	Paleocene Fm.	60.6	88.8
2	1338-19	10480-10510	fine sand	Paleocene Fm.	63.6	91.3
2	1338-19	10660-10690	fine sand/schist	Paleocene Fm.	63.6	92.8
2	1338-19	10810-10840	fine sand/schist	Paleocene Fm.	63.6	94.0
2	1338-19	10990-11020	fine sand/schist	Paleocene Fm.	63.6	95.5

Table 4.5: Summary of apatite fission-track age data. Analysis done by AtoZinc. *Highest quality samples based on error of <10 Ma.

A2Z Sample Number	Accepted Spots	SumNs	[U]m ppm	Dparm	Dperm	Pooled age	-1σ	+1σ
Durango Standard	486 (grains)	3091	2.17E-03	1.52	0.29	31.40	0.8	0.8
1338-01	15	9	2.027829	1.797461	0.3519703	38.17	19.47	39.62
*1338-02	24	245	15.05614	1.770088	0.3161471	28.35	3.57	4.09
1338-03	16	36	2.399709	1.710184	0.3242248	37.04	10.60	14.83
*1338-04	16	95	6.093417	1.833736	0.3405561	32.66	6.18	7.61
*1338-05	32	491	12.95625	1.8328	0.3287028	36.51	3.40	3.75
1338-06	2	2	2.23E-02	1.629064	0.3927105	1772.46	1391.61	4499.35
*1338-07	34	388	7.015243	1.945322	0.3589945	40.47	4.14	4.61
1338-08	28	38	2.460619	1.797366	0.3276868	47.31	13.72	19.30
1338-09	34	30	0.3925543	1.755919	0.329493	84.69	26.04	37.50
1338-10	24	95	3.21108	1.698883	0.2887211	49.89	9.46	11.66
*1338-12	6	52	15.04095	1.858696	0.4376651	25.98	6.38	8.45
1338-13	21	28	0.7724602	1.715592	0.3728422	67.96	21.74	31.88
1338-15	2	17	12.64715	1.813768	0.346351	37.72	14.55	23.65
1338-16	2	33	9.099619	2.053384	0.304206	71.08	21.21	30.16
*1338-17	10	11	11.81415	1.814766	0.3497226	7.79	3.54	6.48
*1338-18	33	604	17.61617	1.906801	0.3340907	41.40	6.54	7.76
*1338-19	20	365	27.24047	1.860194	0.3589945	39.41	4.25	4.76

.

Table 4.6: Summary of apatite fission-track length data. Analysis done by AtoZinc. *Highest quality samples based on error of <10 Ma.

A2Z Sample Number	Number of Tracks	Mean Track Length (µm)	Std. Error (µm)	Std. Dev (µm)	Dparm	Dperm
Durango Standard	138	14.59	0.08	0.98	1.87	2.36
1338-01	20	14.019	0.3967639	1.729454	1.955042	0.3269643
*1338-02	78	13.82936	0.1597402	1.401715	2.205321	0.3435412
1338-03	64	13.87938	0.2031492	1.612446	2.211568	0.3713747
*1338-04	138	14.58058	0.1124437	1.31612	2.396385	0.4392536
*1338-05	152	14.02395	0.1436366	1.765036	2.258121	0.3694753
1338-06	9	14.58778	0.37429	1.058652	2.205917	0.4016078
*1338-07	158	14.42443	0.1196745	1.499517	2.414577	0.4202383
1338-08	78	14.88898	0.7756628	6.806414	2.143751	0.3437575
1338-09	16	14.16375	0.2596543	1.005637	2.080216	0.3410828
1338-10	125	14.34	0.1248655	1.390443	2.151426	0.328077
*1338-12	20	14.3565	0.3391249	1.478211	2.293499	0.422212
1338-13	20	15.1625	0.246094	1.072699	2.154222	0.3518298
1338-15	10	14.671	0.4192511	1.257753	2.255061	0.3834386
1338-16	17	14.42412	0.174486	0.697944	2.678559	0.5159227
*1338-17	15	14.27533	0.3012082	1.127018	2.284014	0.3738858
*1338-18	133	14.28947	0.1031303	1.184877	2.274119	0.407065
*1338-19	49	13.98286	0.2189265	1.516768	2.423302	0.4363175

Only 8 out of 15 samples yielded a sufficient quantity of apatite grains of reasonable quality for analysis. The highest quality samples are marked with asterisks in Tables 4.5 and 4.6. The remaining samples yielded low uranium concentrations or a low number of accepted laser spots, resulting in poor data quality. Poorer quality samples without an asterisk will be included in the discussion of results because they could possibly fit a general trend of ages shown by the higher quality samples and ages reported by other apatite fission-track studies on Jurassic through Early Tertiary plutons in Interior Alaska (Murphy and Bakke, 1993; Dusel-Bacon and Murphy, 2001). However, sample 1338-06 yielded very poor quality data and will not be included in the interpretation.

Sample elevations range from 130 m to 659 m and depths of the basin samples from the Nunivak 1 well range from 5560 ft to 11020 ft (1695 m to 3353 m). Samples collected at Nunivak 1 deeper than 6730 ft (2051 m) exceed 60°C present temperature. Pooled ages range from 7.8 Ma +6.5 or -3.5 (1 sigma error) to 84.7 Ma +37.5 or -26 (1 sigma error), and mean track lengths range from 13.7µ to 15.0µ. Higher-quality samples range in age from 7.8 Ma +6.5 or -3.5 (1 sigma error) and 41.4 Ma+7.8 or -6.5 (1 sigma error), with most ages between 26 and 40 Ma. For all samples, most ages range from ~30 to 50 Ma. Dusel-Bacon and Murphy (2001) reported a similar range in ages, from 35.4 Ma ±1.8 (1 sigma error) to 76.4 Ma ±7.2 (1 sigma error) and track lengths from 12.5µ to 15µ in an apatite fission-track study across the Yukon-Tanana uplands. They also reported a similar dominant age range of ~40-50 Ma.

Chapter 5: Analysis and Discussion

In the following analysis, I will integrate the results of fault mapping and geomorphic, structural, and apatite fission-track analyses in order to build a cohesive structural model for northeast-striking faults of the greater Fairbanks area. The objective is to help better define the tectonic framework of Interior Alaska and its Cenozoic evolution. This structural model could have important ancillary implications for resource development in the Fairbanks Mining District and the Nenana basin. The assessment of relative tectonic activity will be especially important for evaluation of potential seismic hazards in the greater Fairbanks area.

5.1: Evidence for Recent Structural Activity

Geomorphic analyses revealed many anomalies in the Fairbanks area including barbed drainages, strongly linear drainages, basin and valley asymmetry, incised valleys and underfit streams, changes in river morphology, knickpoints in stream profiles, immature stream profiles, and a low sinuosity mountain front. The combination of these anomalies lends indirect support to a tectonic influence on the landscape, particularly near the eastern margin of the Nenana basin.

5.1.1 Geomorphic Indices

I employed or observed multiple geomorphic indices such as basin asymmetry (AF), transverse topographic symmetry factor (T), valley asymmetry, stream-length gradient index (SL), valley floor width-to-height ratio (Vf), and mountain front sinuosity (Mfs), and changes in river morphology along the eastern margin of the Nenana basin, where the highest density of geomorphic anomalies occurs. AF and T values imply slight ground tilt of Goldstream Creek and

the Chatanika River valleys to the southeast and north-northwest, respectively (Figure 5.1). Additionally, Figure 4.8 reveals that a set of asymmetrical terraces developed along lower Goldstream Creek, which may suggest ground tilt to the southeast.

A regional-scale northeast-trending, dome-like topographic high is observed between the lower reaches of Goldstream Creek and the Chatanika River (Figure 5.1). The presence of ground tilt in opposite directions along both drainages bounding this feature (a higher AF value along the Chatanika River (74) and a lower AF value along Goldstream Creek (33) suggests that it may be a growing anticline with a gentler southeast limb and a steeper northwest limb (here, informally named the Minto anticline; Figures 5.1 and 5.2). The change in orientation of lower Goldstream Creek from northeast to east-west over a relatively long distance suggests that the creek may be deflecting around the gentler southeast limb (Figure 5.1). Similarly, a downstream change in flow direction from east-west to northeast suggests that Chatanika River may be deflecting around the steeper northwest limb of a growing anticline (Figure 5.2). Increasing T values along the Chatanika River reflect increasing asymmetry upstream (Figure 5.1; Table 4.2). An abrupt decrease in T values from 0.51 to 0.27 between segments 3 and 4 could reflect the location of the anticline hinge.

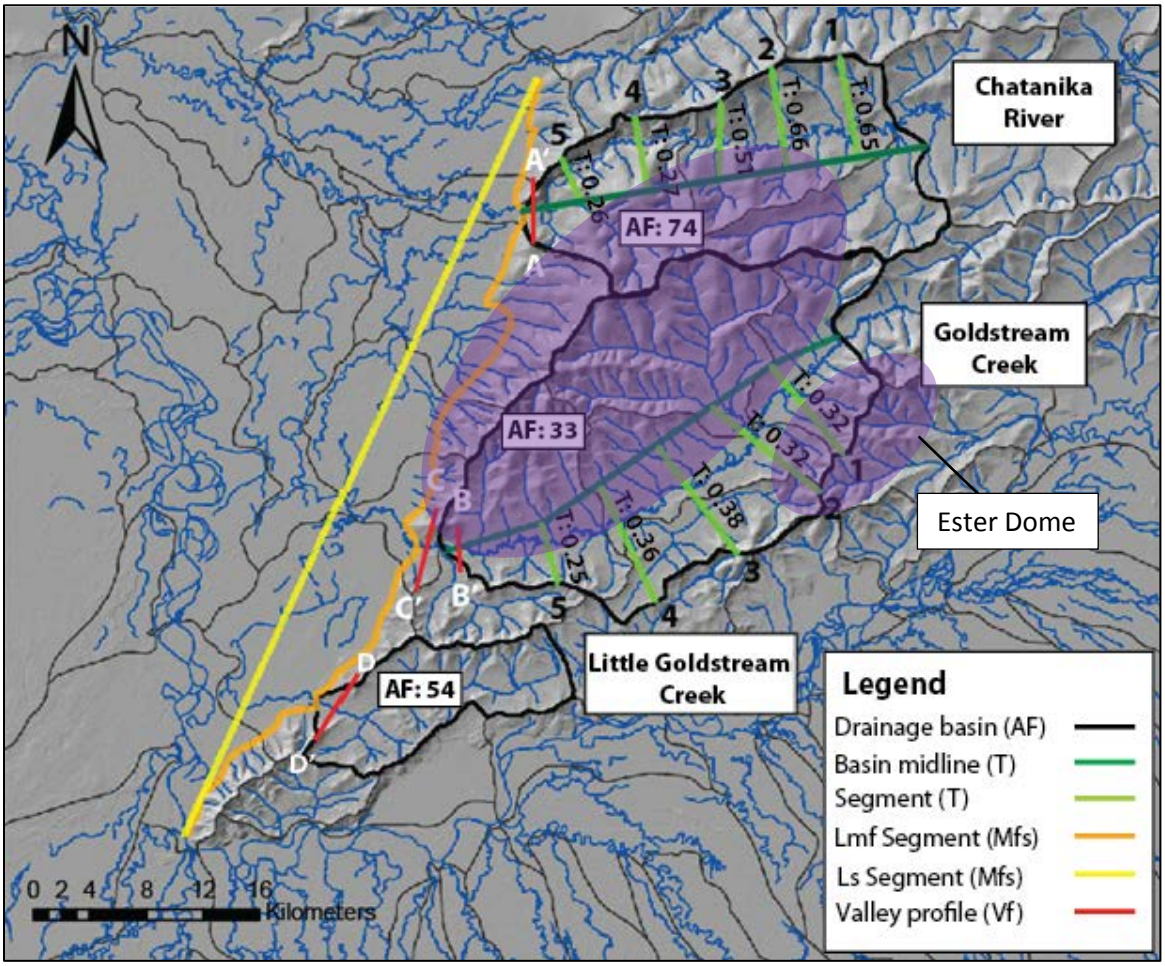

Figure 5.1: Geomorphic indices map including segments or polygons used for calculating the basin asymmetry factor (AF), transverse topographic symmetry factor (T), mountain front sinuosity index (M_{fs}), and the valley floor width-to-height ratio (V_f). Numbers correspond to segments in table 4.2. Map also shows the location of the northeast-trending topographic high between lower Chatanika River and Lower Goldstream Creek. Purple ellipses indicate northeast-trending topographic highs.

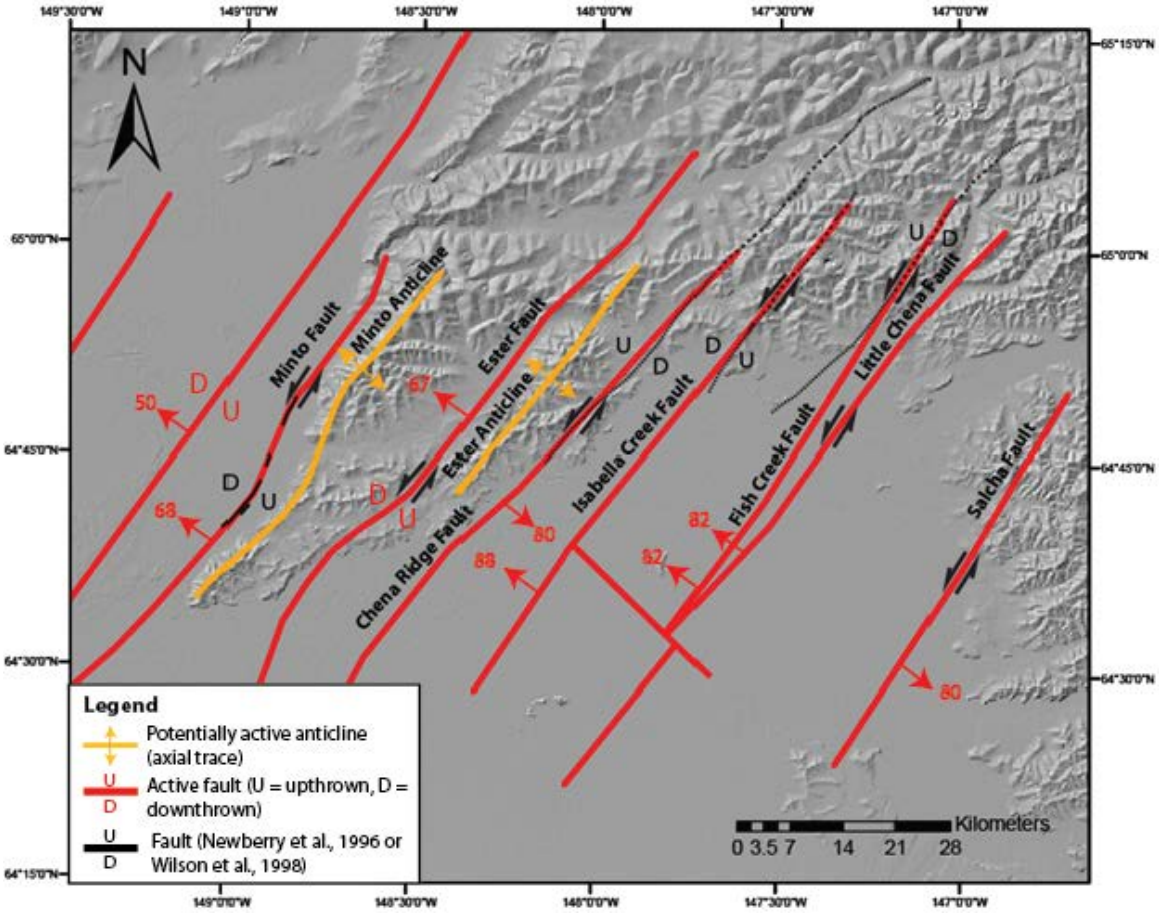

Figure 5.2: Map of potentially active structures in the Fairbanks area.

The stream length gradient index (SL) values show knickpoints along the lower reaches of the Tanana River (Lesh and Ridgway, 2007), Little Goldstream and Goldstream Creeks, and the Chatanika River. All of these knickpoints align in a northeast trend along the eastern Nenana basin margin and correlate closely with the Minto fault (Figure 5.3). Similarly, knickpoints along both the middle reaches of Goldstream Creek and the Chatanika River correlate closely with the Ester fault (Figure 5.3).

There is other geomorphic evidence that suggests that the Minto fault is active. The highest change in SL values occurs at the mouth of the Chatanika River, where the gradient

increases significantly from 48 to 208, and then decreases to 67 (4.11c). This change in SL suggests deep incision through bedrock. In this same area, the Chatanika River changes morphology from more sinuous, to channelized, then back to sinuous where it enters the Nenana basin (Figure 5.3). Also, valley floor width to height ratio (V_f) values along the mouths of Little Goldstream and Goldstream Creeks and the Chatanika River are 2.8, 4.3, and 2.1, respectively, and represent low incision rates. M_{fs} (1.1) for the eastern margin of the Nenana basin indicates a straight mountain front along this margin, and implies that tectonic uplift along a range-bounding fault outpaced the erosion of rivers and streams.

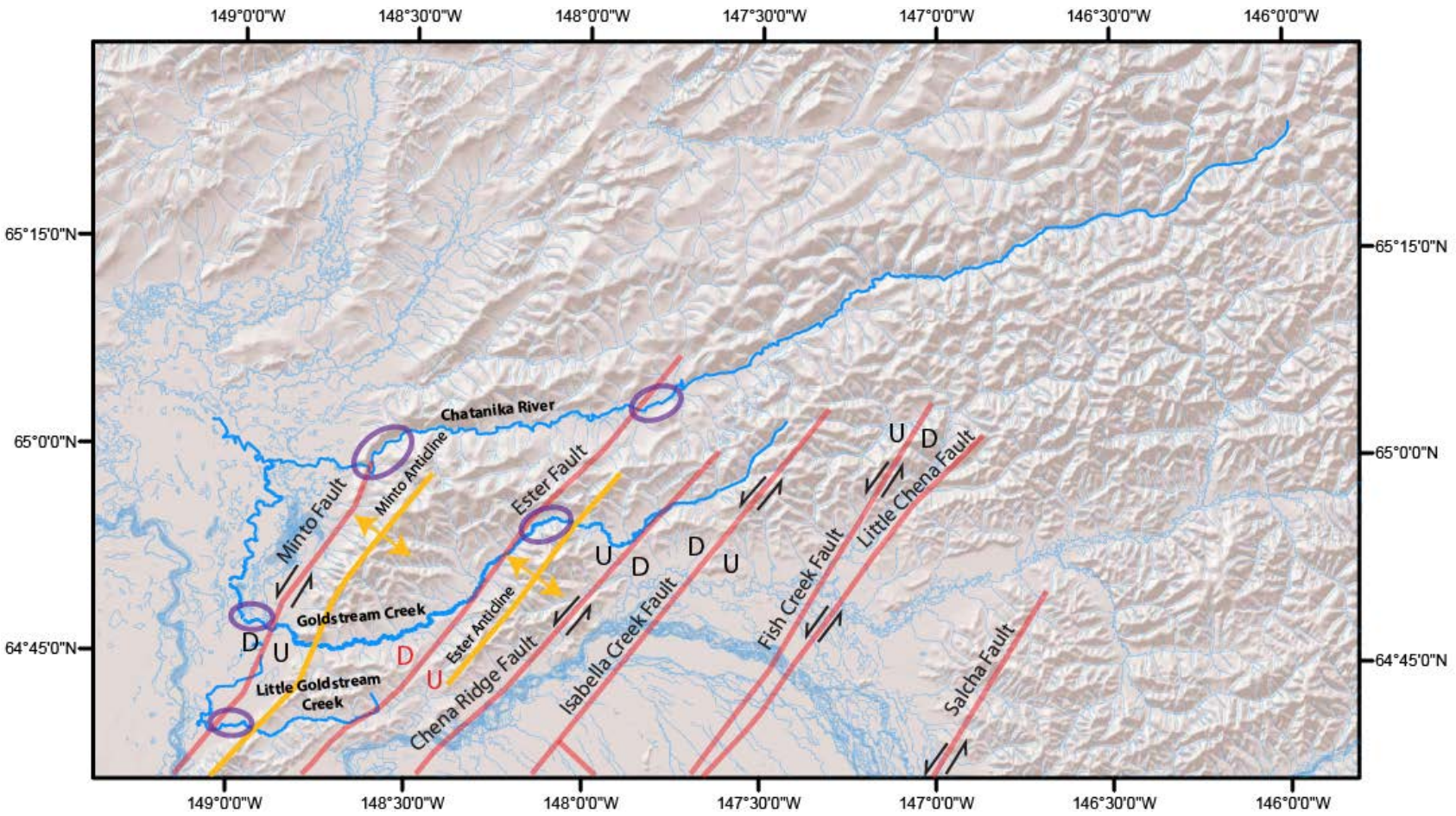

Figure 5.3: Drainage map showing the locations of knickpoints in purple ellipses. Profiles are shown in Figure 4.11.

Several other fluvial geomorphic observations suggest relatively recent tectonic activity on the Minto fault. Several rivers and creeks change flow direction as they cross into the Nenana basin. For instance, the Tanana River abruptly turns 90° to the north into the Nenana basin (Figure 5.3; Lesh and Ridgway, 2007). Little Goldstream and Goldstream Creeks flow southwest in the Yukon-Tanana uplands, but turn abruptly 90°+ to the northeast once they enter the Nenana basin. The highest change in gradient for the Chatanika River occurs near the mouth of the river, where it crosses the Minto fault.

All of this geomorphic evidence supports relatively recent uplift along the east side of the Minto fault, with significant uplift toward the northeast at the mouth of Chatanika River. However, some of the incision at the mouth of the Chatanika River could be related to growth of the Minto anticline. The close association between the Minto fault and the Minto anticline and their topographic signatures suggests that the anticline could be a footwall anticline of the Minto fault. Alternatively, the anticline could also be a product of compression and strike-slip movement between the Minto and Ester faults. The Minto anticline is poorly constrained to the southwest, but may decrease in width toward the southwest end of the Minto fault. The cross section of seismicity indicates a dip of approximately 68° to the northwest for the Minto fault (Figure 4.5c), which is approximately consistent with the asymmetry of the anticline.

These anomalies also suggest rotational displacement along the Minto fault, with normal motion along the entire length of the fault but with decreasing slip to the south (Figure 5.4). This rotational character is also consistent with reverse displacement on the Minto fault to the south. At the southwest end of the fault, a dense cluster of seismicity is concentrated around the Kantishna Hills, which is just northwest of the Denali fault. Focal mechanisms indicate reverse

and reverse-left-lateral motion in this area (Ruppert et al., 2008). It is possible that the Minto fault could be converging in this area with the Denali fault or a structure related to it.

In either scenario, this rotational character implies northeast tilt of the western fault block (informally named the Minto block) and southwest tilt of the eastern fault block (informally named the Nenana block; Figure 5.4). The amount of tilt of both the Minto and Nenana blocks is uncertain, but is probably on the order of <10° based on the north-south slope of the topography.

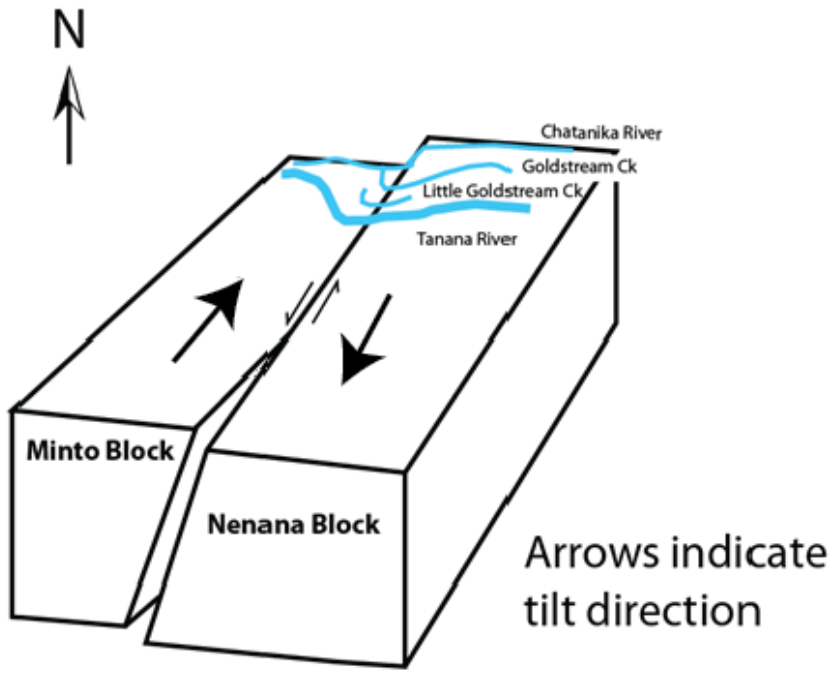

Figure 5.4: Conceptual block model showing rotational movement along the Minto fault. The rotational character of the fault could imply normal motion along the entire fault but with decreasing normal slip to the south, and it could also imply reverse motion along the southern end of the fault.

Ester Dome is another topographic high between the Chena Ridge fault and the Ester fault (Figures 5.1 and 5.3). Avalon (2014) first identified this as a northeast-trending antiform. The asymmetric topographic expression, i.e., the gentler southeast slope and steeper northwest slope, is similar to that of the Minto anticline. A cross section of seismicity suggests that the Chena Ridge fault dips to the northwest, while the Ester fault dips to the southeast, making this a horst structure (Figure 4.5c). The knickpoint along the middle reaches of Goldstream Creek represents an elevated area on trend with Ester Dome, potentially related to the growth of the horst anticline (Figure 5.3). Like the Minto anticline, the height and width of the topography of the Ester anticline is greater to the northeast, toward Goldstream Creek. This may indicate rotational motion with greater dip-slip offset along the northeast part of the fault, however, no evidence of tilt or anomalous changes in drainage behavior were observed to support this hypothesis.

5.1.2 Stream Capture

Figure 5.5 outlines all of the drainages that may have been affected by active tectonics at some point during their development. Many of these drainages show features of stream capture that include barbed tributaries and underfit streams. Barbed drainages tend to occur directly adjacent to northeast-striking faults that I have interpreted to be potentially active based on seismicity and correlation with bedrock structures. Several of these same drainages are underfit, including Goldstream, Little Goldstream, Bonanza, Cripple, and Isabella Creeks (Metz, 1991; Lesh and Ridgway, 2007).

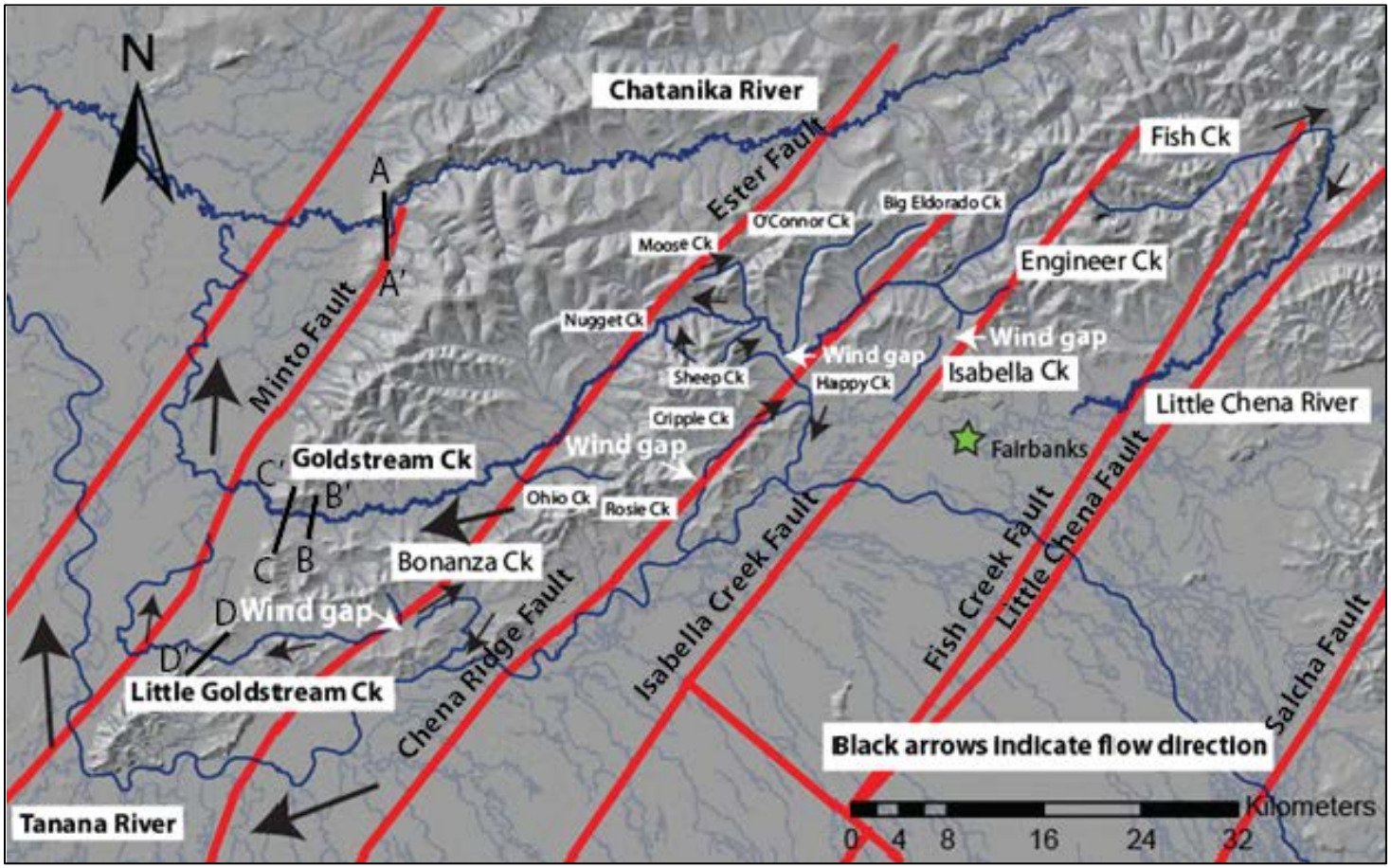

Figure 5.5: Drainage map of the Fairbanks area. Named drainages display features that suggest they may have been affected by active structures. Barbed drainages include Bonanza Creek, Cripple Creek, Moose Creek, Happy Creek, Sheep Creek, Nugget Creek, and Fish Creek.

Perhaps the most profound evidence for stream capture is along Goldstream Creek, where many barbed drainages occur in the same area, near Ester Dome and between the Chena Ridge and Ester faults (Figure 5.5). These drainages include Cripple Creek, Sheep Creek, Happy Creek, Nugget Creek, O'Connor Creek, and Moose Creek. In this area, Goldstream Creek makes a sharp, near-90° turn to the north. It appears that barbed drainages as far west as Nugget Creek may have once flowed east via proto-upper Goldstream Creek and that Goldstream Creek may have flowed south via Happy Creek, where a wind gap is now present between Happy and Goldstream Creeks. This implies that proto-middle Goldstream Creek underwent a flow reversal, initially flowing east and south, now flowing west. Similarly, the barbed and underfit Cripple Creek may once have flowed southwest along its proto-upper reaches and exited to the Tanana River via Rosie Creek. This suggests that Goldstream Creek could have had two possible past exit routes to the Tanana River--via Cripple Creek and/or via lower Happy Creek.

A map of Pliocene to present gold-bearing gravel at the confluence of Cripple Creek and Ester Creek (Figure 4.31; Péwé et al., 1989) shows older stream gravel (presumably Pliocene) oriented north-south as opposed to the northwest-southeast orientation of the present-day channel. This paleo-channel configuration suggests that Pliocene proto-Ester Creek may have flowed southwest to another divergent stream branch, one arm of which could have flowed southwest into uppermost Cripple Creek and then to the Tanana River. This implies that both Goldstream and Cripple Creeks underwent flow reversals.

A stream capture event may also have occurred along Bonanza Creek because it also has a barbed trend. Also, the headwaters of Little Goldstream Creek turn 90° into the trunk of Little Goldstream Creek. Both longitudinal stream profiles for Little Goldstram Creek and Bonanza

Creek are immature (Figures 4.16 and A.1), suggesting that they have not yet graded to equilibrium. It is possible that proto-Bonanza Creek once may have flowed southwest via uppermost Little Goldstream Creek.

5.1.3 Uncertainties

Climate-induced stream rejuvenation can produce knickpoints in a stream profile and stream capture events. In the Fairbanks area, the last major change in climate was in the late Pleistocene (Péwé, 1975). The effects of climate on streams have not been demonstrated in the Fairbanks area. Nonetheless, the close spatial relationship between interpreted potentially active faults and knickpoints in a given stream profile suggests that fault-related activity is also possible.

Changes in base level, such as mining activity, can also cause a knickpoint in a stream profile. Intensive placer mining has occurred along Goldstream Creek since the early 1900s. The second knickpoint along Goldstream Creek is situated downstream of a placer mine, which could indicate that the addition of wastewater and other material to Goldstream Creek may have disrupted the equilibrium of the stream profile. However, when comparing this knickpoint to the length of the stream profile, it is fairly extensive (9 km), and other areas that have been mined along upper Goldstream Creek do not exhibit any changes in the profile. Also, a bedrock high was noted by Metz (1991) from drill logs in this area.

Knickpoints in a stream profile could also be attributed to regional sea level drop; however, the affects of this process typically diminish upstream. Fairbanks is approximately 500

miles from the nearest ocean and it is more likely that knickpoints would be attributed to local processes.

5.2 Fault Character in the Fairbanks Area and Evidence for Recent Strike-slip Motion

5.2.1 Fault Exposure Analyses

The majority of mapped faults in the Fairbanks area exhibit a similar range of characteristics that include: 1) linear and laterally continuous, up to 40+ km long; 2) a dominant orientation of northeast to southwest; 3) generally steep to near vertical dips; 4) a dominant left-lateral strike-slip component as well as a lesser dip-slip component; and 5) changes in the dip-slip component along strike. All of these are common characteristics of strike-slip faults.

Since most of the structural data I collected were from the Ryan Lode and Birch Hill faults, they tended to skew the data analysis. Consequently, I generated a stereoplot showing contoured poles to faults for all of the faults in the Fairbanks area except for the Ryan Lode and Birch Hill faults, which are only shown as average poles to great circles on the stereoplot for comparison (Figure 5.6). Unfortunately, most of the faults lack slip data. However, the stereoplot reveals three different orientations that represent many of the faults of the eastern part of the Fairbanks area, within the Fairbanks seismic zone, particularly close to or within basalt quarries. These three dominant strike orientations are roughly 030°, 345°, and 290°. The moderate northwest dip of a subset of the 030° set suggests a significant dip-slip component, probably normal.

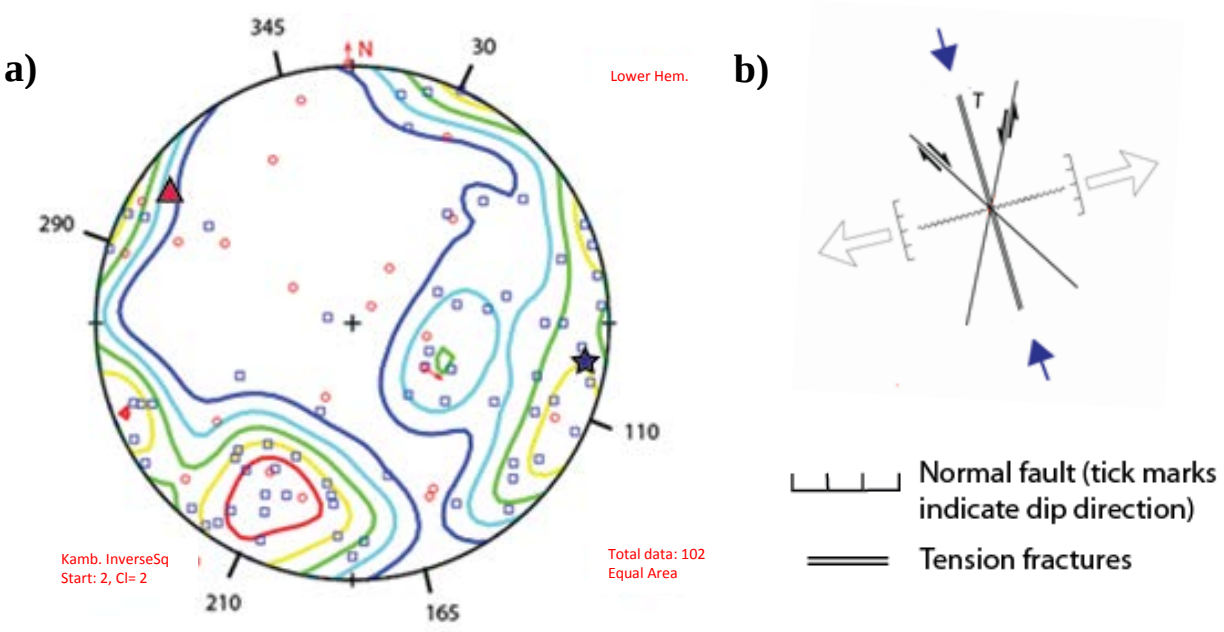

Figure 5.6: Stereoplot for all documented faults in the Fairbanks area and a pure shear model. a) poles to planes for all faults; average orientations as poles to great circles for the Birch Hill and Ryan Lode faults are shown as a purple star and pink triangle, respectively. Plot shows three dominant orientations that correspond with subsidiary structures that form within a pure shear system (b) after Sylvester (1988).

In the Fairbanks area, although the faults measured provided few slip data, fault orientations (Figure 5.6a) are roughly consistent with the orientations of primary structures commonly formed within a pure shear system (Figure 5.6b). The types of primary structures are left-lateral strike-slip faults, normal faults or tension fractures (T), and right-lateral strike-slip faults. Left-lateral and right-lateral strike-slip faults may form at ~60° angle to each other as conjugates. Normal faults and tension fractures (T) may develop parallel to the maximum compressive stress and bisect the dihedral angle between the left-lateral and right-lateral strike-slip faults.

The left-lateral strike-slip faults are oriented at 030° and the right-lateral strike-slip faults are oriented approximately 100° from the R-shears at 290°. The 100° dihedral angle between the primary strike-slip faults is larger than in the ideal model, but such large dihedral angles are not unusual in nature (Sylvester, 1988). Faults oriented at 345° are mostly near-vertical and could fit the orientation of normal faults or tension fractures (T). However, more kinematic information is needed to identify these structures within a pure shear model.

It is unknown when each of the various sets of structures formed and how they relate to the present strain field. Thus, it is assumed that the structures represent the inherited structural grain that is being activated by current seismicity, and that the latest kinematic indicators represent the latest tectonic setting.

5.2.2 Summary of Fault Character in the Fairbanks Area

Geomorphology, seismicity, and structural analyses suggest that geometry along northeast-striking faults changes from west to east, from the Minto fault to the Salcha fault. Toward the west, the stair-step offsets in the base of seismicity and the presence of a footwall anticline based on geomorphology suggest that the Minto fault has pronounced tilted fault block geometry, in which the footwall block tilts to the southeast. Similarly, seismicity and the Ester anticline between the Ester and Chena Ridge faults suggest a tilted fault block, located on the footwall of the Ester fault, that tilts slightly to the southeast (Figure 4.8).

Farther to the east, dips along northeast-striking faults steepen (Figure 4.8). Also, seismicity tends to shallow farther eastward toward the Salcha seismic zone, where the Salcha fault appears to be near-vertical (Figure 4.8). Tilted fault block geometries implied by stair-step

offsets, the Minto and Ester anticlines, and deeper seismicity suggest that faults west of Ester Dome have more extensional characteristics. To the east of Ester Dome, steeper dips, shallower seismicity, and left-lateral offset of the Chena Ridge fault identified by bedrock offsets and drainage restorations suggest that these faults have more strike-slip characteristics. However, focal mechanisms suggest that all faults currently display dominantly left-lateral strike-slip motion.

Geomorphic indices suggest low to moderate rates of tectonic activity in the Fairbanks area. This is in contrast to higher rates of activity in the Alaska Range farther south where, for example, the central Denali fault has a slip rate of ~10 mm/yr (Haeussler, 2008) and there are more measureable and pronounced fault-related features in young sediments. Tectonic geomorphologic anomalies in the Fairbanks area are generally more pronounced to the west, which may indicate more vigorous tectonic activity toward the Nenana basin.

Field evaluation of outcrops and mine pit exposures indicates Pliocene and/or possibly Quaternary displacement along the Chena Ridge fault at the Cripple Creek mine (4.22) and along a fault exposed at Suncrest drive northeast of Fairbanks (possibly along the Fish Creek or Isabella Creek faults; Figure 4.21).

Structural analyses of bedrock exposures, especially the Birch Hill fault (Figure 4.24) and the Ryan Lode fault (Figure 4.30), suggest normal motion along northeast-striking faults that was later overprinted by left-lateral motion. Changes in dip-slip motion are also observed on the Ryan lode fault (4.30) and are implied by the scissor-like character of the Minto fault (Figure 5.4).

5.2.2 Left-Lateral Strike-Slip Faulting

The Chena Ridge fault is the most obvious structure that may have contributed to the capture events along Goldstream and Cripple Creeks discussed in section 5.1.2. Focal mechanisms suggest left-lateral movement and seismicity indicates an 80° dip to the northwest. The drainage patterns and flow reversals described above and the left-lateral motion of the Chena Ridge fault based on focal mechanisms suggest it is possible that left-lateral movement along the Chena Ridge fault shifted upper Goldstream Creek and lower Cripple Creek into their current stream positions.

I propose that tectonic changes in these drainages may be assessed by restoration of left-lateral displacement. A map of faults before restoration of displacement is shown in Figure 5.7. A map of faults after restoration is shown in Figure 5.8 where several geomorphic and structural characteristics are observed that are relevant to restoration.

First, in this restoration, proto-upper Goldstream and proto-middle Goldstream Creek were aligned, and Chena Ridge may form the southeastern valley wall to proto-Cripple Creek (Figures 5.8). This valley wall and the valley wall on the northwest side of proto-Cripple Creek appear to align with each other. Second, the curvature of the southern and northern portions of the Chena Ridge fault suggests that these bends may accommodate contraction (Figure 5.8). Areas of positive relief at the contractional bends could have served as former drainage divides.

No evidence exists to suggest that present drainages in the Fairbanks area existed prior to gravel deposition; gravels were deposited as early as Late Miocene (10 Ma) based on pollen analysis of silt along the Livengood Bench (Karl et al., 1988; Newberry, 2010). Thus, based on

restorable geomorphic characteristics and the relative age of auriferous gravel deposits along Cripple Creek, a total ~5 km of displacement may have occurred on the Chena Ridge fault recently, at least since the Pliocene around the time of auriferous gravel deposition (Péwé, 1975).

The only geologic evidence for left-lateral displacement is observed along the Chena Ridge fault to the northeast, where there is approximately 1 km of total apparent left-lateral displacement of a contact between Precambrian protolith-age schist and Devonian protolith-age eclogite (Figure 5.9; Newberry et al., 1996). The discrepancy between these displacement amounts could be for several reasons: a) there is a dense zone of faults to the northeast of the Chena Ridge fault that show apparent left-lateral displacements. It is possible that displacement was distributed along multiple faults to the northeast rather than one single strand. b) The fault traces and displacements may be different from what is shown on the map. Since outcrops are sparse and poor in quality throughout the Fairbanks area, mapped structures are interpretive and have a large degree of uncertainty. The former possibility (a) is shown in Figure 5.9, where there are two faults that appear on trend with the Chena Ridge fault in which their displacements total ~5 km.

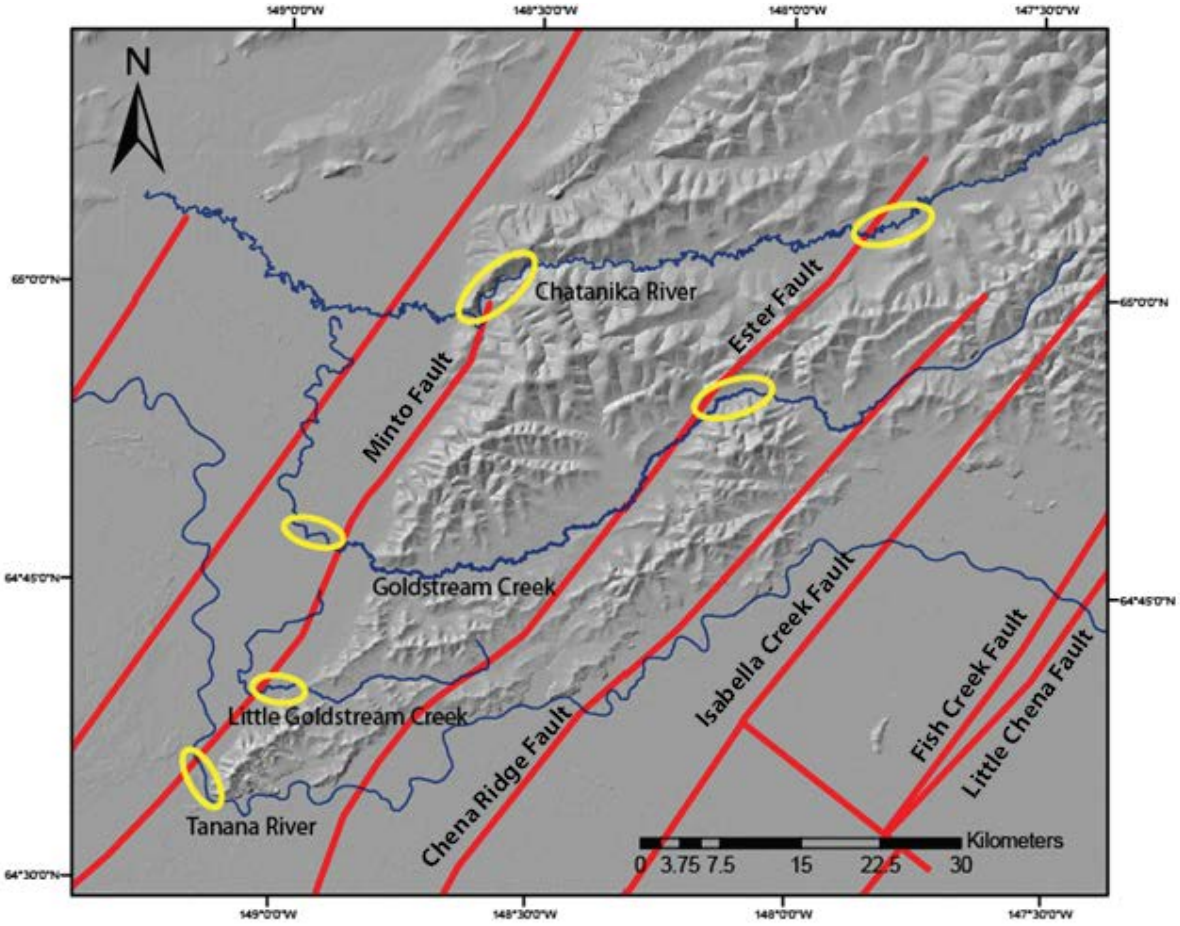

Figure 5.7: Map of potentially active faults before left-lateral restoration. Knickpoints in major drainages are shown in yellow ellipses.

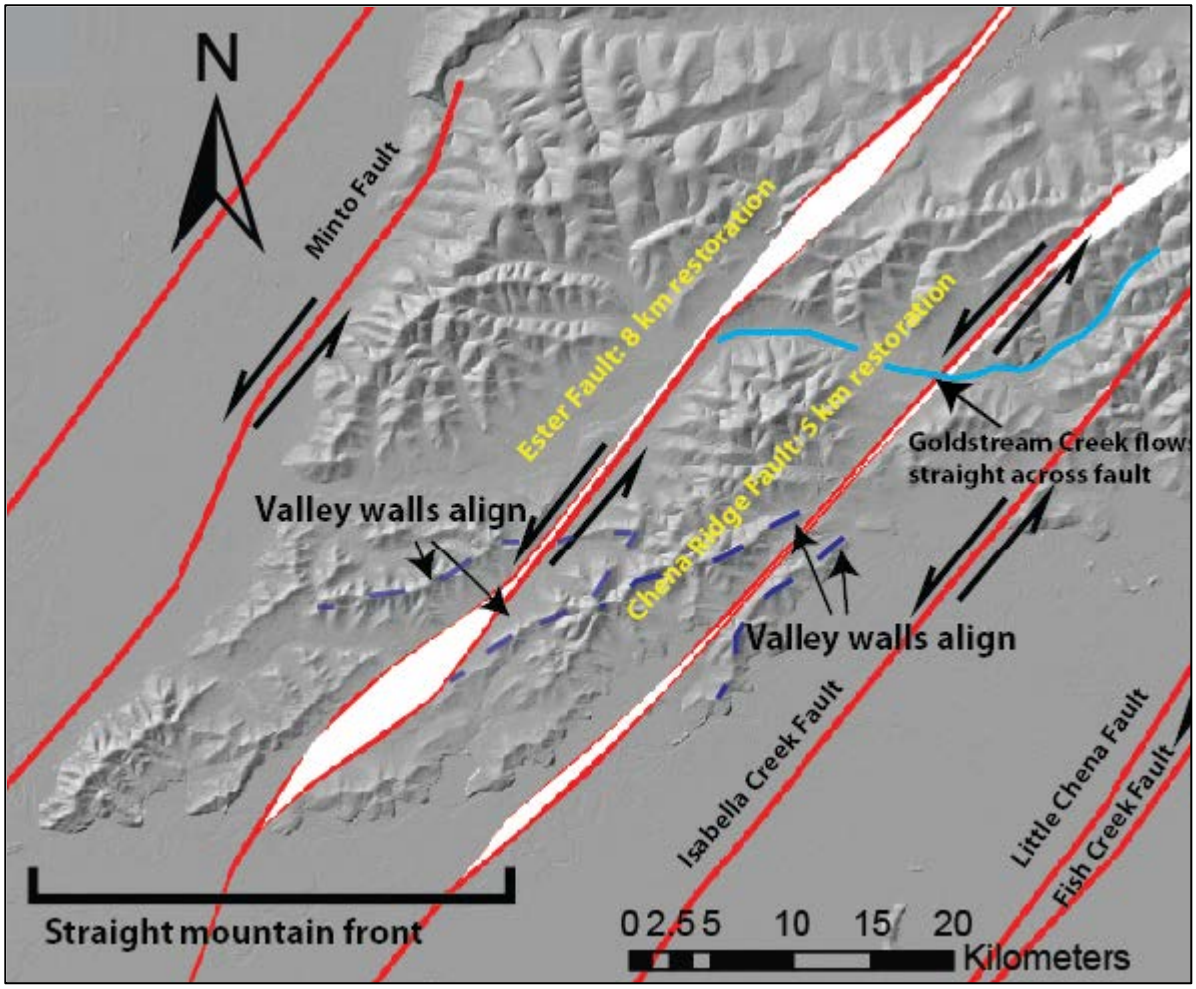

Figure 5.8: Fault restorations of 5 km on the Chena Ridge fault and 8 km on the Ester fault based on restorable geomorphic characteristics of aligned valley walls (dark blue dashed lines), a straight mountain front, and that proto-Goldstream Creek flows straight across the fault (light blue line); white spaces indicate areas where contraction would be expected during fault displacement.

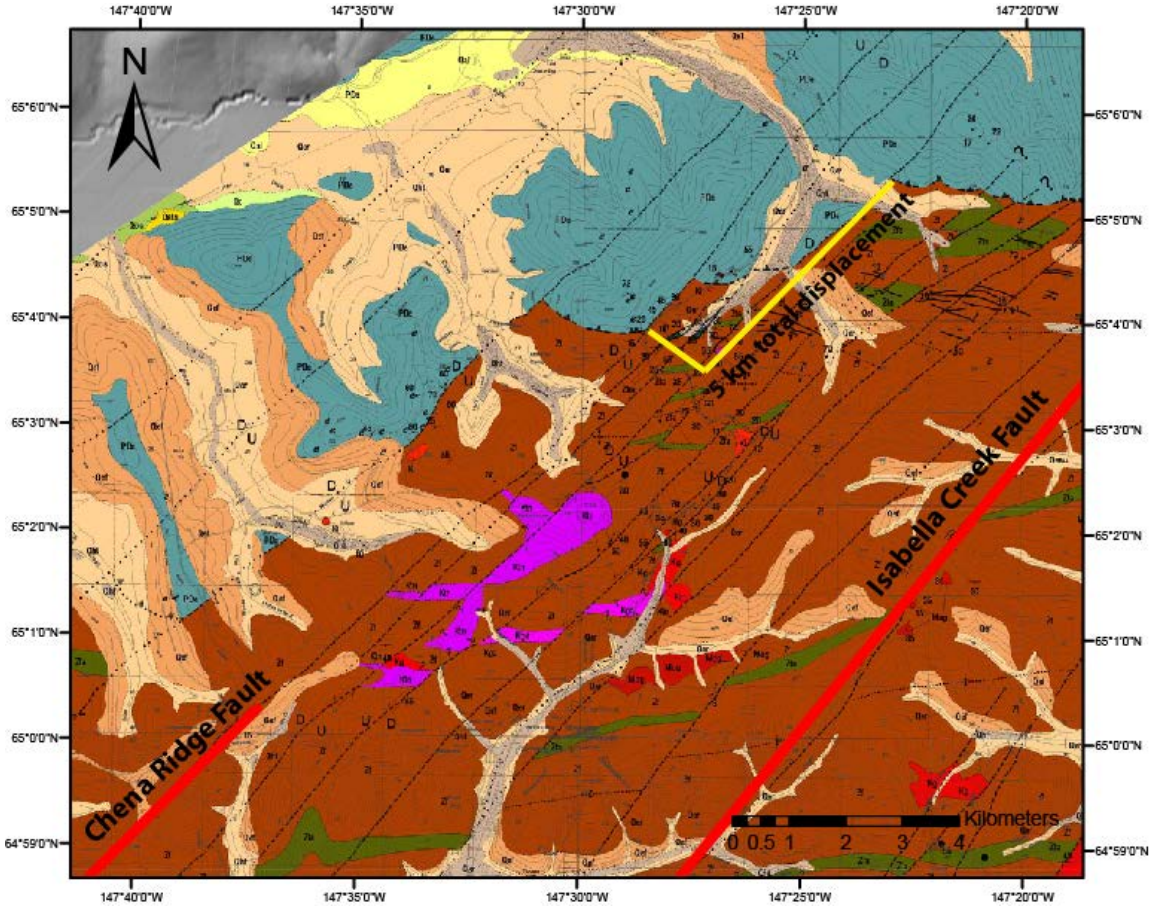

Figure 5.9: Map showing 5 km of total left-lateral displacement distributed amongst faults northeast of the Chena Ridge fault.

Like the Chena Ridge fault, the Ester fault displays left-lateral strike-slip movement according to focal mechanisms (Figure 2.5) and also dips steeply (68°) to the northwest (Figure 4.8b). The Ester fault also runs directly between the headwaters of Little Goldstream Creek and Bonanza Creek. These observations suggest it is possible that Bonanza Creek and Little Goldstream Creek were once connected and left-lateral movement along the Ester fault beheaded Little Goldstream Creek, reversing the flow of proto-Bonanza Creek. Such changes in drainage pattern should be reflected in restoration of displacement on the Ester fault. However, since the

Ester fault has not been previously mapped, evidence for left-lateral displacement has not been recognized along this fault. Thus my restorations were based on the inference that the displacement was similar to what has occurred along the Chena Ridge fault and resulted in the restorable geomorphic characteristics that are described below and shown on Figure 5.8.

With 8 km of left-lateral displacement restored on the Ester fault, several restorable geomorphic characteristics include: 1) the southern front of the Yukon-Tanana uplands is straight; 2) lower Goldstream Creek is oriented east-west, which is the most sensible path of least resistance to the Nenana basin; 3) the northern valley wall of Little Goldstream Creek and the northwestern wall of a tributary of Bonanza Creek align; and 4) the northern wall of Ohio Creek is v-shaped to the northeast, suggesting that it served as a former drainage divide (Figure 5.8). This restoration implies that left-lateral strike-slip deformation occurred along the Ester fault.

Based on the geomorphic restorations that I have described above, I have constructed a Pliocene-Pleistocene paleo-drainage map of the area (Figure 5.10) and superimposed it on the map of fault restorations (Figure 5.8). I infer the drainage patterns and stream capture events that are illustrated in Figures 5.11, 5.12, and 5.13 at the following three times: Time 1) possible drainage configuration before major left-lateral displacement affected drainages (Figure 5.11). Time 2) progressive left-lateral displacement along the Chena Ridge fault may have opened up an eastern branch of proto-Cripple Creek that began flowing southeast into the Tanana basin (Figure 5.12). Sometime in the Pliocene, this drainage became dominant and Cripple Creek was cut off from Rosie Creek, which led to the capture of proto-Cripple Creek by proto-upper Goldstream Creek and flow reversal from southwest to northeast along Cripple Creek. Perhaps this flow reversal reworked the gravels along Cripple and Ester Creeks where Pliocene gold

placers were deposited (Péwé, 1975). Time 3) sometime after the capture of Cripple Creek, left-lateral movement along the Ester fault resulted in aggressive headward migration of proto-lower Goldstream Creek, which eventually led to the capture of proto-middle Goldstream Creek and cut off the connection between proto-upper Goldstream Creek and proto-Cripple Creek, leaving behind a wind gap (Figure 5.13). This capture event reworked the gravels of the entire Goldstream drainage (Metz, 1991), and may have contributed to the deposition of Pleistocene gold placers (Péwé, 1975) along the upper reaches of upper Goldstream Creek and middle Goldstream Creek (Newberry et al., 1996). Perhaps around the same time that Goldstream Creek was captured, proto-Little Goldstream Creek and the unnamed drainages to the south of proto-Little Goldstream Creek were beheaded and headward migration of proto-Bonanza Creek resulted in the capture and flow reversal of the upper reaches of the eastern-most unnamed drainage. The timing of this capture event is less clear, but since the geomorphic restorations along the Ester fault involve Pleistocene gold placers, some of the deformation could have occurred in the Pleistocene.

Although the timing of deformation is not constrained, movement along the Ester fault may have occurred during or just after the Chena Ridge fault moved streams into their current position. Proto-Middle Goldstream Creek was probably originally flowing southeast based on the configurations of barbed drainages around Ester Dome. In order for proto-Middle Goldstream Creek to have been captured, it needed to be flowing southeast first.

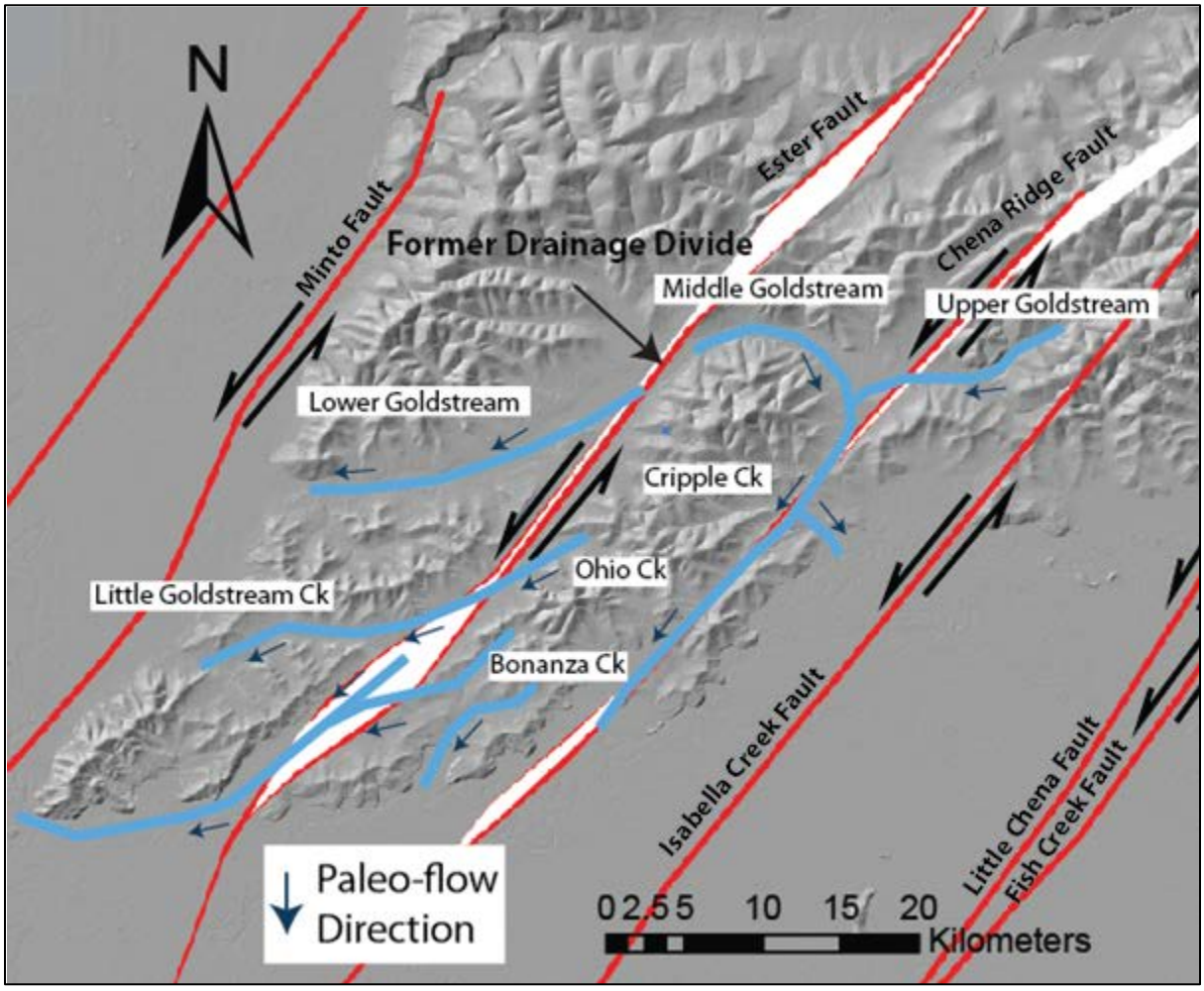

Figure 5.10: Pliocene-Pleistocene paleodrainage map superimposed on the fault restoration map (Figure 5.8).

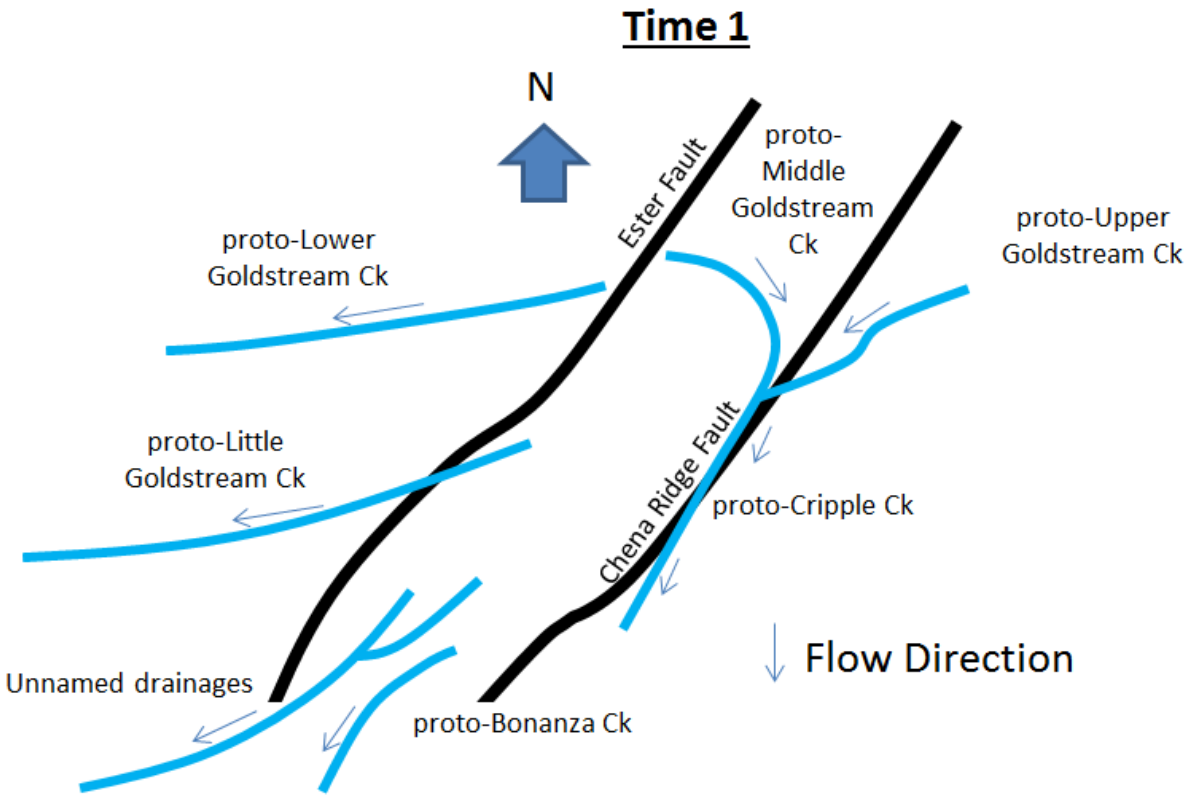

Figure 5.11: Illustration showing possible drainage configurations before the onset of major left-lateral displacement. Proto- Middle Goldstream Creek flowed south via Proto-Cripple Creek. A possible former drainage divide was noted north of Ester Dome (Metz, 1991).

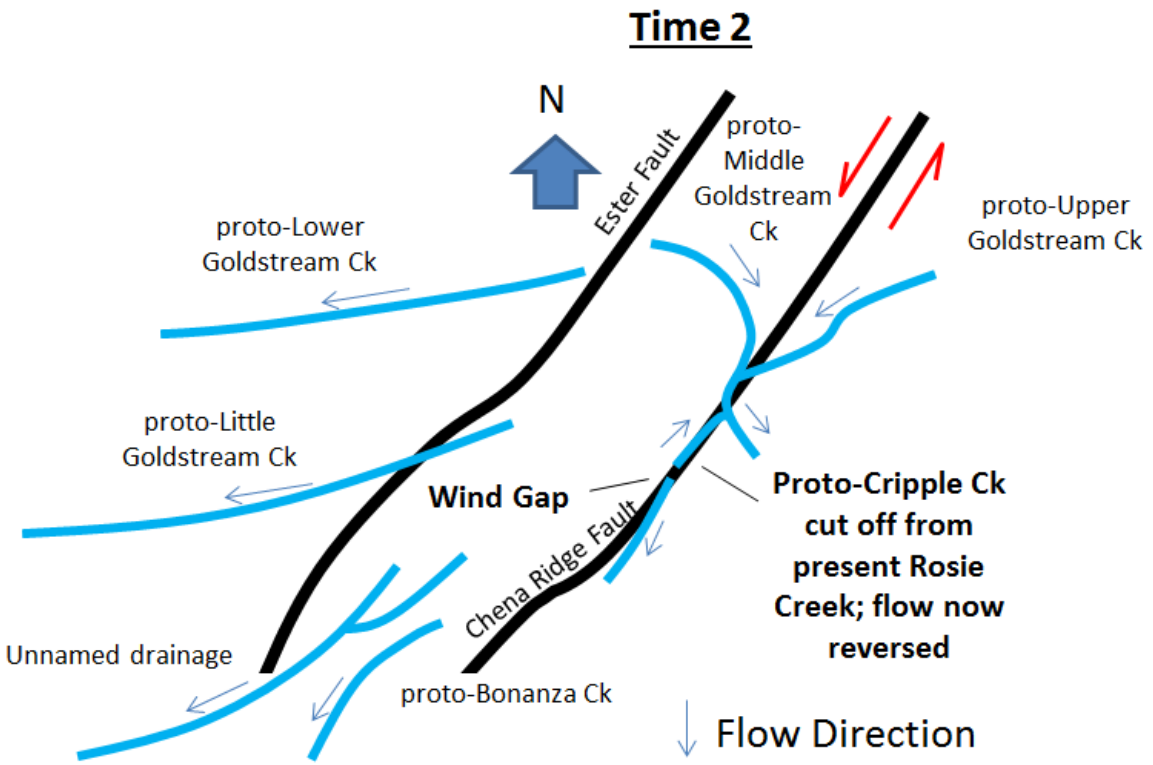

Figure 5.12: Illustration showing possible drainage configurations at time 2. Progressive left-lateral displacement along the Chena Ridge fault may have opened up an eastern branch of proto-Cripple Creek that began flowing southeast into the Tanana basin. Then, proto-Cripple Creek was captured by a more aggressive drainage, reversing its flow direction.

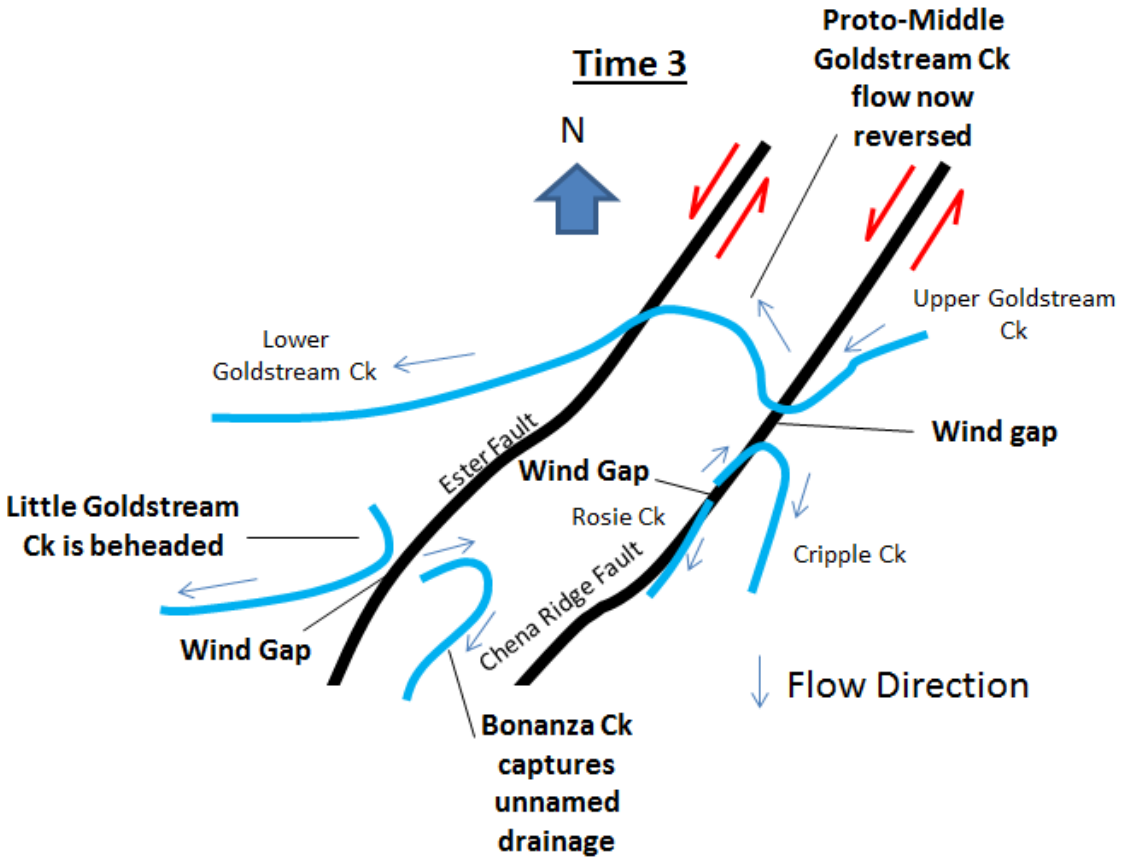

Figure 5.13: Illustration showing possible drainage configurations at time 3. Sometime after the capture of Cripple Creek, left-lateral movement along the Ester fault resulted in aggressive headward migration of proto-lower Goldstream Creek. This eventually led to the capture of proto-middle Goldstream Creek. Progressive displacement along the Chena Ridge fault cut off the connection between proto-upper Goldstream Creek and proto-Cripple Creek and proto-upper Goldstream Creek started flowing via proto-middle Goldstream Creek.

5.3 Apatite Fission-Track Analysis: Timing of Cooling in the Fairbanks Area

5.3.1 Regional Cooling Trends

A location map of apatite fission-track samples is shown in Figure 5.14. Track length distribution charts and HeFty thermal models for the highest quality apatite fission-track samples are shown in Figures 5.15, 5.16, 5.17, and 5.18. Models for samples 1338-18 and 1338-19 included additional stratigraphic age and temperature constraints, as these were sedimentary samples from the Nunivak #1 well (Table 4.4). Part of sample 1338-18 and all of sample 1338-19 were collected at intervals deeper than 6730 ft (2051 m), a depth that has an equivalent downhole temperature of 60°C. This means that the samples were partially to fully within the lower part of the partial annealing zone (PAZ) and the tracks within the apatite grains may have annealed to some degree. Additional models for each sample are shown in Appendix C.

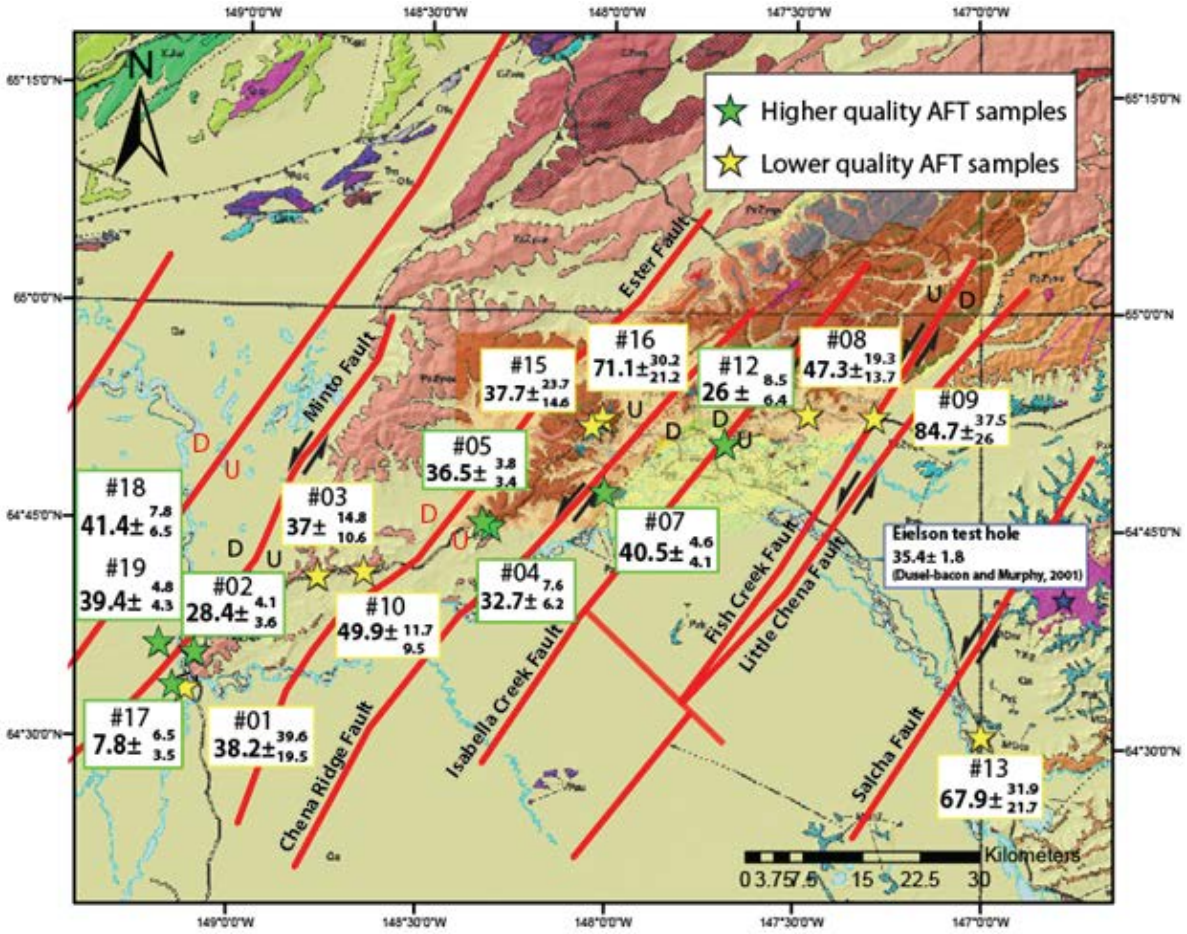

Figure 5.14: Map showing the locations of apatite fission-track samples.

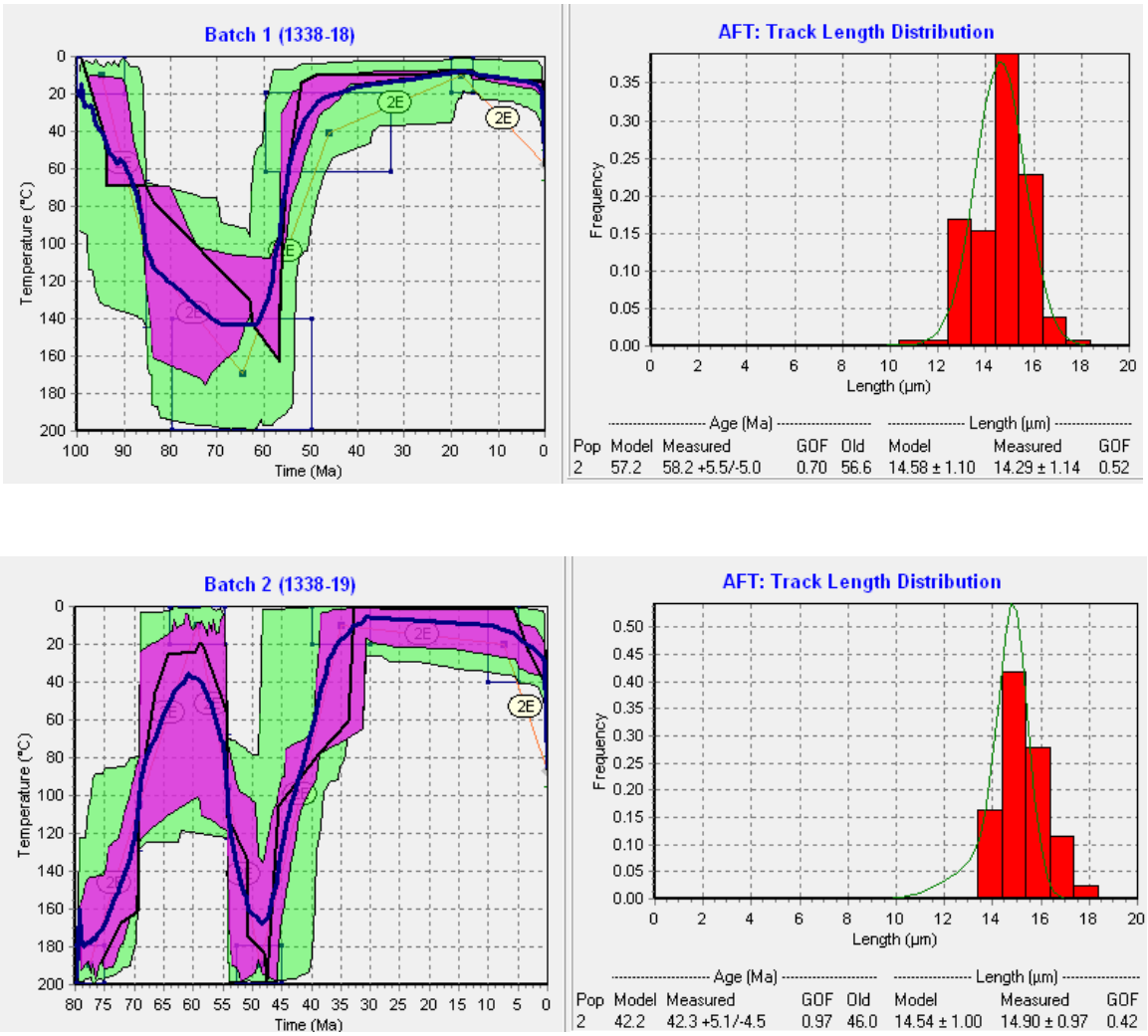

Figure 5.15: HeFty models and track length distributions for samples 1338-18 and 1338-19. Locations of samples are outlined in green on the above map. Pink and green areas represent good and acceptable path envelopes, respectively. Black and dark blue lines represent the best fit curve and the weighted mean path, respectively. Samples were collected by Nilesh Dixit, Alec Rizzo, and myself. The apatite fission-track analysis was conducted by AtoZinc.

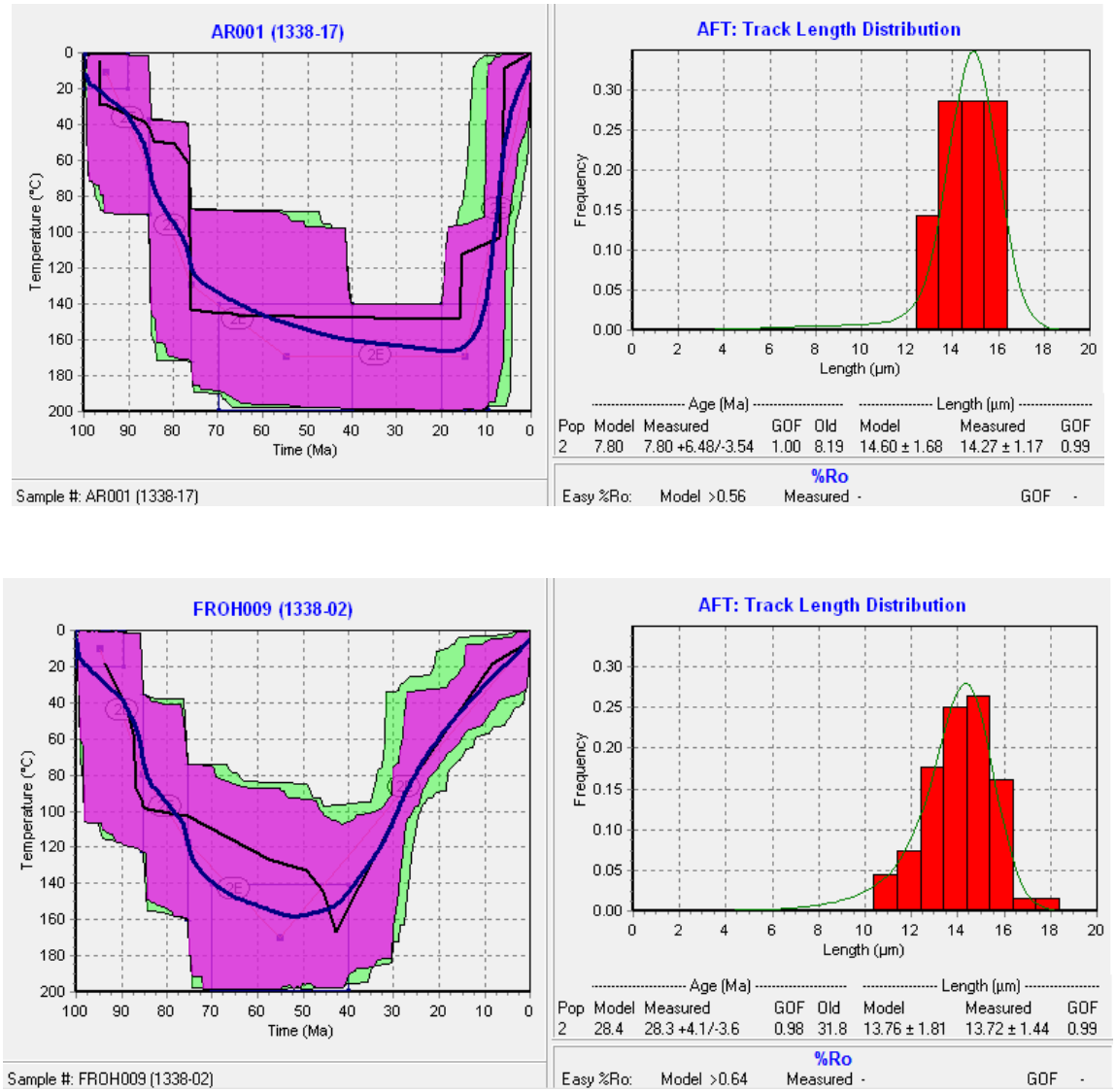

Figure 5.16: HeFty models and track length distributions for samples 1338-17 and 1338-02.

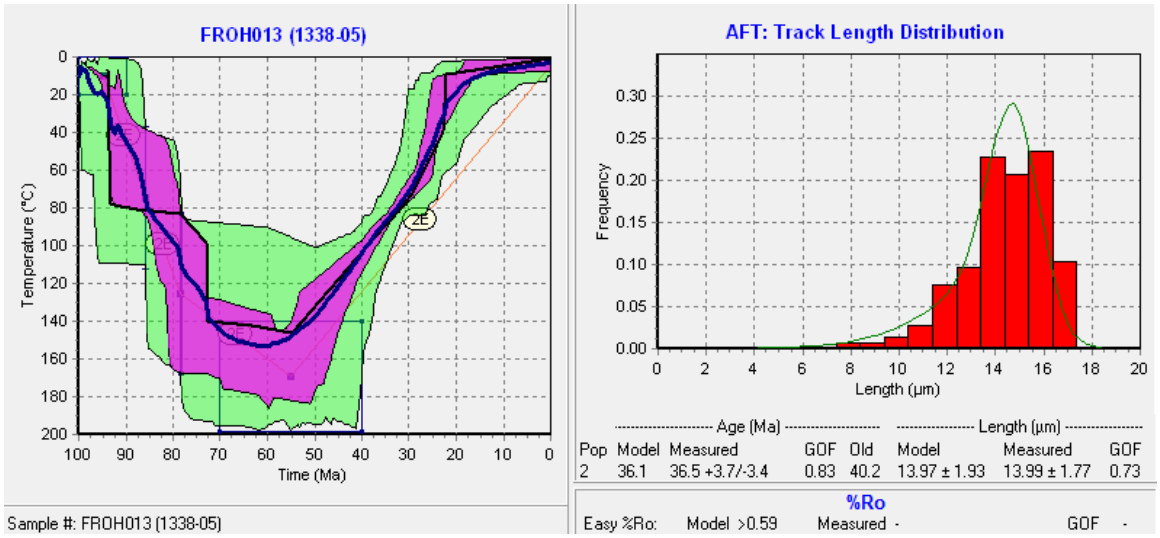

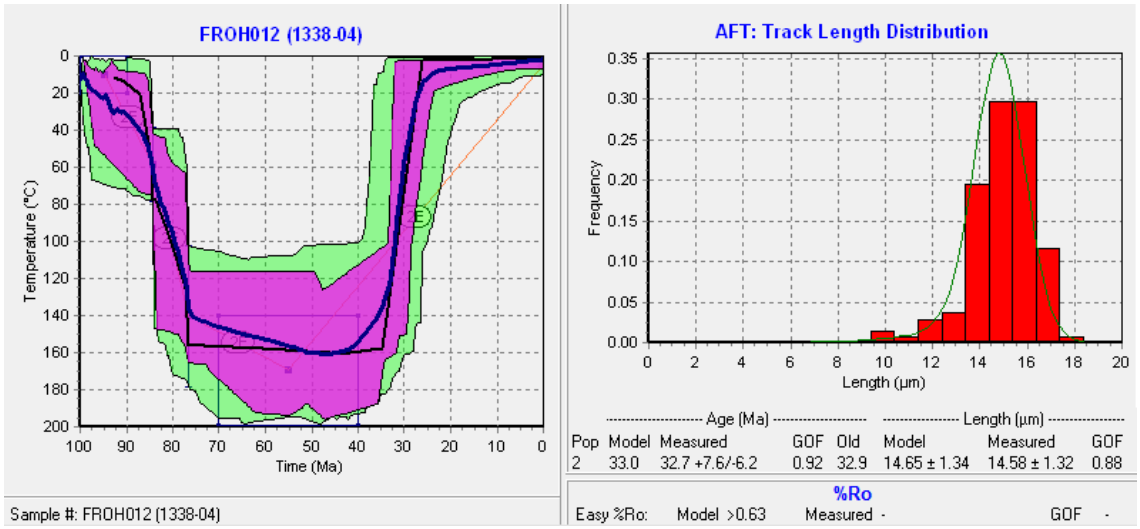

Figure 5.17: HeFty models and track length distributions for samples 1338-05 and 1338-04.

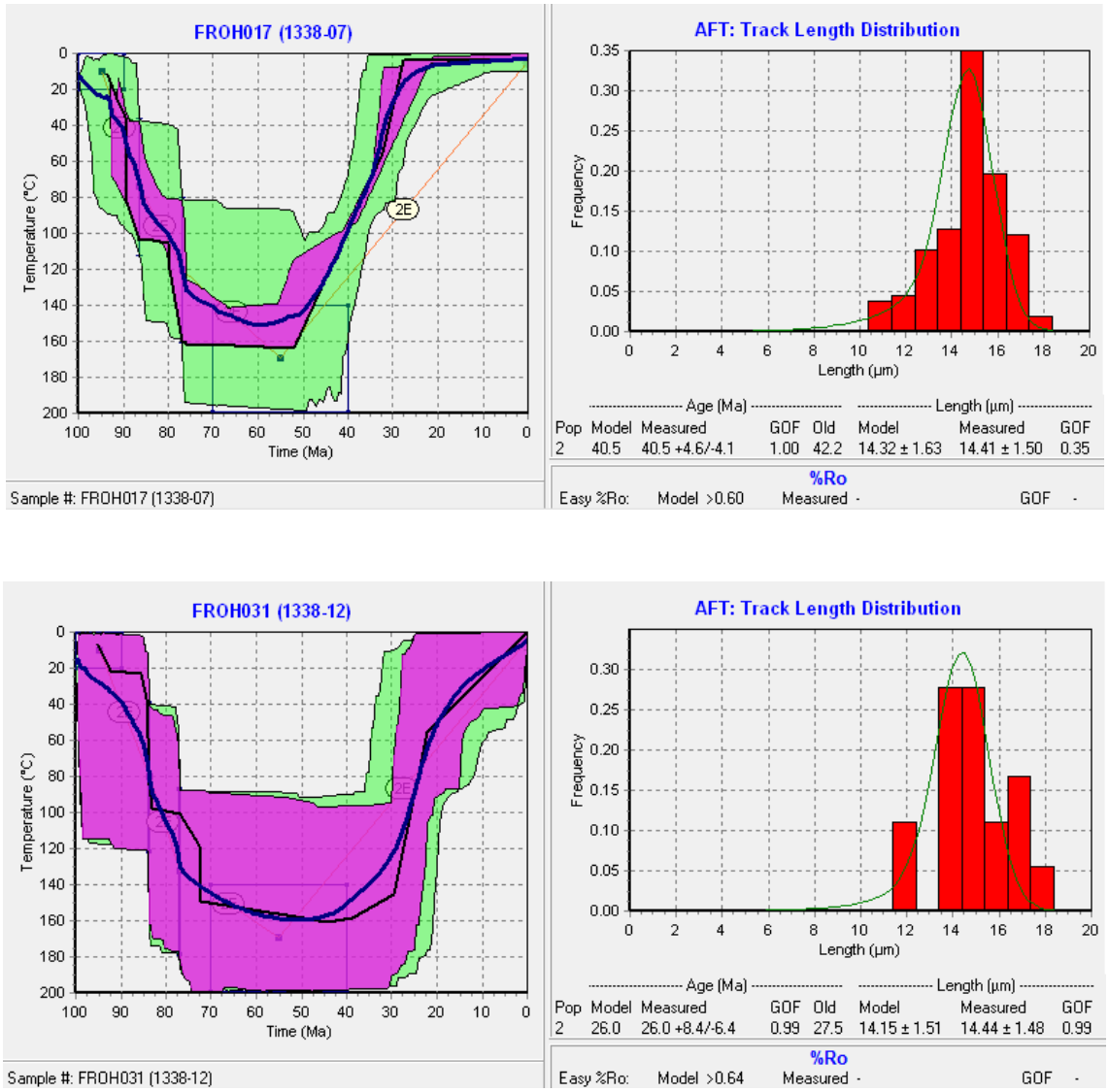

Figure 5.18: HeFty models and track length distributions for samples 1338-07 and 1338-12.

Cooling rates can be calculated from the HeFty models from the slope of the weighted mean curve through a well-constrained temperature window of 60°-120°. The uncertainty of the calculated cooling rates is variable and is based on the margin of error for each HeFty model. The corresponding time interval for the temperature window of 60°-120° varied among the samples. Cooling rates were then converted to exhumation rates using a present-day geothermal gradient in Interior Alaska of 32°C/km, determined from the Eielson test hole (Naeser, 1979; Dusel-Bacon and Murphy, 2001). Previous apatite fission-track studies (e.g., Dusel-Bacon and Murphy, 2001) on metamorphic rocks from the Yukon-Tanana uplands attributed the mechanism of Tertiary cooling to exhumation. However, Dusel-Bacon and Murphy (2001) postulated that a widespread Tertiary heating episode may imply a heightened paleo-geothermal gradient of 45°C/Ma, which suggests that geothermal gradient relaxation, not exhumation, could possibly have been a cooling mechanism. Also, since many faults in the Fairbanks area display evidence of hydrothermal alteration (Newberry et al., 1996; Rhys et al., 2003), it is possible that hot fluids may have reset the apatites of some nearby samples. However, the ages of minerals associated with alteration are mostly Cretaceous (Avalon, 2007; Rhys et al., 2003). Since metamorphic rocks from this study were >10 km away from any nearby intrusions and since there were no other concrete indications of a different mechanism of cooling (e.g., relaxed geothermal gradient; hot fluid migration), exhumation is assumed.

Samples that range from 26 to 50 Ma generally have long mean track lengths (14μ) and higher standard deviations (>1.25μ), indicating residence in the upper part of the PAZ for a sufficient time to allow retention of both short and long tracks (Samples 1338- 1, 2, 3, 4, 5, 7, 10, 12, and 19; Tables 5.1 and 5.2; Figure 5.14). Thermal models imply that the majority of the

samples, which range in age from ~32 to 50 Ma, cooled until ~20-30 Ma and then remained near the surface at shallow depths and low temperatures, near the upper part of the PAZ, until they reached the surface. Thermal models imply that samples with younger ages (Samples 1338- 2 and 12) ~26 and 28 Ma, cooled until ~20 Ma and then continued to cool at slower rates to the present, which can also account for a wider distribution of track lengths.

Samples with cooling ages >50 Ma (Samples 1338- 9, 13, and 16; Tables 5.1 and 5.2; Figure 5.14) have long mean track lengths (14-15μ) and lower standard deviations (0.7μ - 1.1μ), which suggests cooling through the PAZ allowed mostly long tracks to be retained. In contrast, Dusel-Bacon and Murphy (2001) reported that samples with cooling ages of >50 Ma have shorter mean track lengths (<14μ) and larger standard deviations (1.25-3.2 μ), which suggests slower cooling and partial annealing. The >50 Ma samples in this study (Samples 1338- 9, 13, and 16) have a low number of counted tracks (≤20), thus the data are less reliable than the 26-50 Ma samples (Samples 1338- 1, 2, 3, 4, 5, 7, 10, 12, and 19) mentioned previously.

Table 5.1: Summary of apatite fission-track age data. Analysis done by AtoZinc. *Highest quality samples based on error of <10 Ma.

A2Z Sample Number	Accepted Spots	SumNs	[U]m ppm	Dparm	Dperm	Pooled age	-1σ	+1σ
Durango Standard	486 (grains)	3091	2.17E-03	1.52	0.29	31.40	0.8	0.8
1338-01	15	9	2.027829	1.797461	0.3519703	38.17	19.47	39.62
*1338-02	24	245	15.05614	1.770088	0.3161471	28.35	3.57	4.09
1338-03	16	36	2.399709	1.710184	0.3242248	37.04	10.60	14.83
*1338-04	16	95	6.093417	1.833736	0.3405561	32.66	6.18	7.61
*1338-05	32	491	12.95625	1.8328	0.3287028	36.51	3.40	3.75
1338-06	2	2	2.23E-02	1.629064	0.3927105	1772.46	1391.61	4499.35
*1338-07	34	388	7.015243	1.945322	0.3589945	40.47	4.14	4.61
1338-08	28	38	2.460619	1.797366	0.3276868	47.31	13.72	19.30
1338-09	34	30	0.3925543	1.755919	0.329493	84.69	26.04	37.50
1338-10	24	95	3.21108	1.698883	0.2887211	49.89	9.46	11.66
*1338-12	6	52	15.04095	1.858696	0.4376651	25.98	6.38	8.45
1338-13	21	28	0.7724602	1.715592	0.3728422	67.96	21.74	31.88
1338-15	2	17	12.64715	1.813768	0.346351	37.72	14.55	23.65
1338-16	2	33	9.099619	2.053384	0.304206	71.08	21.21	30.16
*1338-17	10	11	11.81415	1.814766	0.3497226	7.79	3.54	6.48
*1338-18	33	604	17.61617	1.906801	0.3340907	41.40	6.54	7.76
*1338-19	20	365	27.24047	1.860194	0.3589945	39.41	4.25	4.76

Table 5.2: Summary of apatite fission-track length data. Analysis done by AtoZinc. *Highest quality samples based on error of <10 Ma.

A2Z Sample Number	Number of Tracks	Mean Track Length (µm)	Std. Error (µm)	Std. Dev (µm)	Dparm	Dperm
Durango Standard	138	14.59	0.08	0.98	1.87	2.36
1338-01	20	14.019	0.3967639	1.729454	1.955042	0.3269643
*1338-02	78	13.82936	0.1597402	1.401715	2.205321	0.3435412
1338-03	64	13.87938	0.2031492	1.612446	2.211568	0.3713747
*1338-04	138	14.58058	0.1124437	1.31612	2.396385	0.4392536
*1338-05	152	14.02395	0.1436366	1.765036	2.258121	0.3694753
1338-06	9	14.58778	0.37429	1.058652	2.205917	0.4016078
*1338-07	158	14.42443	0.1196745	1.499517	2.414577	0.4202383
1338-08	78	14.88898	0.7756628	6.806414	2.143751	0.3437575
1338-09	16	14.16375	0.2596543	1.005637	2.080216	0.3410828
1338-10	125	14.34	0.1248655	1.390443	2.151426	0.328077
*1338-12	20	14.3565	0.3391249	1.478211	2.293499	0.422212
1338-13	20	15.1625	0.246094	1.072699	2.154222	0.3518298
1338-15	10	14.671	0.4192511	1.257753	2.255061	0.3834386
1338-16	17	14.42412	0.174486	0.697944	2.678559	0.5159227
*1338-17	15	14.27533	0.3012082	1.127018	2.284014	0.3738858
*1338-18	133	14.28947	0.1031303	1.184877	2.274119	0.407065
*1338-19	49	13.98286	0.2189265	1.516768	2.423302	0.4363175

I generated a plot to show pooled ages versus perpendicular distance from the Minto fault (Fig 5.19). The plot reveals two possible trends: 1) a general trend of younger-to-southwest and 2) a younger-to-southwest trend within individual fault-bounded blocks. Given the large uncertainty in the data, trend 2 could possibly be an artifact, however, trend 1 is indicated by the highest quality samples.

I also generated a plot showing cooling rates versus perpendicular distance from the Minto fault to complement the age-versus-distance plot and determine cooling patterns across the Yukon-Tanana uplands (Figure 5.20). The cooling rate versus distance plot defines a general higher-cooling-rate-to-west trend at an average of approximately 0.04°C/km to the west. Both plots combined suggest younger tectonic activity and higher exhumation rates to the southwest.

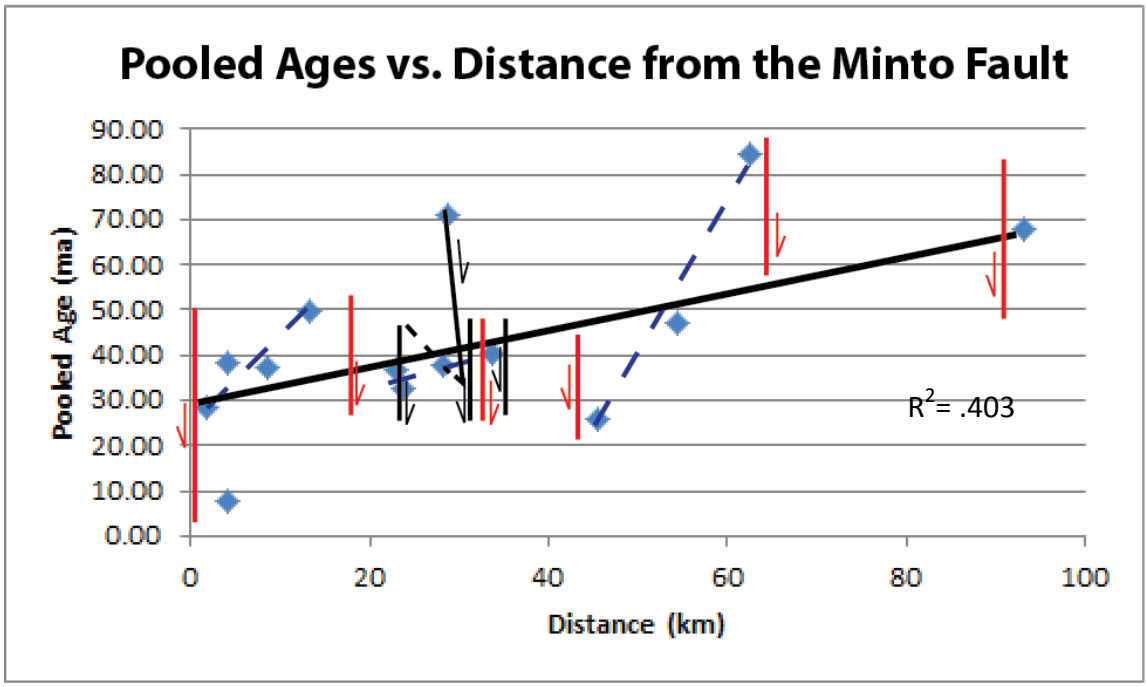

Figure 5.19: Graph of pooled ages vs. distance from the Minto fault. Red lines are interpreted seismically active faults, thin black lines are mapped faults (Newberry et al., 1996), blue dotted lines represent a possibly younger-to-southwest trend in fault-bounded blocks, and the thick black line represents a general trend of younger-to-southwest ages.

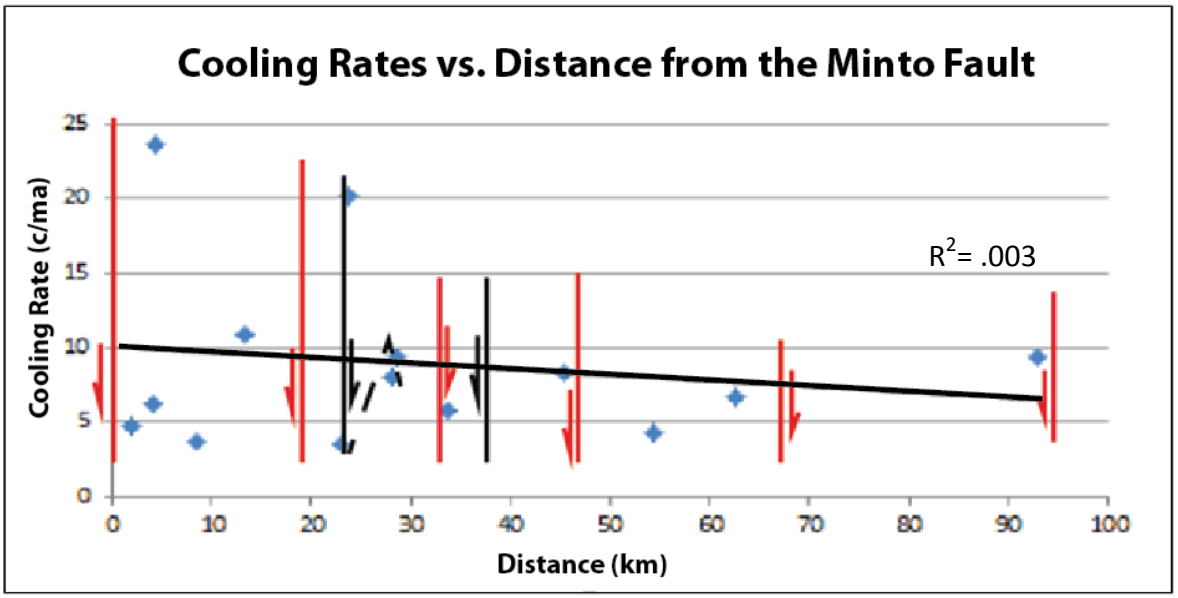

Figure 5.20: Graph of cooling rate vs. distance from the Minto fault. Red lines are interpreted seismically active faults, thin black lines are mapped faults (Newberry et al., 1996), and the thick black line represents a possible trend of higher cooling rate to the southwest.

The following discussion includes a detailed evaluation of the highest quality samples that are marked with asterisks in Tables 5.1, 5.2, and outlined in Figure 5.14. Lower quality samples will not be discussed due to their high margin of error.

5.3.2 Cooling History of Samples 1338-18 and 1338-19

Sample 1338-18 (Tables 5.1 and 5.2; Figure 5.15), from the Nunivak #1 well located at a depth interval of 5560 ft to 7390 ft (1695 m to 2252 m), with a stratigraphic age range of middle Miocene to early-middle Miocene (Wahrhaftig et al., 1969), and on the hanging wall of the Minto fault, yielded a pooled age of 39.4 Ma + 4.8 or - 4.3 (1 sigma error), a long mean track length of 14 ± 0.2µ, and a high standard deviation of 1.5µ. Sample 1338-19 (Tables 5.1 and 5.2;

Figure 5.15), also from the Nunivak 1 well at a depth interval of 9010 to 11020 ft (2746 m to 3359 m), with a stratigraphic age range of early-late late Paleocene (Nilesh Dixit, personal communication), yielded a similar pooled age of 41.4 Ma + 7.8 or -6.5 (1 sigma error), a long mean track length of 14.3 ± 0.1µ, and a lower standard deviation of 1.2µ. The cooling history for sample 1338-18 shows that final cooling occurred through the PAZ between ~58 and ~55 Ma (Figure 5.15). The cooling curve for sample 1338-19 shows that final cooling occurred between ~45 and ~40 Ma (Figure 5.15). Sample 1338-18 is consistent with a relatively earlier exhumation event between ~58 and ~55 Ma, and sample 1338-19 is consistent with a relatively later exhumation event between ~45 and ~40 Ma. Present temperatures for sample 1338-18 range from 50°-65°C and for sample 1338-19, from 79°-95°C. This implies that parts of sample 1338-18 and all of sample 1338-19 are currently within the PAZ, which could mean that tracks have partially annealed.

5.3.3 Cooling History of Samples 1338-17 and 1338-02

Samples 1338-17 and 1338-02 (Tables 5.1 and 5.2; Figure 5.16) are located at the southwestern-most front of the Yukon-Tanana uplands, on the footwall of the Minto fault and the hanging wall of the Ester fault. Samples 1338-17 and 1338-02 yielded very different pooled ages of 7.8 Ma + 6.5 or -3.5 (1 sigma error) and 28.4 Ma + 4.1 or - 3.6 (1 sigma error), respectively, despite the fact that sample 1338-02 is closer to the Minto fault and only a short lateral distance separates the samples from each other (<5 km). Samples 1338-17 and 1338-02 yielded mean track lengths of 14.3± 1.2µ and 13.7 ± 1.4µ, respectively. Sample 1338-17 has a smaller standard deviation of 1.1µ, whereas sample 1338-02 has a larger standard deviation of 1.4µ. The cooling history for sample 1338-17 shows that it cooled through the PAZ between ~10 and 7 Ma

(Figures 5.16 and 5.21). The cooling rate for sample 1338-17 was 23.7°C/Ma within a time interval of ~10-7 Ma, which translates to an exhumation rate of 740.5 m/Ma (Table 5.3). The cooling history for sample 1338-02 shows that it cooled through the PAZ between ~33 and 20 Ma (Figures 5.16 and 5.21). The cooling rate for sample 1338-02 was 4.7°C/Ma through a time interval of ~34-20 Ma, which translates to an exhumation rate of 145.7 m/Ma (Table 5.3).

Table 5.3: Summary of cooling and exhumation rates for all samples. *Highest quality samples.

Sample	Pooled age	± 1 σ	Spots counted	Age Range through PAZ (Ma)	Cooling Rate (°C/Ma)	Exhumation Rate (m/Ma)
*1338-17	7.8	6.5,3.5	10	10-7	23.70	740.56
1338-01	38.2	39.6,19.5	15	43-33	6.18	193.08
*1338-02	28.4	4.1,3.6	24	34-20	4.66	145.73
1338-03	37.0	14.8,10.6	16	43-27	3.75	117.23
1338-10	49.9	11.7,9.5	24	52-46	10.95	342.30
*1338-05	36.5	3.8,3.4	32	45-28	3.51	109.80
*1338-04	32.7	7.6,6.2	16	33-30	20.18	630.73
1338-15	37.7	23.7,14.6	2	43-35	7.96	248.72
1338-16	71.1	30.2,21.2	2	72-66	9.40	293.70
*1338-07	40.5	4.6,4.1	34	45-34	5.80	181.13
*1338-12	26.0	8.5,6.4	6	29-22	8.31	259.64
1338-08	47.3	19.3,13.7	28	54-40	4.26	133.01
1338-09	84.7	37.5,26.0	34	88-78	6.62	206.83
1338-13	68.0	31.9.21.7	21	67-62	9.35	292.34

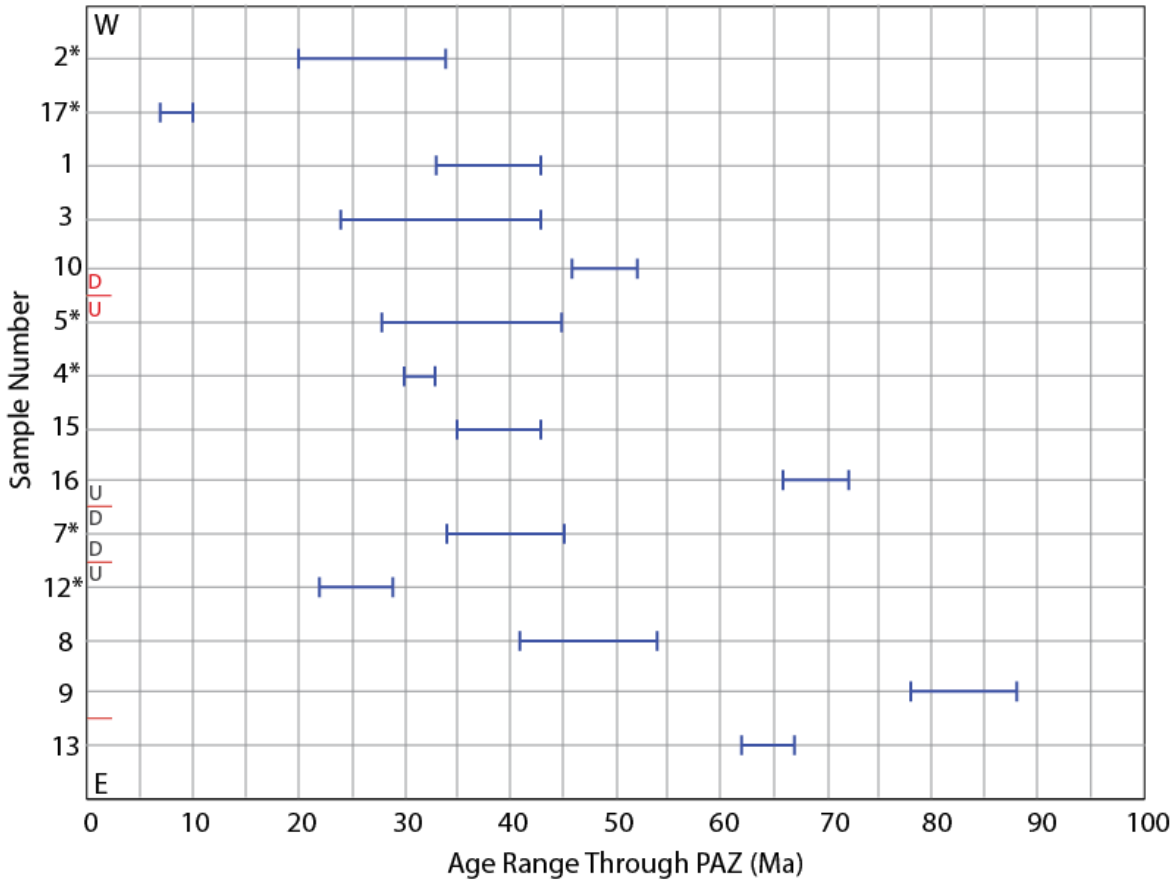

Figure 5.21: Graph showing the age range through the PAZ for all apatite fission-track samples. Red lines indicate interpreted active faults; red U/D indicates interpreted (this study) upthrown and downthrown blocks; black U/D indicates upthrown and downthrown blocks from Newberry et al. (1996). *Highest quality samples.

If the exhumation of sample 1338-17 was related to tectonic events, the discrepancy in ages and exhumation rates could suggest either a) a splay fault between the two samples with significant down-to-west displacement or b) a footwall anticline with sample 1338-17 near the crest. I observed several small-scale west-dipping faults between these samples, however, the significant difference in ages and mean track lengths suggests that a larger, regional-scale fault would better explain the data. Scenario b is more likely, as this would represent the southward continuation of the northeast-trending Minto anticline, which was identified to the north through geomorphic analyses. In this scenario, sample 1338-02 would be located along the southeast limb of the anticline and would have left the PAZ earlier, as it would be closer to the surface, at a shallower structural level. Sample 1338-17, which is on the crest of the anticline, would have remained in the partial annealing zone until later, since it would be at a deeper structural level. Regardless, sample 1338-17 (~7.8 Ma) suggests relatively young uplift along the footwall of the Minto fault and supports young growth of the Minto anticline.

5.3.4 Cooling History of Samples 1338-05 and 1338-04

Samples 1338-05 and 1338-04 (Tables 5.1 and 5.2; Figure 5.17) both lie on the horst between the Ester and Chena Ridge faults. Sample 1338-05 yielded a pooled age of 36.5 Ma +3.8 or -3.4 (1 sigma error) and sample 1338-04 yielded an age of 32.7 Ma +7.6 or -6.2 (1 sigma error). Sample 1338-05 yielded a shorter mean track length of 14 ±0.1µ and a higher standard deviation of 1.8µ than sample 1338-04, which yielded a mean track length of 14.6 ±0.1µ and a standard deviation of 1.3µ. Sample 1338-05 was collected west of a northeast-striking down-to-west fault, which likely represents the continuation of a northeast-striking fault that cuts through Ester Dome (Figure 5.14). Sample 1338-04 was collected east of the fault.

The cooling history for sample 1338-05 (Figure 5.17) shows that this sample cooled through the PAZ between ~45 and 28 Ma (Figure 5.21). The cooling rate was 3.5°C/Ma within a time interval of ~45-28 Ma, which translates to an exhumation rate of 109.8 m/Ma (Table 5.3). On the east side of the fault, sample 1338-04 (Figure 5.17) cooled within the PAZ between ~33 and 30 Ma (Figure 5.21). The cooling rate was 20.2°C/Ma within a time interval of ~33-30 Ma, which translates to an exhumation rate of 630.7 m/Ma.The sample east of the fault yielded a significantly higher exhumation rate and a younger age over a small distance (1 km) than the sample west of the fault, which would imply down-to-west motion along the fault.

Along the fault mapped on trend to the northeast (Figure 5.14), sample 1338-15 was collected west of the fault and yielded an age of 37.7 Ma +23.7 or -14.6 (1 sigma error), and sample 1338-16 was collected east of the fault and yielded an age of 71.1 Ma +30.2 or -21.2 (1 sigma error). Despite the large margin of error for both samples, the significantly older age east of the fault and younger age west of the fault is consistent with down-to-east motion along the fault.

There are two possibilities that could explain this apparent difference in motion sense: 1) positive error in sample 1338-04 is 7.6 Ma, which would then exceed the age of sample 1338-05; or 2) a later switch in the vertical sense of motion from down-to-west to down-to-east. The simplest and most plausible explanation would be error in the sample age. However, many faults in the Fairbanks area have exhibited changes in the vertical sense of motion along strike and/or at different times in the same locality (e.g., the Ryan Lode fault). The latter case could imply scissor-like fault motion, with older down-to-east motion toward the northeast end of the fault and younger down-to west motion toward the southwest end of the fault. This scissor-like

character is similar to what was observed in the geomorphology along the Minto fault; however, data quality is too poor to make definitive conclusions.

5.3.5 Cooling History of Samples 1338-07 and 1338-12

Sample 1338-07 (Tables 5.1 and 5.2; Figure 5.18) lies on the hanging wall of the Chena Ridge fault and the footwall of the Isabella Creek fault. This sample yielded a pooled age of 40.5 Ma + 4.6 or -4.1 (1 sigma error), a long mean track length of 14.4± 0.1µ, and a standard deviation of 1.5µ. The cooling history suggests that the sample cooled through the PAZ between ~45 and 34 Ma. The cooling rate was 5.8 °C/Ma within a time interval of ~45-34 Ma, which translates to an exhumation rate of 181.1 m/Ma (Table 5.3).

Sample 1338-12 (Tables 5.1 and 5.2; Figure 5.18) lies to the east of the Isabella Creek fault. Sample 1338-12 yielded a pooled age of 26 Ma +8.5 or -6.4 (1 sigma error), a long mean track length of 14.4 ± 0.3µ, and standard deviation of 1.5µ. The cooling history for sample 1338-12 shows that this sample cooled through the PAZ between ~29 and 22 Ma (Figure 5.21), then cooling began to slow to the present. The cooling rate was 8.3°C/Ma within a time interval of ~29-22 Ma (Figure 5.21), which translates to an exhumation rate of 256.6 m/Ma (Table 5.3).

The age of sample 1338-12 (~26 Ma) is consistent with relatively young exhumation east of the Isabella Creek fault. The age of sample 1338-07 (~40 Ma) is consistent with older exhumation east of the Chena Ridge fault.

5.3.6 Summary of Apatite Fission-Track Evidence for Exhumation

The majority of samples were exhumed between 54 and 20 Ma within the PAZ, with the exception of sample 1338-17, which was exhumed between 10 and 7 Ma within the PAZ (Figure 5.21). The time interval of maximum exhumation was between 45 and 24 Ma.

Exhumation rates tend to have a broad range (109.8-740.6 m/Ma) over a relatively short distance (70 km from eastern-most to western-most sample), pooled ages have a broad range (~40-7 Ma), and there is little topographic relief between the highest and lowest sample (325 m). This suggests that vertical displacement along faults may have played a larger role in local control on exhumation than other processes that caused regional surface uplift and consequent exhumation. If samples were primarily exhumed due to regional erosion, one would expect more consistency of exhumation rates and pooled ages over a small distance (70 km) and little relief (325 m).

Since vertical displacement along faults could account for exhumation, the observation that most samples were out of the PAZ by 20 Ma could suggest that significant vertical displacement decreased during this time along the majority of faults, with the exception of the Minto fault.

5.4: Structural Model for the Fairbanks Area

Little is known about the origin and evolution of the present-day northeast-striking faults. However, some authors have suggested initiation of faulting as early as the Cretaceous followed by periods of reactivation in the Tertiary and Quaternary (Foster et al., 1994; Page et al., 1995;

McCoy et al., 1997; Rhys et al., 2003). The preferred model that I will present in the following discussion is a modified version of the block rotation model proposed by Page and others (1995), in which northeast-striking left-lateral faults rotate clockwise within a regional-scale dextral shear system between the Denali and Tintina faults. New geomorphic, structural, and apatite fission-track data collected in this thesis provide more information on the evolution of the northeast-striking faults in Interior Alaska throughout Cenozoic time, which has implications for the timing of dextral shear on the Denali and Tintina faults.

I have integrated the data analysis from this study with previous geochronological and geological studies of dextral movement along the Denali and Tintina faults and faults in the Yukon-Tanana uplands and the Fairbanks area. Data analyses support three time periods that represent separate phases of fault evolution within the Fairbanks area. These time periods include: 1) 93-90 Ma, 2) 56-20 Ma, and 3) 20 Ma-present. Alternatively, 6 Ma-present can be represented as the last phase of fault evolution.

5.4.1 Timing of Structural Events in the Fairbanks Area: ~93–90 Ma

Available evidence from the Ryan Lode and the Pogo gold deposit shows that a northeast-striking structural fabric developed in the Fairbanks area at ~93-90 Ma that was inherited by later structures (McCoy et al., 1997; Rhys et al., 2003; Avalon, 2014; Figure 2.3). However, the east- to northeast-striking left-lateral faults at Pogo differ in orientation from the north-northeast- to northeast-striking faults in the Fairbanks area.

Wallace and Ruppert (2012) created a schematic representation of northeast-striking faults in the Fairbanks area restored to their original strike. This reconstruction is approximately

to scale and uses the average fault spacing, measured orientations, and apparent horizontal displacements from Newberry and others (1996) (Figure 5.22a). The restored average strike direction is approximately N13°E. This suggests that, prior to dextral shear, faults that now strike northeast (~N40°E) were oriented ~N13°E, possibly as early as ~93 Ma. Regional plate motion vectors for the Farallon plate relative to southern Alaska for 100-85 Ma show a similar north-northeast direction (Wallace and Engebretson, 1984). Assuming that plate motion vectors corresponded with the regional maximum principal stress at the time, this is consistent with northwest to southeast extension as suggested by Rhys and others (2003) and the restored orientations of northeast-striking faults. Thus, it is possible that northeast-striking faults originated during a phase of low magnitude northwest-southeast extension. These faults probably did not form as normal faults because they are very linear, near vertical, and they do not display large amounts of dip-slip offset. Instead, their characteristics are more consistent with origin as vertical extension fractures that form at relatively low differential stress. Their lateral extent is too great for them to simply represent minor extension fractures, but they may represent later structures whose orientation was strongly controlled by the structural grain from existing extension fractures.

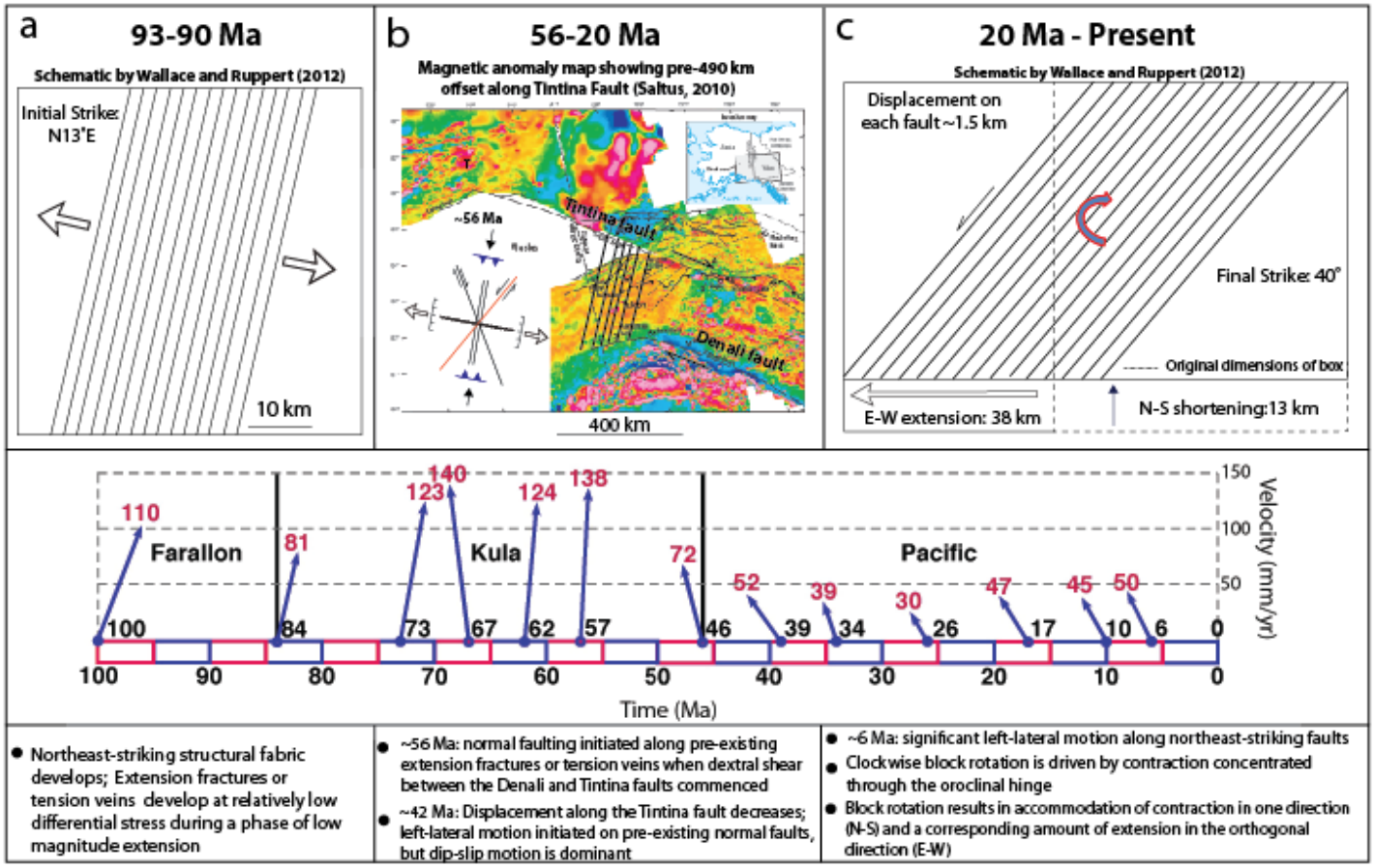

Figure 5.22: Diagram showing the structural evolution of northeast-striking faults. a) a schematic reconstruction showing the initial configuration of faults and how they may have originated, b) faults at their initial strike overlain on a magnetic anomaly map showing the Tintina fault before 490 km offset, which approximates the spatial position of faults at ~56 Ma; b also shows how faults moved by simple shear between Denali and Tintina faults between ~56 Ma and ~42 Ma, and c) a schematic model showing the final configuration of faults from ~20 Ma-present and how they are deforming presently. Faults in boxes a and c schematically represent faults from Newberry and others (1996) in the Fairbanks Mining District. Blue arrows represent plate vectors from Wallace and Engebretson (1984) and Doubrovine and Tarduno (2008) for the Farallon, Kula, and, Pacific plates.

5.4.2 Timing of Structural Events in the Fairbanks Area: ~56–20 Ma

Geological and geochronological studies along the Denali and Tintina faults suggest that significant dextral shear occurred between them at ~56-42 Ma. In addition, apatite fission-track data from this study support exhumation across the western Yukon-Tanana uplands between 45 and 20 Ma. The Nunivak #1 well in the Nenana basin records significant thickness of Late Paleocene sediments that accumulated at least to ~55 Ma. An unconformity above this package separates ~55 Ma sediments from ~24 Ma sediments, and renewed deposition began at ~24 Ma (Doyon, 2014). This suggests significant uplift and erosion of the Nenana basin between ~55 and ~24 Ma, however, it is unclear when uplift and erosion began. Fission-track data from this study and other studies (Naeser, 1979; Murphy and Bakke, 1993; Dusel-Bacon and Murphy, 2001) and well data discussed above (Doyon, 2014) support exhumation of the western Yukon-Tanana uplands and the Nenana basin between ~56 Ma and ~20 Ma. The orientation of the Kula-North America plate motion vector between ~57 and ~46 Ma parallels the orientation of northeast-striking faults at that time (Figure 5.22b). These orientations are favorable for extension along northeast-striking faults. It is likely that normal faulting initiated along pre-existing structures at ~56 Ma, when dextral shear between the Denali and Tintina faults commenced. Several northeast-striking faults that were examined in the Fairbanks area (e.g., the Birch Hill and Ryan Lode faults) exhibit a significant early normal component. In the case of the Birch Hill fault, which cuts ~55 Ma (Newberry et al., 1996) basalt, kinematic indicators indicate that normal fault motion occurred after the basalt formed. Then, normal fault motion was overprinted by left-lateral motion. Also, paleo-stress analyses and kinematic indicators suggest that the Ryan Lode

fault formed as a normal fault. Significant normal motion along northeast-striking faults could account for the exhumation recorded in the apatite fission-track well data mentioned previously.

Evidence including early, significant normal motion along northeast-striking faults (this study), exhumation (Dusel-Bacon and Murphy, 2001; this study), and basaltic volcanism (Roe and Stone, 1993; Newberry et al., 1996) suggests extension-related normal faulting at ~56 Ma. Basalts in the Fairbanks area are closely spaced in the eastern portion of the Fairbanks seismic zone and appear to be closely associated with northeast-striking left-lateral faults and west-northwest-striking normal faults.

Evidence suggests that motion along the Tintina fault slowed significantly at ~42 Ma. Around this time, the Pacific-North America plate motion vector, and thus presumably the maximum compressive stress, was oblique to the orientation of northeast-striking faults at their original strike of N13°E. This is a favorable orientation to develop left-lateral strike-slip motion (Figure 5.22b). This suggests that at ~42 Ma, northeast-striking faults developed a minor left-lateral strike-slip component, facilitating minor clockwise block rotation. However, since the Tintina fault was significantly less active than the Denali fault after 42 Ma, it may have served as a passive backstop rather than an active thoroughgoing strike-slip fault after 42 Ma (Haeussler, 2008). This would imply that any left-lateral faulting and clockwise block rotation after 42 Ma was driven by northward directed contraction resulting from northwestward plate convergence in southern Alaska rather than simple shear between master strike-slip faults. Left-lateral fault motion and consequent block rotation resulted in north-south shortening.

Apatite fission-track data indicate that periods of exhumation continued after 42 Ma until ~20 Ma in the western Yukon-Tanana uplands, with the exception of sample 1338-17, which yielded a pooled age of ~8 Ma (Naeser, 1979; this study). It is possible that exhumation in this time period continued as a result of dip-slip faulting along northeast-striking faults, which could occur as the maximum compressive stress (corresponding with the Pacific-North American plate motion vector; Figure 5.21b) rotated from north-northeast to north-northwest with respect to the strain field. If exhumation was related to vertical movement along northeast-striking faults, dip-slip motion was likely the dominant motion and left-lateral strike-slip motion was minor along northeast-striking faults until ~20 Ma (as indicated by apatite fission-track data that shows that the majority of samples were out of the PAZ by ~20 Ma).

5.4.3 Timing of Structural Events in the Fairbanks Area: ~20 Ma- Present

In this model, from ~20 Ma to present was a time when the rate of left-lateral strike-slip motion increased relative to the component of dip-slip. A possible reason that the left-lateral component of slip increased along northeast-striking faults at ~20 Ma may be that faults were in the most appropriate orientation with respect to the maximum compressive stress to develop a stronger strike-slip component (Figure 5.22c). However, the Nunivak #1 well in the Nenana basin records an increased subsidence rate with deposition of the Nenana Gravel beginning at ~6 Ma (Doyon, 2014; Nilesh Dixit, personal communication). Also, apatite fission-track data record cooling along the Minto fault footwall between ~10 and ~7 Ma (sample 1338-17; Figure 5.16) and renewed heating at ~6 Ma in the Nunivak #1 well (sample 1338-19; Figure 5.15). These data suggest an increase in subsidence in the Nenana basin, and thus significant vertical motion along the Minto fault in at least the last ~10-6 Ma. Pliocene-Pleistocene drainage restorations that I

have proposed, high levels of background seismicity, and the strong dominance of left-lateral focal mechanisms in the Fairbanks area suggest that left-lateral strike-slip motion is the dominant contemporary (<6 Ma) style of deformation.

5.4.4 Alternative Interpretation

Based on plate vectors and fault restorations, northeast-striking faults could have been in a favorable position to develop a left-lateral strike-slip component as early as ~42 Ma, but no direct evidence exists to determine the magnitude of strike-slip motion between ~42-6 Ma. Apatite fission-track data is only useful for defining the timing of exhumation, which may correspond to the vertical motion along faults. Based on the evidence presented above, the time interval of exhumation was between ~56-20 Ma.

An alternative interpretation could be that little to no left-lateral strike-slip motion developed along northeast-striking faults between ~42-20 Ma, and exhumation in that time interval was driven by dip-slip motion (Figure 5.23). Instead, significant left-lateral motion occurred along northeast-striking faults only during the last ~6 Ma, based on my proposed restorations of several Pliocene-Pleistocene drainages in the Fairbanks area (Figure 5.8).

I prefer the alternative interpretation that significant left-lateral motion has occurred along northeast striking faults during the last ~6 Ma because it can account for the numerous and recent drainage anomalies that occur in the Fairbanks area and the lack of direct evidence for left-lateral strike-slip motion along northeast striking faults between ~42-20 Ma. The original interpretation suggests that left-lateral strike-slip motion occurred as early as ~42 Ma, which implies that strike-slip motion occurred over a long period of time. This would negate the

drainage restorations because it is unlikely that the topography upon which the restorations are based would survive for 10 My or more, especially during the more rapid exhumation at ~42-20 Ma.

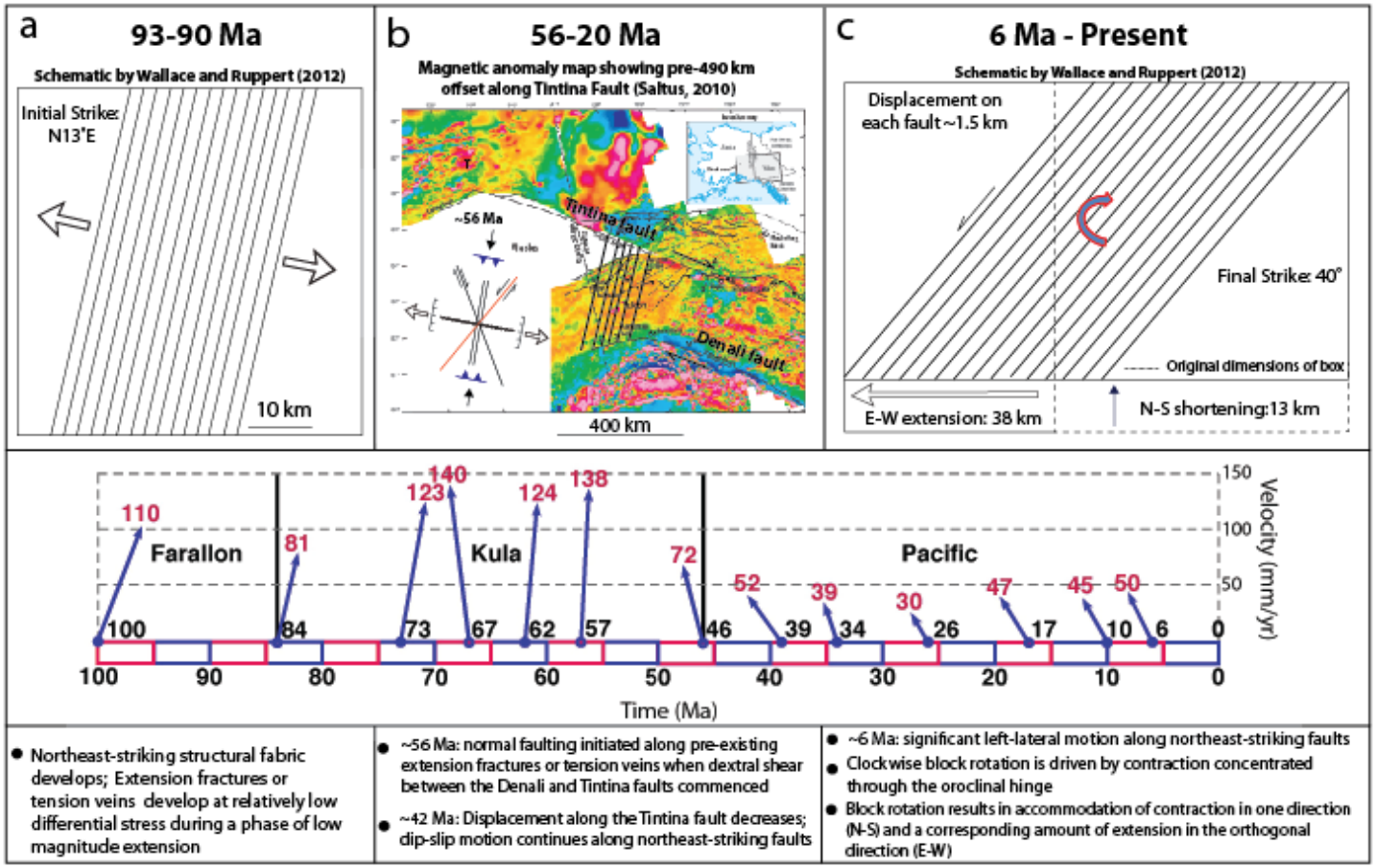

Figure 5.23: Diagram showing the alternative interpretation for the structural evolution of northeast-striking faults. a) a schematic reconstruction showing the initial configuration of faults and how they may have originated, b) faults at their initial strike overlain on a magnetic anomaly map showing the Tintina fault before 490 km offset, which approximates the spatial position of faults between ~56 Ma; b also shows how faults moved by simple shear between Denali and Tintina faults at ~56 Ma and ~42 Ma, and c) a schematic model showing the final configuration of faults from ~6-present and how they are deforming presently. Blue arrows represent plate vectors from Wallace and Engebretson (1984) and Doubrovine and Tarduno (2008).

5.4.5 Kinematics

Page and others (1995) originally proposed right-lateral simple shear between the Denali and Tintina faults as the mechanism to explain clockwise block rotation in Interior Alaska (Figure 5.24). However, several lines of evidence are not consistent with this model. These lines of evidence include: 1) stress tensors calculated from earthquakes in the Fairbanks and Salcha seismic zones show the maximum compressive stress (Sigma 1) oriented north-south (Ruppert, 2008; Figure 5.25); 2) seismicity is concentrated north of the Alaska Range Northern Foothills Fold and Thrust Belt, within the oroclinal hinge, and is largely absent to the east and west; 3) linear zones of seismicity that indicate active faults are discontinuous to the north toward the Tintina fault and to the south where they truncate at the Northern Foothills Fold and Thrust Belt north of the Denali fault; and 4) Evidence for young displacement on the Tintina fault is limited to an area north of the seismic zones.

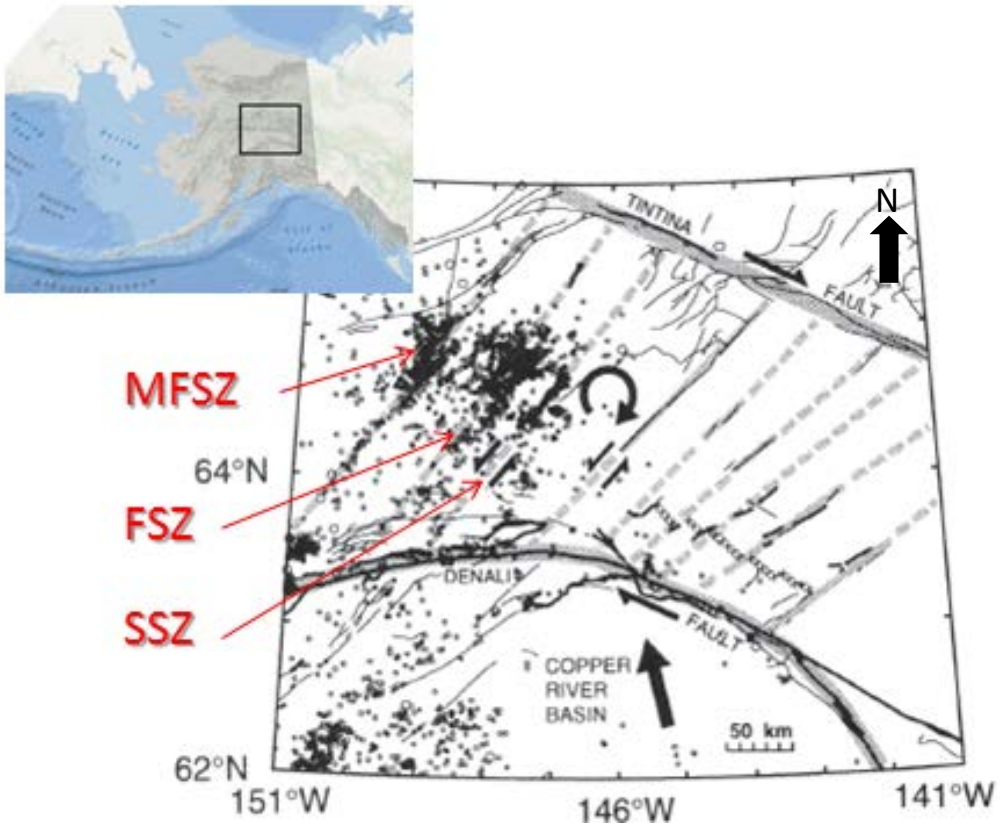

Figure 5.24: Clockwise block rotation model after Page and others (1995). MFSZ, Minto Flats seismic zone; FSZ, Fairbanks seismic zone; SSZ, Salcha seismic zone.

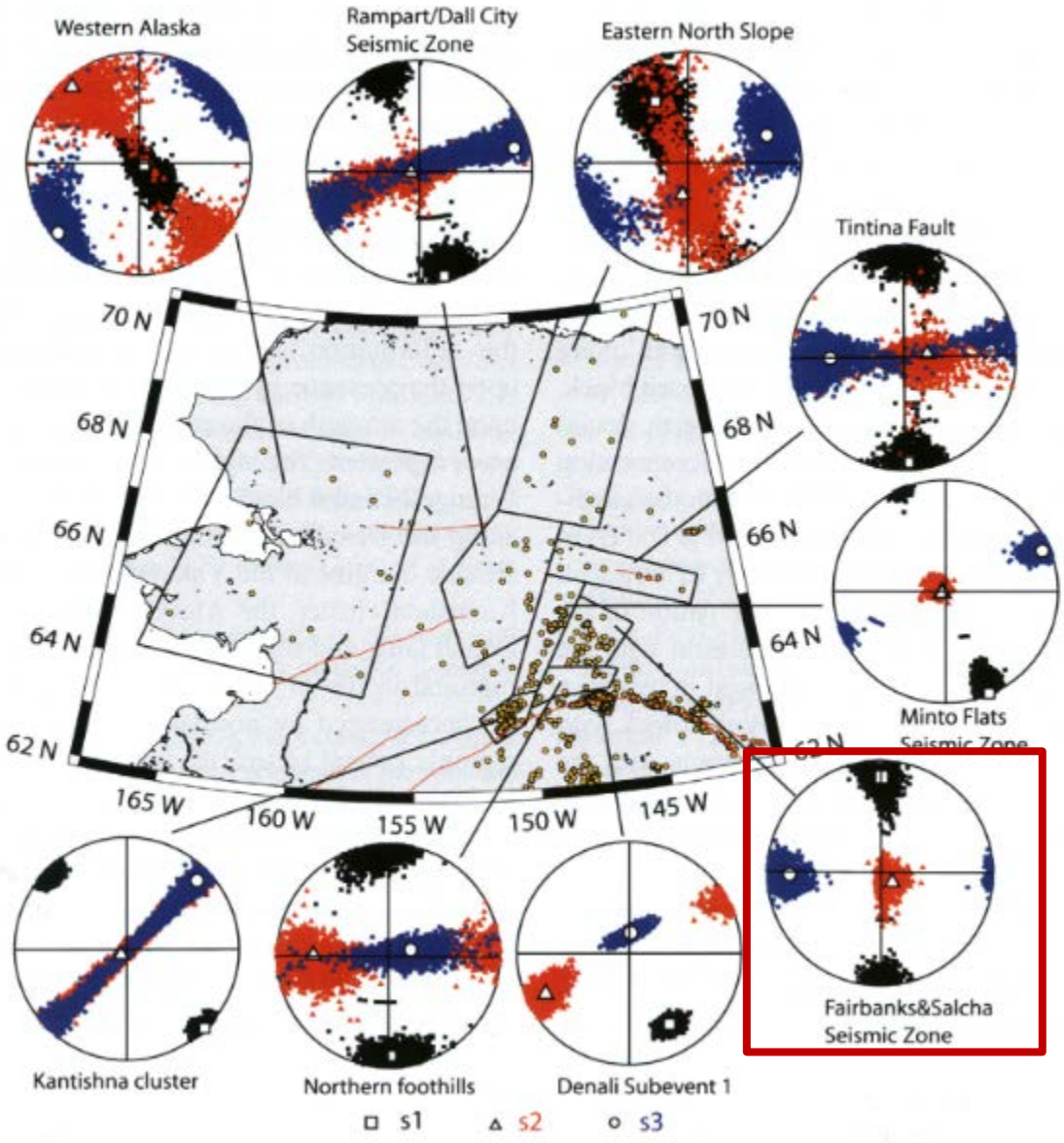

Figure 5.25: Map of stress tensors calculated from earthquakes in Interior Alaska. Stress tensors from the Fairbanks and Salcha seismic zones show the maximum compressive stress (Sigma 1) oriented north-south (Ruppert, 2008).

The simple shear model of Page and others (1995) calls for horizontal simple shear between the Denali and Tintina faults. However, one would expect the maximum compressive stress from stress tensors for the Fairbanks and Salcha seismic zones to be oriented more

northwest-southeast rather than north-south relative to the orientations of the Denali and Tintina faults to develop left-lateral strike-slip faults (Figure 5.25). Also, one would expect the seismic zones to be continuous to the north and south to the Denali and Tintina faults, and that northeast-striking faults east of the oroclinal hinge would be active (Figure 5.25). Seismicity does not indicate activity to the east of the oroclinal hinge or that northeast-striking faults are continuous to either the Denali or the Tintina faults.

Instead, it is more likely that left-lateral motion and block rotation is driven by contraction that is concentrated in the oroclinal hinge. Contraction is concentrated in and along the oroclinal hinge, where it acts as an indenter as the oroclinal hinge tightens and is pushed northward (W.K. Wallace, personal communication; Figure 5.26). This mechanism explains the spatial distribution of seismicity in Interior Alaska and the stress tensors that show Sigma 1 oriented north-south. This also explains the distribution of structures within the Northern Foothills Fold and Thrust belt, which are contractional structures oriented approximately east-west and localized within the oroclinal hinge (Figure 5.26).

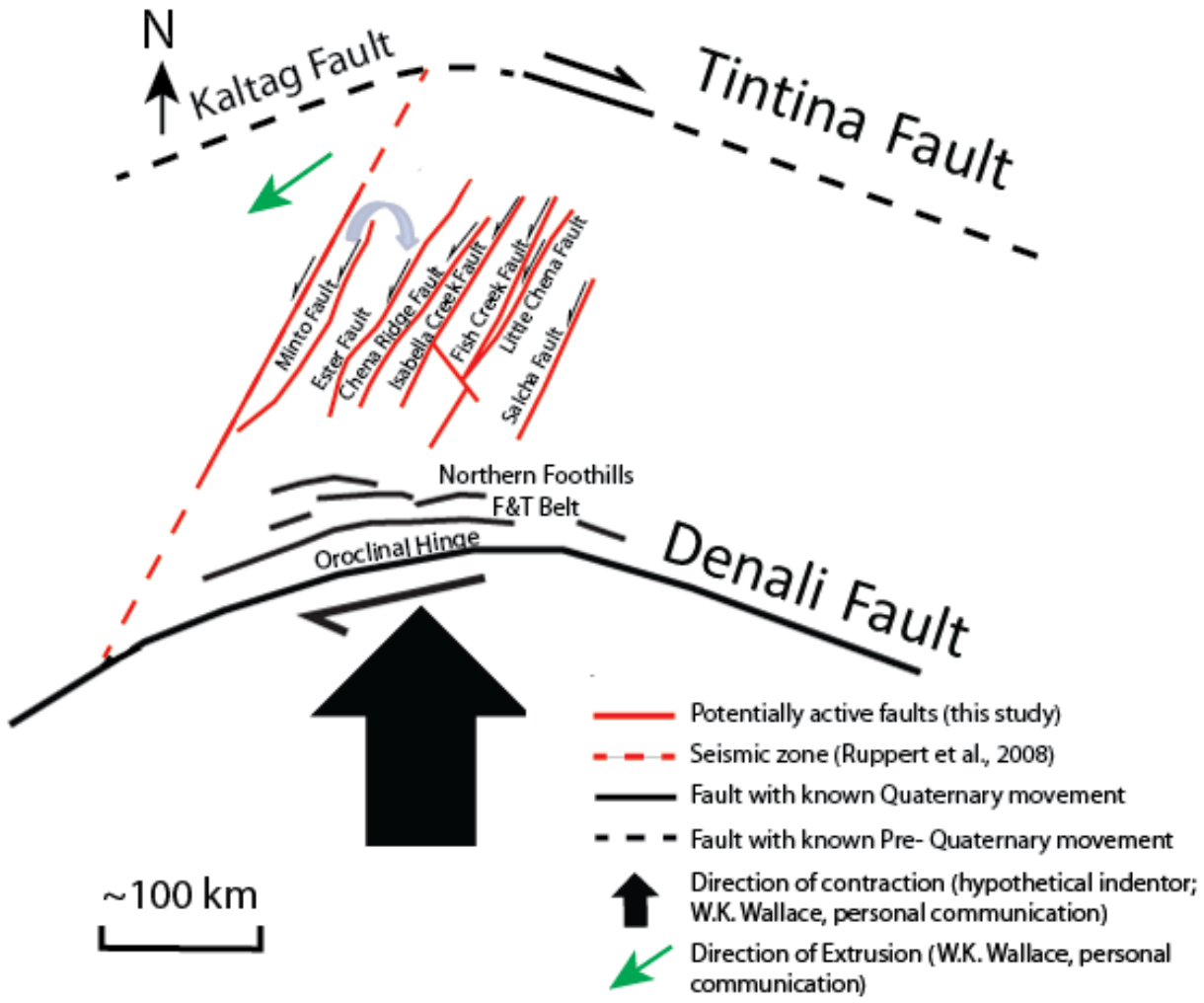

Figure 5.26: Conceptual model of clockwise block rotation driven by contraction directed through the oroclinal hinge. Contraction is concentrated in and along the oroclinal hinge, where it acts as an indentor as the oroclinal hinge tightens and is pushed northward (W.K. Wallace, personal communication).

Figure 5.23c shows a schematic model (Wallace and Ruppert, 2012), of northeast-striking left-lateral faults in their current orientation of N40°E. This schematic model represents how clockwise block rotation results in accommodation of contraction in the north-south direction and a corresponding amount of extension in the orthogonal direction (east-west). The change in

the north-south dimension from the original configuration of faults (N13°E; represented by dashed outline of box) approximates the shortening and the change in the east-west dimension from the original configuration approximates the extension. This implies 27° of clockwise rotation of faults since ~42 Ma from their initial orientation of N13°E. Wallace and Ruppert (2012) also estimated that these faults have accommodated approximately 13 km of north-south shortening and 38 km of extension to the west since their initial formation. This model essentially represents a pure shear strain model in which no change in surface area results because no thrust or normal component is required. However, the strain is accommodated in detail by a single sense of simple shear distributed throughout the area; thus, strain is asymmetrical. This asymmetry of strain creates a space problem with respect to the triangular bounding blocks in the northwest and southeast corners of the box (W.K. Wallace, personal communication; Figure 5.23c).

The Minto fault is clearly atypical of the left-lateral faults in interior Alaska as it forms the eastern boundary of the anomalously deep (7.6 km) Nenana basin. In this model, the Minto fault is on the west edge of the hypothetical indentor, where the northeast side of the Minto block may be accommodating subsidence and extrusion to the southwest between the Minto fault and the westward continuation of the Tintina fault to the Kaltag right-lateral bounding fault (Figure 5.26; W.K. Wallace, personal communication). This may solve the problem with strain asymmetry in the northwest corner of the box and may also explain the period of renewed subsidence in the Nenana basin starting at ~24 Ma and the later increase in subsidence at ~6 Ma (Doyon, 2014; this study; Nilesh Dixit, personal communication). However, evidence for recent

movement along the presumed connection between the Tintina and Kaltag faults is not well documented aside from some shallow seismicity.

Changes in dip-slip motion over time, from normal to reverse, were documented from kinematic indicators on the Ryan Lode fault. Also, the Minto fault exhibits rotational style faulting, as indicated by geomorphology and the possible change from normal in the Nenana basin to reverse in the Kantishna Hills to the southwest. Changes in dip-slip along strike and over time in a single area on a given fault are common on strike-slip faults (Cheon et al., 2012) and can be attributed to several possibilities. These include the orientation of the faults with respect to the paleo-stress field and changes as faults rotate with respect to the strain field. However, changes in dip-slip along strike are not required if strike-slip movement accommodates all of the strain.

Clockwise block rotation with varying strike-slip and dip-slip motion on subsidiary faults similar to that proposed in this model has been well documented locally and regionally within many major strike-slip shear systems. These include the Ocheon fault system in South Korea (Cheon et al., 2012), the Tibetan Plateau in central Asia (Wang et al., 2014), and the San Andreas fault system in southern California (Hornafius, 2002). A regional dextral shear zone within the Ocheon fault system in South Korea contains subsidiary faults that were initially normal and then changed to left-lateral-normal as dextral shear progressed. This was attributed to changes in the strain field as blocks rotated along many subsidiary faults (Cheon et al., 2012). The southeast margin of the Tibetan Plateau is currently deforming as a result of southeastward extrusion of a large crustal block (the Chuandian fragment) that is rotating clockwise around the northeastern syntaxis of the Himalayas (Wang et al., 2014). Block rotation has also been noted

along the San Andreas fault in southern California, where the Transverse Ranges represent the western boundary of a series of rotated blocks and the Mojave Desert dextral shear zone represents the eastern boundary (Hornafius, 2002).

Chapter 6: Conclusions and Recommendations

6.1 Conclusions

Geomorphology and seismicity suggest that moderate tectonic activity may exist throughout the Fairbanks area. Geomorphic anomalies such as valley and basin asymmetry, pronounced linearity of drainages, barbed drainages, incised valleys, and changes in river morphology suggest relatively recent tectonic activity on a variety of structures. Stratigraphic relationships documented at the Cripple Creek Mine, east of the Steese Highway along the Isabella Creek fault, and at the Birch Hill fault provide direct evidence of Pliocene and possibly later tectonic activity.

Seismic, structural, and geomorphic analyses indicate that faults in the eastern Fairbanks and Salcha seismic zones exhibit dominantly strike-slip characteristics. Left-lateral strike-slip fault restorations for the Chena Ridge and Ester faults, based on restorable geomorphic features and stream capture events presumably related to the deposition of ~6 Ma placer deposits, suggest left-lateral displacements up to 8 km since ~6 Ma. This suggests that significant left-lateral motion has occurred within the last ~6 Ma.

In the western Fairbanks and Minto Flats seismic zones and the Nenana basin, tilted fault block geometries suggest a larger normal component of dip slip. This is supported by analysis of bedrock exposures of northeast-striking faults in and around the Fairbanks area. This analysis suggests that significant normal motion occurred on many of these faults, followed by left-lateral strike-slip motion along them. The Ryan Lode fault and the faults at Cripple Creek mine showed evidence of reverse motion. Changes in dip-slip motion along strike and over time are common

along strike-slip faults and can be attributed to changes in the strain field as faults rotate clockwise.

The structural model presented in this thesis provides a mid-Cretaceous to Cenozoic tectonic framework for the Fairbanks area and accounts for the evolution of northeast-striking faults over time. The data show that potentially active northeast-striking faults may have developed during a time of low magnitude, northwest-southeast directed extension at ~93-90 Ma when extension fractures, veins, and dikes formed throughout the region. Major dextral shearing between the Denali and Tintina faults between ~56 and ~42 Ma resulted in normal motion along faults that formed parallel to pre-existing extension fractures oriented orthogonal to the direction of convergence. Evidence suggests that the Tintina fault significantly slowed at ~42 Ma, but contraction from northward-directed plate convergence progressed, resulting in continued motion on the northeast-striking faults in the Fairbanks area. This is supported by apatite fission-track data that are consistent with exhumation resulting from inferred dip-slip motion along northeast-striking faults between ~42 and 20 Ma.

Since ~6 Ma, left-lateral strike-slip faulting and consequent clockwise block rotation has been driven by north-directed contraction distributed through the oroclinal hinge. The change in character of motion from dominantly strike-slip in the eastern Fairbanks area to dip-slip in the western Fairbanks and Minto areas may be a product of contraction transmitted through the oroclinal hinge, allowing for accommodation of extension to the west.

Results of this research provide additional constraints on seismic hazards in the Fairbanks area, the evolution of petroleum systems in the Nenana basin, and the evolution of gold placer deposits within the Fairbanks Mining District.

6.2 Recommendations

More information on timing and rates of deformation are needed for more accurate definition of Neogene tectonic activity along faults and seismic hazard assessment. The best access to a fault exposure would be through a mining pit along a fault valley, in which trenching studies could be conducted. Ideally, the trenches would contain an abundance of datable material and stratigraphic or structural features that could be used to measure amount, direction, and shear-sense of displacement. A swampy or ponded area may contain organic matter in the younger strata that could be carbon-dated. Another preferable spot to excavate trenches might be along the 20 km series of escarpments of the Minto fault as mapped by Péwé and others (1966). This fault scarp is located west of Fairbanks and north of Nenana on the western border of the Yukon-Tanana uplands.

A more indirect way of determining rates of deformation may be radiocarbon dating of loess deposits along terrace steps in the lower Goldstream valley. This could define the rate of incision, which may be used to determine the rate of uplift along the Minto fault. Rates of ground tilt may also be determined by sampling and measuring asymmetrical terraces along the lower Goldstream valley.

Gravel exposures should be investigated along Goldstream, Little Goldstream, Cripple, and upper Bonanza Creeks to validate the drainage restorations that I have presented.

Paleocurrent indicators should be documented to test for evidence of drainage reversals and sediment samples should be taken to determine the geologic provenance. Gravel exposures are uncommon in the Fairbanks area, but can be accessed where there is mining or construction activity.

Depth to bedrock maps should be compiled for different levels of surficial deposits to determine anomalous or sudden changes in depth and thickness, and should be concentrated where I have interpreted seismically active faults. This would require obtaining water well logs and placer mining data from local mining companies.

Further documentation of faults in active mines and quarries is needed, as abandoned mines have often sustained substantial loss of surficial deposits and thus opportunity to find good fault exposures in Neogene strata. The Cripple Creek mine and Brown's Hill quarry should be revisited to record as much evidence as possible for recent deformation and kinematics. Records may be available for both the Cripple Creek mine and Brown's Hill quarry and it is possible that these records could be used in conjunction with information that I have presented to perform a reconstruction of fault offsets or document locations and orientations of faults that have since had their exposures destroyed.

References

AEIC, 2011. Alaska Earthquake Information Center, Geophysical Institute, University of Alaska Fairbanks: http://www.aeic.alaska.edu/ (accessed March 2014).

Athey, J.E., and Craw, P.A., 2004, Geologic maps of the Livengood SW C-3 and SE C-4 quadrangles, Tolovana mining district, Alaska: ADGGS PIR 2004-3, 24 p.

Anderson, E. M. 1951, The Dynamics of Faulting: Oliver & Boyd, 2nd ed., Edinburgh, 191 p.

Avalon Development Corporation Prospect Submittal Summary, 2014, Ryan Lode: 8 p.: http://www.avalonalaska.com/RL-2014-Summary1.pdf (accessed September 2014).

Bacon, C.R., Foster, H.L., and Smith, J.G., 1990, Rhyolitic calderas of the Yukon-Tanana terrane, east-central Alaska; Volcanic remnants of a mid-Cretaceous magmatic arc: Journal of Geophysical Research, v. 95, no. B13, p. 21, 451-21,461.

Bakke, A.A., 1995, The Fort Knox "porphyry" gold deposit—Structurally controlled stockwork and shear quartz vein, sulphide-poor mineralization, hosted by a Late Cretaceous pluton, east central Alaska, *in* Schroeter, T.G., ed., Porphyry deposits of the northwestern Cordillera of North America: Canadian Institute of Mining, Metallurgy and Petroleum Special Volume 46, p. 795–802.

Bakke, A.A., Morrell, B.G., Odden, J., Bergstrom, T., and Woodman, J., 2000, Kinross Gold USA's activities in the Fairbanks mining district, K2K, *in* Tucker, T.L., and Smith, M.T., eds., The Tintina gold belt—Concepts, exploration, and discoveries: British Columbia and Yukon Chamber of Mines, Special Volume 2, p. 89–98.

Bemis, S.P., and Wallace, W.K., 2007, Neotectonic framework of the north-central Alaska Range foothills, *in* Ridgway, K.D., Trop, J.M., Glen, J.M.G., and O'Neill, J.M., eds., Tectonic growth of a collisional continental margin: Crustal evolution of southern Alaska: Geological Society of America Special Paper 431, p. 549-572.

Bemis, S.P., Carver, G.A., and Koehler, R.D., 2012, The Quaternary thrust system of the northern Alaska Range: Geosphere, v. 8, no. 1, p. 196–205, 6 figures, 1 table, doi: 10.1130/GES00695.1.

Benowitz, J., Vansant, G., Roeske, S., Layer, P.W., Hults, C., and O'Sullivan, P.B., 2012, Eocene to present slip rate history of the eastern Denali Fault System: American Geophysical Union, Abstracts, T11A-2547, 1 p.

Boswell, J.C., 1979, History of Alaskan operations of United States Smelting, Refining & Mining Company, University of Alaska Fairbanks, Mineral Industries: Research Laboratory report, 126 p.

Bramhall, E. H., 1938, The central Alaska earthquake of July 22, 1937: Bulletin of the Seismological Society of America, v. 28, p. 71 – 75.

Brogan, G. E., Cluff, L. S., Korringa, M. K., and Slemmons, D. B., 1975, Active faults of Alaska: Tectonophysics, v. 29, p. 73 – 85.

Bull, W.B. and McFadden, L.D, 1977, Tectonic geomorphology north and south of Garlock fault, California, *in* Doehring, D.O, ed., Geomorphology in Arid Regions: Binghamton State University, N.Y., p. 115-138.

Burbank, D.W., Anderson, R.S., 2001. Tectonic Geomorphology: Blackwell Scientific, Oxford. 270 p.

Burns, L.E., Fugro Airborne Surveys Corp., and Stevens Exploration Management Corp., 2004, Total magnetic field of the Fairbanks Mining District, Interior Alaska: Alaska Division of Geological & Geophysical Surveys Geophysical Report 2004-1-1A, 2 sheets, scale 1:63,360.

Cox, R.T., 1994, Analysis of drainage-basin symmetry as a rapid technique to identify areas of possible Quaternary tilt-block tectonics: An example from the Mississippi Embayment: Geological Society of America Bulletin 106, p. 571-581.

Donelick, R. A., O'Sullivan, P. B., and Ketcham, R. A., 2005, Apatite Fission-Track Analysis, *in* Reiners, P. W., and Ehlers, T. A., eds., Low-Temperature Thermochronology: Techniques, Interpretations, and Applications, p. 49-94.

Doubrovine, P.V., and Tarduno, J.A., 2008, A revised kinematic model for the relative motion between Pacific oceanic plates and North America since the Late Cretaceous: Journal of Geophysical Research: Solid Earth (1978–2012) v. 113, no. B12, 20 p.

Dusel-Bacon, C., and Murphy, J.M., 2001, Apatite fission-track evidence of widespread Eocene heating and exhumation in the Yukon-Tanana Upland, Interior Alaska: Canadian Journal of Earth Sciences, v. 38, no. 8, p. 1191-1204.

Doyon. Limited, 2014, Alaska onshore rift basins, Nenana and Yukon Flats, 1 p.: http://doyonoil.com/Content/pdfs/NenanaYukon_NenanaBasin.pdf (accessed March 2014).

Eberhart–Phillips, D., Haeussler, P.J., Freymueller, J.T., Frankel, A.D.,Rubin, C.M., Craw, P., Ratchkovski, N.A., Anderson, G., Carver, G.A., Crone, A.J., Dawson, T.E., Fletcher, H., Hansen, R., Harp, E.L., Harris, R.A., Hill, D.P., Hreinsdóttir, S., Jibson, R.W., Jones, L.M., Kayen, R., Keefer, D.K., Larsen, C.F., Moran, S.C., Personius, S.F., Plafker, G., Sherrod, B., Sieh, K., Sitar, N., and Wallace, W.K., 2003, The 2002 Denali fault earthquake, Alaska: A large-magnitude, slip partitioned event, Science 300, p1113-1118.

Evenchick, C.A., 1988, Stratigraphy, metamorphism, structure, and their tectonic implications in the Sifton and Deserters ranges, Cassiar and northern Rocky Mountains, northern British Columbia: Geological Survey of Canada, Bulletin 376, 90 p.

Fossen, 2010, Structural Geology, Ch. 9, kinematics and paleostress in the brittle regime: Cambridge University Press, p. 189-200.

Foster, H.L., Laird, J., Keith, T.C., Cushing, G.W., and Menzie, W.D., 1983, Preliminary geologic map of the Circle Quadrangle, Alaska: U.S. Geological Survey Open-File Report 83-170-A, 30 p., 1 sheet, scale 1:250,000.

Foster, H.L., and Keith, T.E.C., 1994, Geology of the Yukon-Tanana area of east-central Alaska, in Plafker, George, and Berg, H.C., The Geology of Alaska: Geological Society of America, p. 205-240.

Fletcher, H. J., 2002, Crustal deformation in Alaska measured using the global positioning system [Ph.D. thesis]: University of Alaska Fairbanks, 257 p.

Gabrielse, H., 1985, Major dextral transcurrent displacements along the northern Rocky Mountain Trench and related lineaments in north-central British Columbia: Geological Society of America Bulletin, v. 96, no. 1, p. 1–14.

Gabrielse, H., Murphy, D.C., and Mortensen, J.K., 2006, Cretaceous and Cenozoic dextral orogen-parallel displacements, magmatism, and paleogeography, north-central Canadian Cordillera, *in* Haggart, J.W., Enkin, R.J., and Monger, J.W.H., eds., Paleogeography of the North American Cordillera; Evidence for and against large-scale displacements: Geological Association of Canada Special Paper 46, p. 255–276.

Gedney, L., Shapiro, L., and VanWormer, D., 1972, Correlation of epicenters with mapped faults, east-central Alaska, 1968-1971: U.S. Geological Survey Open-File Report 72-128, 7 p., 1 sheet, scale 1:1,000,000.

Gedney, L., Estes, S., and Biswas, N.N., 1980, Earthquakes migration in the Fairbanks, Alaska seismic zone: Bulletin of Seismological Society of America, v. 70, p 223-241.

Gesch, D., Oimoen, M., Greenlee, S., Nelson, C., Steuck, M., and Tyler, D., 2002, The National Elevation Dataset: Photogrammetric Engineering and Remote Sensing, v. 68, no. 1, p. 5-11.

Gleadow, A. J., Duddy, I. R., Green, P. F., and Hegarty, K. A., 1986, Fission track lengths in the apatite annealing zone and the interpretation of mixed ages, .Earth and Planetary Science Letters 78, no. 2, p. 245-254.

Green, P.F., Duddy, I.R., Gleadow, A.J.W., Tingate, P.R., and Laslett, G.M., 1986, Thermal annealing of fission tracks in apatite: A qualitative description: Chem. Geol., v. 59, p. 237-253.

Hack, J.T., 1973, Stream-profile analysis and stream-gradient index: Journal Research U.S. Geological Survey, v. 1, no. 4, p. 421-429.

Hansen, V. L., and Dusel-Bacon, C., 1998, Structural and kinematic evolution of the Yukon-Tanana upland tectonites, east-central Alaska: A record of late Paleozoic to crustal assembly: Geological Society of America Bulletin, v. 110, p. 211–230.

Haeussler, P. J., Schwartz, D.P., Dawson, T.E., Stenner, H.D., Lienkamper, J.J., Sherrod, B.L., Cinti, F.R., Montone, P., Craw, P.A., Crone, A.J., and Personius, S.F., 2004, Surface rupture and slip distribution of the Denali and Totschunda faults, *in* the 3 November 2002 M79 earthquake, Alaska: Bulletin of the Seismological Society of America 94, v.6B, S23-S52.

Haeussler, P. J., 2008, An overview of the neotectonics of Interior Alaska: Far-field deformation from the Yakutat Microplate collision: Geophysical monograph 179, p. 83-108.

Hornafius, J.S., Luvendyk, B.P., Terres, R.R., and Kamerlind, M.J., Timing and extend of Neogene tectonic rotation in the western Transverse Ranges, California, 2002, *in* Structural geomorphology, petroleum and water resources of the northwestern Transverse Ranges, Santa Barbara and Ventura County California, Annual Field Trip Guidebook: South Coast Geological Society 30, p. 149-160.

Hubbard, T.D., Koehler, R.D., and Combellick, R.A., 2011, High-resolution LiDAR data for Alaska infrastructure corridors, in DGGS Staff, LiDAR Datasets of Alaska: Alaska Division of Geological & Geophysical Surveys Raw Data File 2011-3, 291 p.

Karl, S.M., Ager, T.A., Hanneman, and Teller, S.D., 1988, Tertiary gold-bearing gravel at Livengood, Alaska, *in* Galloway, J.P. and Hamilton, T.D., eds. Geological Studies in Alaska by the U.S. Geological Survey during 1987: U.S. Geol Sur Circular 1016, p. 61–63.

Keller, E.A., and N. Pinter. 2002. Active Tectonics, 2nd edition: Upper Saddle River, New Jersey, Prentice Hall, 362 p.

Ketcham, R., 2005, Forward and inverse modeling of low temperature thermochronometry data, *in* Reiners, P.W., and Ehlers, T.A., eds., Thermochronology: Reviews in Mineralogy and Geochemistry, v. 58, p. 275–314.

Ketcham, R.A., Donelick, R.A., and Carlson, W.D., 1999, Variability of apatite fission track annealing kinetics III: Extrapolation to geological time scales: American Mineralogist, v. 84, p. 1235-1255.

Koehler, R.D., 2013, Quaternary Faults and Folds (QFF): Alaska Division of Geological & Geophysical Surveys Digital Data Series 3 http://maps.dggs.alaska.gov/qff/. doi:10.14509/24956 (accessed October 2014).

Koehler, R.D., Farrell, Rebecca-Ellen, Burns, P.A.C., and Combellick, R.A., 2012, Quaternary faults and folds in Alaska: A digital database, in Koehler, R.D., Quaternary Faults and Folds (QFF): Alaska Division of Geological & Geophysical Surveys Miscellaneous Publication 141, 31 p., 1 sheet, scale 1:3,700,000. doi:10.14509/23944.

Koehler, R.D., Personius, S.F., Schwarz, D.P., Haeussler, P.J., and Seitz, G.G., 2011, A Paleoseismic study along the central Denali Fault, Chistochina Glacier area, south-central Alaska: Alaska Division of Geological & Geophysical Surveys Report of Investigation 2011-1, 17 p. doi:10.14509/22361.

Laslett, G.M., Green, P.F., Duddy, I.R., and Gleadow, A.J.W, 1987, Thermal annealing of fission tracks in apatite: 2. A quantitative analysis: Chem. Geol. (Isotope Geoscience Section) 65, p. 1–13.

Lesh, M. E., and Ridgway, K.D., 2007, Geomorphic evidence of active transpressional deformation in the Tanana foreland basin, south-central Alaska, *in* Ridgway, K.D., Trop, J.M., Glen, J.M.G., and O'Neill, J.M., eds., Tectonic growth of a collisional continental margin: Crustal evolution of southern Alaska: The Geological Society of America Special Paper 431: p. 573-593.

Matmon, A., Schwartz, D.P., Haeussler, P.J., Finkel, R., Lienkaemper, J.J.,Stenner, H.D., and Dawson, T.E., 2006, Denali Fault slip rates and Holocene-late Pleistocene kinematics of central Alaska: Geology, v. 34, p.645-648.

Mariaux, A. S., Sieh, K., Finkel, R.C., Rubin, C. M., Taylor, M. H., Meltzner, A. J., and Ryerson, F. J., 2009, Kinematic behavior of southern Alaska constrained by westward decreasing postglacial slip rates on the Denali Fault, Alaska: Journal of Geophysical Research 114, B03404, doi:10.1029/2007JB005053.

McCoy D, 2000, Mid-Cretaceous plutonic-related gold deposits of Interior Alaska: Metallogenesis, characteristics, gold-associative mineralogy and geochronology [PhD thesis]: University of Alaska Fairbanks, 177 p.

McCoy, D., Newberry, R.J., Layer, P., Dimarchi, J.J., Bakke, A., Masterman, J.S., and Minehane, D.L., 1997, Plutonic-related gold deposits of Interior Alaska, *in* Goldfarb, R.J., and Miller, L.D., eds., Mineral deposits of Alaska: Economic Geology Monograph 9, p. 191-241.

Metz, P.A., 1991, Metallogeny of the Fairbanks Mining District, Alaska and adjacent areas: University of Alaska Mineral Industry Research Laboratory Report No. 90, p. 58-63.

Meyer, J.F., Jr., Saltus, R.W., Barnes, D.F., and Morin, R.L., 1996, Bouguer gravity Map of Interior Alaska: U.S. Geological Survey Geophysical Investigations Map 1016, sheet 2, scale 1:500,000.

Moll-Stalcup, E.J., Brew, D.A., and Vallier, T.L., 1994, Latest Cretaceous and Cenozoic Magmatic rocks of Alaska, *in* The geology of Alaska, G. Plafker and Berg, H.C., eds., Geological Society of America, Boulder, Colo., The Geology of North America: vol. G-1, Plate 5, scale 1 : 2500000.

Murphy, J.M., and Bakke, A., 1993, Low-temperature thermal history of the Gilmore Dome area, Fairbanks Mining District, Alaska: Canadian Journal of Earth Sciences 30, p. 764–768.

Naeser, C.W., 1979, Fission-track dating and geologic annealing of fission tracks, in Lectures in isotope geology, Jäger, E., and Hunziker, J.C., eds.: Springer Publishing Co., Inc., New York, p. 154–169.

Naeser, C.W., 1976, Fission-track dating: U.S. Geological Survey Open-File Report, 76-190, 68 p.

National Research Council, 1986, Active Tectonics: Impact on Society: The National Academies Press, Washington D.C., 1986: p. 125-136.

Newberry, R.J., 2010, Lodes, placers, faults, gold, and how they tie together in the Livengood area, Friends of the Pleistocene guidebook, 10 p. http://www.uaf.edu/files/aqc/FOP2010_RL_lo.pdf (accessed October 2014).

Newberry, R.J., Bundtzen, T.K., Clautice, K.H., Combellick, R.A., Douglas, Tom, Laird, G.M., Liss, S.A., Pinney, D.S., Reifenstuhl, R.R., and Solie, D.N., 1996, Preliminary geologic Map of the Fairbanks Mining District, Alaska: Alaska Division of Geological & Geophysical Surveys Public Data File 96-16, 17 p., sheet 1, scale 1:63,360.

Nokleberg, W.J., Jones, D.L., and Silberling, N.J., 1985, Origin and tectonic evolution of the Maclaren and Wrangellia terranes, eastern Alaska Range, Alaska: Geological Society of America, Bulletin, v. 96, no. 10, p. 1251-1270.

Nokleberg, W.J., Plafker, G., and Wilson, F.H., 1994, Geology of south-central Alaska, *in* Plafker, G., and Berg, H.C., eds., The Geology of Alaska: Geological Society of America, p. 311-364.

Page, R. A., Biswas, N. N., Lahr, J. C., and Pulpan, H., 1991, Seismicity of continental Alaska, *in* Slemmons, D. B., Engdahl, E. R., Zoback, M. D., and Blackwell, D. D., eds., Neotectonics of North America: Boulder, Colorado, Geological Society of America, Decade Map Volume l.

Page, R. A., Plafker, George, and Pulpan, H., 1995, Block rotation in east-central Alaska: a framework for evaluating earthquake potential?: Geology, v. 23, no. 7, p. 629-632.

Patton, W.W., Jr., and Hoare, J.M., 1968, The Kaltag Fault, west-central Alaska, *in* U.S. Geological Survey, Geological survey research 1968, Chapter D: U.S. Geological Survey Professional Paper 600-D, p. D147-D153.

Péwé, T.L., 1975, Quaternary stratigraphic nomenclature in unglaciated central Alaska: U.S. Geological Survey Professional Paper 862, 32 p.

Péwé, T. L. and Reger, R. D., and Westgate, J.A., 1989, Front Matter, *in* Quaternary Geology and Permafrost Along the Richardson and Glen Highways Between Fairbanks and Anchorage, Alaska: Fairbanks to Anchorage, Alaska July 1-7, 1989: American Geophysical Union, p. 3-17.

Péwé, T.L., Wahrhaftig, Clyde, and Weber, F.R., 1966, Geologic Map of the Fairbanks quadrangle, Alaska: U.S. Geological Survey Miscellaneous Geologic Investigations Map 455, 5 p., Sheet 1, scale 1:250,000.

Péwé, T.L., Westgate, J.A., Preece, S.J., Brown, P.M., Leavitt, S.W., 2009, Late Pliocene Dawson Cut Forest Bed and new tephrochronological findings in the Gold Hill Loess, east-central Alaska: Geological Society of America Bulletin 121, p. 294–320.

Plafker, George, and Berg, H.C., 1994, Review of the geology and tectonic evolution of Alaska, *in* Plafker, George, and Berg, H.C., eds., The Geology of Alaska: Boulder, Colorado, Geological Society of America, The Geology of North America, v. G-1, p. 989–1,021.

Ratchkovski, N. A., and Hansen, R., 2002, New constraints on tectonics of Interior Alaska: earthquake locations, source mechanisms, and stress regime: Bulletin of the Seismological Society of America, v. 92, no. 3, p. 998-1014.

Rhys, D., DiMarchi, J., Smith, M., Friesen, R., and Rombach, C., 2003, Structural setting, style and timing of vein-hosted gold mineralization at the Pogo deposit, east central Alaska: Mineralium Deposita 38: p. 863-875.

Robinson, M.S., Smith, T.E., and Metz, P.A., 1990, Bedrock geology of the Fairbanks mining district, Alaska: Alaska Division of Geological & Geophysical Surveys, Professional Report 106, 2 sheets, 1:63,360.

Roe, J.T., and Stone, D.B., 1993, Paleomagnetism of the Fairbanks basalts, Interior Alaska, in Solie, D.N., and Tannian, F., eds., Short Notes on Alaskan Geology 1993: Alaska Division of Geological & Geophysical Surveys Professional Report 113G, p. 61-69. doi:10.14509/2311.

Ruppert, N.A., 2008, Stress map for Alaska from earthquake focal mechanisms, *in* Freymueller, J.T., Haeussler, P.J., Wesson, R., and Ekström, G., eds., Active Tectonics and Seismic Potential of Alaska: Washington, D.C., American Geophysical Union Geophysical Monograph Series 179, p. 351–367.

Ruppert, N.A., Ridgway, K.D., Freymueller, J.T., Cross, R.S., and Hansen, R.A., 2008, Active tectonics of Interior Alaska—Seismicity, GPS geodesy, and local geomorphology, *in* Freymueller, J.T., Haeussler, P.J., Wesson, R.L., and Ekström, G., eds., Active Tectonics and Seismic Potential of Alaska: Washington, D.C., American Geophysical Union, Geophysical Monograph 179, p. 109–133.

Saltus, R.W., 2010, Matching magnetic trends and patterns across the Tintina Fault, Alaska and Canada -- evidence for offset of about 490 kilometers, *in* Gough, L.P., and Day, W.C., eds., Recent U.S. Geological Survey studies in the Tintina Gold Province, Alaska, United States, and Yukon, Canada -- results of a 5 year project: U.S. Geological Survey Scientific Investigations Report 2007-5289-C, p. C1-C7.

Schwartz, D. P., Haeussler, P.J., Seitz, G.G., and Dawson, T.E., 2012, Why the 2002 Denali fault rupture propagated onto the Totschunda fault: Implications For Fault Branching and Seismic Hazards: Journal of Geophysical Research, v. 117, no. B11, p. 2156-2202, doi:10.1029/2011JB008918.

Sylvester, A.G., 1988, Strike-slip faults: Geological Society of America Bulletin 100: p.1666-1703.

Till, A.B., Bradley, D., Roeske, S.M., Layer, P., Semler, L., Farmer, E., Ridgway, K., and Reifenstuhl, R., 2003, Early Tertiary extensional zone linking the Tintina and Kaltag fault systems, central Alaska: Geological Society of America Abstracts with Programs, v. 35, no. 6, p. 474.

Till, A.B., O'Sullivan, P., Bradley, D., and Roeske, S., 2004, Apatite fission-track evidence for repeated Tertiary movement on the Tintina Fault system, Alaska: Geological Society of America Abstracts with Programs, v. 36, no. 5, p. 512.

Till, A.B., Roeske, S.M., Bradley, D.C., Friedman, R., and Layer, P.W., 2007, Early Tertiary transtension-related deformation and Magmatism along the Tintina Fault system, Alaska, *in* Till, A.B., Roeske, S.M., Sample, J.C., and Foster, D.A., eds., Exhumation Associated with Continental Strike-Slip Fault Systems: Geological Societyof America Special Paper 434, p. 233–264.

Van Kooten, Gerald K., Richter, M., Zippi, P.A., 2012, Alaska's Interior rift basins: A new frontier for discovery, Oil and Gas journal, 10 p. http://www.doyon.com/lands/oil_gas/DoyonNenanaOGJ.pdf (accessed April 2014).

Wahrhaftig, Clyde, Wolfe, J.A., Leopold, E.B., and Lanphere, M.A., 1969, The coal-bearing group in the Nenana coal field, Alaska: U.S. Geological Survey Bulletin 1274-D, p. D1-D30.

Wallace, W. K, and Engebretson, D. C., 1984, Relationships between plate motions and Late Cretaceous to Paleogene magnetism in southwestern Alaska: Tectonics, v. 3, no. 2, p. 295-315.

Wallace, W.K., and Ruppert, N., 2012, Young tectonics of a complex plate boundary zone: Indentation, rotation, and escape in Alaska: American Geophysical Union fall meeting, San Francisco, CA, Abstract T14A-08, 3 December, 2012.

Wang, E., Meng., K., Su, Z., Meng, Q., Chu, J.J., Chen, Z., Wang, G., Shi, X., Liang, X., 2014, Block rotation: Tectonic response of the Sichuan basin to the southeastward growth of the Tibetan plateau along the Xianshuihe-Xiaojiang fault: Tectonics, v. 33, no. 5, p. 686-718, doi: 10.1002/2013TC003337.

Weber, F.R., and Foster, H.L., 1982, Tertiary (?) conglomerate and Quaternary faulting in the circle quadrangle, Alaska, *in* Coonrad, W.L., ed., The U.S. Geological Survey in Alaska: Accomplishments during 1980: U.S. Geological Survey Circular 844, p. 58-60.

White, B., 2012, Gas pipeline builder plans precautions for spanning earthquake zones: http://www.arcticgas.gov/Gas-pipeline-builder-plans-precautions-for-spanning-earthquake-zones (accessed April 2012).

Wilson, F.H., Dover, J.H., Bradley, D.C., Weber, F.R., Bundtzen, T.K., and Haeussler, P.J., 1998, Geologic Map of Central (Interior) Alaska: U.S. Geological Survey Open-File Report 98-133-A, sheet 1, scale 1:500,000.

Appendix A

Longitudinal profiles of drainages around the Fairbanks area that may have been affected by recent tectonic activity. Locations of drainages are shown in Figure 5.5.

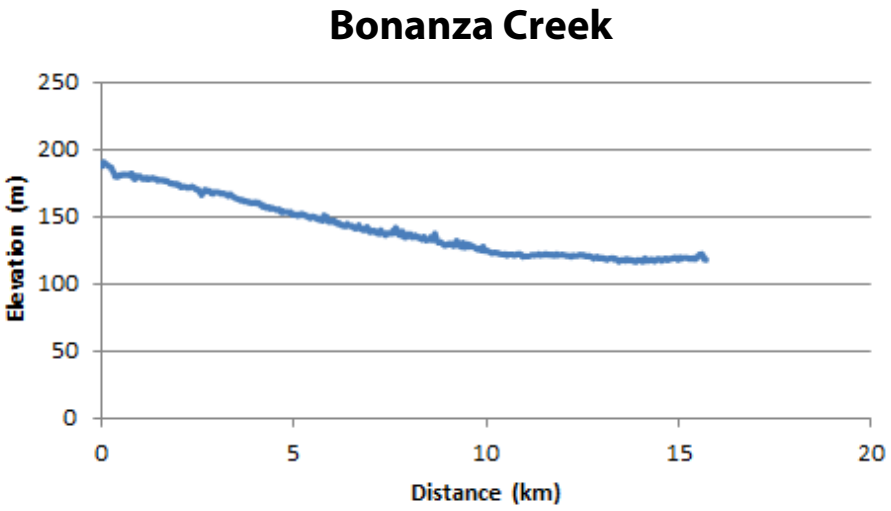

Figure A.1: Longitudinal profile of Bonanza Creek.

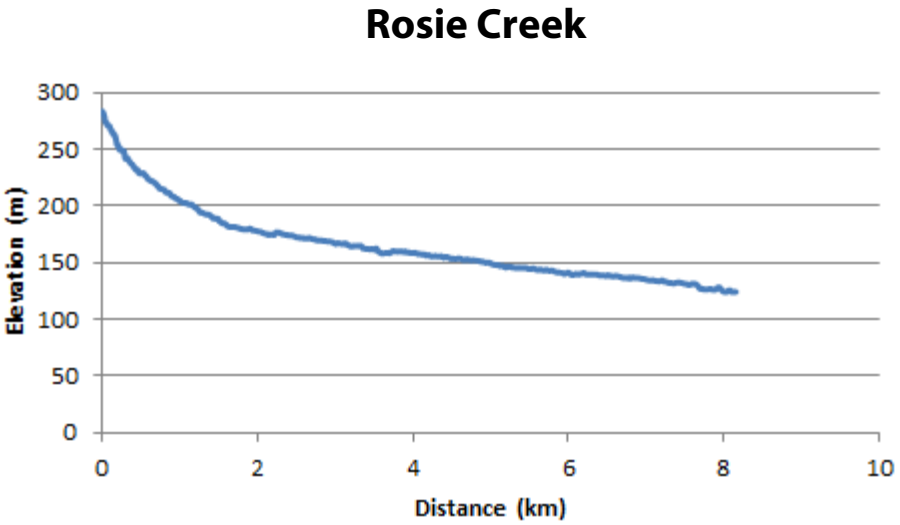

Figure A.2: Longitudinal profile of Rosie Creek.

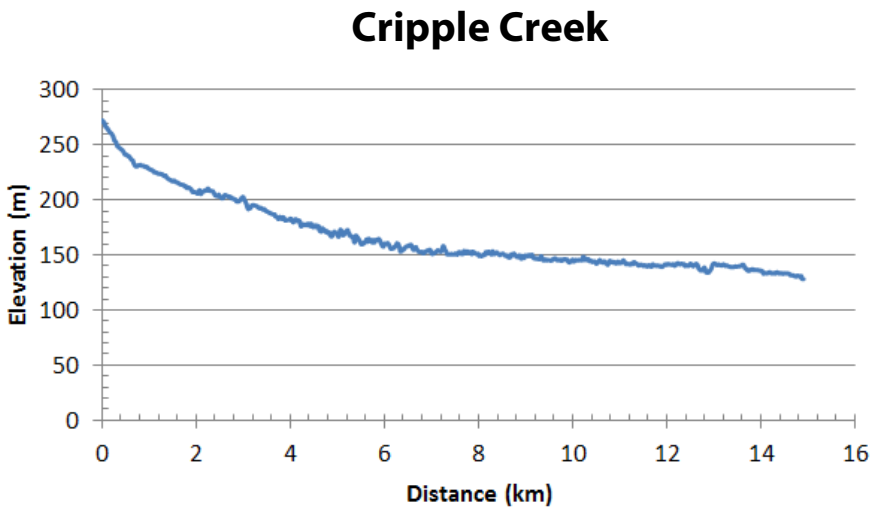

Figure A.3: Longitudinal profile of Cripple Creek.

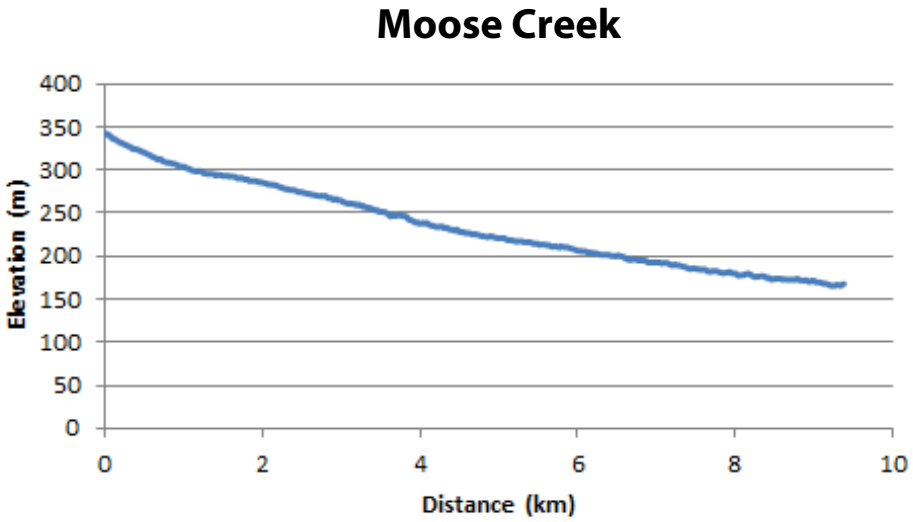

Figure A.4: Longitudinal profile of Moose Creek.

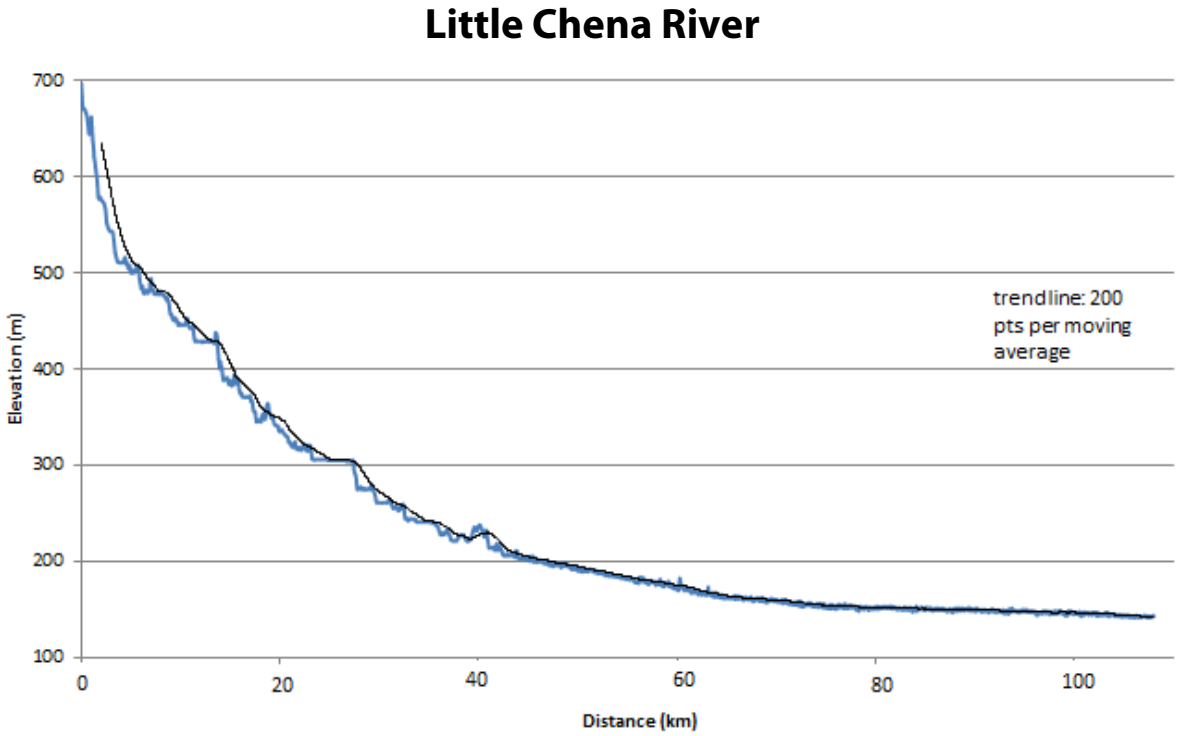

Figure A.5: Longitudinal profile of the Little Chena River.

Appendix B1

Table B1.1: Full apatite fission-track age data table

A2Z Sample Number	Total Spots	Accepted Spots	SumNs	SumRho	1sig SumRho	Dparm	Dperm	[U]m ppm
1338-01	40	15	9	1.94E-06	2.49E-07	1.797461	0.3519703	2.027829
1338-02	40	24	245	7.13E-05	9.79E-07	1.770088	0.3161471	15.05614
1338-03	40	16	36	8.02E-06	1.72E-07	1.710184	0.3242248	2.399709
1338-04	40	16	95	2.40E-05	3.55E-07	1.833736	0.3405561	6.093417
1338-05	40	32	491	1.11E-04	9.80E-07	1.8328	0.3287028	12.95625
1338-06	30	2	2	8.11E-09	3.43E-09	1.629064	0.3927105	2.23E-02
1338-07	40	34	388	7.91E-05	6.16E-07	1.945322	0.3589945	7.015243
1338-08	40	28	38	6.62E-06	3.57E-07	1.797366	0.3276868	2.460619
1338-09	40	34	30	2.91E-06	6.55E-08	1.755919	0.329493	0.3925543
1338-10	40	24	95	1.57E-05	2.75E-07	1.698883	0.2887211	3.21108
1338-12	10	6	52	1.65E-05	3.24E-07	1.858696	0.4376651	15.04095
1338-13	27	21	28	3.39E-06	1.30E-07	1.715592	0.3728422	0.7724602
1338-15	5	2	17	3.72E-06	8.65E-08	1.813768	0.346351	12.64715
1338-16	4	2	33	3.82E-06	1.27E-07	2.053384	0.304206	9.099619
1338-17	40	10	11	1.17E-05	2.42E-07	1.814766	0.3497226	11.81415
1338-18	40	33	604	1.20E-04	8.91E-06	1.906801	0.3340907	17.61617
1338-19	40	20	365	7.64E-05	1.19E-06	1.860194	0.3589945	27.24047

Table B1.1 continued

[Th]m ppm	[Sm]m ppm	wm pz:sz UCa	wm pz:unk Ca	relerr pz:sz	relerr analyst	relerr deficit	relerr Ca apfu	pZeta	1sig pZeta
6.784635	3.19807	1.304160171	1.01416884	2.31E-02	0	0	0	8.272661	0.1407127
39.43091	75.37334	1.244188383	1.006109348	2.31E-02	0	0.72	0	8.272661	0.1407127
8.520956	22.63258	1.204229333	1.012540692	2.31E-02	0	0.128	0	8.272661	0.1407127
15.01663	45.45553	1.151726417	1.011242859	2.31E-02	0	1	0	8.272661	0.1407127
25.92153	102.4715	1.246699393	1.011478639	0.0245884	0	0.788	0	8.272661	0.1407127
5.288417	2.076545	1.249995932	1.01669511	0.0245884	0	0	0	8.272661	0.1407127
0.9639627	37.84854	1.324236001	1.012449613	0.0245884	0	0.176	0	8.272661	0.1407127
8.283278	12.0934	1.233091177	1.008787618	0.0245884	0	1	0	8.272661	0.1407127
9.814652	6.120792	1.334693662	1.016671865	0.0245884	0	0	0	8.272661	0.1407127
13.48667	32.97418	1.183714054	1.008481235	0.0245884	0	0.777	0	8.272661	0.1407127
345.6703	55.85574	1.254506186	1.011884968	0.0245884	0	1	0	8.272661	0.1407127
9.782402	25.27566	1.206266614	1.008451179	0.0245884	0	1	0	8.272661	0.1407127
37.57368	71.13615	1.210502619	1.012610234	0.0245884	0	0.69	0	8.272661	0.1407127
33.55997	78.6563	1.25847287	1.007043073	0.0245884	0	0	0	8.272661	0.1407127
10.56138	33.35618	1.211957093	1.013379107	0.0245884	0	0	0	8.272661	0.1407127
22.82288	68.3143	1.226223542	1.00902647	0.0245884	0	0.542	0	8.272661	0.1407127
108.4657	66.73042	1.243920992	1.009269894	0.0245884	0	0.144	0	8.272661	0.1407127

Table B1.1 continued

Chi-squared	Q(chi-squared)	Pooled age	95%-CI	95%+CI
21.20565283	9.65E-02	38.17	19.47	39.62
77.2113599	8.93E-08	28.35	3.57	4.09
26.12400861	3.67E-02	37.04	10.60	14.83
144.5730777	2.87E-23	32.66	6.18	7.61
166.4458707	1.81E-20	36.51	3.40	3.75
0.373983074	0.540841117	1772.46	1391.61	4499.35
67.68243628	3.50E-04	40.47	4.14	4.61
113.8405929	1.24E-12	47.31	13.72	19.30
20.09189328	0.962178789	84.69	26.04	37.50
85.60319652	3.84E-09	49.89	9.46	11.66
118.4795632	6.59E-24	25.98	6.38	8.45
146.0283265	3.61E-21	67.96	21.74	31.88
17.49439657	2.88E-05	37.72	14.55	23.65
0.522745056	0.469673065	71.08	21.21	30.16
12.34357177	0.194625965	7.79	3.54	6.48
233.4218232	1.83E-32	41.40	6.54	7.76
45.53433064	5.77E-04	39.41	4.25	4.76

Appendix B2

Table B2.1: Full apatite fission-track length data table

A2Z Sample Number	Mean Track Length (µ)	Std. error(µ)	Std. dev (µ)	Skewness	Kurtosis	Number tracks	Dparm	Dperm	[U]m ppm
1338-01	14.019	0.3967639	1.729454	-1.922967	3.234397	20	1.955042	0.3269643	26.44195
1338-02	13.82936	0.1597402	1.401715	-0.4966946	0.03308604	78	2.205321	0.3435412	49.8991
1338-03	13.87938	0.2031492	1.612446	-0.6196573	0.1646336	64	2.211568	0.3713747	3.141016
1338-04	14.58058	0.1124437	1.31612	-1.129707	2.467256	138	2.396385	0.4392536	21.90827
1338-05	14.02395	0.1436366	1.765036	-0.9923282	1.005878	152	2.258121	0.3694753	12.70647
1338-06	14.58778	0.37429	1.058652	-0.0696	-1.295609	9	2.205917	0.4016078	0.00751
1338-07	14.42443	0.1196745	1.499517	-0.6456191	0.2592104	158	2.414577	0.4202383	5.559224
1338-08	14.88898	0.7756628	6.806414	7.852189	63.96723	78	2.143751	0.3437575	355.7634
1338-09	14.16375	0.2596543	1.005637	-0.5484411	0.0126	16	2.080216	0.3410828	0.3918141
1338-10	14.34	0.1248655	1.390443	-0.8682324	1.639022	125	2.151426	0.328077	963.326
1338-12	14.3565	0.3391249	1.478211	-0.0854	-0.7636189	20	2.293499	0.422212	4.487506
1338-13	15.1625	0.246094	1.072699	-0.3487809	0.1836165	20	2.154222	0.3518298	11.59308
1338-15	14.671	0.4192511	1.257753	-0.0339	-1.214869	10	2.255061	0.3834386	11.0569
1338-16	14.42412	0.174486	0.697944	0.0738	-1.01655	17	2.678559	0.5159227	17.14839
1338-17	14.27533	0.3012082	1.127018	-0.2051495	-1.353171	15	2.284014	0.3738858	76.21291
1338-18	14.28947	0.1031303	1.184877	-0.2790662	0.026	133	2.274119	0.407065	17.23803
1338-19	13.98286	0.2189265	1.516768	-0.5774722	1.752095	49	2.423302	0.4363175	29.26377

Table B2.1 continued

[Th]m ppm	[Sm]m ppm	Minimum (μ)	Minimum f_g_l	Maximum (μ)	Maximum f_g_l
52.00555	108.1795	8.36	2_15_1	15.53	2_5_1
101.7666	173.936	10.07	2_16_3	17.02	2_22_1
3.12555	15.58934	9.39	2_45_2	16.59	2_19_1
48.89079	69.549	9.22	2_41_1	17.04	2_11_1
23.24895	62.23502	7.51	2_33_3	16.96	2_34_3
0	0.6459912	12.88	2_8_1	16.06	2_2_2
0.5145558	28.03305	10.12	2_37_4	17.56	2_33_7
302.0833	108.7358	10.02	2_38_1	72.75	2_34_1
13.08716	9.965704	11.71	2_5_1	15.69	2_8_1
1054.629	64.91306	9.35	2_3_6	17.89	2_36_1
30.36927	97.73267	11.56	2_2_2	17.03	2_5_5
90.10054	69.62273	12.69	2_1_1	17.44	2_4_1
48.15685	83.53153	12.47	2_2_4	16.56	2_2_5
91.91812	134.6577	13.28	2_1_2	15.67	2_1_8
56.13451	124.4769	12.38	2_8_4	15.88	2_7_1
17.68624	76.50616	10.86	2_20_2	17.4	2_29_3
42.36256	55.65589	8.65	2_10_5	17.53	2_1_2

Appendix C

Additional HeFty models for each apatite fission-track sample. Locations of samples are shown in Figure 5.14.

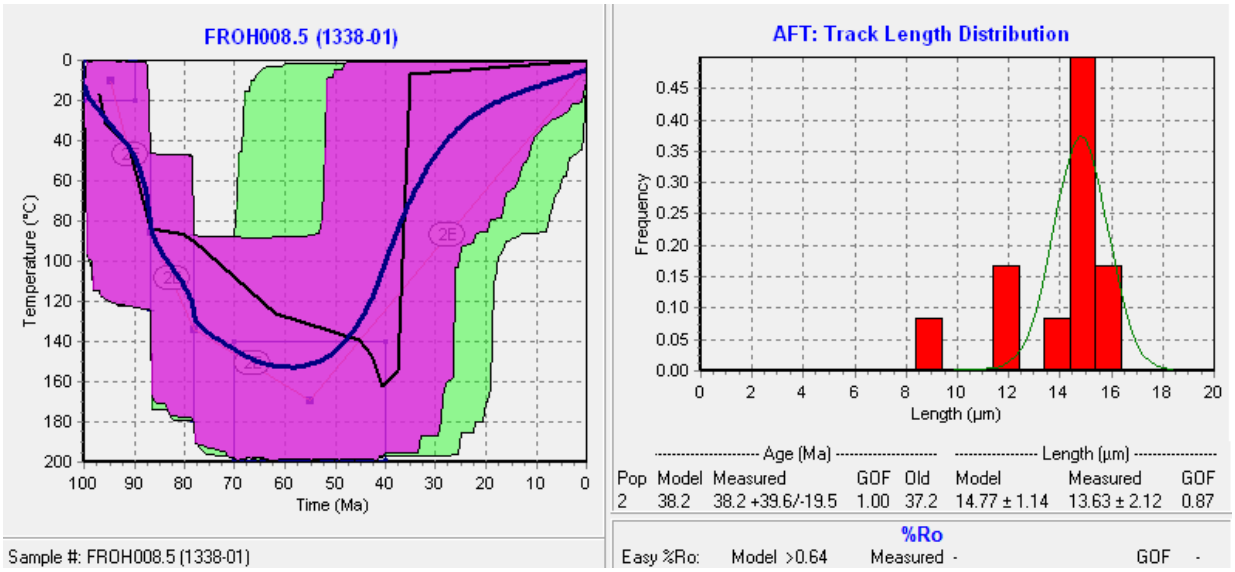

Figure C.1: Model 1 for apatite fission-track sample 1338-01.

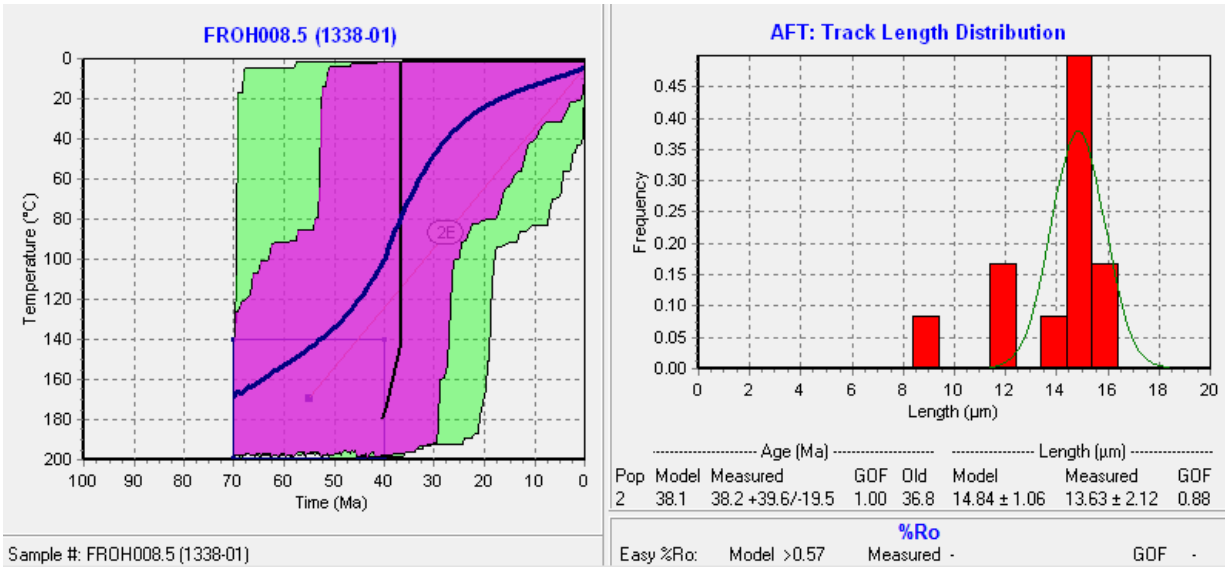

Figure C.2: Model 2 for apatite fission-track sample 1338-01.

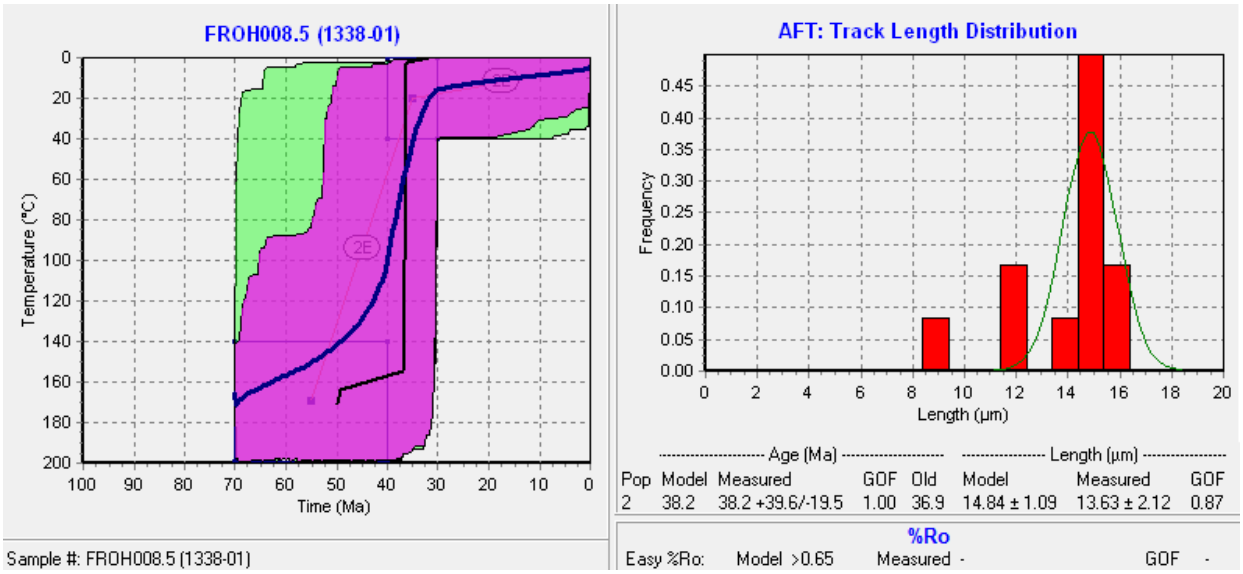

Figure C.3: Model 3 for apatite fission-track sample 1338-01.

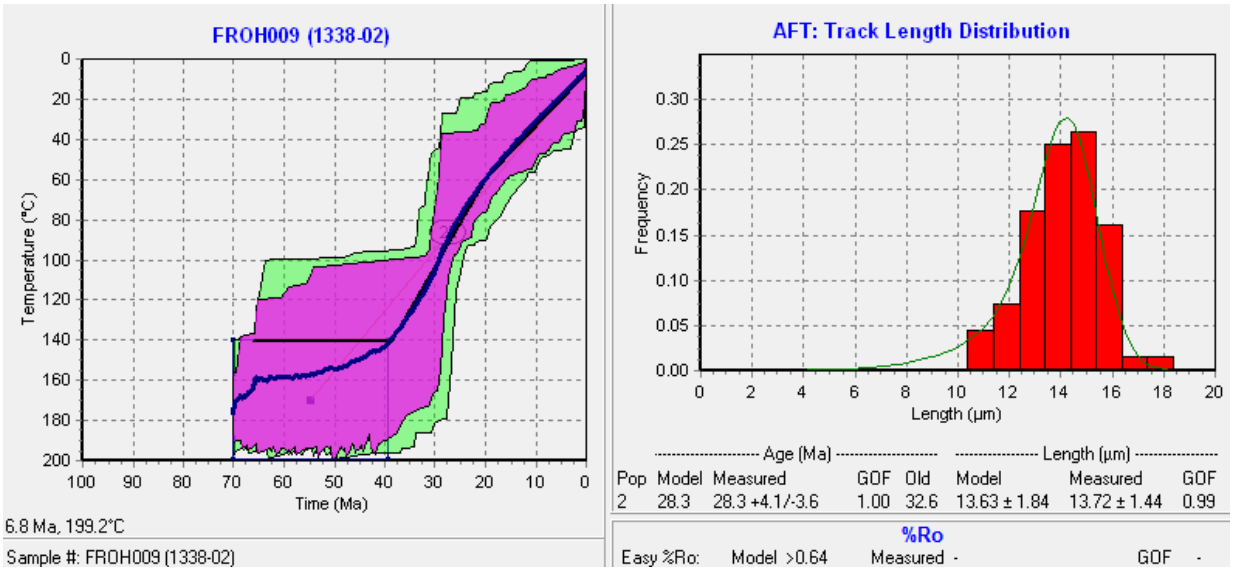

Figure C.4: Model 2 for apatite fission-track sample 1338-02.

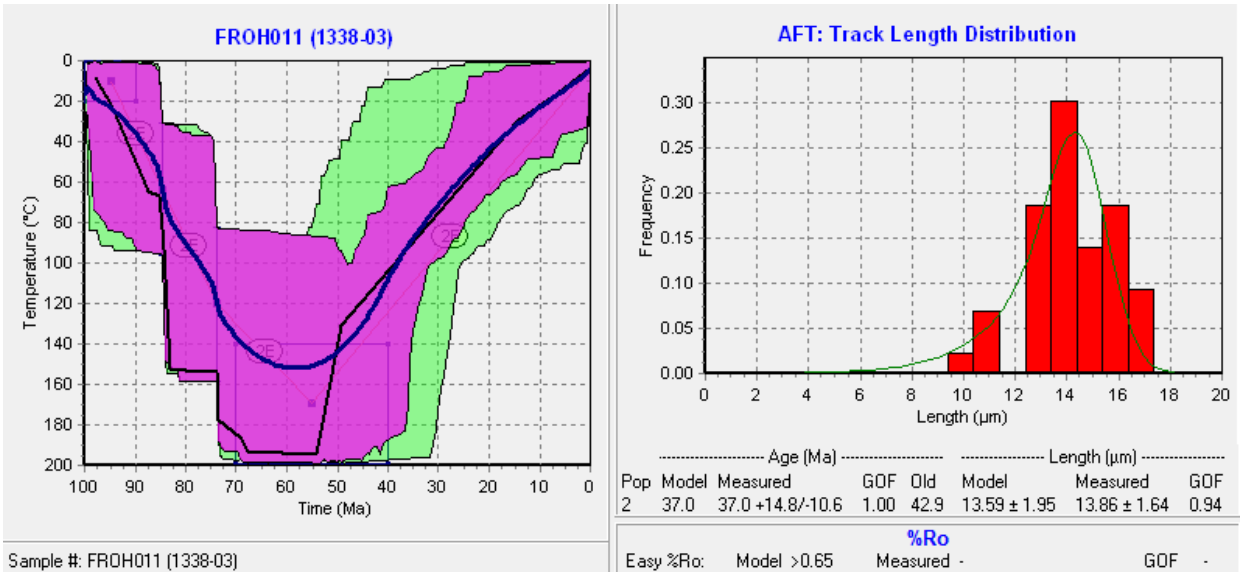

Figure C.5: Model 1 for apatite fission-track sample 1338-03.

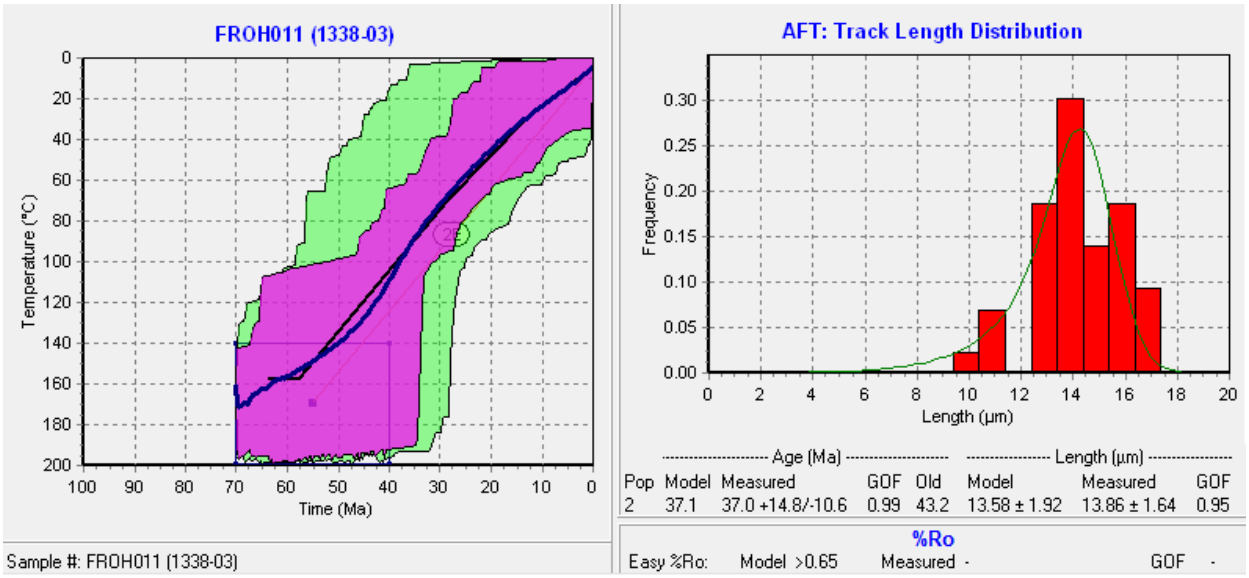

Figure C.6: Model 2 for apatite fission-track sample 1338-03.

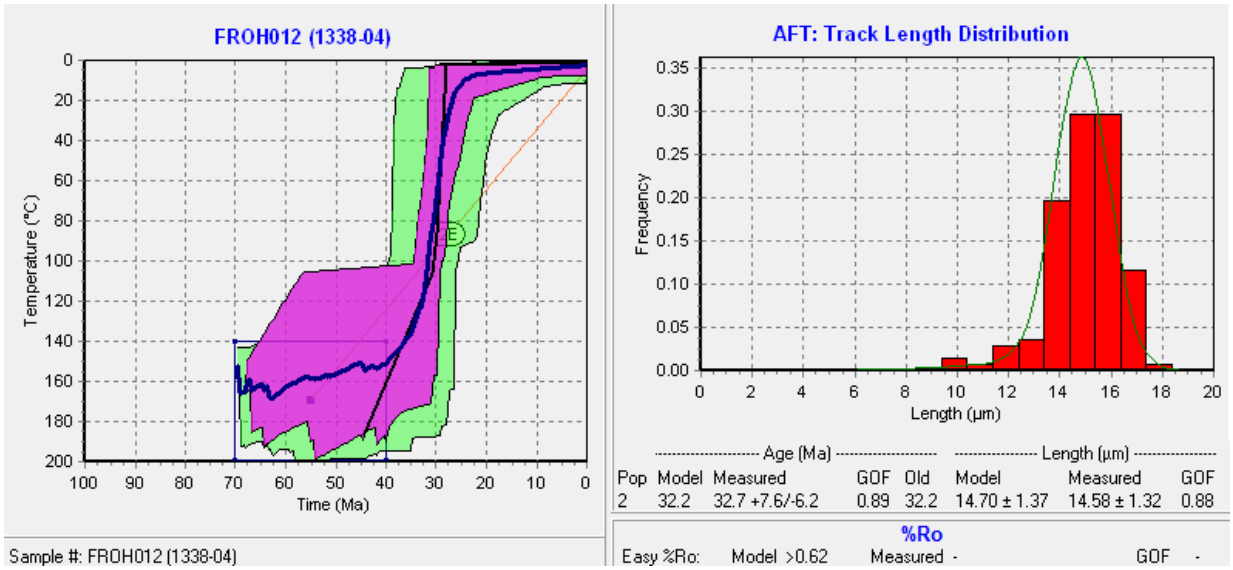

Figure C.7: Model 2 for apatite fission-track sample 1338-04.

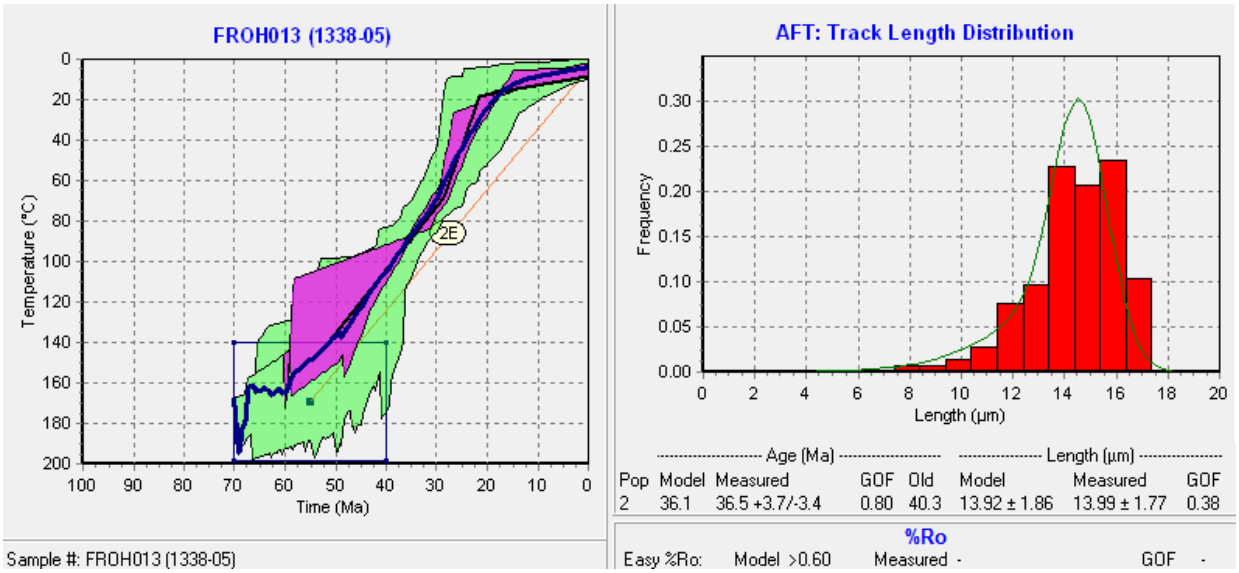

Figure C.8: Model 2 for apatite fission-track sample 1338-05.

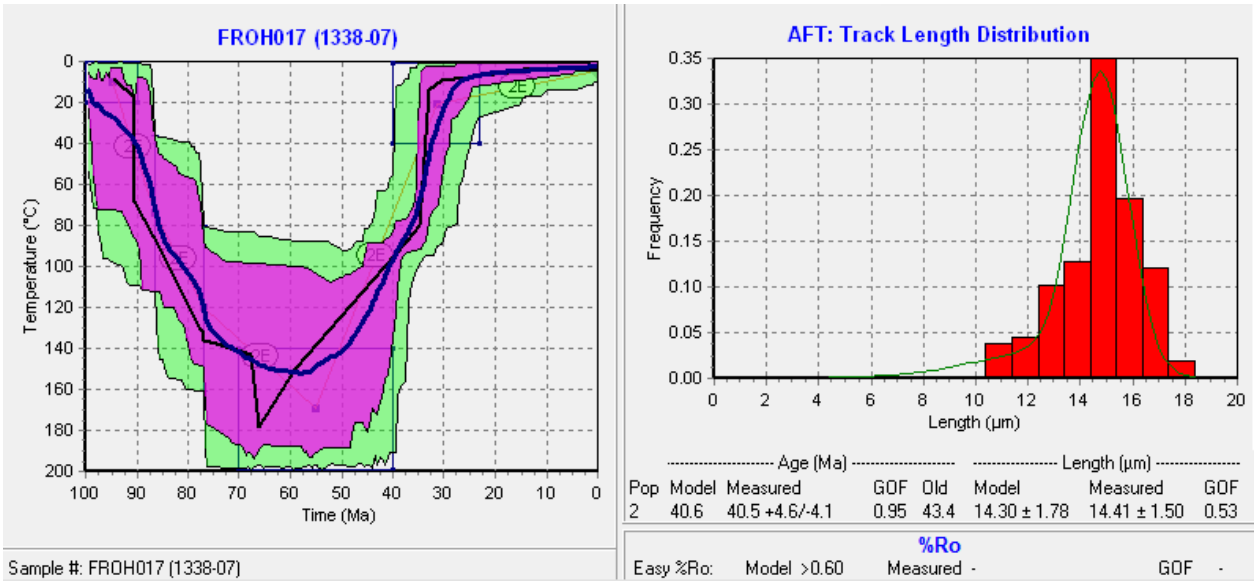

Figure C.9: Model 2 for apatite fission-track sample 1338-07.

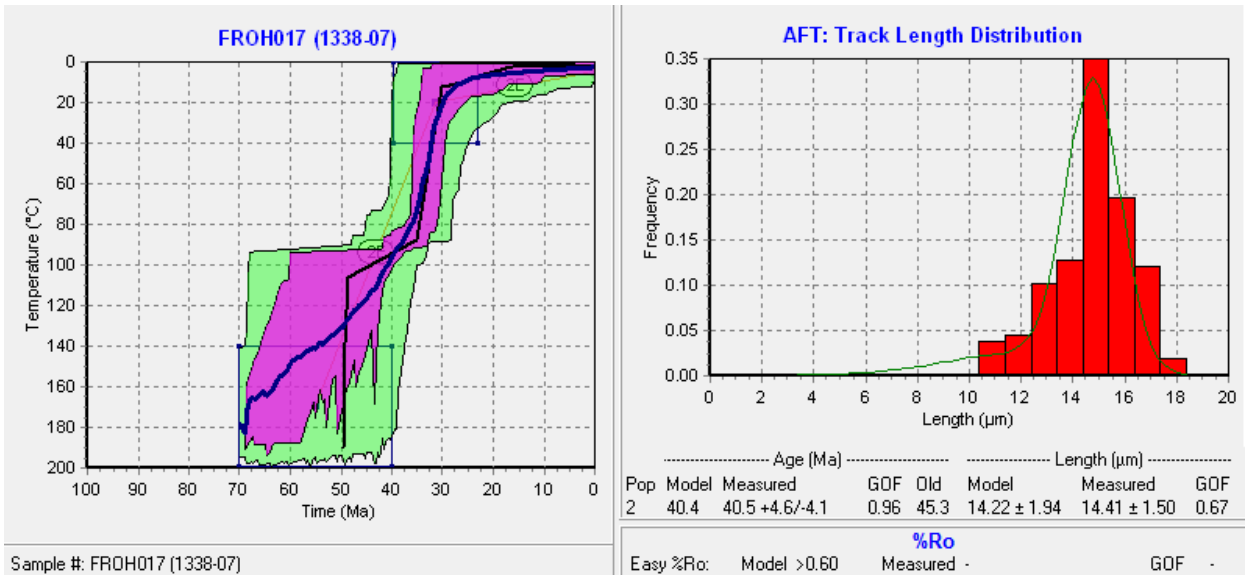

Figure C.10: Model 3 for apatite fission-track sample 1338-07.

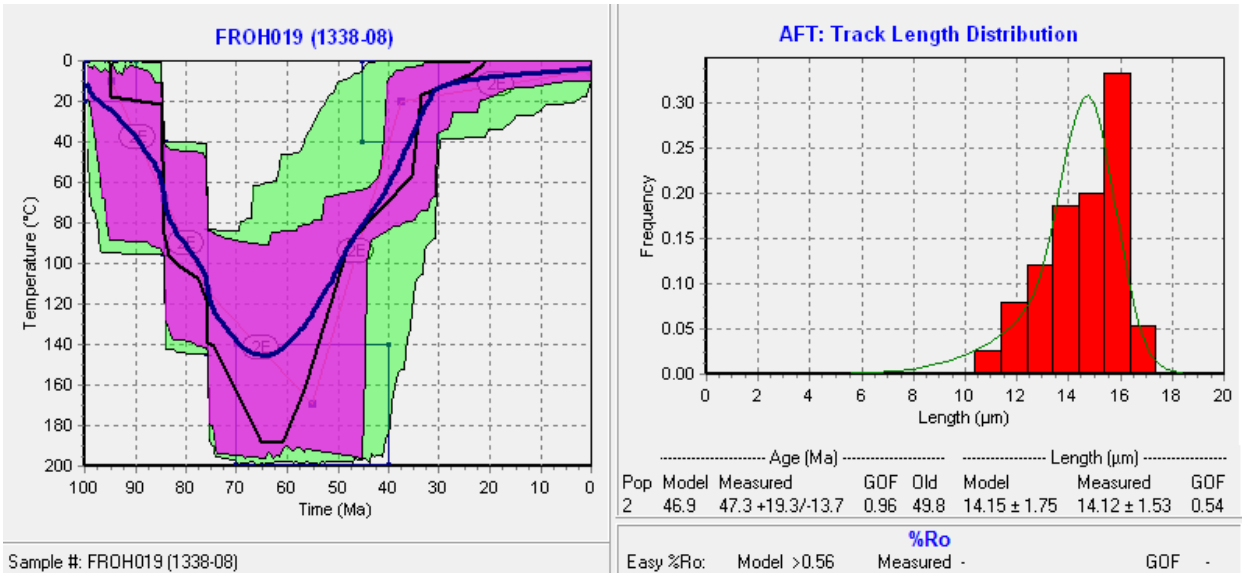

Figure C.11: Model 1 for apatite fission-track sample 1338-08.

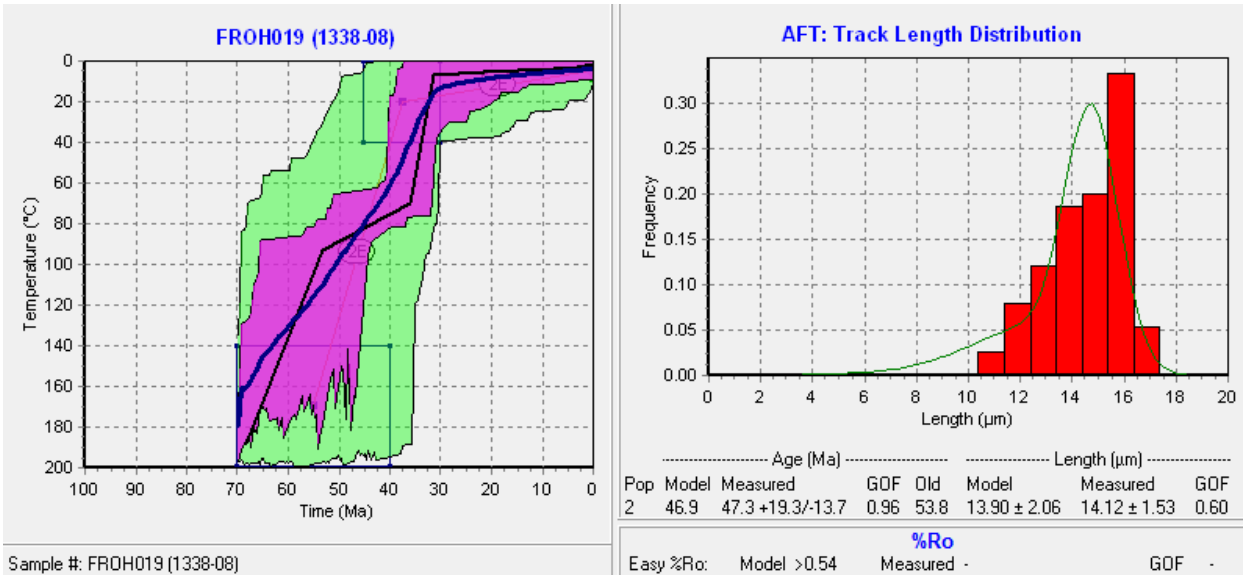

Figure C.12: Model 2 for apatite fission-track sample 1338-08.

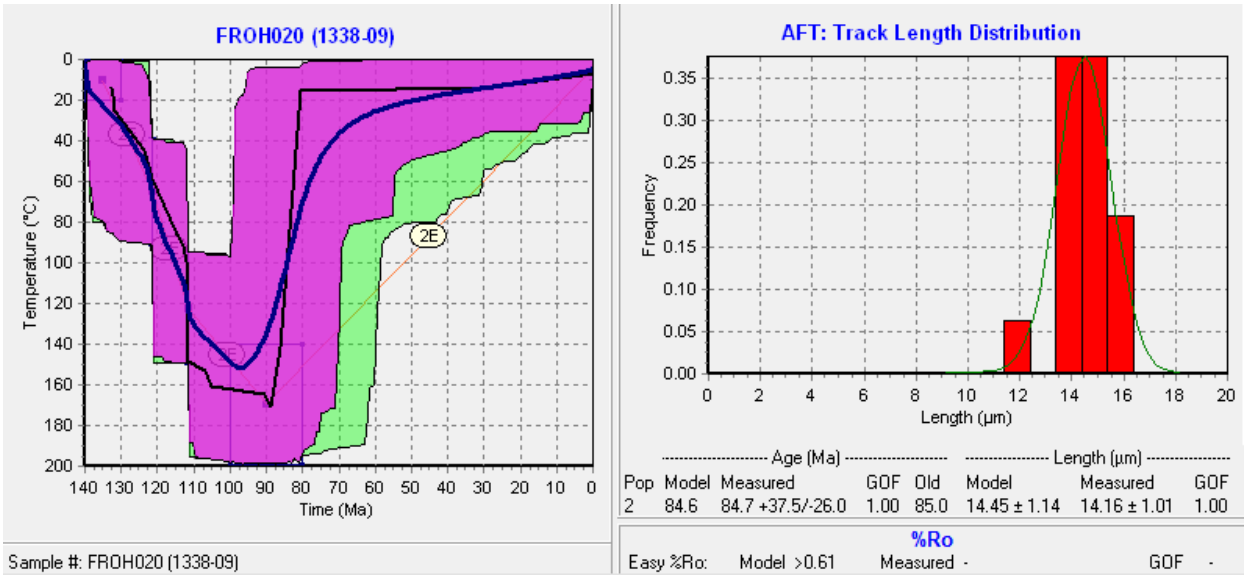

Figure C.13: Model 1 for apatite fission-track sample 1338-09.

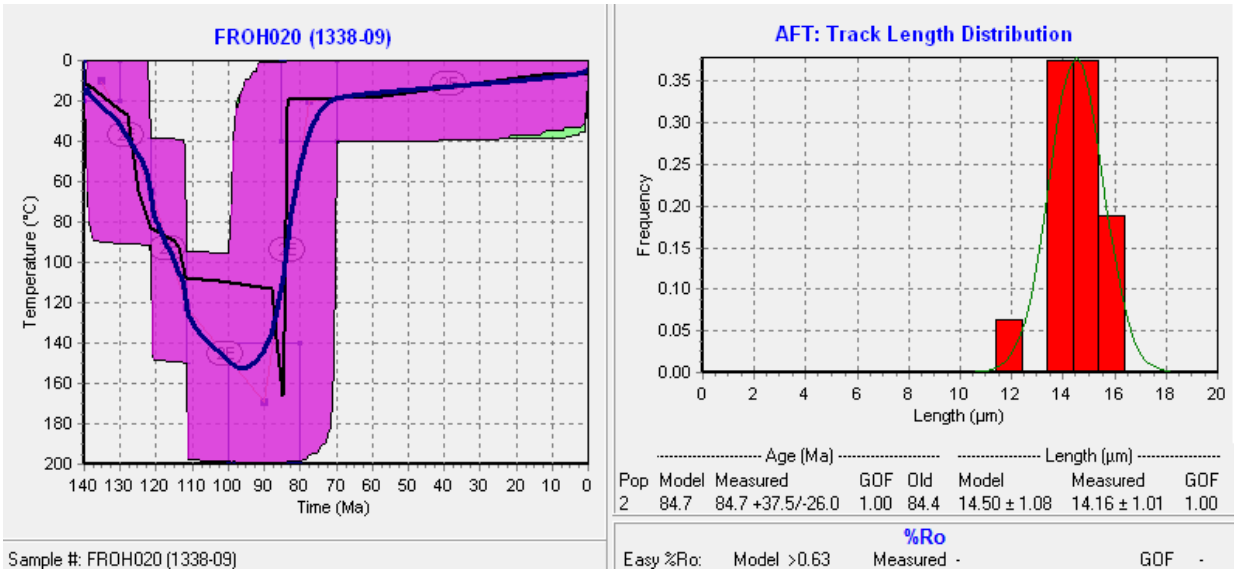

Figure C.14: Model 2 for apatite fission-track sample 1338-09.

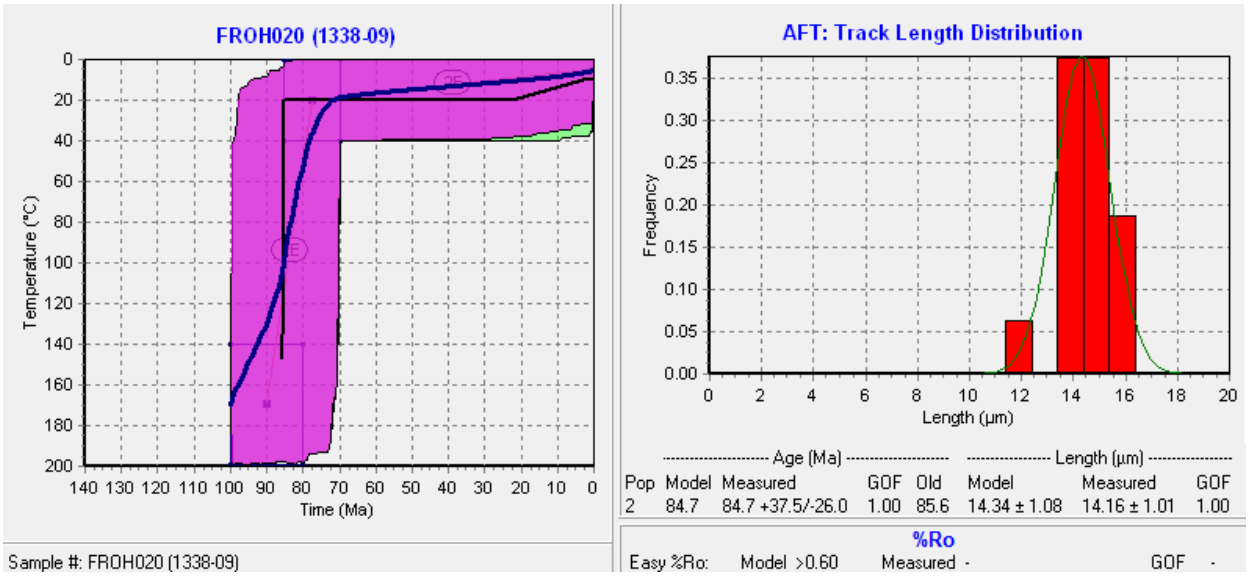

Figure C.15: Model 3 for apatite fission-track sample 1338-09.

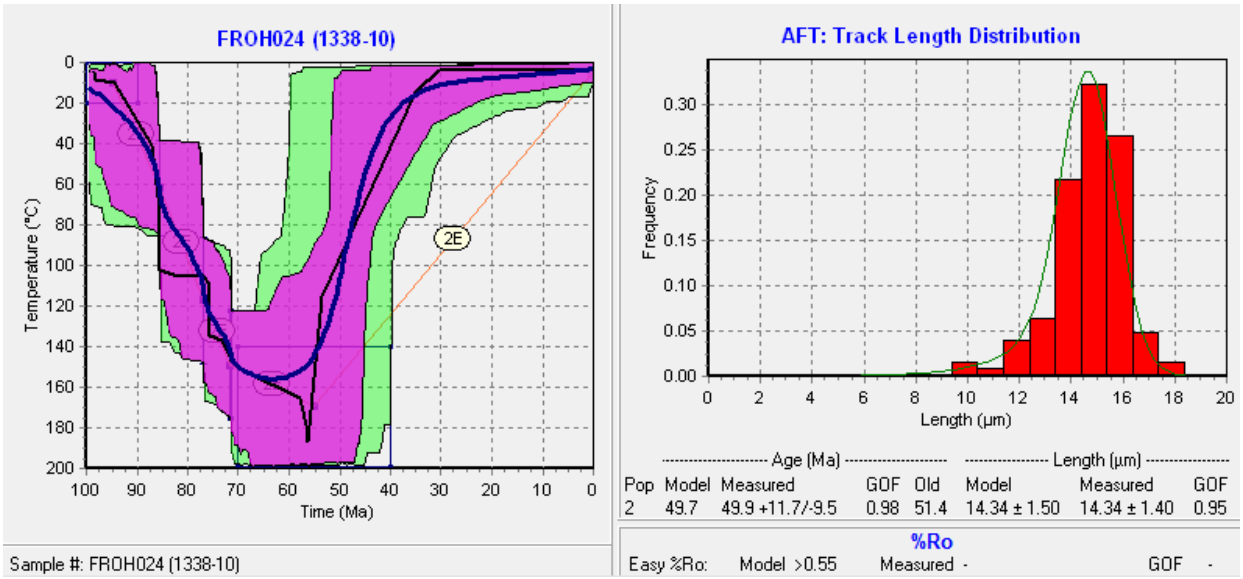

Figure C.16: Model 1 for apatite fission-track sample 1338-10.

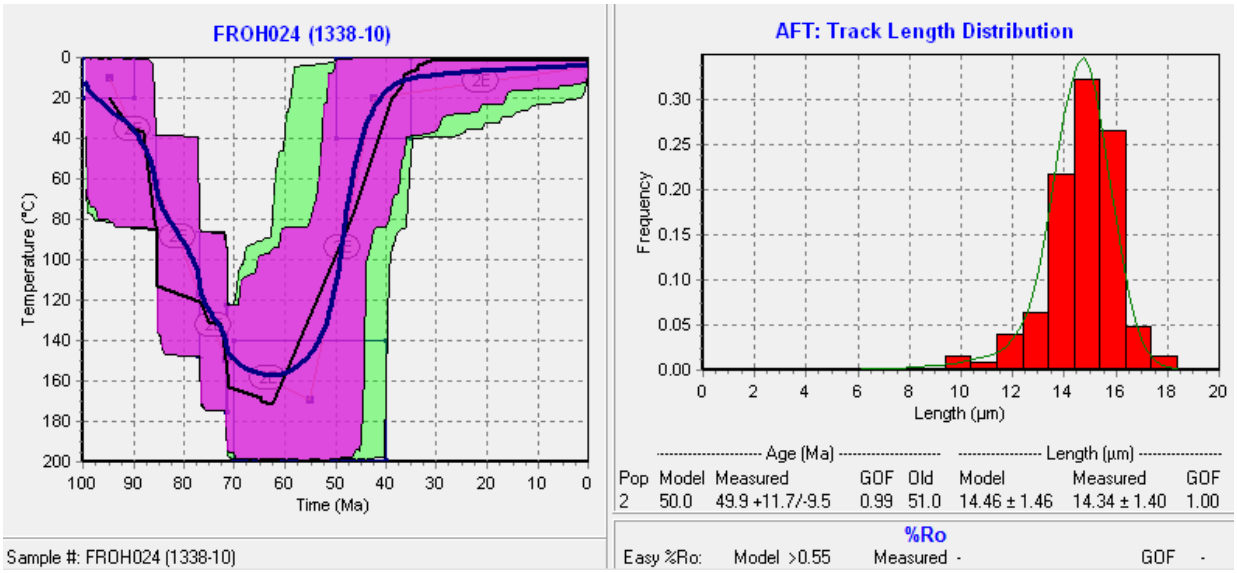

Figure C.17: Model 2 for apatite fission-track sample 1338-10.

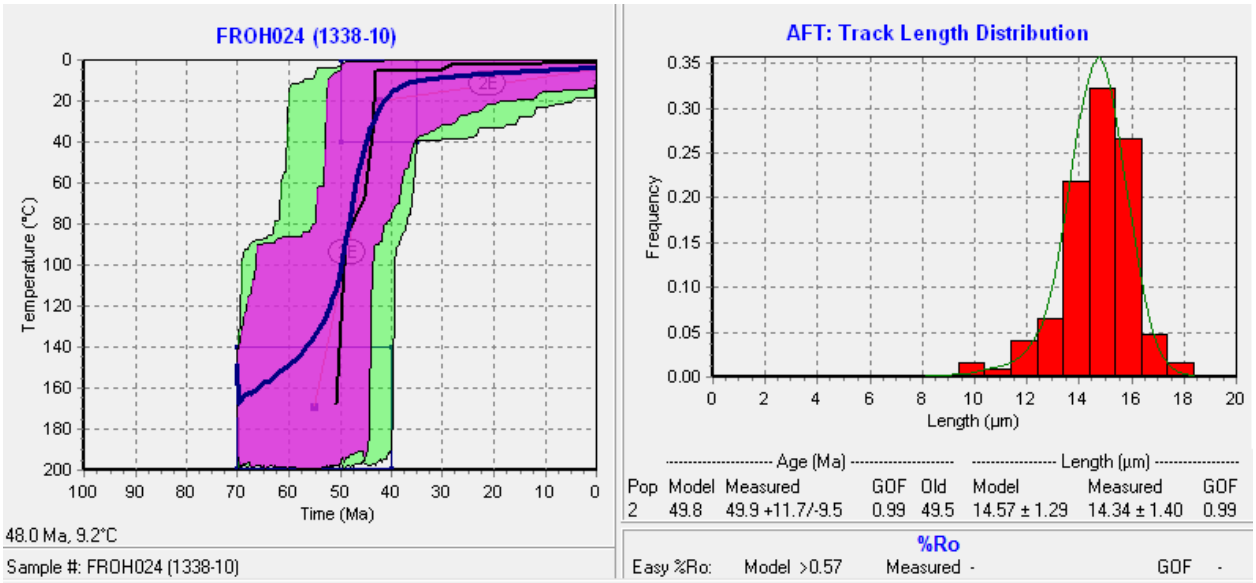

Figure C.18: Model 3 for apatite fission-track sample 1338-10.

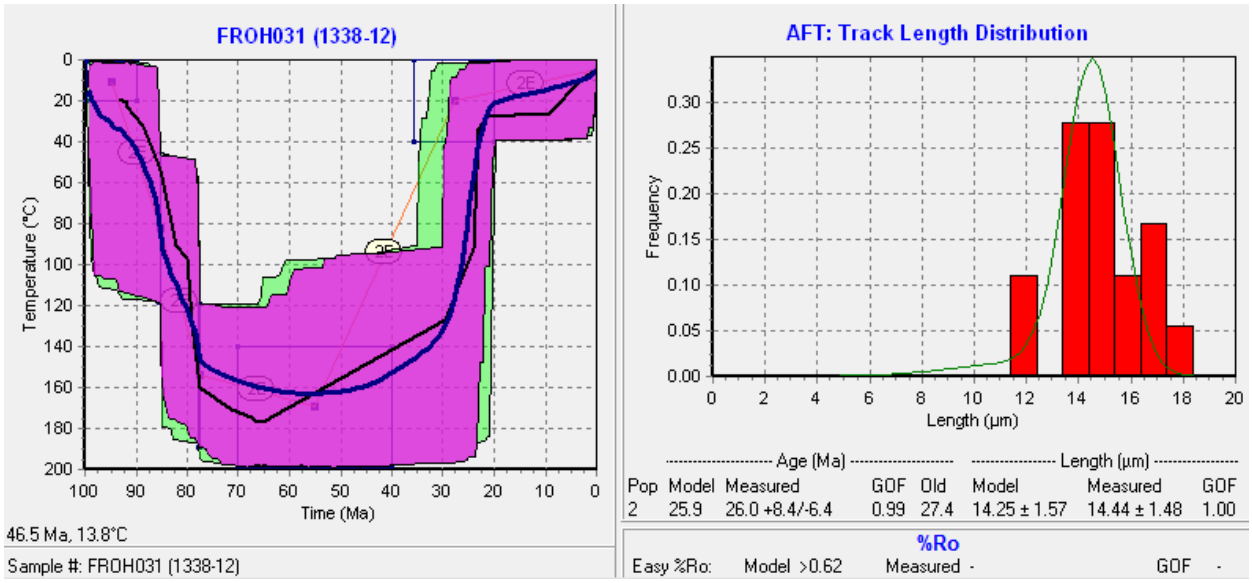

Figure C.19: Model 2 for apatite fission-track sample 1338-12.

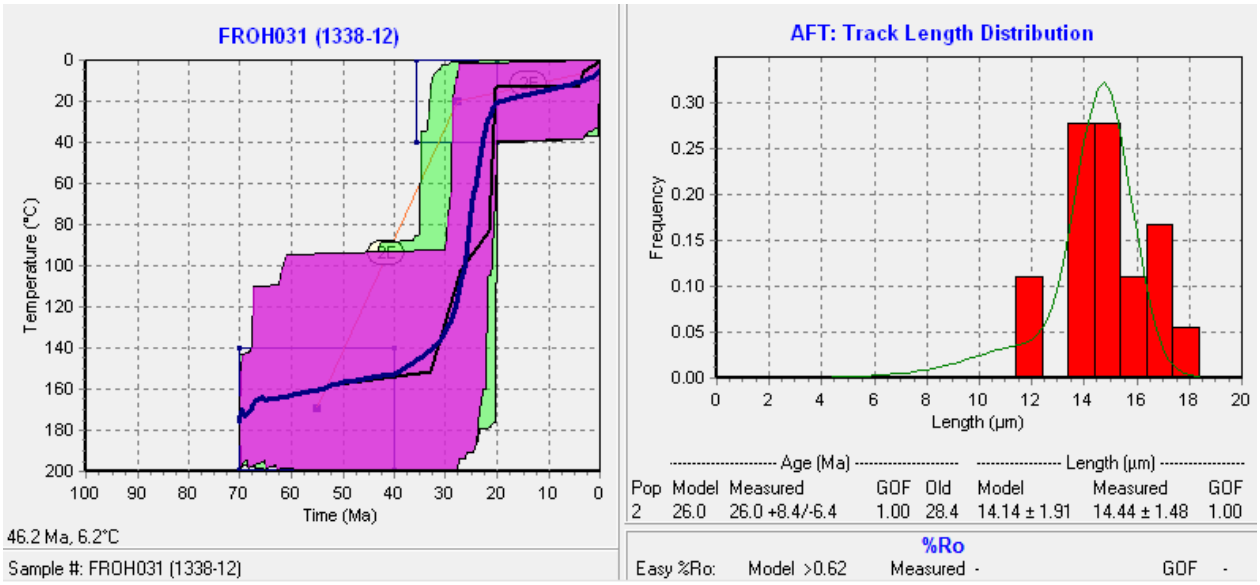

Figure C.20: Model 3 for apatite fission-track sample 1338-12.

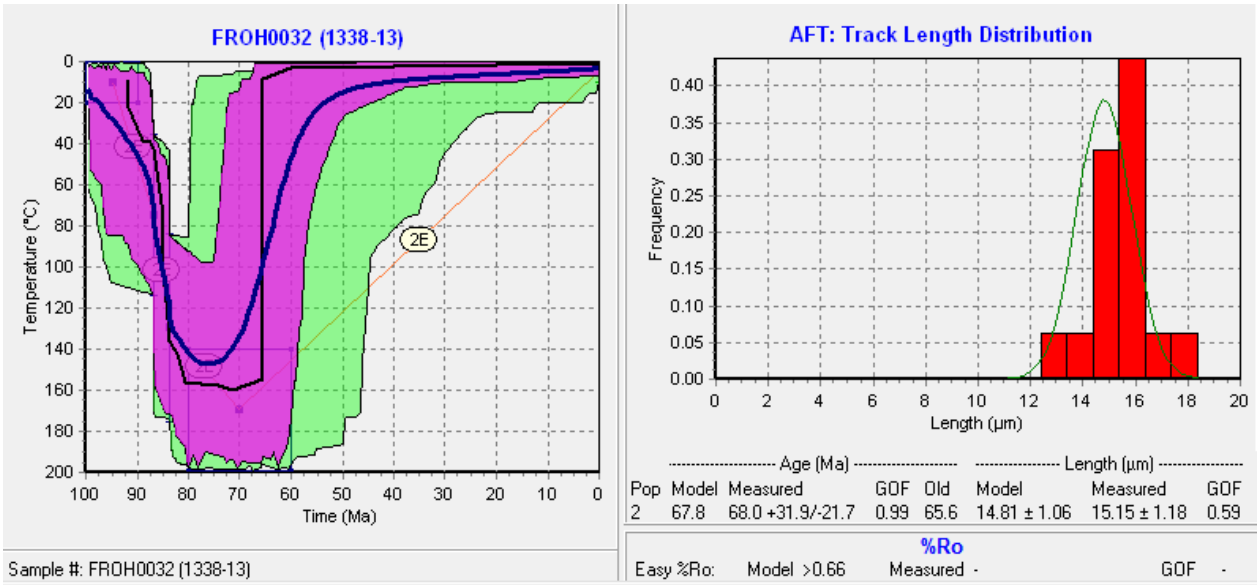

Figure C.21: Model 1 for apatite fission-track sample 1338-13.

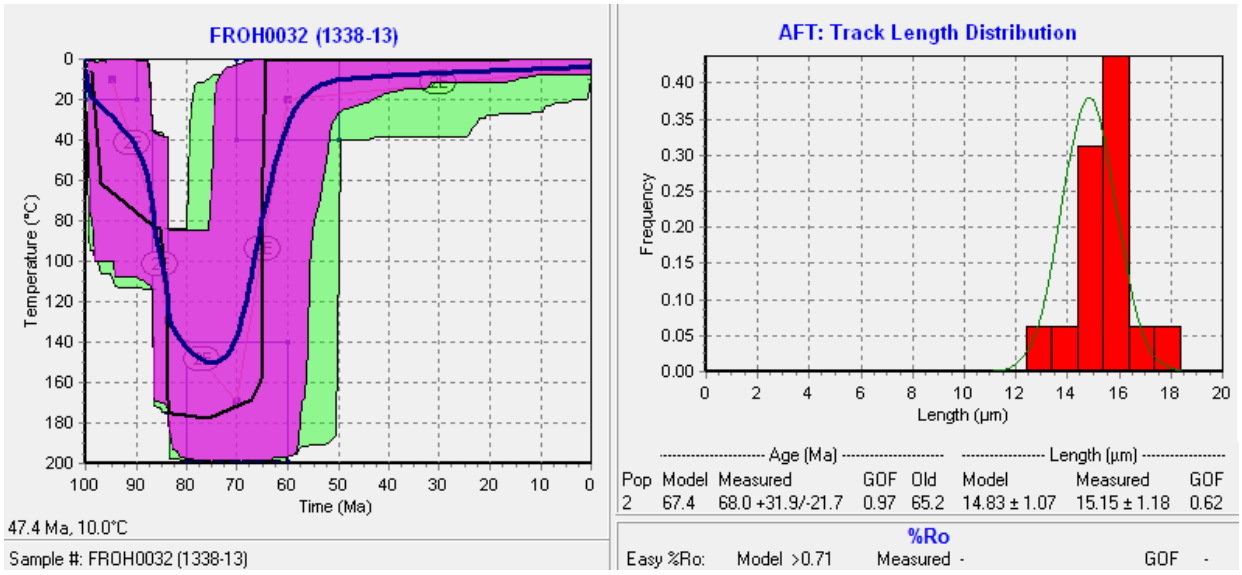

Figure C.22: Model 2 for apatite fission-track sample 1338-13.

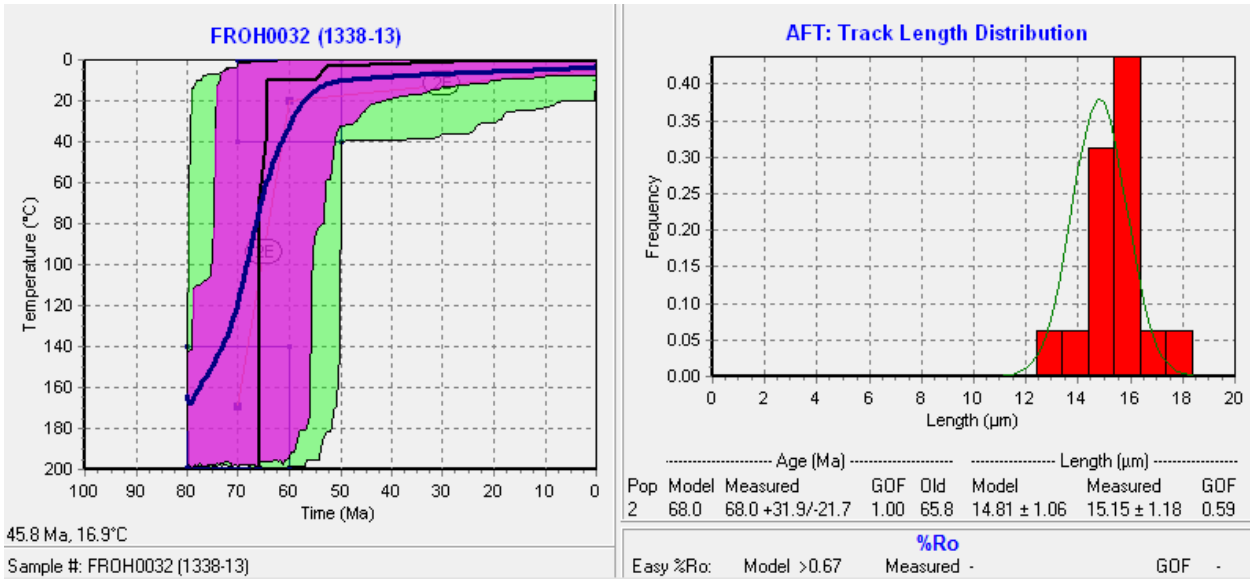

Figure C.23: Model 3 for apatite fission-track sample 1338-13.

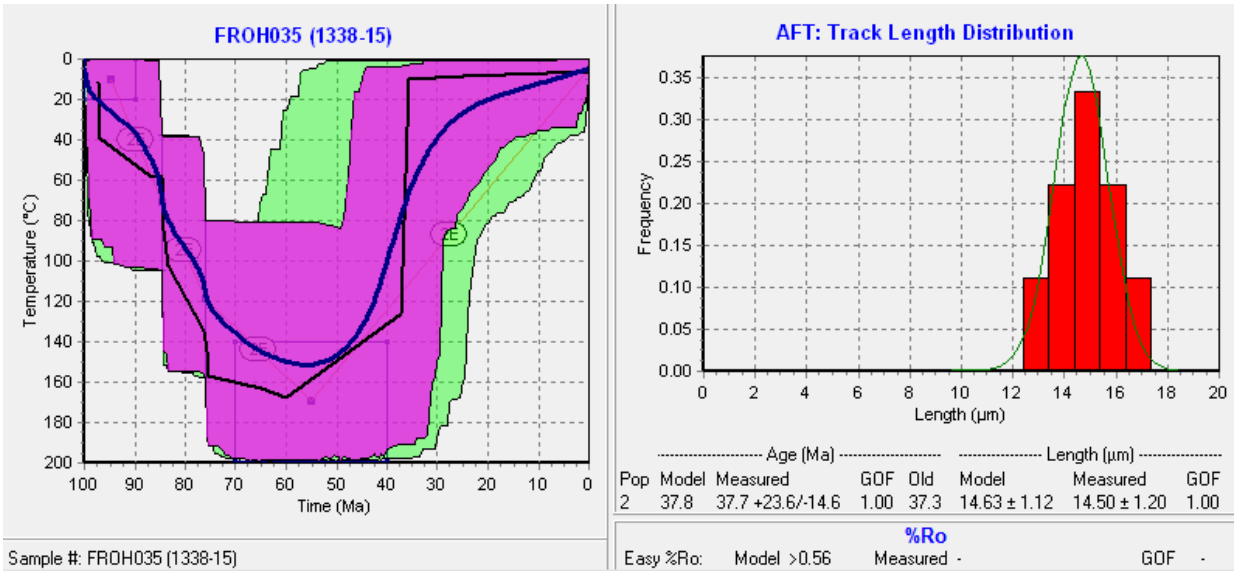

Figure C.24: Model 1 for apatite fission-track sample 1338-15.

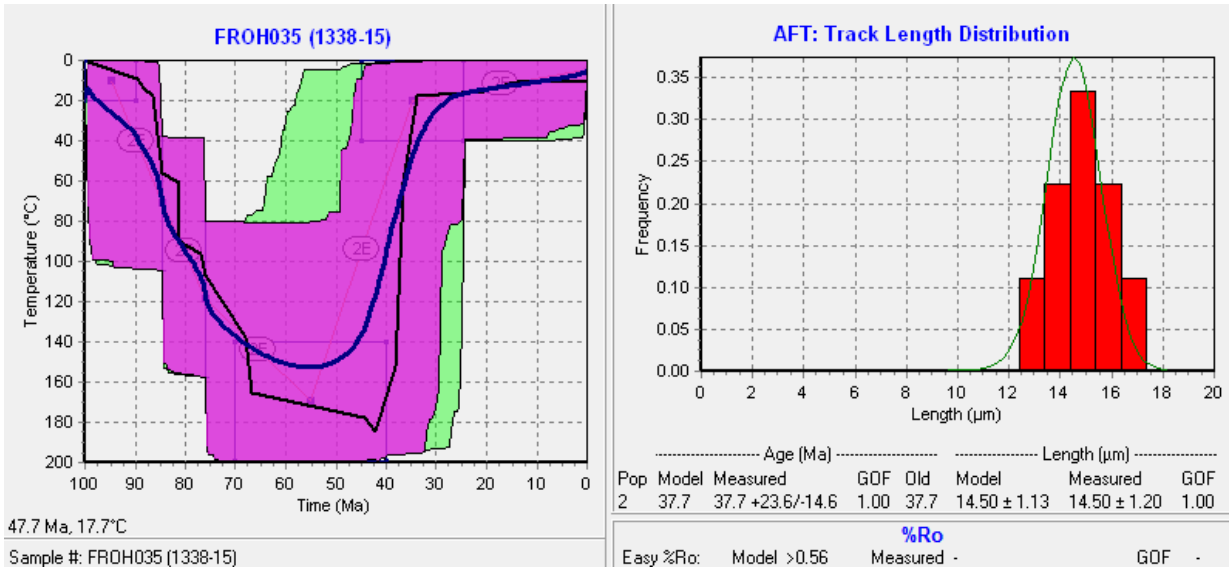

Figure C.25: Model 2 for apatite fission-track sample 1338-15.

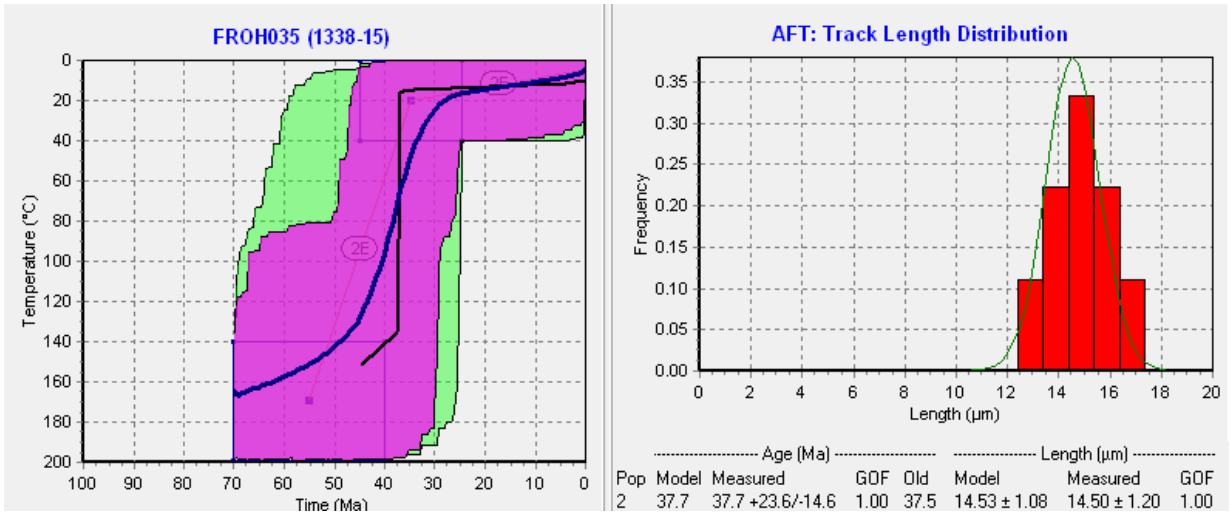

Figure C.26: Model 3 for apatite fission-track sample 1338-15.

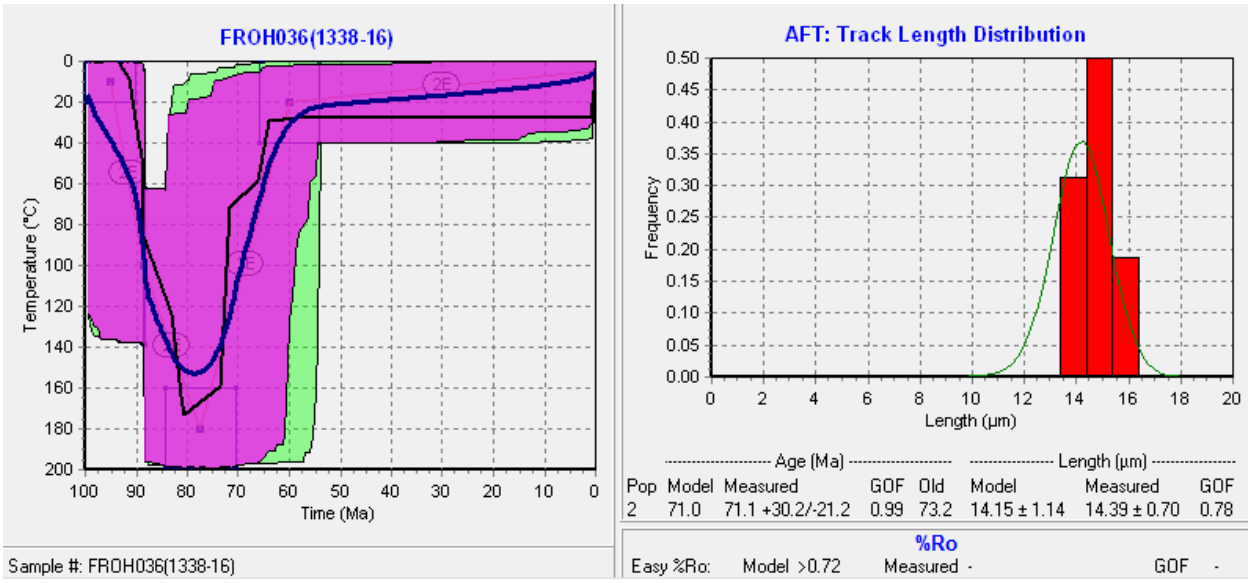

Figure C.27: Model 1 for apatite fission-track sample 1338-16.

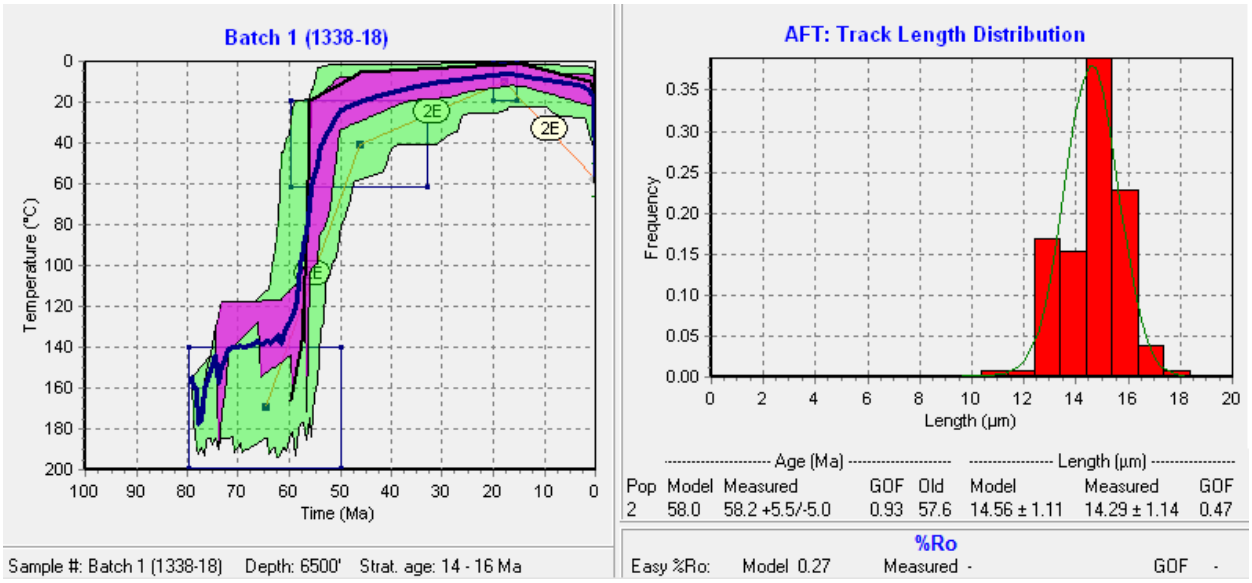

Figure C.28: Model 2 for apatite fission-track sample 1338-18.